

University of New Mexico

UNM Digital Repository

Nuclear Engineering ETDs

Engineering ETDs

Spring 5-10-1977

Effective Equation of State Measurements on Uranium Dioxide

Kenneth Orvis Reil

Follow this and additional works at: https://digitalrepository.unm.edu/ne_etds



Part of the [Nuclear Engineering Commons](#)

THE UNIVERSITY OF NEW MEXICO
ALBUQUERQUE, NEW MEXICO 87106

POLICY ON USE OF THESES AND DISSERTATIONS

Unpublished theses and dissertations accepted for master's and doctor's degrees and deposited in the University of New Mexico Library are open to the public for inspection and reference work. *They are to be used only with due regard to the rights of the authors.* The work of other authors should always be given full credit. Avoid quoting in amounts, over and beyond scholarly needs, such as might impair or destroy the property rights and financial benefits of another author.

To afford reasonable safeguards to authors, and consistent with the above principles, anyone quoting from theses and dissertations must observe the following conditions:

1. Direct quotations during the first two years after completion may be made only with the written permission of the author.
2. After a lapse of two years, theses and dissertations may be quoted without specific prior permission in works of original scholarship provided appropriate credit is given in the case of each quotation.
3. Quotations that are complete units in themselves (e.g., complete chapters or sections) in whatever form they may be reproduced and quotations of whatever length presented as primary material for their own sake (as in anthologies or books of readings) ALWAYS require consent of the authors.
4. The quoting author is responsible for determining "fair use" of material he uses.

This thesis/dissertation by Kenneth Orvis Reil has been used by the following persons whose signatures attest their acceptance of the above conditions. (A library which borrows this thesis/dissertation for use by its patrons is expected to secure the signature of each user.)

NAME AND ADDRESS

DATE

_____	_____
_____	_____
_____	_____
_____	_____
_____	_____

This dissertation, directed and approved by the candidate's committee, has been accepted by the Graduate Committee of The University of New Mexico in partial fulfillment of the requirements for the degree of

DOCTOR OF PHILOSOPHY

EFFECTIVE EQUATION OF STATE MEASUREMENTS
ON URANIUM DIOXIDE

Title

Kenneth Orvis Reil

Candidate

Department of Chemical and Nuclear Engineering

Department

Berman Spolsky

Dean

May 10, 1977

Date

Committee

August Cronenberg
Theodore B. Schuchter
Arthur V. Houghton
Robert L. Long

Chairman

EFFECTIVE EQUATION OF STATE MEASUREMENTS
ON URANIUM DIOXIDE

BY
KENNETH ORVIS REIL
B.S., University of Nevada Reno, 1970
M.S., University of New Mexico, 1972

DISSERTATION

Submitted in Partial Fulfillment of the
Requirements for the Degree of
Doctor of Philosophy in Nuclear Engineering
in the Graduate School of
The University of New Mexico
Albuquerque, New Mexico

May, 1977

LD
3781
N564R2725
cop. 2

ACKNOWLEDGMENTS

Many people assisted me during my research and the preparation of this dissertation. I would like to thank them at the risk of neglecting some.

I wish to express my appreciation to the members of my dissertation committee: Dr. August W. Cronenberg, Chairman, Dr. Robert L. Long, and Dr. Arthur V. Houghton, all from the University of New Mexico; and Dr. Theodore R. Schmidt from Sandia Laboratories. I am particularly grateful to Dr. Schmidt for his technical advice and guidance, and personal support throughout this project. I would also like to thank Dr. David M. Lucoff from Westinghouse, formerly of the University of New Mexico, for his assistance in identifying the research topic. I would like to thank Dr. Glenn A. Whan, Acting Chairman of the Chemical and Nuclear Engineering Department, for his support and assistance during my graduate studies at the University of New Mexico.

I am grateful to the U.S. Nuclear Regulatory Commission and Sandia Laboratories for funding this research and to Oak Ridge Associated Universities (A.E.C./ERDA Special Fellowship), Associated Western Universities, and Sandia Laboratories for financial support. I would like to thank Dr. Richard L. Coats of the Reactor Studies Division at Sandia Laboratories for his assistance, patience, and understanding during this work.

I would like to express deep appreciation to many members of Sandia Laboratories: to Allyn R. Phillips for advice and

programming assistance for the Data Acquisition and Display System; to Dale G. Pipher for assistance in procurement and fabrication of components; to J. C. Conant, Frank V. Thome, Robert D. Meyer, and Robert L. Williams from the ACPR operations group for their assistance; and to Dr. Daniel J. Sasmor for assistance in procuring the fuel samples and for postmortem microscopic examinations.

I am very grateful to Marilyn Smiel for typing and assembly of the final draft of this dissertation.

I am most grateful to my wife, Elizabeth; my children, Stefani and Steven; my parents; and Elizabeth's parents for their patience, assistance, understanding, and encouragement during this arduous and trying experience.

EFFECTIVE EQUATION OF STATE MEASUREMENTS
ON URANIUM DIOXIDE

BY
Kenneth O. Reil

ABSTRACT OF DISSERTATION

Submitted in Partial Fulfillment of the
Requirements for the Degree of
Doctor of Philosophy in Nuclear Engineering
in the Graduate School of
The University of New Mexico
Albuquerque, New Mexico
May, 1977

ABSTRACT

EFFECTIVE EQUATION OF STATE MEASUREMENTS ON URANIUM DIOXIDE

Kenneth O. Reil, Ph.D.
Department of Chemical and Nuclear Engineering
The University of New Mexico, 1977

The safety analysis of Liquid Metal Fast Breeder Reactor (LMFBR) systems requires knowledge of the vapor pressure of reactor fuels up to 6000 K. A new technique was developed to obtain experimental vapor pressure data for reactor fuel materials at high temperatures and pressures. Fuel samples are pulse fission heated in the Annular Core Pulse Reactor (ACPR) at heating rates comparable to those anticipated during a severe LMFBR transient. The vapor of reactor fuels may contain several dissociated fuel species, volatile fission products, and/or fission gas. The evolution of that pressure may be time or rate dependent. For these reasons, the terminology Effective Equation of State (EEOS) measurements was used to differentiate those results from the vapor pressure of pure materials. This technique can be easily applied to plutonium bearing and previously irradiated fuels.

A pressure transducer is used to monitor the pressure in a sealed graphite-lined volume containing the fuel sample during an ACPR transient. The energy input history to the sample is derived from the reactor power history, fission product inventory measurements, and neutron transport calculations. Energy losses from the sample are determined by linear inverse heat conduction

techniques using temperature histories derived from thermocouples located in the walls of the confining pressure cell. Because of nonuniformities in the distribution of fission energy deposition within the sample and because of the energy losses from the sample, it is not possible to define a unique energy content history. It is possible, however, to define bounds on the energy content. Bounds on the vapor pressure (formulated as pressure as a function of energy content) are derived through a point by point comparison of the pressure history with the bounds on energy content.

The EEOS technique was used to determine the vapor pressure of high purity uranium dioxide with an oxygen-to-metal ratio of 2.08. Energy depositions of up to 2720 J/g relative to room temperature were obtained, resulting in measured pressures in excess of 38 MPa. Bounds on the vapor pressure of $\text{UO}_{2.08}$ were found to be:

$$P(\text{MPa}) = \exp \left[(10.004 \pm 1.497) - \frac{(13.365 \pm 2.535)}{E(\text{kJ})} \right]$$

(upper pressure bound for $1.4 \text{ kJ} \leq E \leq 1.9 \text{ kJ}$), and

$$P(\text{MPa}) = \exp \left[(10.894 \pm 1.198) - \frac{(18.298 \pm 3.386)}{E(\text{kJ})} \right]$$

(lower pressure bound for $1.6 \text{ kJ} \leq E \leq 2.0 \text{ kJ}$). These results bound previous high temperature data reported by other investigators.

EFFECTIVE EQUATION OF STATE MEASUREMENTS
ON URANIUM DIOXIDE

BY
Kenneth O. Reil

ABSTRACT OF DISSERTATION

Submitted in Partial Fulfillment of the
Requirements for the Degree of
Doctor of Philosophy in Nuclear Engineering
in the Graduate School of
The University of New Mexico
Albuquerque, New Mexico
May, 1977

ABSTRACT

EFFECTIVE EQUATION OF STATE MEASUREMENTS ON URANIUM DIOXIDE

Kenneth O. Reil, Ph.D.
Department of Chemical and Nuclear Engineering
The University of New Mexico, 1977

The safety analysis of Liquid Metal Fast Breeder Reactor (LMFBR) systems requires knowledge of the vapor pressure of reactor fuels up to 6000 K. A new technique was developed to obtain experimental vapor pressure data for reactor fuel materials at high temperatures and pressures. Fuel samples are pulse fission heated in the Annular Core Pulse Reactor (ACPR) at heating rates comparable to those anticipated during a severe LMFBR transient. The vapor of reactor fuels may contain several dissociated fuel species, volatile fission products, and/or fission gas. The evolution of that pressure may be time or rate dependent. For these reasons, the terminology Effective Equation of State (EEOS) measurements was used to differentiate those results from the vapor pressure of pure materials. This technique can be easily applied to plutonium bearing and previously irradiated fuels.

A pressure transducer is used to monitor the pressure in a sealed graphite-lined volume containing the fuel sample during an ACPR transient. The energy input history to the sample is derived from the reactor power history, fission product inventory measurements, and neutron transport calculations. Energy losses from the sample are determined by linear inverse heat conduction

techniques using temperature histories derived from thermocouples located in the walls of the confining pressure cell. Because of nonuniformities in the distribution of fission energy deposition within the sample and because of the energy losses from the sample, it is not possible to define a unique energy content history. It is possible, however, to define bounds on the energy content. Bounds on the vapor pressure (formulated as pressure as a function of energy content) are derived through a point by point comparison of the pressure history with the bounds on energy content.

The EEOS technique was used to determine the vapor pressure of high purity uranium dioxide with an oxygen-to-metal ratio of 2.08. Energy depositions of up to 2720 J/g relative to room temperature were obtained, resulting in measured pressures in excess of 38 MPa. Bounds on the vapor pressure of $\text{UO}_{2.08}$ were found to be:

$$P(\text{MPa}) = \exp \left[(10.004 \pm 1.497) - \frac{(13.365 \pm 2.535)}{E(\text{kJ})} \right]$$

(upper pressure bound for $1.4 \text{ kJ} \leq E \leq 1.9 \text{ kJ}$), and

$$P(\text{MPa}) = \exp \left[(10.894 \pm 1.198) - \frac{(18.298 \pm 3.386)}{E(\text{kJ})} \right]$$

(lower pressure bound for $1.6 \text{ kJ} \leq E \leq 2.0 \text{ kJ}$). These results bound previous high temperature data reported by other investigators.

CONTENTS

	<u>Page</u>
ACKNOWLEDGMENTS	iii
ABSTRACT	vi
CONTENTS	viii
LIST OF FIGURES	xi
LIST OF TABLES	xvi
ABBREVIATIONS AND SYMBOLS	xviii
CHAPTER I DEFINITION OF RESEARCH PROBLEM	1
OVERVIEW OF FAST REACTOR SAFETY	2
DEFINITION OF EQUATION-OF-STATE	7
COUPLED NEUTRONICS-HYDRODYNAMICS METHODS	9
DEFINITION OF EFFECTIVE-EQUATION-OF-STATE	13
DESCRIPTION OF RESEARCH PROBLEM	14
CHAPTER II LITERATURE SURVEY	15
LOW TEMPERATURE EXPERIMENTS	15
HIGH TEMPERATURE TECHNIQUES	19
ANALYTICAL FORMULATIONS	30
CHAPTER III EXPERIMENT DESIGN AND PROCEDURES	39
EXPERIMENT CRITERIA	39
ACPR DESCRIPTION	40
TYPES OF EXPERIMENTS	45
EXPERIMENT COMPONENTS	46
DATA ACQUISITION AND REPRODUCTION SYSTEMS	66
TRANSDUCER CALIBRATION	70
EXPERIMENT PROCEDURES	71

CONTENTS, continued

	<u>Page</u>
CHAPTER IV DATA REDUCTION AND ANALYSIS	79
NOTATION	79
DIGITIZATION AND CONVERSION	80
RADIATION NOISE CORRECTION AND DIGITAL FILTERING TECHNIQUES	84
ENERGY INPUT HISTORIES	87
ENERGY LOSS HISTORY	92
PRESSURE-ENERGY FUNCTIONAL RELATIONSHIPS	102
CHAPTER V EXPERIMENT RESULTS AND DISCUSSION	105
BUILDUP EXPERIMENTS	105
VAPOR-PRESSURE EXPERIMENTS	109
ESTIMATES OF ERRORS	128
VAPOR PRESSURE ESTIMATES BASED ON CHEMICAL EQUILIBRIUM	135
COMPARISON WITH OTHER RESULTS	151
POSTMORTEM	157
CHAPTER VI CONCLUSIONS AND RECOMMENDATIONS	173
APPENDIX A SELECTED MECHANICAL AND THERMOPHYSICAL PROPERTIES OF MATERIALS	177
APPENDIX B MECHANICAL DRAWINGS OF EXPERIMENTAL COMPONENTS	183
APPENDIX C DESCRIPTIONS OF COMMERCIAL PRESSURE CELL COMPONENTS	195
"C"-SEALS	195
THERMOCOUPLES	195
STRAIN GAGES	195
ADHESIVES	195

CONTENTS, concluded

	<u>Page</u>
KAMAN PRESSURE TRANSDUCER	196
APPENDIX D DETAILED EXPERIMENT PROCEDURES	201
APPENDIX E FISSION ENERGY DEPOSITION MEASUREMENT BY 140Ba - 140La FISSION PRODUCT INVENTORY ANALYSIS	208
APPENDIX F DIGITAL FILTERING TECHNIQUE	214
APPENDIX G INVERSE HEAT CONDUCTION TECHNIQUES	221
APPENDIX H REPRESENTATIVE DATA FROM ONE EXPERIMENT	226
APPENDIX I DETAILED ASSESSMENT OF EXPERIMENTAL ERRORS	257
COMBINATION OF ERRORS	257
PRESSURE	257
AVERAGE ENERGY INPUT	258
PEAK ENERGY CONTENT	259
ENERGY LOSSES	259
CORRECTED AVERAGE ENERGY CONTENT	261
APPENDIX J JUSTIFICATION OF THE USE OF SPECIFIC HEAT AT CONSTANT PRESSURE	263
REFERENCES	269
CURRICULUM VITAE	275

LIST OF FIGURES

<u>Figure</u>		<u>Page</u>
I-1	P-V-T Surface for a Pure Material	8
I-2	Simplified Block Diagram for Coupled Neutronics Hydrodynamics Methods	11
II-1	Effusion Cell Experiment Geometry	17
II-2	Schematic Diagram of Electron Beam Heating Technique	28
II-3	Pressure Vs. Internal Energy (Menzies EOS)	33
II-4	Temperature Vs. Internal Energy (Menzies EOS)	34
III-1	Elevation of ACPR Reactor	41
III-2	Relative Axial Fluence	43
III-3	Relative Radial Fluence	43
III-4	ACPR Experiment Cavity Neutron Spectrum	44
III-5	Cross-Section of EEOS Inpile Package	47
III-6	Photo Micrographs of Transverse Section of Fuel Samples	53
III-7	Cross-Section of EEOS Pressure Cell	54
III-8	EEOS Pressure Cell Components	56
III-9	Typical Thermocouple Penetration	60
III-10	Components of EEOS Inpile Package	65
III-11	Block Diagram of Data Acquisition System	67
III-12	Block Diagram of Data Reproduction System	69
III-13	Sealed Pressure Cell Assembly	72
III-14	Completed Inner Assembly	74
III-15	EEOS Inpile Package	75
IV-1	Block Diagram of Data Reproduction System	81

LIST OF FIGURES, continued

<u>Figure</u>		<u>Page</u>
IV-2	Results of Radiation Noise Correction and Filtering Techniques for Typical Thermocouple Data	86
IV-3	Typical ACPR Pulse Shapes and Corresponding Pulse Integrals	89
IV-4	Fraction of Energy in Pulse Tail Vs. Total Pulse Energy Release	89
IV-5	Relative Fission Density for 30 Percent Enriched UO ₂ Irradiated in ACPR with 2.75 cm Polyethylene	91
IV-6	Heat Flux Histories Predicted by IHC Technique for Three "Average Temperatures"	96
IV-7	Heat Flux Integrals Predicted by IHC Technique for Three "Average Temperatures"	97
IV-8	Experimental Temperature and Calculated Temperatures at Thermocouple Location	99
IV-9	Heat Flux Histories Predicted by IHC Technique for Three Thermocouple Locations	100
IV-10	Heat Flux Integrals Predicted by IHC Technique for Three Thermocouple Locations	101
V-1	Results of EOS Buildup Experiments	107
V-2	Summary of Pressure Histories from EOS Vapor Pressure Measurements	113
V-3	Pressure and Energy Histories from EOS-UO2-1	118
V-4	Pressure and Energy Histories from EOS-UO2-2	119
V-4A	Pressure and Energy Histories from EOS-UO2-2 (continuation)	120
V-5	Pressure and Energy Histories from EOS-UO2-3	121
V-6	Pressure and Energy Histories from EOS-UO2-4	122
V-7	Pressure and Energy Histories from EOS-UO2-5	123
V-8	Pressure Vs. Energy Relationships Using Pressure and Peak Energy Data from EOS-UO2-1,2,3,4	124

LIST OF FIGURES, continued

<u>Figure</u>		<u>Page</u>
V-9	Pressure Vs. Energy Relationships Using Pressure and Corrected Average Energy Data from EEOS-UO2-2,3,4	126
V-10	Upper and Lower Bounds on Vapor Pressure of $\text{UO}_{2.08}$	127
V-11	Comparison of Pressure Vs. Peak Energy Relationships from EEOS-UO2-4 and EEOS-UO2-5	129
V-12	Net Experimental Uncertainties in Energy Bounds on the Vapor Pressure of $\text{UO}_{2.08}$	134
V-13	Comparison of Two Vapor Pressure Models Using Two Specific Heat Models	141
V-14	Vapor Pressures for UO_x Predicted by Blackburn Model	144
V-15	Total Pressure over Urania as a Function of Oxygen to Metal Ratio Predicted by Blackburn Model	145
V-16	Partial Pressures of Species over Urania Predicted by Blackburn Model	146
V-17	Total and Partial Pressures of Species over Urania as a Function of Oxygen to Metal Ratio for Energy Content of 2000 J/g Predicted by Blackburn Model	147
V-18	Species Flows in Evaporating Urania	150
V-19	Oxygen Concentration Profile in Evaporating Urania	150
V-20	Forced Congruent Evaporation of UO_2	150
V-21	Equilibrium Evaporation of UO_2	150
V-22	Total Vapor Pressure Above $\text{UO}_{2.00}$ for Equilibrium and Forced Congruent Vaporization	152
V-23	Comparison of EEOS Results with Other Experimental Data	154

LIST OF FIGURES, continued

<u>Figure</u>		<u>Page</u>
V-24	Comparison of EEOS Results with Extrapolations of Low Temperature Data	156
V-25	Comparison of EEOS Results with Blackburn Results	158
V-26	Sketch of Postmortem Graphite Crucible	160
V-27	Photo Micrograph of Crucible Fracture Surface	161
V-28	Photo Micrograph of Surface Transducer Buffer Disc	162
V-29	Photo Micrograph of Loose Debris on Bottom of Postmortem Crucible	163
V-30	Photo Micrograph Showing Spherical Debris	164
V-31	Photo Micrograph Showing Porous and Dense Debris	164
V-32	Cross-Section of Postmortem Graphite Crucible	166
V-33	Photo Micrograph of Right Edge of Buffer Disc	167
V-34	Photo Micrograph of Right Edge of Buffer Disc (Bright Illumination)	167
V-35	Photo Micrograph of Left Edge of Buffer Disc (Bright Illumination)	168
V-36	Photo Micrograph of Large Debris (Bright Illumination)	168
V-37	Photo Micrograph of UO_2 on Fracture Surface	170
V-38	Photo Micrograph of Colored Inclusions	171
V-39	Photo Micrograph of Colored Spherical Debris	171
V-40	Kaman Pressure Transducer with Buffer Disc	172
F-1	Butterworth Filter Power Gain Characteristics	215
F-2	Block Diagram of Filter with N_s Stages	217
F-3	Zero Phase Shift Filter Using Time Reversal	217

LIST OF FIGURES, concluded

<u>Figure</u>		<u>Page</u>
F-4	Larger Data Set Formed to Eliminate Discontinuities	219

LIST OF TABLES

<u>Table</u>		<u>Page</u>
I-1	Properties of Reactor Fuels	3
II-1	Summary of Measurements of Vapor Pressure over Urania	20
II-2	Vapor Pressure over UO_2 from the Ohse Technique	25
II-3	Vapor Pressure Data from Benson Technique	30
II-4	Critical Constants for UO_2 Estimated by Different Authors	36
II-5	Typical Vapor Pressures for Irradiated Mixed Oxide Fuel	37
III-1	Isotopic Analysis of UO_2 Powders	50
III-2	UO_2 Powder (Unwaxed) Data	50
III-3	UO_2 Research Samples Spectrochemical Analysis Results (ppm)	51
III-4	UO_2 Research Samples Fabrication Data (Average)	52
IV-1	Fraction of Total Energy Release Associated with Prompt Pulse	90
V-1	Summary of EEOS Pressure Measurement Experiments	112
V-2	Computation of Initial Pressure Condition in EEOS- UO_2 -5 Pressure Experiment from Pressure Vs. Peak Energy Relationships	130
V-3	Estimated Errors in Measured and Derived Parameters	132
A-1	Selected Properties of Uranium Dioxide	178
A-2	Thermophysical and Mechanical Properties of Uranium Dioxide	179
A-3	Room Temperature Properties of AXF Graphite	180
A-4	Thermophysical Properties of AXF Graphite	181
A-5	Selected Properties for Inconel-718	182

LIST OF TABLES, concluded

<u>Table</u>		<u>Page</u>
E-1	Summary of Errors Associated with Fission Product Inventory	213
H-1	Filtered Experiment Data Histories from ACPR No. 7863 Corrected for Radiation Induced Signals by Data from ACPR No. 7836 for Sample 30-10	227
H-2	Integrated Reactor Power Histories from ACPR No. 7836 and ACPR No. 7863	240
H-3	Filtered Experiment Data Histories from ACPR No. 7866 Corrected for Radiation Induced Signals by Data from ACPR No. 7842 for Sample 30-11	242
H-4	Integrated Reactor Power Histories from ACPR No. 7842 and ACPR No. 7866	255

ABBREVIATIONS AND SYMBOLS

a	distance
a	inner radius
a	reflection parameter
A	constant
A	transition probability
A	area
a_n	weighting coefficients
a_x	chemical activity of species x
$A_{i,j}$	polynomial coefficient
ACPR	Annular Core Pulse Reactor
ADC	Analog to Digital Converter
At%	atom percent
b	backscatter parameter
b	outer radius
B	constant
B	bulk modulus
b_n	weighting coefficients
B'	$\partial B / \partial P$
C	constant
C	magnitude of calibration voltage
C_p	specific heat at constant pressure
C_{pj}	$\frac{\partial T_{m+j}}{\partial A_p}$
C_{sat}	specific heat along the saturation curve
C_v	specific heat at constant volume

ABBREVIATIONS AND SYMBOLS, continued

CINDA-3G	Chrysler Improved Numerical Differencing Analyzer for Third Generation Computers
d	effusion target - cell dimension
d	decay probability
D, d	data value
D	constant
D	diffusion coefficient
DADS	Data Acquisition and Display System
E, e	energy
EOS	Equation of State
EEOS	Effective Equation of State
EEOS-UO2-x	designation of vapor pressure measurement series
EFRAC	fraction of energy deposited during prompt pulse
f	filter input
F	force
f_c	cutoff frequency
$f(x)$	function
f_o	force
f_{rel}	number of degrees of freedom
FM	frequency modulated
FPI	fission product inventory
g	filter output
g	transition statistical weight
G	modulus of rigidity
H	enthalpy

ABBREVIATIONS AND SYMBOLS, continued

$H(z)$	power gain function
HCDA	Hypothetical Core Disruptive Accident
I	moment of inertia
I	relative spectrum intensity
\dot{I}_z	thrust
IHC	inverse heat conduction
IP, ip	integral power
IR	infra-red
j_x	net flow of species x
k	thermal conductivity
K	chemical equilibrium constant
l	length
L	characteristic length
LASL	Los Alamos Scientific Laboratory
LMFBR	Liquid Metal Fast Breeder Reactor
M, m	mass
\dot{m}	mass flow rate
M	molecular weight
N, n	number of moles
n_x	number of moles of species x per mole of uranium
N_p	number of counts per minute in photopeak
N_s	number of filter stages
N_x	number of atoms of species x
O/M	oxygen-to-metal ratio
O/U	oxygen-to-uranium ratio

ABBREVIATIONS AND SYMBOLS, continued

P	peak-to-total ratio
P	pressure
ppm	parts per million
PTA	peak to average
PWHM	pulse width at half maximum
\dot{Q}, \dot{q}	heat flux
r	number of future temperatures
r	radial coordinate
r	radius
R	gas constant
REBA	Relativistic Electron Beam Accelerator
RP, rp	reactor pulse
S, s	magnitude of data signal voltage
S	entropy
S_o	area of effusion orifice
S_c	circumferential stress
S_r	radia stress
t	thickness
t	time
t	Temperature
T(E)	geometric detector efficiency
$T_{1/2x}$	half-life of species x
T_p	time of peak power
T.D.	theoretical density

ABBREVIATIONS AND SYMBOLS, continued

TF	tape factor
V	vaporization velocity
V	volume
V, v	voltage
W	velocity
W	weight
w/o	weight percent
Wt	weight
Wt%	weight percent
.. x	acceleration
z	axial coordinate
z	compressibility
α	compressibility
α	ratio of the rate of neutron capture to the rate of fission
α	thermal diffusivity
β	delayed neutron fraction
β	volume expansivity
γ	C_p/C_v
Δd	depth
ΔG_f^O	Gibbs free energy of formation
Δt	time step
ϵ	filter design parameter
η	fission factor
η	order of expansion of heat flux

ABBREVIATIONS AND SYMBOLS, continued

θ	oscilloscope angle
κ	isothermal compressibility
λ	wave length
λ_x	decay constant of species x
ν	average number of neutrons released per fission
ρ	density
σ_f	microscopic fission cross-section
σ	standard deviation
τ	Fourier Modulus
τ_h	half width
ϕ	temperature response function
ω	angular velocity

SUBSCRIPTS

ac	corrected average
avg	average
c	carrier gas
c	critical
cn	negative calibration
cp	positive calibration
e	experimental
eff	effective
f	final
f	fuel
i	initial

ABBREVIATIONS AND SYMBOLS, concluded

i	at time step
i	data channel
i	ith nonfuel species
L	lower
min	minimum
o	initial value
o	zero pressure
P	peak
r	reduced
sat	saturation
u	upper
u	uranium

CHAPTER I

DEFINITION OF RESEARCH PROBLEM

As the United States seeks new sources of energy for the future, considerable effort is being devoted to the development of the Liquid Metal Fast Breeder Reactor (LMFBR) power system. A significant portion of that development program has been devoted to the assessment of the impact of an LMFBR power plant on public health and safety. The safety analysis has attempted to describe the response of the reactor system to extreme accident conditions. During such accident excursions, the temperature of the reactor fuel could reach 6000 K. To accurately assess the consequences of such a hypothetical accident, it is necessary to know the thermophysical properties (particularly the equation of state and heat capacity) of the core materials at these extreme conditions.

The development of an experimental technique to measure the vapor pressure of reactor fuel materials at high temperatures and pressures is the subject of this dissertation.

This chapter describes the need for such data and its use in accident analysis. In Chapter II, a summary of previous vapor pressure measurements and analytical methods is presented. Subsequent chapters describe this new experimental technique, the methods of data reduction and analysis, the results of measurements on fresh UO_2 , and a comparison of those data with other experimental and analytical results.

OVERVIEW OF FAST REACTOR SAFETY

The large LMFBR systems under design today employ a stainless steel clad, mixed-oxide ($\text{PuO}_2\text{-UO}_2$) fuel and sodium coolant. The fuel, containing up to 20 percent plutonium by weight, is helium bonded to the cladding having a diameter of approximately 0.250 inches. A typical core may contain as many as 10^5 such fuel pins. Slightly more than one-third of the core volume is occupied by fuel. The sodium coolant volume is less than one-half of the core volume. The remainder of the core is made up of cladding and structural material. Typical peak fuel-element power ratings are 15 kW/ft.

Because of the large inventory of fissile material in the core (many critical masses), the very short prompt neutron life time (10^{-7} sec in fast reactors compared to 10^{-3} - 10^{-5} sec in thermal reactors), and the small delayed neutron fraction for Plutonium-239 (see Table I-1), the reactivity initiated accident has been of prime consideration for LMFBR safety analysis. These accidents can be divided into two classes. The first group are transients that are expected to occur during the lifetime of the reactor and which result in little or no damage to the fuel. The second group (designated Hypothetical Core-Disruptive accidents (HCDA)), which are not expected to occur during the life of the plant, would result in significant damage or disassembly of the reactor core.

Three reactivity feedback mechanisms are significant in the short term transient behavior of an LMFBR (Ke70, Sh69, Ok69).

TABLE I-1

Properties of Reactor Fuels*

Constants	Fissionable Fuels										Fertile Materials	
	Thermal					Fast					Fast	
	U ²³³	U ²³⁵	Pu ²³⁹	Pu ²⁴¹	U ²³³	U ²³⁵	Pu ²³⁹	Pu ²⁴¹	Th ²³²	U ²³⁸		
σ_f	527	577	790	1000	2.2	1.4	1.78	2.54	0.025	0.112		
β	0.0026	0.0065	0.0020	†	0.0027	0.0065	0.0020	0.0053	0.0204	0.0147		
ν	2.51	2.40	2.90	2.98	2.59	2.50	3.0	3.04	2.04	2.6		
η	2.28	2.06	2.10	2.13	2.42	2.20	2.6	2.73	2.0	2.27		
α	0.10	0.17	0.5	0.4	0.068	0.15	0.15	0.114		1.44		

σ_f - barn - microscopic fission cross-section.

β - delayed neutron fraction.

ν - average number of neutrons released per fission.

η - average number of neutrons emitted from fission per neutron absorbed in the fissile isotope.

α - ratio of the rate of neutron capture to the rate of fission.

* - Reference (E171).

† - No value given.

These are 1) the Doppler effect, 2) sodium voiding, and 3) fuel motion. The most reliable negative reactivity feedback in the LMFBR is the Doppler effect. The large amounts of sodium in the core and the oxygen in the fuel moderate the neutron flux to provide a number of neutrons with energies in the range 0.5 to 20 keV. As the fuel temperature increases, the total resonance absorption increases due to the decrease in self-shielding resulting from the Doppler broadening of the neutron capture resonances. The Doppler effect results in increased production of neutrons from the fissionable nuclei ^{233}U , ^{235}U , or ^{239}Pu , as well as increased neutron capture in fertile nuclei such as ^{238}U . Thus, there may be a net increase or decrease in reactivity, or a positive or negative Doppler coefficient, depending upon the ratio of numbers of fissile and fertile nuclei in the fuel. For reactors containing fuels of normal enrichments, the negative contribution of ^{238}U is much greater than the positive contribution from ^{235}U or ^{239}Pu resulting in an overall negative Doppler coefficient. The Doppler effect is sufficient to terminate small reactivity excursions.

Voids or density changes in the sodium coolant can have significant reactivity effects. These effects may be either positive or negative depending on location in the core. The loss of coolant reduces the parasitic absorption in sodium resulting in a positive reactivity effect. More importantly, as sodium is removed, the neutron spectrum becomes harder (more high energy neutrons). As the spectrum hardens, the ratio of capture to

fission in plutonium decreases (see Table I-1), the fast fission yield from ^{238}U and ^{240}Pu increases, and the ratio of the fission in plutonium to parasitic capture in ^{238}U and in fission products increases. These are all positive reactivity effects. The harder energy spectrum also reduces the magnitude of the negative Doppler effect. The loss of sodium also increases neutron leakage which is a negative reactivity effect. However, as the size of the core increases, the importance of neutron leakage decreases. As a result, sodium voiding has a strong spatial dependence. Near the center of the reactor where the leakage effects are small, the net sodium voiding coefficient of reactivity is positive. For large excursions where sodium density changes or sodium voiding are significant, the sodium reactivity effects can exceed the Doppler contributions.

Fuel expansion and motion constitute the third reactivity mechanism significant to LMFBR transient behavior. Fuel motion can be categorized in three general classes, dependent on the state of the core. These are:

- 1) fuel motion within cladding prior to clad failure;
- 2) motion of fuel into coolant channels following clad failure while subassemblies are still intact;
- 3) whole core motion during disassembly.

Like sodium voiding, fuel motion may yield either positive or negative effects. Prior to cladding failure, thermal expansion of the fuel and cladding can cause axial movement of the fuel which decreases fuel density and yields a negative reactivity effect.

This is a major mechanism for metallic fuels; however, its effectiveness in irradiated oxide fuels is reduced by fuel cracking and bonding to the clad. Molten fuel may move axially under the driving force of vapor bubble growth and expansion. These bubbles may contain fission gas, volatile fission product vapor, and/or fuel vapor. The magnitude of these effects is dependent on previous irradiation history including burnup and power histories which control the quantity of fission products and where they are retained in the fuel. Fuel bowing due to differential expansion in a thermal gradient also alters fuel density.

After cladding failure gross fuel motion is possible. Internal pressure, due to fission gas, volatile fission products, and/or fuel vapor, can force molten fuel through ruptures in the cladding into the coolant channel. There it may be swept along with sodium liquid or vapor to less reactive regions of the core (upper plenum regions, etc.). This would reduce fission rates and terminate the excursion. Molten fuel may freeze out at points near a cladding rupture with little reactivity effect. It is, however, conceivable that fuel could be swept from lower regions of the reactor to more reactive positions at the center of the core. It is also possible that fuel could slump into a more reactive configuration under the forces of gravity and vapor pressure. If this slumping were to occur coherently, involving significant amounts of fuel, very large positive reactivity insertion rates could occur, resulting in a prompt critical burst.

The ultimate termination of a prompt critical burst may be

rapid disassembly of the core. Such motion would leave the core in a less dense subcritical configuration terminating the power excursion.

The driving forces for fuel motion are (Ke73):

- 1) internal expansion pressures caused by heating the fuel;
- 2) internal pressures due to heating fission gas and volatile fission products found in irradiated fuel;
- 3) internal pressure due to fuel vapor;
- 4) external forces due to relative motion, past the fuel, of fission products, sodium vapor, or sodium liquid;
- 5) gravity.

Forces 1) through 3) above are defined by the energy content of the fuel and the equations of state (EOS) of the fuel and fission products.

DEFINITION OF EQUATION-OF-STATE

In the most general sense, an equation-of-state is an algebraic expression connecting $n+1$ state variables for a thermodynamic system characterized by n independent variables. Usually these equations apply to PvT systems which relate pressure P , specific volume v , temperature T , and composition.

The relationship of specific volume to temperature and pressure for a pure substance can be represented by a surface in three dimensions as shown in Figure I-1, where S , L , and G represent solid, liquid, and gas phases, respectively. The material behavior of real systems is often too complicated to be faithfully described by equations of convenient simplicity,

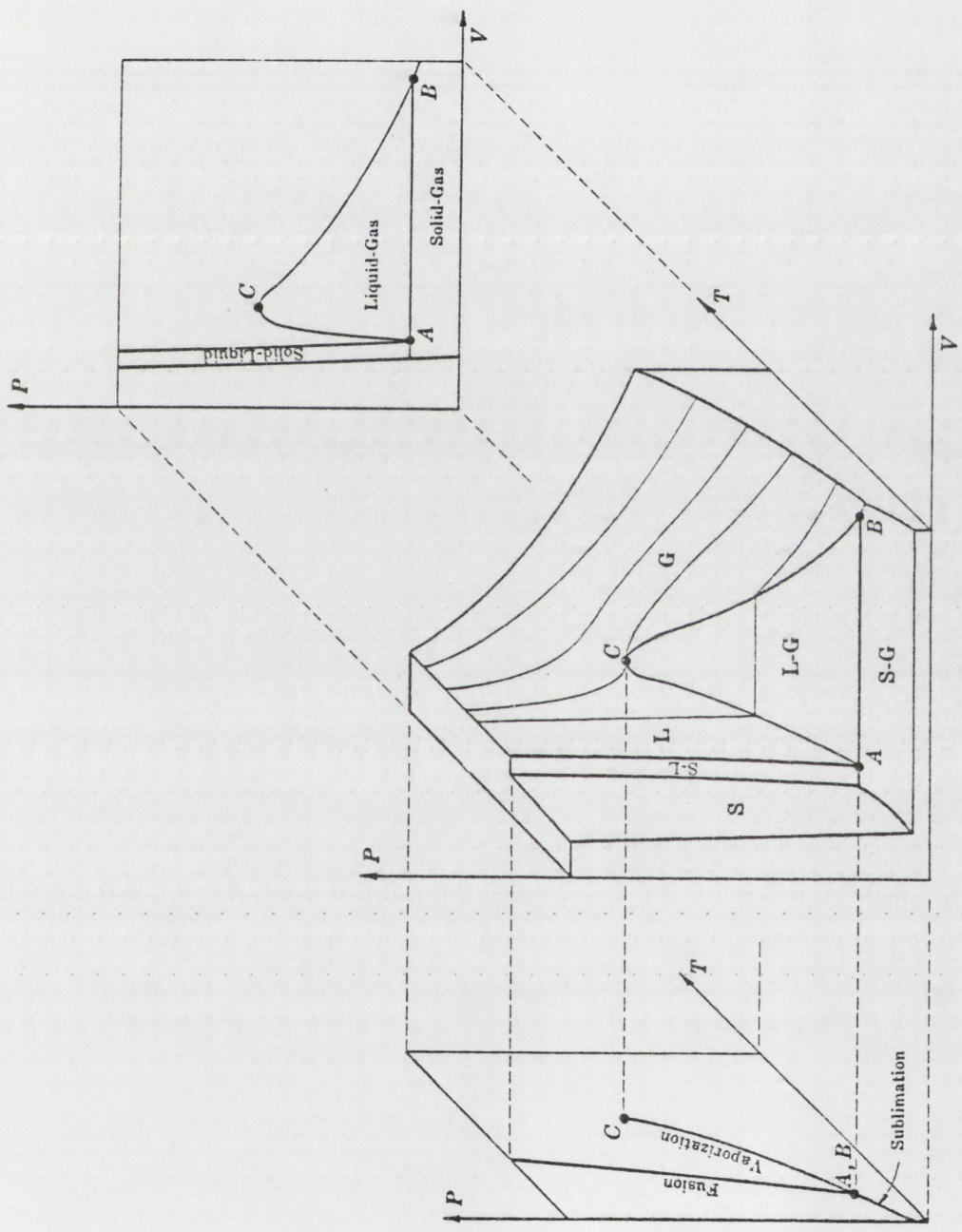


Figure I-1
P-V-T Surface for a Pure Material

except over very limited ranges of the state variables. One such limited range of state variables is the saturated vapor pressure curve shown on the P-T plane in Figure I-1. As shown in Figure I-1 for those conditions where liquid and vapor (L-G) coexist, pressure is a function of temperature only.

COUPLED NEUTRONICS-HYDRODYNAMICS METHODS

An HCDA can be divided into at least two phases: 1) a pre-disassembly phase, in which heat transfer is important, and 2) a disassembly phase, in which hydrodynamic effects are dominant. The pre-disassembly phase begins with an initiating system failure and proceeds through fuel failure and reassembly of the core into a prompt critical configuration. At that point the disassembly phase begins and continues until the prompt burst is terminated and the reactor is in a subcritical configuration.

The first analytical technique for determining the energy released during a disassembly accident was developed by Bethe and Tait (Be56). In its original form, this technique contained the following assumptions (Sh71):

- 1) The core can be modeled in spherical geometry.
- 2) Both the power-density distribution and the material reactivity worth are assumed to be independent of time.
- 3) Reactivity changes due to material motion can be calculated by first-order perturbation theory.
- 4) The duration of the disassembly excursion is so short that fuel expansion is negligible, thus permitting the

time behavior of the pressure to be calculated by ignoring any change in the fuel density.

- 5) The effects of pressure wave propagation can be neglected.

In this formulation, the only reactivity feedback was due to fuel motion. Other investigators (Ni64, Hi65, Me65) have modified the original Bethe-Tait analysis to include Doppler feedback and a density dependent equation-of-state. Other investigators (Ok59) developed techniques to explicitly compute the reactivity effects of fuel motion by neutron transport techniques. That formulation was still in one dimension. In the more recent accident analysis codes such as MARS (Hi67), VENUS (Sh70), and VENUS-II (Ja72), the hydrodynamics are solved in two-dimensional coordinates, but the methods are otherwise similar to the modified Bethe-Tait analysis. Since no clearly defined initiating event and pre-disassembly accident scenario exist, the input description of the core geometry, states of the core materials, and reactivity input rates for these codes has been subject to certain arbitrariness.

A simplified block diagram of the coupled neutronics-hydrodynamics methods is shown in Figure I-2. Note that the equation of state serves to couple the neutronic energy input with the hydrodynamic fuel motion. Thus, a formulation of pressure as a function of fuel energy content is the most convenient form for equation of state information.

The general form of the density-dependent equation of state used in accident analysis can be described in terms of three

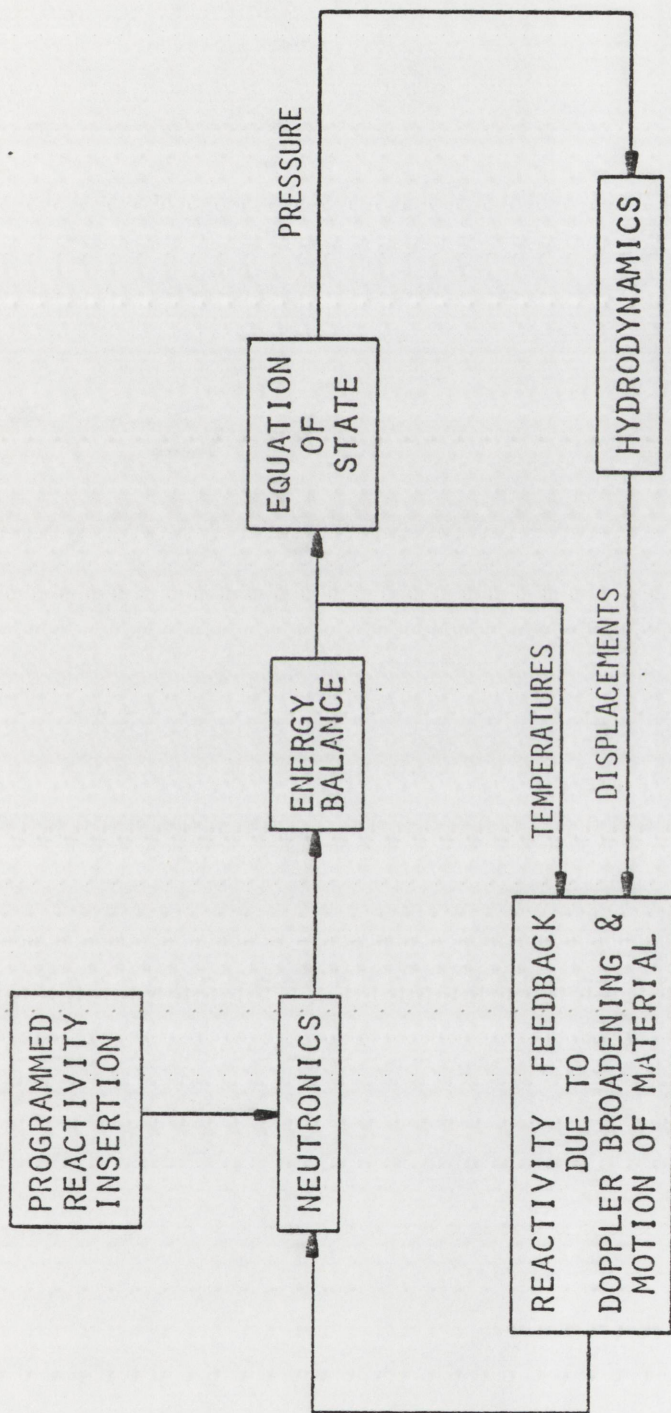


Figure I-2
Simplified Block Diagram for Coupled
Neutronics Hydrodynamics Methods

coupled equations (Sh71, Sh70):

$$P(t) = f_1(E(t), \rho_f(t)) = f_2(T(t), \rho_f(t)); \quad (1)$$

$$\rho_i(t) = \rho_{i,0} \left[\frac{P(t)B'}{B_0} + 1 \right] \frac{1}{B'} \approx \rho_{i,0} \exp \left[\alpha_i (P(t) - P_0) \right] \quad (2)$$

$$\rho_f(t) = \frac{M_f}{V_T(t) - \sum_i \frac{M_i}{\rho_i(t)}} \quad (3)$$

where

P and T are the pressure and temperature;

ρ_i , M_i , and α_i are the densities, masses, and compressibilities of the nonfuel materials;

ρ_f and M_f are the density and mass of the fuel;

P_0 and $\rho_{i,0}$ are the initial pressure and initial density of the nonfuel materials, respectively;

B_0 is the bulk modulus at zero pressure;

B' is $\partial B / \partial P$;

V_T is the total mesh volume enclosing constants M_i and M_f in the Lagrangian coordinates.

The nonfuel core materials, such as coolant, structure, and cladding, influence the equation of state only because they occupy space that would otherwise be available for fuel expansion. The nonfuel materials can be treated as either compressible or noncompressible.

If there is sufficient free volume in the core for fuel vapor to exist, the equation of state can be described by the

equilibrium vapor pressure curve at constant volume which can be expressed in the general form:

$$P(r,z,t) = A \exp \left[B - \frac{C}{T(r,z,t)} + D \ln T(r,z,t) \right]$$

where A, B, C, and D are empirical constants.

Most investigators have treated the fuel as pure UO_2 and have assumed that the vapor produced is UO_2 , disregarding dissociation. One such density dependent equation of state which has been designated the ANL-EOS (Sh70) is described in Chapter II.

DEFINITION OF EFFECTIVE-EQUATION-OF-STATE

The fuels to be used in the LMFBR under design are not pure UO_2 , but are mixed plutonium-uranium oxide. It is known that UO_2 and mixed oxides dissociate to yield many vapor species (Ac65, Ga72). Furthermore, as the fuel is burned in the reactor, fission products are produced, many of which are much more volatile than the fuel species (Br72, Ga72, Bo74, Br75). The presence of fission products should yield much higher internal pressures for a given energy content that would be expected from the fuel alone. Finally, it has been postulated that the vapor pressure of fresh and irradiated fuels may be heating-rate dependent (Br72, Br75, Be77). For these reasons, the term "effective-equation-of-state" is used to describe the vapor pressure measured of both fresh and irradiated fuels when fission heated at rates comparable to those expected during a hypothetical LMFBR accident.

DESCRIPTION OF RESEARCH PROBLEM

The purpose of this work was to develop a technique to obtain effective-equation-of-state data for various reactor fuel materials. These results will provide at least a relative comparison of the response of different fuel materials under LMFBR accident conditions. The validity of the technique was demonstrated for fresh UO_2 . Because of the nature of the technique vapor pressure data is determined as a function of fuel energy content. This dissertation describes the technique, the results of the measurements on UO_2 , and a comparison of these results with other measurements and analytical models.

CHAPTER II

LITERATURE SURVEY

The equation of state data used for disassembly analysis of fast reactors have, in the past, been analytical extrapolations of low temperature experimental vapor pressure data. Such extrapolations have spanned many orders of magnitude in pressure to reach the high energy states that are of interest for accident analysis. Until 1974, no experimental vapor pressure data was obtained at temperatures above the boiling point of UO_2 , and only one set of measurements (Re72) had been performed with molten UO_2 . Since then, several investigators (Bo75-1, Bo75-2, Oh75, Oh76, As75, Be75, Be76) have developed new techniques and have obtained limited data for UO_2 and for mixed oxide fuels at temperatures up to 10^4 K. Other investigators (Ga72, Bo74, Ka74, Br75) have developed new analytical techniques to estimate the vapor pressure of reactor fuels including the effects of fission products in irradiated fuel. In this chapter the several experimental techniques and analytical formulations will be discussed.

LOW TEMPERATURE EXPERIMENTS

The two experimental techniques that have been used to obtain vapor pressure data of solid and molten reactor fuels for temperatures up to 3390 K are 1) the Knudsen cell or vacuum effusion technique and 2) the transpiration technique. Both techniques involve the steady state heating of a sample in a container

fabricated from a refractory material (usually tungsten) and, hence, are limited to temperatures below the melting point of that container. In addition, both techniques are limited to pressures much less than 1 atm.

The early vapor pressure measurements on ceramic reactor fuels involved the Knudsen cell or vacuum effusion techniques. In this technique a sample is heated (by induction or electron bombardment) in a crucible or cell which contains a small orifice. (See Figure II-1.) The vapor effuses through the orifice and is collected on a cold target. The region surrounding the effusion cell and the target is evacuated. If the vapor effusing through a thin edged orifice (area S_0) of an effusion cell is condensed on a target (radius r at a distance d above the orifice as shown in Figure II-1), then the weight W of vapor collected in time t is related to the vapor pressure P by the expression (Ac56)

$$P = \frac{W}{S_0 t} \left(\frac{2\pi RT}{M} \right)^{\frac{1}{2}} \frac{(d^2 + r^2)}{r^2} \quad (1)$$

where R , T , and M are the gas constant, temperature, and the molecular weight of the vapor, respectively. The use of this equation assumes: 1) molecular evaporation occurs (i.e., no dissociation occurs), 2) S_0 is negligible compared to the target area, 3) the vapor is an ideal gas, 4) the orifice is infinitely thin, 5) no scattering of the vapor occurs between the orifice and the target, and 6) that the condensation coefficient of effusate on the target is unity (i.e., all effusate incident upon

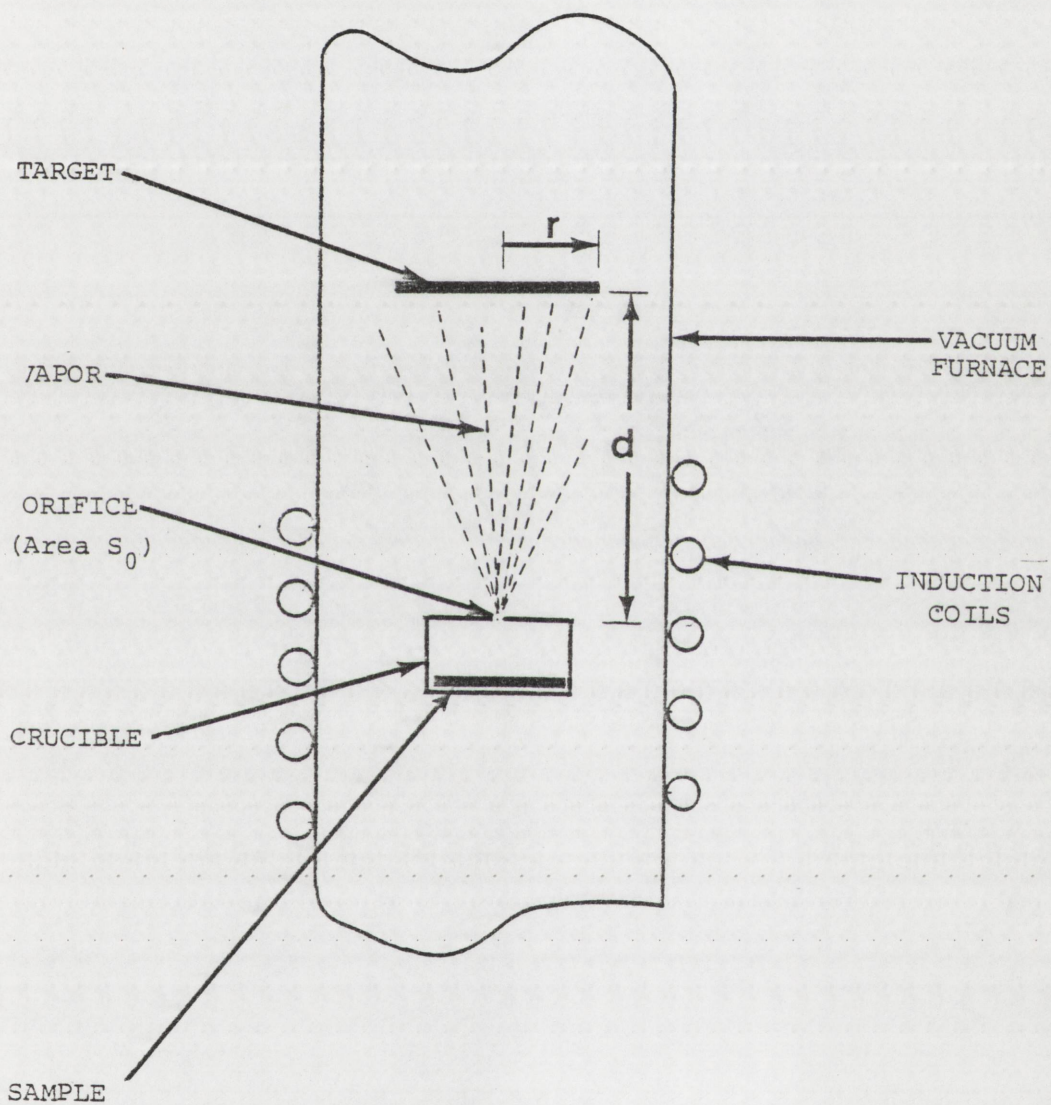


Figure II-1
Effusion Cell Experiment Geometry

the target is condensed). No control of the composition of the condensed and vapor species is possible. Several investigators (Ac62-1, Ac65) have examined the composition of the effusate through the use of a mass spectrometer. Ackermann, et al., (Ac65) found that at low temperatures (2000 C) the vapor of stoichiometric urania is primarily UO_2 and over substoichiometric urania ($\text{O/M} < 1.95$) the vapor is primarily UO . As is discussed later in this chapter and in Chapter V, the composition of the vapor of UO_{2+x} varies both with stoichiometry and temperature.

The second method of low temperature vapor pressure measurement is the transpiration technique (Sz68). In this technique, the sample is allowed to vaporize in a furnace through which a carrier gas is flowing. The vapor pressure is calculated from the specimen weight loss or by monitoring the carrier gas. The vapor pressure P can be computed as (Sz68)

$$P = \frac{W}{M} \frac{RT}{V} \quad (2)$$

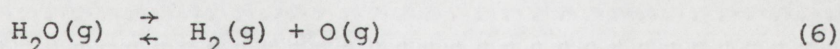
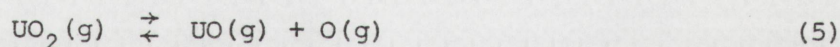
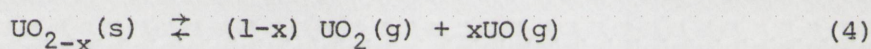
where W is the weight loss in the specimen, M is the molecular weight of the vapor, R is the gas constant, and V is the volume of the carrier gas at temperature T . The vapor pressure can also be computed as (Re72)

$$P = \frac{P_t}{1 + N_c/N_u} \quad (3)$$

where P_t is the transpiration system pressure, N_c is the number of moles of carrier gas and N_u is the number of moles of uranium

bearing species. This analysis assumes the vapor behaves as ideal gas, and that the carrier gas is saturated with the vapor species. This technique can be used at higher pressures than the effusion technique, but is subject to the same temperature constraints.

The greatest advantage of the transpiration technique is that the composition of the vapor and condensed species can be fixed by controlling the oxygen potential of the carrier gas. This is usually accomplished by adjusting the relative amounts of H_2 and H_2O in the carrier gas. For hypostoichiometric UO_{2-x} , the overall reaction can be expressed by the following individual reactions which describe the evaporation of solid UO_{2-x} and the dissociations of $UO_2(g)$ and $H_2O(g)$



There exists in the literature several summaries of vapor pressure measurements and related properties of urania (Ac62-2, Ac66, Mi65, Ch73) that were derived from effusion or transpiration measurements. A summary of the vapor pressure measurements for uranium bearing species over UO_{2-x} is shown in Table II-1.

HIGH TEMPERATURE TECHNIQUES

In order to measure the vapor pressures of reactor fuels at temperatures greater than 3400 K, several new techniques have

TABLE II-1

Summary of Measurements of Vapor Pressure of Urania

Vapor Species	Least Squares Fit to Data Log P (atm)* =	Remarks	Temperature Range (K)	Reference
UO ₂	$(-33,115 \pm 371)/T - 4.026 \log T$ + $(25.686 \pm .205)$	Vacuum Effusion	1600-2000	Ac56
UO ₂	9.22-32,150/T	Vacuum Effusion	1920-2220	Iv62, Ac66
UO ₂	9.545-33,180/T	Vacuum Effusion	2200-2800	Oh66
UO ₂	$(7.74 \pm .14) - (3.018 \pm .03)10^4/T$	Vacuum Effusion	1900-2500	Ac69
All U Species	$(7.25 \pm .15) - (27,020 \pm 250)/T$	Vacuum Effusion	1900-2500	Ac69
All U Species	7.373-27,426/T	Transpiration Over Molten Urania	<3390	Re72
All U Species	$(8.61 \pm .27) - (31,284 \pm 640)/T$	Transpiration	2080-2705	Te70
UO _{1.88}	$(6.60 \pm .17) - (25667 \pm 434)/T$	Transpiration	2500-2900	Sz68
UO _{1.92}	$(6.34 \pm .26) - (25710 \pm 738)/T$	Transpiration	2500-2900	Sz68
UO _{1.94}	$(6.56 \pm .65) - (26492 \pm 651)/T$	Transpiration	2500-2900	Sz68

* T in K.

been developed. The data published to date involve transient measurements using samples heated with pulsed lasers or pulsed electron beams. These techniques and the data obtained by them are described in this section.

Several investigators have developed techniques involving pulsed laser heating (Bo75-1, Bo75-2, Oh75, Oh76, As75). Since the several methods differ considerably from one another, each will be described. In the technique developed by Bober, et al. (Bo75-1, Bo75-2), a CO_2 laser is used to heat the surface of a specimen that is suspended as a ballistic pendulum from the pan of a microbalance in a vacuum chamber. The recoil momentum of the target, the evaporation area and duration, and the mass and momentum of the vapor jet expanding into a vacuum are measured. The effective final velocity, W_{eff} , of the vapor is obtained from the measured mass flow rate \dot{m} and thrust \dot{I}_z via the simple rocket formula (Bo75-2)

$$\dot{I}_z = \dot{m} W_{\text{eff}} \quad (7)$$

which holds for a one-dimensional jet. This velocity W_{eff} is smaller than the real final velocity W because of the angular expansion of the jet. The shape of the jet and, hence, the relationship between W_{eff} and W are dependent on the number of degrees of freedom that participated in the relaxation of translational and rotational energy into jet kinetic energy. Bober (Bo75-1) estimated the number of such degrees of freedom to be 5

($f_{rel} = 5$). From the effective final velocity, W_{eff} , and integration of the velocity angular distribution for $f_{rel} = 5$, the final vapor velocity, W , was given by (Bo75-1)

$$W = 1.38 W_{eff} \quad (8)$$

The evaporation temperature T was derived from the final velocity W via the following equations which involve the enthalpy decrease of the vapor ΔH during its adiabatic expansion in the gas dynamic flow region (Bo75-2)

$$\Delta H = H_{initial} - H_{final} = \frac{1}{2} M W^2 \quad (9)$$

$$\Delta H = (f_{rel} + 2) R (T - T_{final})/2 \quad (10)$$

$$T_{final} \approx 0 \quad (11)$$

where M is the average molecular weight of the vapor and R is the gas constant.

The vapor density, ρ , was determined from the mass flow density at the evaporating surface, \dot{m}/F , from the following equation from Mach 1 effusion theory (Bo75-2)

$$\frac{\dot{m}}{F} = \rho \left(\frac{2}{\gamma+1} \right)^{1/(\gamma-1)} \left(\frac{2}{\gamma+1} \right)^{1/2} \left(\frac{RT}{M} \right)^{1/2} \quad (12)$$

where

$$\gamma = \frac{(f_{rel} + 2)}{f_{rel}} \quad (13)$$

For an "open evaporator," the vapor density, ρ , is different from the saturated vapor density, ρ_s , as shown in the following relation (Bo75-2)

$$\rho_s = \rho \cdot \frac{2}{1+b} \bigg/ \frac{a}{1-b(1-a)} \quad (14)$$

where the backscatter parameter $b < 1$ takes into account the lack of balance of the vapor flow rates to and from the surface and a is the condensation coefficient; $1-a$ is the reflected fraction of vapor molecules incident on the liquid surface. Finally, the vapor pressure, P , is obtained by assuming the vapor was an ideal gas

$$P = \rho_s \frac{RT}{M} \quad (15)$$

Bober, et al. (Bo75-1, Bo75-2) report a number of data scattered between 4000 K and 4400 K with pressures between 4 and 9 atm. Errors of 10 percent in energy and 30 percent in pressure were estimated (Bo75-2). The scatter in the experimental data is within that range. The total evaporation time was approximately 1 msec.

Different methods were employed by Ohse, et al. (Oh75, Oh76) to determine temperature and vapor pressure during the pulsed laser heating of a sample. Fast optical pyrometry methods were used to measure the temperature at the center of the laser heated region on the sample surface. Since the energy density is not uniform across the laser beam and the pyrometer reading is the

average temperature over a finite area, it is necessary to correct the pyrometer data to obtain the peak temperature at the center of the vaporized crater.

Ohse, et al. (Oh76) argued that this technique can be characterized as free molecular evaporation which is described by the equation

$$\frac{1}{A} \left(\frac{dm}{dT} \right) = P_s \sqrt{\frac{M}{2\pi RT}} \quad (16)$$

where dm/AdT is the evaporation rate per unit area, P_s is the saturated vapor pressure, M is the molecular weight of the vapor. If only the center of the crater is considered

$$\frac{1}{A} \left(\frac{dm}{dT} \right) \cong \rho \frac{\Delta d}{\Delta T} \quad (17)$$

where ρ is the sample density, and Δd is the change in the depth of evaporated crater formed in time Δt . Thus, in addition to the evaporation temperature at the center of the heated surface, the evaporation time (typically 100 μ sec) and the maximum depth of the evaporated crater are measured. The vapor pressure is then determined from equations (16) and (17). This method was applied to mixed plutonium-uranium oxide and to uranium oxide (Oh75, Oh76). The results for UO_2 are tabulated in Table II-2.

For both this and the previous technique, the possibility exists of preferential laser heating of the vapor over the liquid. This could lead to higher measured temperatures and lower calculated vapor pressures. The lower pressures would result

TABLE II-2

Vapor Pressure over UO_2 from the Ohse Technique (Oh76)

Temperature (K)	Vapor Pressure (atm)
4420	32.69
4603	40.10
4603	41.93
4603	53.93
4615	73.53
4687	76.28
4710	65.28

from enhanced backscatter and recondensation at the liquid surface (Oh76).

A third technique utilizing laser heating was developed by Asami, et al. (As75). In this technique a sample which is attached to a torsion pendulum is pulse heated with a ruby laser with a 15 to 16 nsec pulse-width-at-half-maximum power. The temperature is determined by a spectroscopic temperature measurement (Boltzman plot technique). The following relationship exists for the relative intensity of a spectrum (As75)

$$\log \left(\frac{I\lambda}{gA} \right) = C - \frac{5040}{T} E \quad (18)$$

where I is the relative intensity of the spectrum, g is the statistical weight of the upper level of the transition, A is the transition probability, λ is the wave length, E is the energy

of the upper state (eV) and T is absolute temperature (K). Thus, if the relative intensities of several known lines in a spectrum are measured, a plot of the left side of equation (18) as a function of energy can be made. The temperature can then be determined from the slope of the resulting line. This technique suffers from a poor signal-to-noise ratio and possible self-absorption of the photons. It is, therefore, only useful at very high temperatures.

The vapor pressure is determined from the response of the torsion pendulum. For a torsion pendulum in the shape of a rectangular rod suspended on a wire, the oscillation energy U is given by (As75)

$$U = \frac{\pi G r^4}{4 \ell} \theta^2 = \frac{1}{2} I \omega^2 \quad (19)$$

where G is the modulus of rigidity, r and ℓ are the radius and length of the torsion wire, θ is the oscillation angle of the pendulum, ω is the angular velocity of the pendulum, and I is the moment of inertia. If the pendulum is accelerated by the impulse for $f\tau$, the angular velocity of the pendulum is

$$\omega = \frac{a}{I} f \cdot \tau \quad (20)$$

where a is the distance between the center of oscillation and the point of application of the force.

The wave form of the vapor ejection pressure is measured by a bar type piezoelectric gage. The wave form was found to be triangular for all experiments with a half-width of $\sim 1 \mu\text{sec}$.

The vapor pressure, P , can then be determined from the following relation (As75)

$$P = \frac{f_o}{s} = \frac{1}{s} \frac{f \cdot \tau}{\tau_h} \quad (21)$$

where f_o is the peak force of vapor ejection, s is the area on the sample from which vapor is ejected, and τ_h is the half-width of the triangular wave. Thus, from measurements of the evaporated area, the maximum angular displacement of the pendulum and the half-width of the force pulse, the vapor pressure can be determined from equations (19), (20), and (21). Only two data of vapor pressure versus temperature obtained by this technique have been published indicating a pressure of 11,000 atm at ~10,000 K and 2300 atm at ~8200 K.

All of the laser heating techniques are characterized by the surface heating of a sample and the free expansion of the vapor into a vacuum or air at atmospheric pressure. The technique developed by Benson (Be75, Be76) which involves pulsed electron beam heating is characterized by nearly uniform heating of the bulk sample and the expansion of the inertially confined vapor. The experimental apparatus of Benson's technique (Be75) is displayed schematically in Figure II-2. A finely divided powdered sample is sandwiched between two thin graphite pistons which are pressed into a graphite cylinder, thus forming a crucible which confines the vapor. This target is irradiated in the pulsed electron beam of the Sandia Laboratories Relativistic Electron

REBA PULSED VAPORIZATION EXPERIMENT

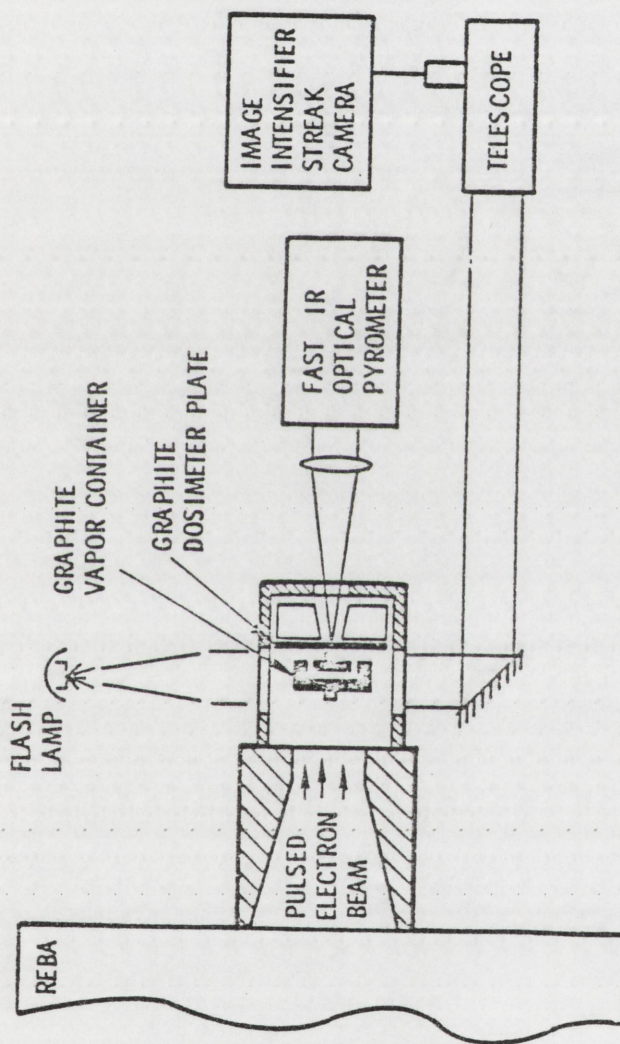


Figure II-2
Schematic Diagram of Electron Beam Heating Technique (Be75)

Beam Accelerator (REBA) which has been modified to provide an electron pulse with a .6 μ sec pulse-width-at-half-maximum power. Because of the high heat capacity of the graphite, its temperature rise due to electron heating is less than 2000 C, while the vapor sample is heated to much higher temperatures.

After the sample is heated, the pistons are accelerated in opposite directions by the vapor pressure corresponding to the energy absorbed in the sample. The displacement of each piston is recorded by streak camera photography. From the displacement as a function of time records, velocity histories and accelerations are derived. The force, $F(t)$, on the interior face of the piston is given by

$$F(t) = m \ddot{X} \quad (22)$$

where m is the mass of the piston and \ddot{X} is the piston acceleration. The force is due to momentum transfer from the liquid as well as the vapor pressure. Benson (Be75) demonstrates that the impulse due to liquid momentum dissipates quickly, and after an initial transient, the acceleration is due to the vapor pressure alone. Thus, after a short time,

$$F(t) = PA \quad (23)$$

where P is the vapor pressure and A is the area of the piston.

The data for this technique is presented as vapor pressure versus internal energy. The internal energy, which is taken as the peak electron energy deposited in the sample, is derived

from electron transport calculations which are normalized to the energy absorbed in the graphite dosimeter plate. That energy diagnostic is derived from the temperature rise in the dosimeter plate as measured by the fast infrared optical pyrometer.

Benson (Be76) has applied this technique to measure the vapor pressure of uranium dioxide. These results are summarized in Table II-3. The uncertainties in energy are estimated to be ± 5 percent.

ANALYTICAL FORMULATIONS

Theoretical and analytical techniques have been used to extend low temperature vapor pressure measurements to high temperature regions. Other techniques have been used to estimate

TABLE II-3

Vapor Pressure Data from Benson Technique (Be76)

Internal Energy* (J/g)	Vapor Pressure (Bar)
1860	43
1990	66
2030	96
2490	322
3030	1500

* Internal energy equal zero at room temperature

the changes in vapor composition due to dissociation and the effects of these changes on the total and partial vapor pressures of reactor fuels. Finally, models have been formulated to estimate the effects of fission products on the vapor pressures of irradiated fuels. These several techniques are described in this section.

Several investigators (MW64, Me66) have used the principle of corresponding states (CSP), which states that a substance can be characterized by its thermodynamic critical parameters: critical pressure (P_c), critical temperature (T_c), and critical volume (v_c). Furthermore, two materials with the same reduced temperature (T_r), pressure (P_r), and volume (v_r) will demonstrate similar behavior. The reduced temperature is the ratio of the actual temperature of the material to its critical temperature. Reduced pressure and volume are similarly defined as:

$$\begin{aligned} T_r &= \frac{T}{T_c} \\ P_r &= \frac{P}{P_c} \\ v_r &= \frac{v}{v_c} \end{aligned} \quad (24)$$

the equation of state may be written

$$Pv = znRT \quad (25)$$

where z is termed the compressibility factor and is a function of pressure, temperature, and the nature of the gas ($z = f(P_r, T_r)$ where f is a universal function). If the CSP as stated above

were valid, the critical compressibility, z_c , would be the same for all materials. z_c actually ranges from 0.2 to 0.3 for real substances. Therefore, Hougen, et al. (Ho59) concluded that an additional parameter was needed to specify the compressibility of real materials. They chose to use the critical compressibility

$$z_c = \frac{P_c v_c}{R T_c} \quad (26)$$

for that additional parameter. With this modification, the compressibility can be expressed as

$$z = f(P_r, T_r, z_c) \quad (27)$$

Hougen, et al. (Ho59) have developed generalized tables of the compressibility factors for gases and liquids and for the departures from ideal gas behavior of enthalpy, entropy, and heat capacity. Thus, if those universal functions are valid, one need only measure or estimate the critical parameters of a material to define its equation of state (EOS). This was done for UO_2 by Meyer and Wolfe (MW64) and Menzies (Me66). They estimated the critical constants from the low temperature vapor pressure measurements and from empirical relations involving the reduced parameters. Menzies (Me66) derived a density dependent equation of state for UO_2 by these techniques, which included the single phase liquid region as well as the two phase saturation region. This formulation, which is shown graphically in Figures II-3 and II-4, has been used by several investigators (Sh69, Sh70, Sh71)

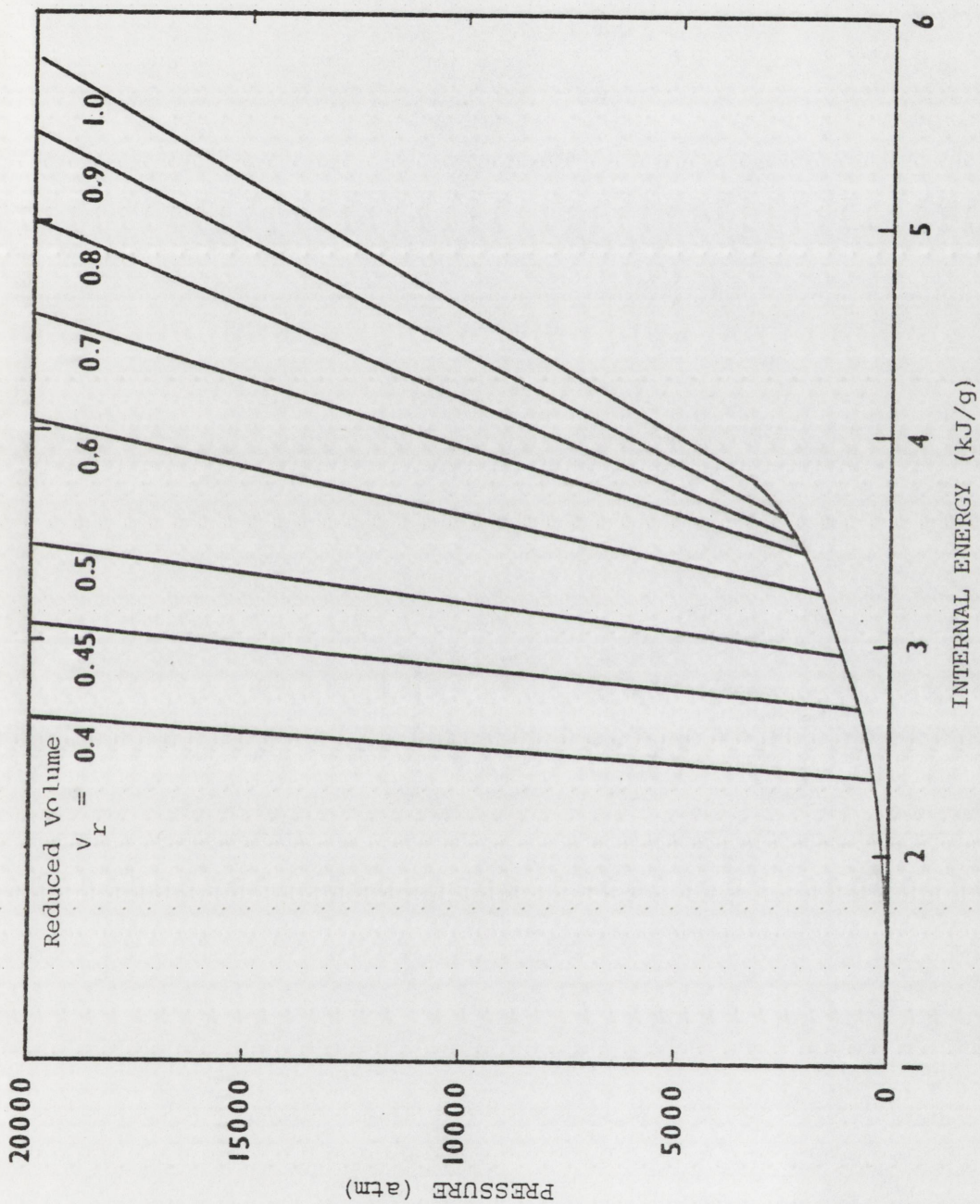


Figure 11-3

Pressure Vs. Internal Energy (Menzies EOS) (Me66)

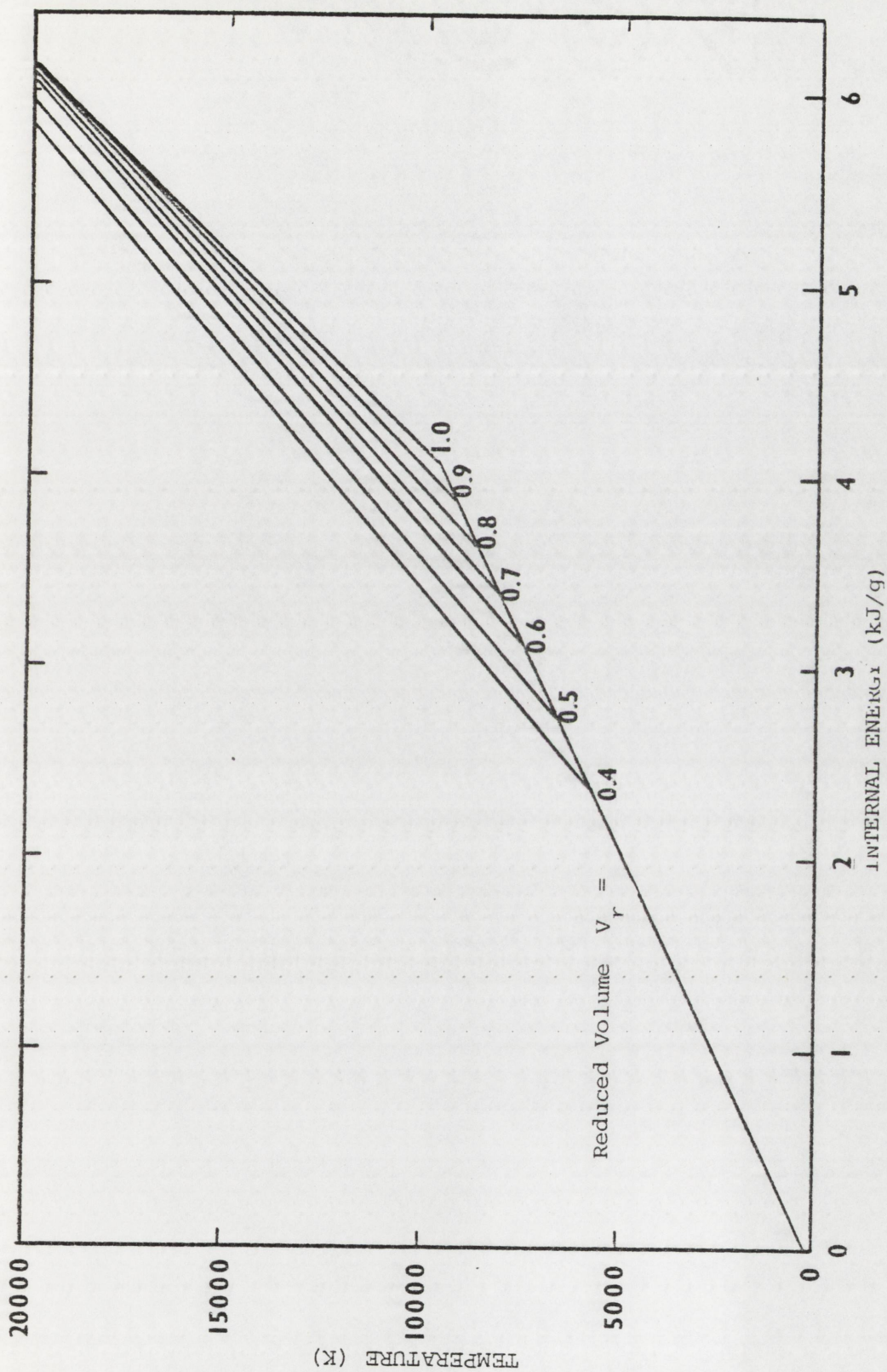


Figure II-4
Temperature Vs. Internal Energy (Menzies EOS) (Me66)

for analysis of disassembly accidents. With the inclusion of the heat of fusion (18 K cal/gm-mole), Menzies' work (Me66) becomes the basis for the ANL-EOS used in VENUS-II: An LMFBR Disassembly Program (Ja72).

The large possible variations in the estimates of the critical constants of UO_2 and the resulting EOS have been noted by Robbins (Ro66) and Miller (Mi65). Some of the estimates of the critical constants for UO_2 are given in Table II-4. In addition to the uncertainties in the critical constants, it should be noted that the data of Hougen, et al. (Ho59) was based on ordinary gases and hydrocarbons. Many materials do not follow the "universal" relationships defined by those tabulations and empirical relationships.

The above formulations and much of the analysis of experimental data have assumed that the vapor is composed of one species, namely UO_2 . As was described earlier, the vapor of urania is composed of a number of uranium bearing species and oxygen, even at low temperatures (Ac65). Even more species are present with mixed plutonium-uranium oxide. Furthermore, the vapor pressure of irradiated fuels also includes the effects of fission products, many of which are much more volatile than the fuel species. These effects have been investigated analytically by Brook (Br72), Blackburn (Bl73), Gabelnich and Chasanov (Ga72), Borgensberger, Fischer and Schmuck (Bo74), and Breitung (Br75).

Brook (Br72) considered the effects of the presence of fission products on the vapor pressure of reactor fuels.

TABLE II-4

Critical Constants for UO_2 Estimated by Different Authors

Author	Reference	T_c (K)	P_c (atm)	ρ_c (g/cm ³)	z_c
Meyer & Wolfe	(MW64)	7300	1900	3.16	.272
Miller	(Mi65)	9110	1230	1.59	.27
Menzies	(Me66)	8000	1980	3.01	.27
Katz	(Ka74)	8190	1315	1.94	.272
Gillan	(Gi75)	6960	1070	1.64	.308
Gillan	(Gi75)	9330	1450	1.63	.308
Fischer, et al.	(Fi76)	7560	1210	1.66	.316

He compiled formulations for the vapor pressures of all the fuel and fission product species and considered various models for the combination of these pressures to yield a total vapor pressure. These results demonstrate much higher pressures at all temperatures for irradiated fuels as would be expected.

These effects were defined in more detail by other investigators (Bl73, Ga72, Bo74, Br75). These techniques which are based on equilibrium chemical thermodynamics yield estimates of the total pressure and composition of the vapor of the reactor fuel. The calculational approach of these techniques is described in Chapter V for UO_2 . Typical results are shown in Table II-5 for $(\text{U}_{0.8} \text{Pu}_{0.2}) \text{O}_{1.98}$ with 3 percent burn up and a fuel smear

TABLE II-5

Typical Vapor Pressures for Irradiated Mixed Oxide Fuel*

Temperature (K)	3000	4000	5000
Kr + Xe	65	108	150
Other Fission Products	36	83.5	346
Fuel Species	.014	4.5	198
Oxygen	1.6×10^{-6}	.0004	.0091
Total	101	196	694

* Ref. (Bo74) Pressures in bars.

density of 5 gm/cc. These techniques all assume thermodynamic equilibrium exists. The free energy of formation data required for the chemical thermodynamics calculations is not available for the temperatures of interest, but must be inferred from low temperature data and theoretical formulations.

Breitung (Br75) presented a general analysis of the evaporation kinetics of multicomponent systems. A summary of that discussion with regard to types of steady state evaporation is given in Chapter V.

CHAPTER III

EXPERIMENT DESIGN AND PROCEDURES

A new experimental technique was developed to measure the vapor pressure of fissionable materials at high temperatures and pressures. This chapter describes the design criteria for the EEOS experiments and the means by which these criteria were realized. Following a description of the Annular Core Pulse Reactor (ACPR), the different types of experiment are defined. The various incore components of the experiment are described along with the data acquisition and reproduction system. Finally, the experimental procedures followed during the conduct of the experiments are detailed.

EXPERIMENT CRITERIA

The design criteria imposed on the EEOS experiment are:

1. to heat a fuel sample to the desired energy states;
2. to measure the pressure produced of the sample
as a function of time;
3. to determine the energy content of the sample as a
function of time;
4. to confine the high-temperature, high-pressure
fuel vapor within a small volume;
5. to provide absolute biological containment of the
experiment.

Several of these criteria imply other considerations. It was desired to heat the sample uniformly at rates comparable to those

anticipated during a severe LMFBR accident. The initial reactor period during a maximum ACPR pulse (~1.3 msec) closely approximates the anticipated period during an LMFBR accident (~1 msec). Thus, pulse fission heating of a reactor fuel sample during ACPR transients was selected for these experiments. Relatively uniform fission energy deposition is attainable through proper selection of sample geometry and irradiation environment. Previous experiments in the ACPR (Sc74) indicated that the desired energy states (>2200 J/g) could be reached by moderating the neutron spectrum in the ACPR cavity and by using enriched uranium samples. The determination of the energy content of the fuel as a function of time requires knowledge of energy input to and heat losses from the sample.

ACPR DESCRIPTION

The Annular Core Pulse Reactor (ACPR) (BM74) is an open-pool TRIGA-type reactor capable of both steady-state and pulse operation. An elevation of the ACPR is shown in Figure III-1. The core, including reflectors, is approximately 0.6 m high and 0.6 m in diameter with a 0.23 m dry experiment cavity in the center. The 156 stainless steel clad fuel elements are arranged in a close-packed hexagonal array surrounding the experiment cavity. The cavity is nominally .305 m high and is centered vertically within the active core height. The upper and lower reflector plugs can be removed to accommodate longer experiments.

The active portion of the fuel-moderator elements consists of a homogeneous mixture of enriched uranium and zirconium

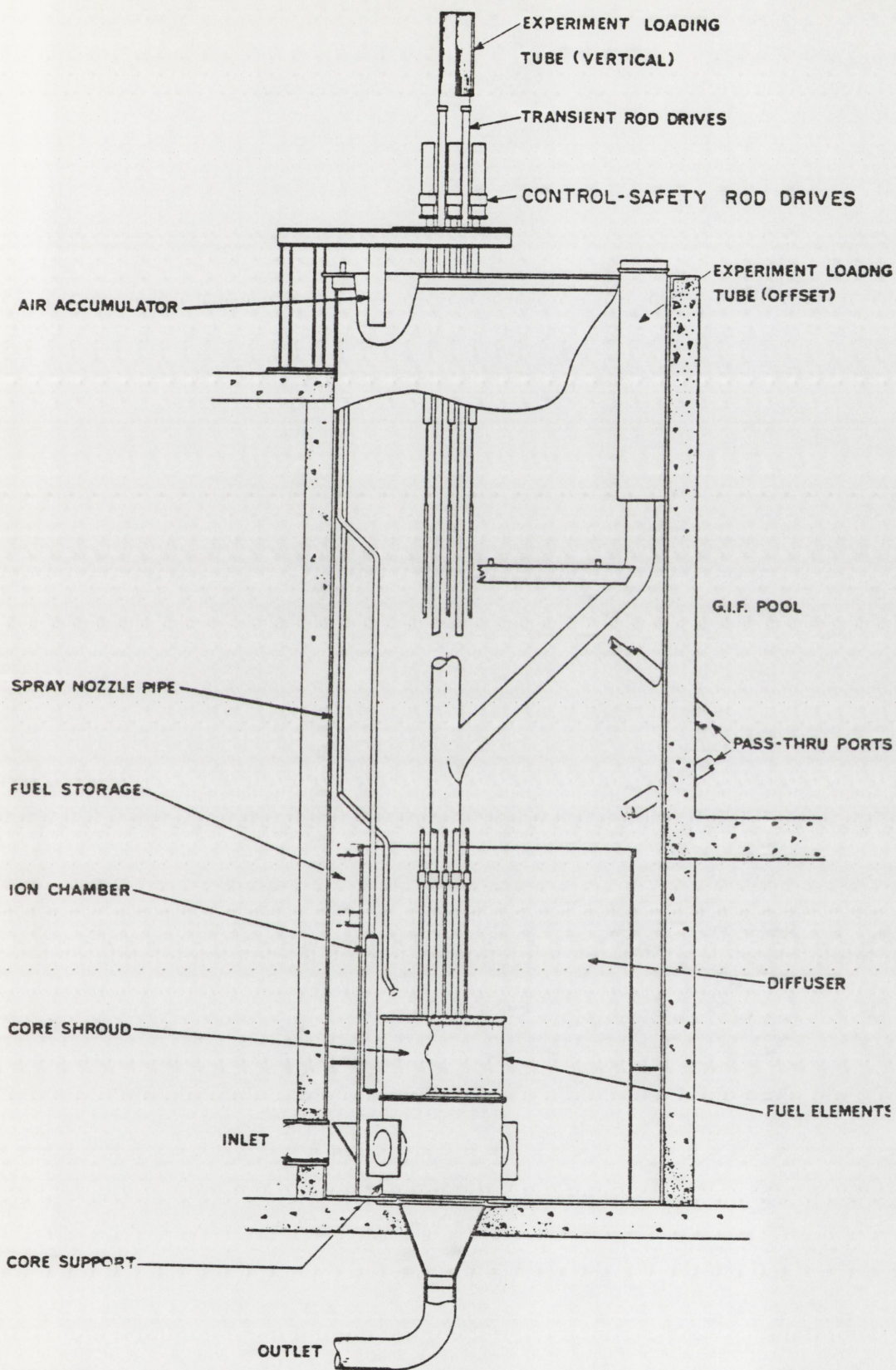


Figure III-1 Elevation of ACPR Reactor

hydride moderator which is .381 m long and 35.6 mm in diameter. The mixture contains 12 percent uranium by weight which has been enriched to 20 percent ^{235}U . The hydrogen-to-zirconium ratio is 1.625 to 1. Graphite cylinders 88 mm long above and below the active region within each element serve as reflectors.

The reactor is controlled by means of six fuel-followed control rods and three air-followed transient rods. The six motor driven control rods are used to establish delayed critical conditions. The transient rods are pneumatically activated to provide the reactivity insertion necessary for super-prompt-critical pulse operation. The total reactivity worth of the transient bank (~ 4.70) can be removed in 40 to 50 msec to yield a net reactivity insertion rate of approximately $\$100/\text{sec}$. The resultant super-prompt critical excursion is terminated by the large prompt negative temperature coefficient of reactivity that is characteristic of the $\text{U-ZrH}_{1.62}$ fuel.

The maximum energy pulse in the ACPR yields a peak power of approximately 15,000 Mw with a pulse-width-at-half-maximum reactor power of 4.7 msec. A total core energy release of 108 MJ occurs during a maximum pulse, producing in the central experiment cavity a neutron fluence greater than 10 keV of 1.7×10^{15} neutrons per cm^2 and a total fluence in excess of 3×10^{15} neutrons per cm^2 . With the reflector plugs in place, the relative axial and radial neutron fluence profiles in the empty cavity are as shown in Figures III-2 and III-3. The neutron energy spectrum has been measured (Cr72) and is shown in Figure III-4.

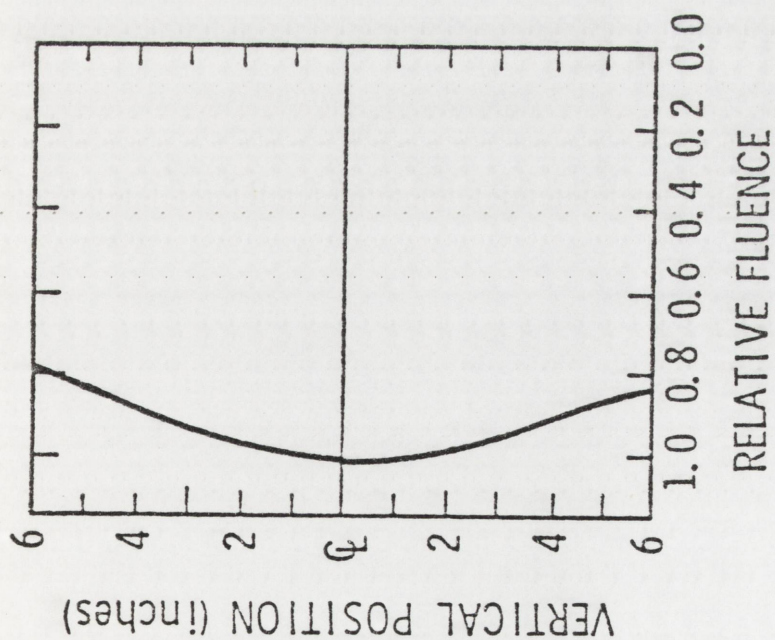


Figure III-2

Relative Axial Fluence

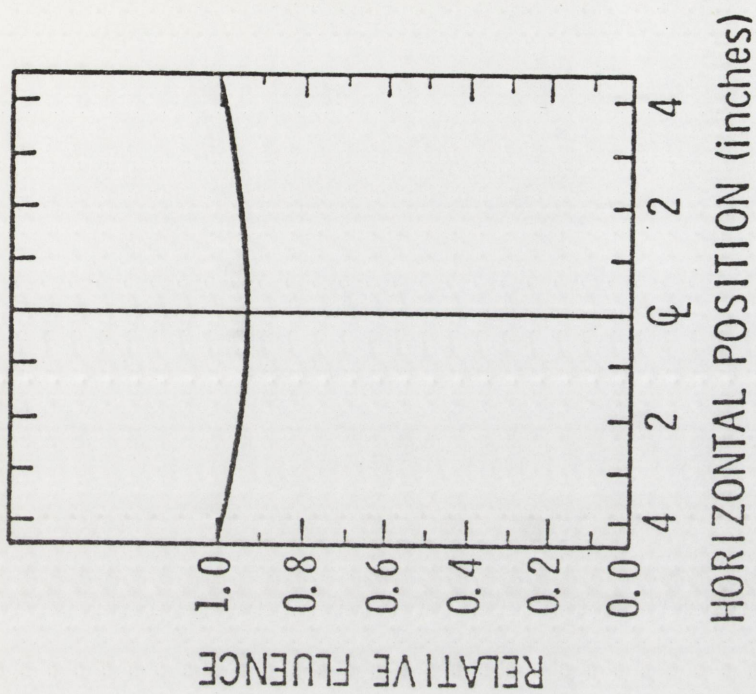


Figure III-3

Relative Radial Fluence

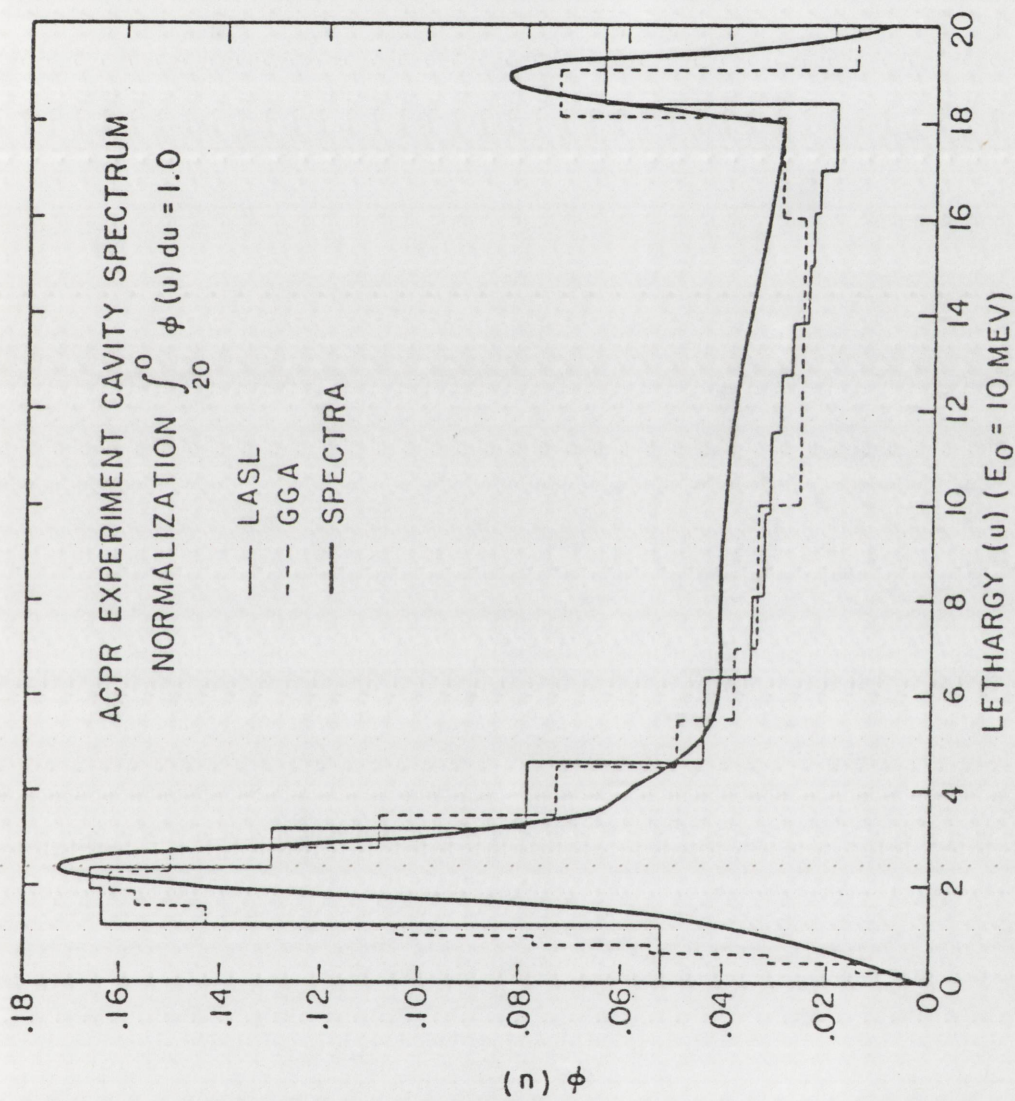


Figure III-4

ACPR Experiment Cavity Neutron Spectrum

An experiment in the central cavity exposed to a maximum pulse also receives a gamma radiation dose of approximately 1 megarad-H₂O.

TYPES OF EXPERIMENTS

Three groups of experiments or tests were performed during the course of this experimental program. The first tests involved proof tests of the experiment components and instrumentation. These involved hydrostatic pressure tests on the pressure bearing components and determination of the responses of the various transducers to radiation during ACPR pulses. The second group of experiments (the buildup series) was performed to determine the total fission energy deposited in a fuel sample irradiated in the final experimental geometry for various combinations of reactor pulse amplitude, sample enrichment, and neutron moderator thickness. During the third group of experiments, the vapor pressure measurements were performed. This group involved two types of experiments: one containing a pressure transducer to determine the pressure history; the second type was instrumented to determine heat losses from the sample during the irradiation.

In addition to the inpile irradiation, every fueled experiment involved a fission product inventory (FPI) assay performed after the irradiation to determine the total number of fissions that occurred during the experiment. From this information, the total fission energy deposited in the sample was determined. This fission product inventory technique, which was used in previous ACPR experiments on urania (Sc74, Cr75) is described in Appendix E.

EXPERIMENT COMPONENTS

The hardware for these experiments consisted of an inpile package, several fixtures used during the assembly of each experiment, external instrumentation electronics for signal conditioning and data recording, a multichannel pulse height gamma spectrometer used for the fission product inventories, and the Sandia Data Acquisition and Display System (DADS) (Po71), which was used for digital processing of the data. This section will describe the inpile package and the fixtures required for assembly of that package.

A cross-sectional view of the inpile package is shown in Figure III-5. The experiment consists of an instrumented pressure cell assembly which contains the fuel sample and the necessary transducers to measure the pressure history and to determine heat losses from the sample. The pressure cell is supported from and contained within two sealed cans (i.e., the inner and outer containments). The neutron spectrum was moderated by the two polyethylene cylinders (i.e., internal and external polyethylene moderators). The outer containment serves to locate the experiment within the ACPR cavity and to position the fuel sample at the point of maximum neutron flux. (Detailed drawings of the components are shown in Appendix B.)

The urania samples used in these experiments were prepared by Los Alamos Scientific Laboratory (LASL) (Ga76). Urania discs nominally 12 mm in diameter weighing approximately 1 g were fabricated in three enrichments (10 percent ^{235}U , 20 percent ^{235}U , 30 percent ^{235}U). (Other samples enriched to 93 percent

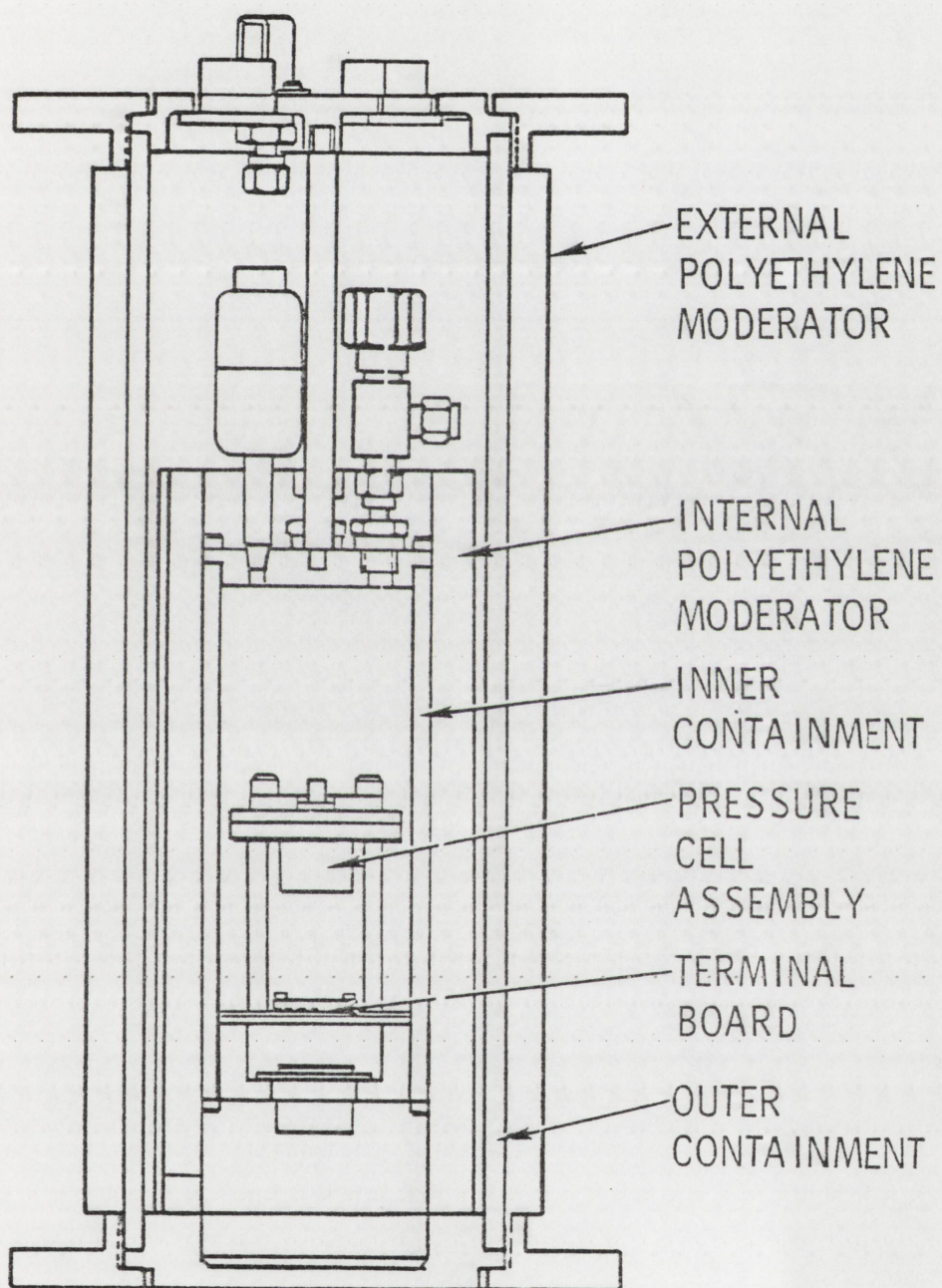


Figure III-5
Cross-Section of EEOS Inpile Package

^{235}U were fabricated but were not used in these experiments.) The following fabrication procedures were used by LASL personnel (Ga76):

Triuranium octoxide (U_3O_8), of a known isotopic composition, was dissolved in nitric acid to produce a 0.2 M $\text{UO}_2(\text{NO}_3)_2$ (uranyl nitrate) solution. A precipitate of $\text{UO}_4 \cdot x \text{H}_2\text{O}$ (uranium peroxide) was obtained from the $\text{UO}_2(\text{NO}_3)_2$ solution at a constant pH of 1.7 by simultaneous addition of 30 percent H_2O_2 and dilute NH_4OH solutions. The $\text{UO}_2(\text{NO}_3)_2$ solution contained 0.04 M malonic acid as a flocculent and 0.004 M citric acid to complex impurity iron and prevent decomposition of the H_2O_2 . The precipitated $\text{UO}_4 \cdot x \text{H}_2\text{O}$ was separated from the supernatant by filtration, transferred to platinum boats, and calcined in air for 8 h at 300°C , to obtain a composition approximating UO_3 . The UO_3 was then reduced for 1 h in flowing He and H_2O vapor at 650°C , to obtain a ceramic type UO_2 that is stable in air. The UO_2 was sieved to -30 mesh and samples were taken for chemical analysis, powder characterization, and metallographic examination.

The sieved UO_2 powder was prepared for pressing by adding 3.0 wt% Carbowax PF 4000 (a polyethylene glycol), to serve as a binder. This was accomplished by heating the Carbowax to produce a solution, mixing this solution with excess CCl_4 , and adding the composite solution to the UO_2 powder. The batch was then constantly stirred under a heat lamp, until the CCl_4 was completely evaporated, leaving an intimate mixture of the Carbowax and UO_2 powder. The waxed UO_2 powder was sieved to -65 mesh and placed in a plastic jar for storage.

The research samples were fabricated using conventional ceramic processing techniques. A charge of

1.030 \pm 0.002 g of waxed UO₂ powder was pressed at 15,000 psi, using a 0.625 in. diameter "double action" cylinder die. This produced a "green" disk which measured ~0.628 in. in diameter by 0.047 \pm 0.002 in. in length. The disks were fired in flowing dry H₂, [at 1800°C for 24 hours] in a molybdenum fixture which was specially designed to eliminate warpage during firing.

The isotopic composition of the uranium in the samples was determined by LASL. These are shown in Table III-1. Characteristics of the unwaxed powders are shown in Table III-2. Note that the samples were all slightly hyperstoichiometric urania. Table III-3 summarizes the spectrochemical analysis of impurities in the samples. The dimensional and density characteristics of the samples are listed in Table III-4. Figure III-6 is a photomicrograph of transverse sections through several samples. The density variation (porosity) between enrichments can be observed. Radiography revealed the presence of both high and low density inclusions, and the mottled appearance of many of the discs, but no cracks were observed. The high density inclusions are probably UO₂ agglomerates, and the low density inclusions and mottled appearance are possibly porosity and/or pitting on the sample surfaces.

The heart of the experiment is the instrumented pressure cell. A cross-sectional view of a pressure cell is shown in Figure III-7. A fuel sample is contained in a free volume (200 to 500 mm³) that is bounded by a graphite crucible and a graphite disc (fabricated from AXF graphite) which covers the face of the pressure transducer.

TABLE III-1

Isotopic Analysis of UO_2 Powders

Mass	10% Enriched [CU-657 (F-2)]		20% Enriched (CU-696)		30% Enriched (CU-697)		93% Enriched (CU-699)	
	At%	Wt%	At%	Wt%	At%	Wt%	At%	Wt%
234	-	0.05	0.143	0.141	0.212	0.210	0.870	0.866
235	-	10.10	20.23	20.02	30.34	30.08	93.01	92.95
236	-	0.09	0.085	0.084	0.123	0.123	0.264	0.265
238	-	89.67	79.55	79.75	69.32	69.59	5.85	5.92

TABLE III-2

 UO_2 Powder (Unwaxed) Data

Batch	Enrichment (% ^{235}U)	UO_x	Scott Density (g/ml)	Fisher Porosity (%)	Fisher Average Particle Size (μm)	BET Surface Area (m^2/kg)
CU-657 (F-2)	10	2.10	-	0.732	0.72	6,861
CU-696	20	2.08	1.15	0.778	0.71	6,546
CU-697	30	2.08	1.01	0.792	0.65	7,166
CU-699	93	2.11	1.14	0.789	0.71	6,544

TABLE III-3

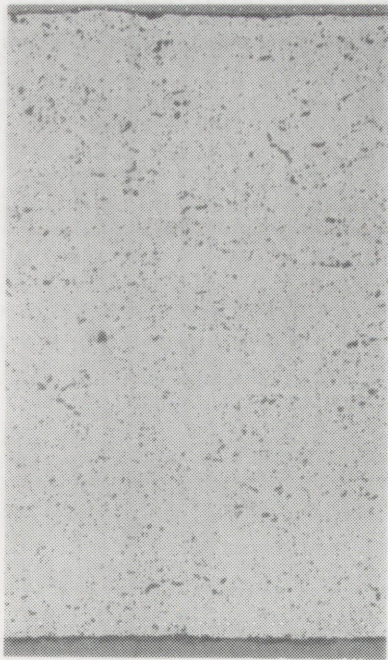
UO₂ Research Samples Spectrochemical Analysis Results (ppm)

Impurity	10% Enriched [CU-657(F-2)]	20% Enriched (CU-696)	30% Enriched (CU-699)	93% Enriched (CU-699)
Li	< 0.2	< 0.2	< 0.2	< 0.2
Be	< 0.2	< 0.2	< 0.2	< 0.2
B	< 0.2	< 0.2	< 0.2	< 0.2
Na	< 1	< 1	< 1	< 1
Mg	1	1	1	1
Al	30	20	15	10
Si	3	3	3	3
P	< 100	< 100	< 100	< 100
Ca	< 5	< 5	< 5	< 5
Ti	20	20	50	15
V	< 3	< 3	< 3	< 25
Cr	< 1	< 1	< 1	< 1
Mn	< 1	< 1	< 1	< 1
Fe	7	6	5	5
Co	< 6	< 6	< 6	< 6
Ni	< 5	< 5	< 5	< 5
Cu	< 1	< 1	< 1	< 1
Zn	< 25	< 25	< 25	< 25
Sr	< 20	< 20	< 20	< 20
Zr	< 10	< 10	< 10	< 10
Nb	< 10	< 10	< 10	< 10
Mo	< 3	< 3	< 3	< 3
Ag	< 1	< 1	< 1	< 1
Cd	< 2	< 2	< 2	< 2
Sn	< 1	< 1	< 1	< 1
Sb	< 5	< 5	< 5	< 5
Ba	< 5	< 5	< 5	< 5
Ta	< 30	< 30	< 30	< 30
W	< 3	< 3	< 3	< 3
Pb	< 1	< 1	< 1	< 1
Bi	< 2	< 2	< 2	< 2

TABLE III-4
UO₂ Research Samples
Fabrication Data (Average)

Batch	Enrichment (% ²³⁵ U)	Dimensions (in.)		Wt. (g)	%T.D. (Geometric)
		Diameter	Length		
CU-657 (F-2)	10	0.463±0.001	0.035±0.001	0.987±0.002	92.24
CU-696	20	0.465±0.002	0.035±0.001	0.988±0.002	92.54
CU-697	30	0.463±0.001	0.035±0.001	0.991±0.001	93.18
CU-699*	93	0.468±0.001	-----	0.50±0.05	95.01

* These samples initially weighed 0.992±0.001 g and measured 0.034 in. in length, but were ground to a weight of 0.50±0.05.



10%



20%



30%

Figure III-6
Photo Micrograph of Transverse Section of Fuel Samples

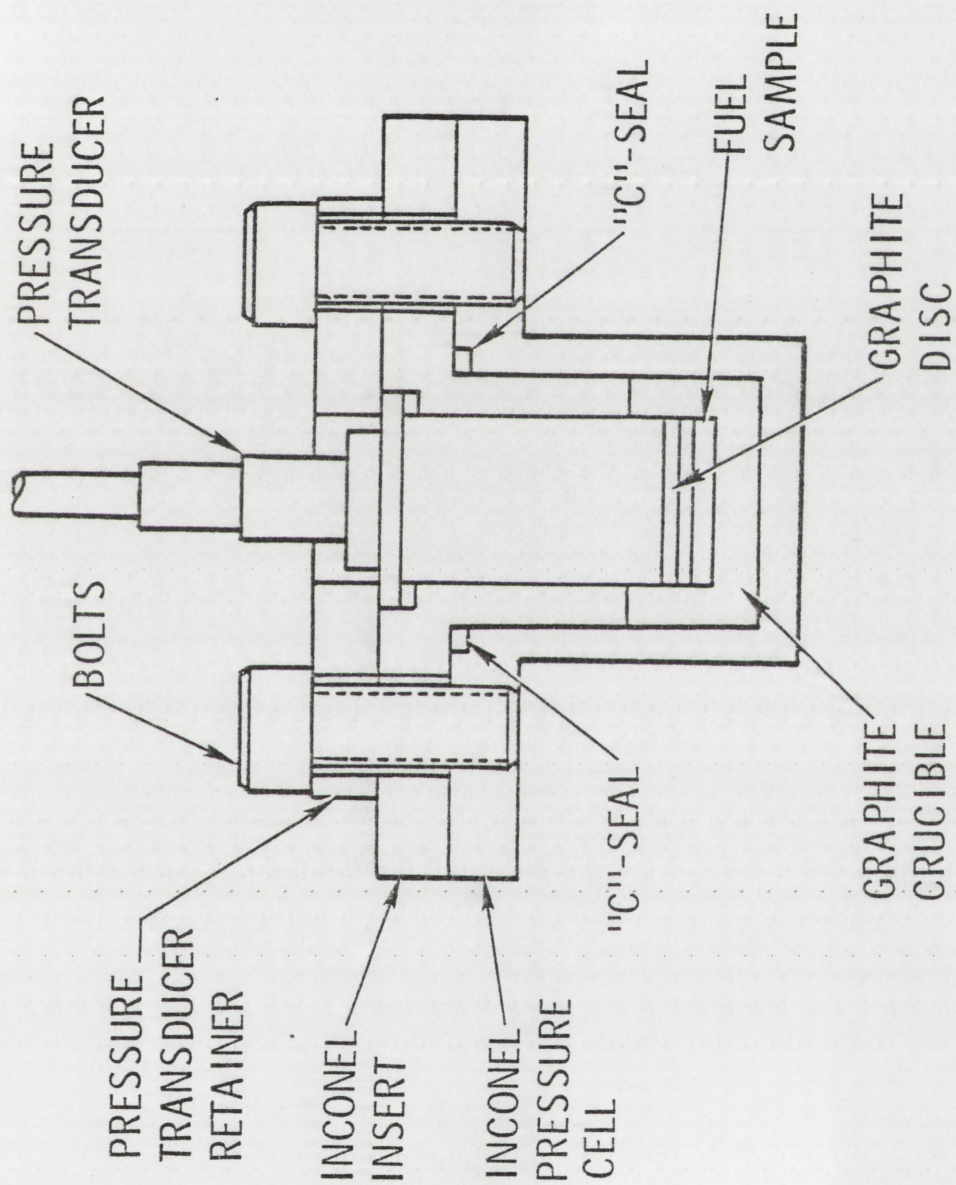


Figure III-7
Cross-Section of EOS Pressure Cell

The graphite crucible is constrained by a pressure cell fabricated from Inconel-718. The pressure transducer is positioned by an Inconel insert and a flat retainer plate. The pressure cell is assembled with four high-strength socket head cap screws and is sealed with two metallic "C-seals." ("C-seals" are hollow metallic O-rings with a "C" shaped cross-section and are described in Appendix C.) The various components of a pressure cell are shown in the photograph in Figure III-8.

Several considerations influenced the design of the pressure cell. The first constraint was the geometry of the pressure transducer. Since it was necessary to make the pressure measurements during an ACPR transient, only a transducer that was not damaged by the radiation and which did not produce a large radiation induced signal was suitable. The transducer had to measure pressures from 0 to 5000 psia with a frequency response of at least 10 kHz. It was also desirable to have a transducer that could survive transient temperatures in excess of 500 C. One commercially available transducer that meets all of these requirements is manufactured by Kaman Measuring Systems and is described in Appendix C. The diameter of sensing diaphragm of this transducer (12.7 mm) defines the diameter of the internal free volume of the pressure cell.

The transducer diameter dictated the sample geometry that was described previously. It was desired that the total free volume of the pressure cell be small so that only a small portion of the sample would be vapor and so that the total sample would ultimately be confined to a small volume for the fission product

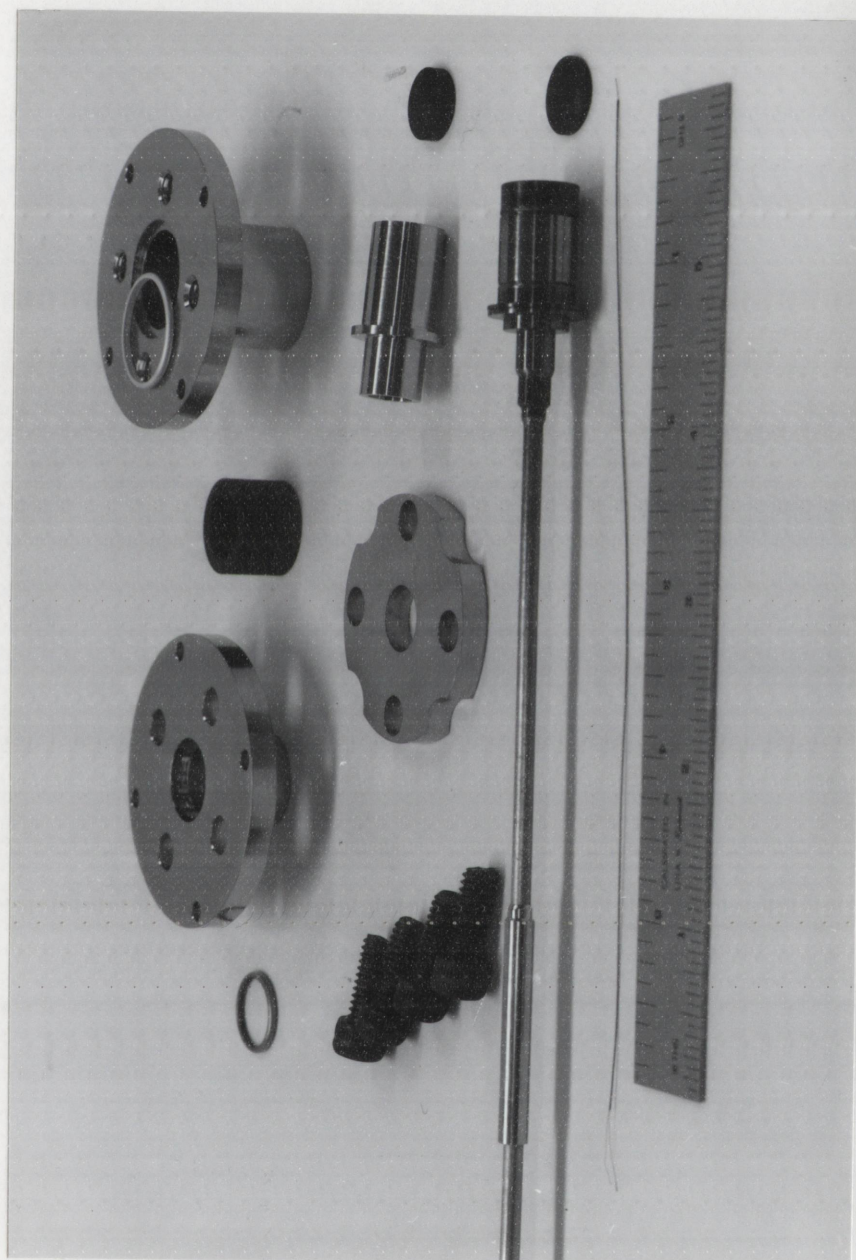


Figure III-8
EOS Pressure Cell Components

inventory analysis. The free volume must be large enough, however, to preclude high pressures due to single phase expansion if the volume were to be totally filled with liquid. The critical density of UO_2 has been estimated to be between 1.6 and 3.2 g/cc (Fi76). These correspond to critical specific volumes between 630 and 310 mm^3 . If the volume of the pressure cell were larger than the critical volume, no possibility of high pressures resulting from single phase expansion exists below the critical point. However, the maximum design pressure for these experiments (400 atm) is much less than the estimated critical pressure (1100 to 2000 atm (Fi76)). Thus, smaller volumes can be used. The pressure cell was designed to obtain free volumes from 200 to 500 mm^3 by changing the lengths of the cylindrical side of the graphite crucible and pressure cell. (See drawings in Appendix B.)

Since the sample would be heated to temperatures as high as 6000 K, it was necessary for the pressure cell to be lined with a high temperature material. The crucible material must have a small neutron absorption cross-section to prevent shielding of the sample. Graphite (sublimation temperature 3800 K) satisfies these requirements. The thermal mass of the graphite crucible was chosen such that if it and the sample were an adiabatic system, they would equilibrate at less than 1000 C when 1000 cal/gm of fission energy are deposited in the fuel. Therefore, no temperature hazard exists for the pressure-bearing portions of the pressure cell. Since graphite has a much higher thermal conductivity than UO_2 (see Appendix A), the highest temperature seen

by the inside surface of the graphite crucible should not exceed the melt temperature of UO_2 (3115 K).

The design maximum internal operating pressure for the pressure cell is 6000 psig. The cell was designed for twice that pressure or 12,000 psig. The following analysis was employed in the design of the pressure cell. It was conservatively assumed that the graphite crucible had no strength and that the entire pressure acted on the inside surface of the Inconel pressure cell. The pressure cell was considered as two parts: 1) a cylindrical body and 2) a flat end plate with the edges fixed. For a disc of radius r and thickness t , loaded uniformly with pressure P , the limiting stress is the radial stress at the edge (Ro65). This stress can be computed from the following equation:

$$S_r = \frac{3Pr^2}{4t^2} \quad (1)$$

For a cylinder with inner radius a and outer radius b , loaded internally with pressure P , the limiting stress is the circumferential stress at the inner surface (Ro65). That stress can be computed from Equation (2).

$$S_c = P \frac{b^2 + a^2}{b^2 - a^2} \quad (2)$$

For the final pressure cell design and an internal pressure of 12,000 psig, these design stresses are:

$$S_r = 122,000 \text{ psi} \quad (1a)$$

$$S_c = 51,000 \text{ psi} \quad (2a)$$

The yield stress of Inconel-718 is approximately 140,000 psi at 500 C (Ma74). Hence, the pressure cell design is adequate at twice the design operating pressure.

The sealing surfaces and seat dimensions for the "C-seals" were designed in accordance with the manufacturer's recommendations to provide a helium tight seal to pressures greater than 12,000 psig. Only two of the socket head cap screws were needed from stress considerations. Four were used, however, to ensure uniform compression of the "C-seals."

To monitor heat losses from the fuel sample, thermocouples were embedded in the graphite crucible. The thermocouples were chromel-alumel couples sheathed in Inconel-600 and are described in Appendix C. The outside sheath diameter was .25 mm with 0.038 mm diameter wires. Both grounded- and exposed-junction thermocouples were used. The thermocouples which penetrated the sides and bottom of the pressure cell were sealed with soft silver solder, as shown in Figure III-9. Six thermocouples were located in the graphite crucible: four in the flat bottom, and two in the cylindrical side. The four in the bottom were equally spaced on a circle with radius 3.2 mm. Three were located 0.38 mm from the inside surface; the other was located 1.27 mm from that surface. The two in the side were located at different elevations 0.38 mm from the inside surface. (See drawing in Appendix B.)

It is required that all pressure vessels used in Sandia Laboratory reactors be proof tested to at least 1.5 times the maximum operating pressure. A pressure cell was hydrostatically

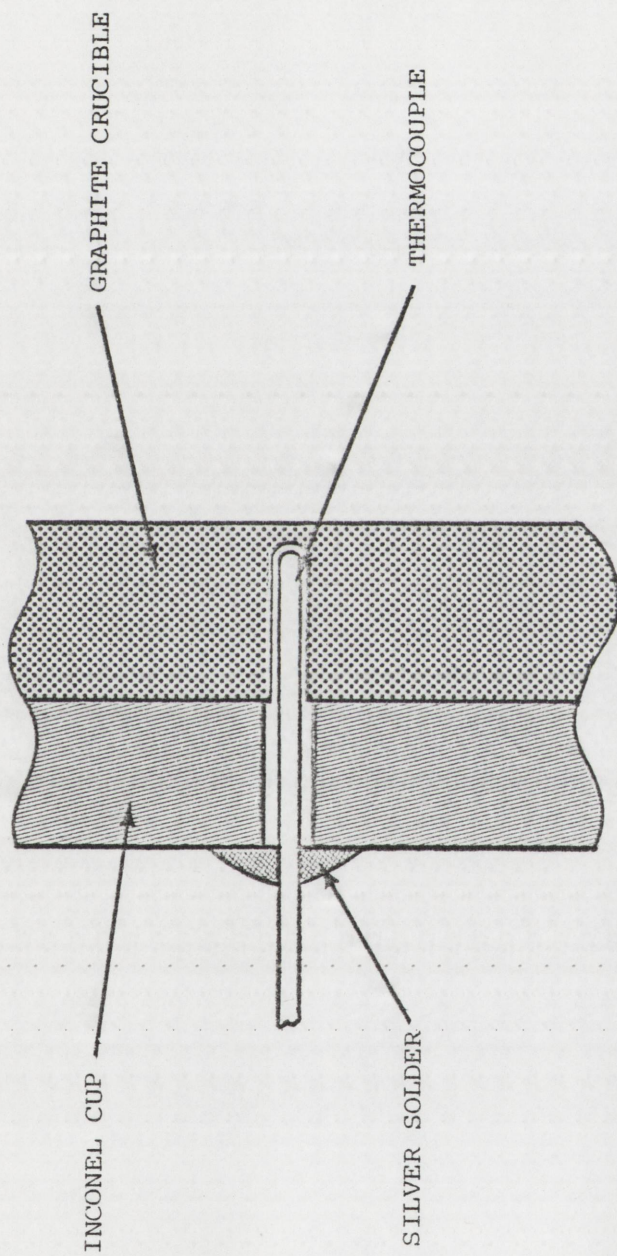


Figure III-9
Typical Thermocouple Installation

tested to 9130 psig with no detectable leaks or deformation. The cell was coupled to the pressure system with a hollow test fixture which replaced the pressure transducer. (See drawing in Appendix B.)

Only a small number of experiments contained pressure transducers. In all other experiments the pressure transducer was replaced with a dummy having the same external geometry as the Kaman transducer. Two types of dummy transducers were used. In the buildup experiments an Inconel plug was used which had been counterbored from the outside to approximate the neutronic effects of the Kaman transducer. (See drawing in Appendix B.) The other type of dummy transducer, which was instrumented with thermocouples, was used during the vapor pressure experiments to estimate heat losses from the sample to the pressure transducer. The three thermocouples in the instrumented dummy transducer were equally spaced on a circle with radius 3.2 mm. Two were located 0.38 mm from the exposed graphite surface; the other was located 1.27 mm from that surface. (See drawing in Appendix B.)

As shown in Figure III-5, the pressure cell is enclosed within two sealed aluminum containers. These containers served to locate and support the various experimental components in the ACPR cavity. More importantly, however, they provided absolute containment of the fuel sample and fission products to preclude any release to the environment. The pressure cell is supported from the bottom end cap of the inner container. The thermocouple and strain gage leads are soldered to a terminal board on that bottom end cap and penetrate the two containers via

hermetically sealed, multi-pin connectors. The only penetration common to both containers is the metal sheathed transducer cable. It penetrates the upper lid of each container via O-ring sealed feed-throughs. The inner container is suspended from the upper lid of the outer container. The container and all penetrations through the lids are sealed with Buna-N O-rings.

The design criteria for the containers required that no leaks be detected at the maximum possible internal pressure. The following analysis was used to estimate that maximum pressure. It is assumed that the fuel volume is expanded isothermally at the pressure cell design pressure of 6000 psi (= ~41 MPa) until 50 percent of the sample is vapor. The resulting volume of vapor at saturation at 41 MPa is then expanded in a reversible adiabatic process to the free volume of the inner container. The resulting pressure becomes the design pressure for both the inner and outer containers. To estimate the volume of the vapor, the vapor pressure model used in the VENUS code (Sh70) is used to estimate the temperature. (This model is described in Chapter V.) For a vapor pressure of 41 MPa that model predicts a temperature of approximately 6300 K. If it is assumed that the vapor behaves as an ideal gas, the volume associated with a 0.5 g of vapor at saturation at 41 MPa can be estimated from the ideal gas law.

$$PV = nRT \quad (3)$$

or

$$V = \frac{nRT}{P} \quad (4)$$

Thus,

$$V = \left(\frac{.5}{270} \right) \frac{(8.3)(6300)}{41 \times 10^6} = 2.4 \times 10^{-6} \text{ m}^3 = 2.4 \text{ cc} \quad (5)$$

where the mole weight of UO_2 is taken to be 270 g/mole. For an ideal reversible adiabatic process

$$P_i V_i^\gamma = P_f V_f^\gamma \quad (6)$$

where the subscripts i and f indicate the initial and final states respectively and γ is the ratio of specific heats.

$$\gamma = C_P / C_V$$

Menzies (Me66) estimated the value of γ from ideal gas considerations to be 1.15. The free volume of the inner container is approximately 480 cc. Thus,

$$P_f = P_i \left(\frac{V_i}{V_f} \right)^\gamma = 41 \left(\frac{2.4}{480} \right)^{1.15} = 0.093 \text{ MPa} \quad (7)$$

Thus, a design pressure of 1 atm was selected. Because of the large heat of vaporization of UO_2 (1700 ± 200 J/g (Le76)), the above analysis is extremely conservative. The isothermal evaporation of 0.5 g of UO_2 would require the addition of 850 J to the sample. Thus, the expansion of the fuel volume would actually cool the sample resulting in a lower pressure. Since all of the walls and structure of the inner container are cold, the assumption of an adiabatic expansion is also conservative.

The final designs of the two containers greatly exceed the 1 atm pressure requirement. Both containers were hydrostatically tested at 15 atm with no detectable leakage or damage. During the assembly of every fueled experiment both containers were helium leak tested at 2 atm gage pressure as described later in this chapter.

The total fission energy in a fuel sample irradiated during an ACPR transient can be altered in three ways. Increasing the magnitude of the ACPR pulse increases the total energy deposition and decreases the total heating time. Increasing the ^{235}U concentration (i.e., enrichment) in the sample will increase the total energy deposition, but will severely alter the energy distribution because of increased self-shielding within the sample. The third means of altering the energy deposition is by modifying the energy spectrum of neutrons incident on the sample. Since the fission cross-section of ^{235}U increases with decreasing neutron energy, moderation of the neutron flux impinging upon the sample will increase the fission energy deposited in the fuel. In these experiments high density polyethylene was used for the moderator. As shown in Figure III-5, polyethylene cylinders of various thicknesses can be located either between the two containers or outside the outer container. The maximum thickness of the polyethylene annulus between the two containers is 15 mm. The photograph in Figure III-10 shows all of the components of the EEOS experiment package.

If the pressure cell contained a gas atmosphere (air, helium, etc.) during a sample irradiation, there would be a



Figure III-10
Components of EEOS Inpile Package

pressure increase due to heating of the gas in addition to the fuel vapor pressure. To eliminate this problem, it was desirable to evacuate the pressure cell prior to irradiation. While the inner and outer containers were fitted with valves to seal them after evacuation and/or backfilling with helium, no such structure could be incorporated into the pressure cell design. Thus, a special fixture was needed to facilitate sealing the pressure cell in an evacuated environment. The fixture consisted of a cylindrical body, a base designed to mate with the lower endcap of the inner container, and a transparent top which was equipped with four vacuum-tight wrench feed-throughs for tightening the cap screws which seal the pressure cell. (See drawings in Appendix B.) The fixture and, hence, the pressure cell, can be evacuated and the pressure cell then sealed with the desired vacuum environment inside. The vacuum is monitored with a thermocouple-type vacuum gage in the top of the fixture.

DATA ACQUISITION AND REPRODUCTION SYSTEMS

A block diagram of electronic system used to record the instrumentation signals is shown in Figure III-11. The outputs from the various types of instrumentation were recorded on a 14-channel, frequency modulated (FM) tape recorder (Ampex PR2200). A console containing the tape recorder, linear amplifiers, and a calibration unit was located in the ACPR low-bay facility adjacent to the reactor high-bay. (The overall frequency response of the system was 40 kHz.) The calibration unit provided a mechanism by which known voltages could be imposed at the input to the system

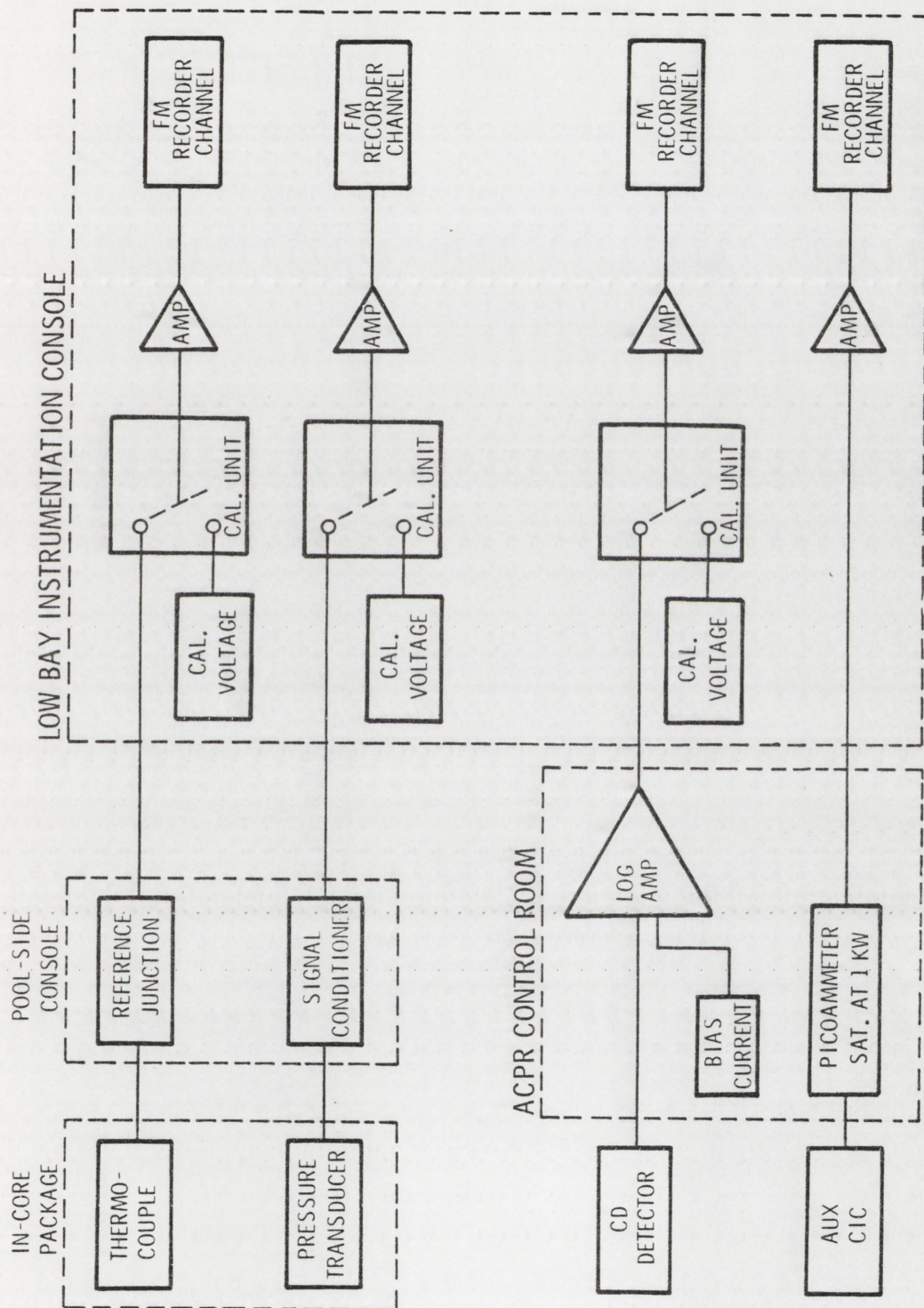


Figure III-11
Block Diagram of Data Acquisition System

amplifiers and the FM recorder. As described in Chapter IV, these calibration signals were used in the reproduction of the recorded data. The thermocouple reference junction and the signal conditioning electronics for the pressure transducer were located at the side of the ACPR pool, as near as practicable to the inpile package. Two signals associated with reactor power were derived from neutron detectors located in or near the reactor core via electronics located in the ACPR control room. Since more than ten decades of reactor power are traversed during the reactor pulse, a signal proportional to the base-10 logarithm of reactor power (expressed in megawatts) was recorded. That signal was derived from an inpile cadmium self-powered neutron detector via a logarithmic amplifier. The need for the bias current shown in Figure III-11 is discussed in Chapter IV. The output from a compensated ion chamber, located near the reactor core, is monitored with a picoammeter, the output of which is set to saturate at a power level of approximately 1 kW. This fiducial is recorded and is used as a time reference in subsequent data processing.

Figure III-12 shows a block diagram of the data processing system used to reproduce the recorded information. The recorded data was digitized and otherwise processed via the Sandia Data Acquisition and Display System (DADS) (Po71). The recorded data channels (temperature, pressure, and reactor power) are digitized one at a time via the DADS high speed analog-to-digital converter (ADC) with the "1 kW" fiducial used as the start signal for the ADC using the procedures described in Chapter IV. The digital

LOW BAY INSTRUMENTATION CONSOLE

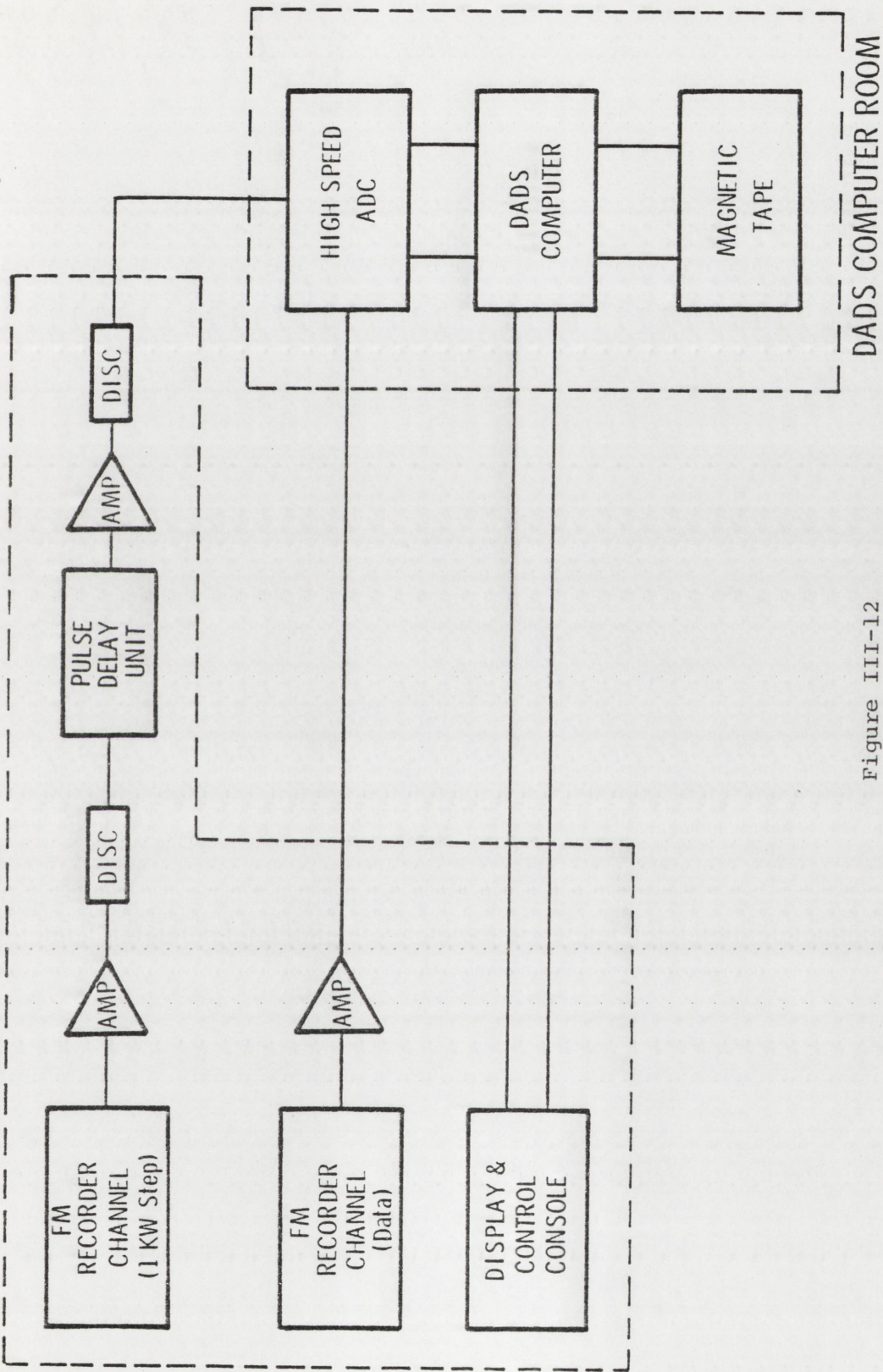


Figure III-12

Block Diagram of Data Reproduction System

data was displayed graphically and stored on magnetic tape for subsequent processing.

TRANSDUCER CALIBRATION

As is described in Chapter V, all of the pressure transducers, after the first experiment, were buffered by a disc of graphite bonded to its sensing diaphragm. Since the presence of that graphite disc did affect the transducer sensitivity, it was necessary to recalibrate each transducer. To infer pressure from the strain measurements, the output from the strain gage system was calibrated at known internal pressures. (The strain gage system consisted of the strain bridge located in the inpile package, the cables between the inpile package and the poolside console, the supply battery, and a linear amplifier (gain x 100) used to amplify the strain bridge output.) These calibrations were performed by attaching the pressure cell and the pressure transducer to a system in which the internal helium pressure could be adjusted by filling from a gas cylinder or by venting to the atmosphere. The system pressure was monitored by a standard pressure gage from 0 psig to 1900 psig. The pressure cell was adapted to this system with the same test fixture that was used for the hydrostatic test. (See drawing in Appendix B.) After calibration at a number of pressures, a polynomial was fitted to the data using least squares techniques, and the resulting equation was used in the reduction of the digitized experimental data as described in Chapter IV. The pressure transducers were subsequently calibrated to 5000 psig by the Sandia Transducer Laboratory.

EXPERIMENT PROCEDURES

The detailed experimental procedures used for assembly and disassembly of the inpile package are given in Appendix D. Briefly, the pressure cell was assembled and instrumented with thermocouples and strain gages. It was then attached to the lower end cap of the inner container, and the instrumentation leads were soldered to the terminal board on the bottom end cap. The pressure transducer or instrumented dummy transducer was prepared, and the transducer and/or pressure cell was calibrated as described above. If the experiment were to contain fuel, the desired sample was removed from the safe and placed in the pressure cell. The "C-seal," transducer or dummy, retainer, and cap screws were installed, but the cell was not sealed. The assembly was then inserted into the loading fixture (described previously), and the fixture was purged of air by alternately evacuating and backfilling with dry helium. The loading fixture and, hence, the pressure cell were then evacuated to approximately 10^{-4} torr, and the pressure cell was sealed by tightening the cap screws via the wrench feed-throughs in the loading fixture. A photograph of the sealed pressure cell assembly is shown in Figure III-13.

The sealed pressure cell assembly was then installed in the inner containment. That vessel was purged of air and pressurized to 2 atm gage pressure with helium. The assembly was immersed in denatured alcohol and any leaks were noted by the presence of bubbles. If leaks were observed, the container was disassembled,

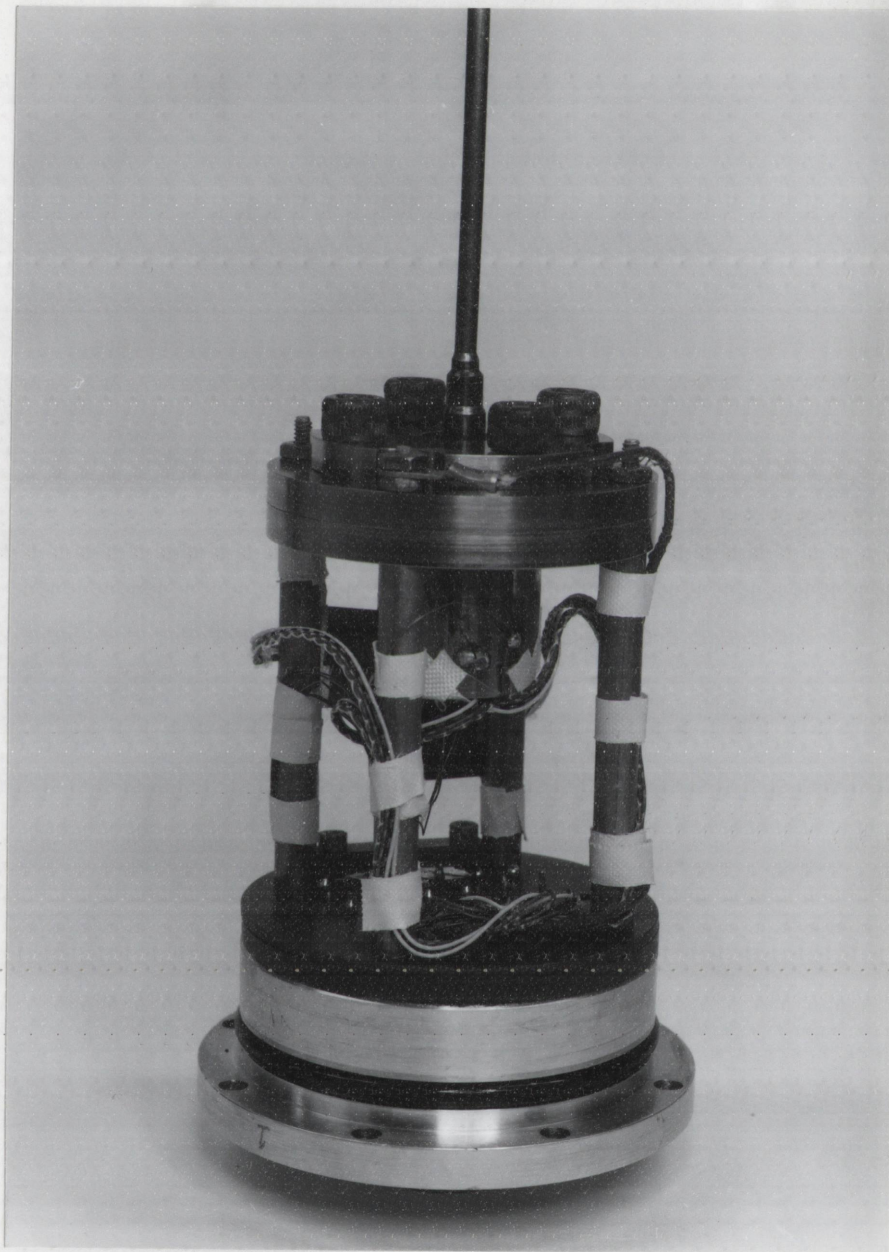


Figure III-13
Sealed Pressure Cell Assembly

reassembled, and retested. After a successful leak test, the inner container was evacuated to 10^{-4} torr; the valve was closed and capped. If used, the internal polyethylene moderator was attached to the inner containment which was suspended from the top lid of the outer container. All cables between the inner and outer containers were connected. This assembly is shown in the photograph in Figure III-14.

The inner assembly was then placed in the outer containment; external polyethylene moderator, if used, was installed; and the outer container was sealed. After air was purged from the outer container, it was leak tested as above. After the leak test the helium pressure was reduced to atmospheric pressure, and the valve was closed and capped. A fully assembled inpile EEOS package is shown in the photograph in Figure III-15. At all stages of assembly, the continuity of the instrumentation leads was verified by resistance measurements between the leads, and between the leads and the assembled package. Certification of the sample enrichment and total polyethylene thickness, witnessed by another person, and certification of successful leak tests of the two containers are required by the ACPR Supervisor prior to irradiation of the experiment.

After the experiment was loaded, and all cables between the inpile package and the several instrumentation consoles were connected and checked, known calibration voltages were recorded on the FM tape via the scaling amplifiers through the use of the calibration unit located in the low-bay instrumentation console.

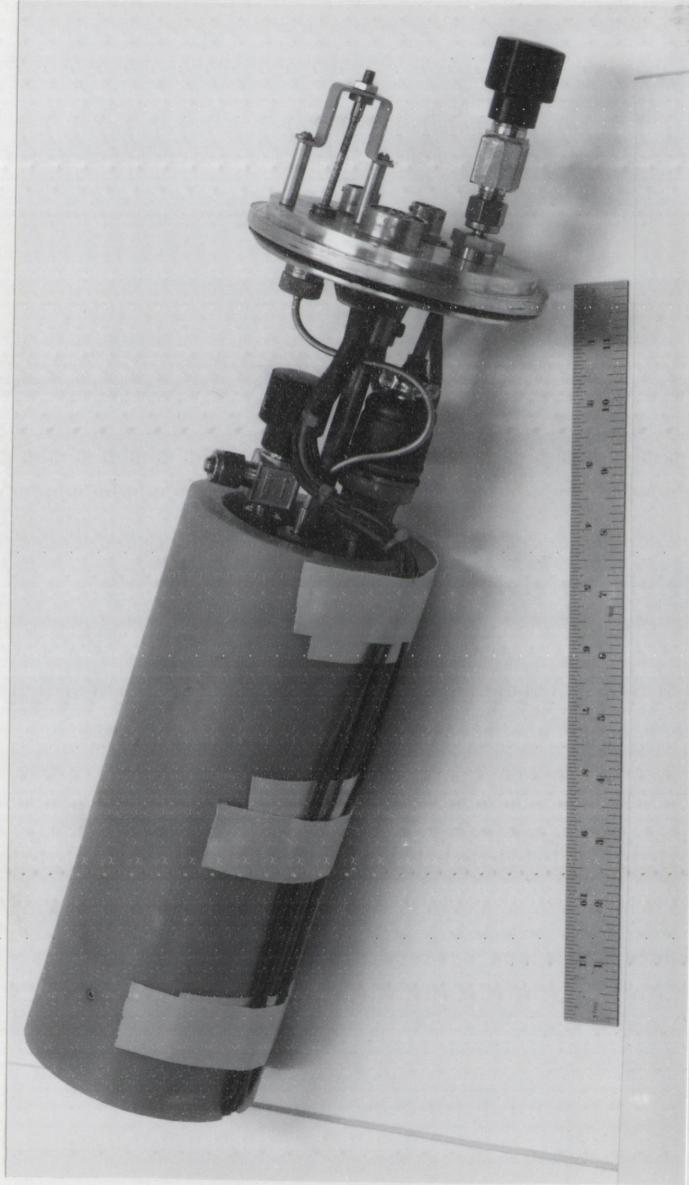


Figure III-14
Completed Inner Assembly

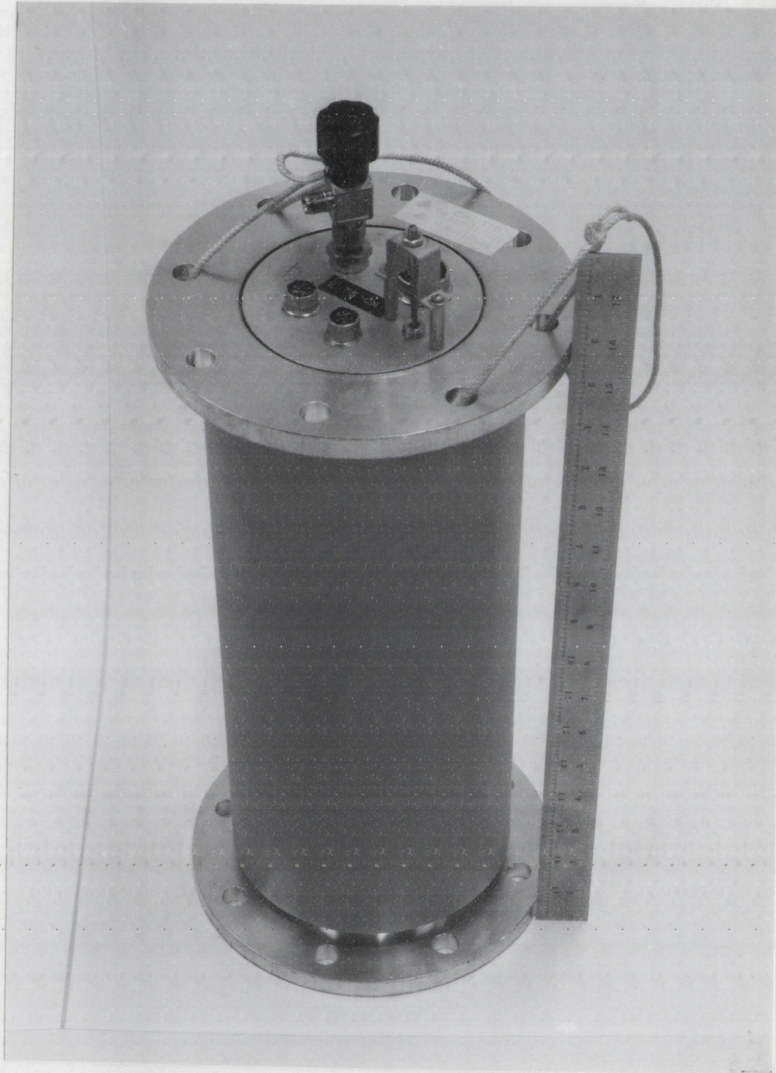


Figure III-15
EEOS Inpile Package

(See block diagram in Figure III-11.) The magnitudes of the calibration voltages were chosen to correspond to the maximum transducer signal anticipated during the experiment. The gains of the scaling amplifiers were set so that the recorded signal was 50 percent of the maximum recorder deflection when the calibration voltages were imposed on the amplifier inputs. Thus, transducer signals twice as large as those anticipated would still be recorded without distortion. The instrumentation signals were recorded from approximately thirty seconds before the reactor pulse to three minutes after the pulse.

After the experiment had been designed and the proof tests had been completed, several irradiations were performed without fuel samples to determine the radiation responses of the various transducers during the reactor transient. The output of each transducer did exhibit a radiation induced signal. These signals and the techniques used to eliminate them are discussed in Chapter IV. The procedure involves the two irradiations for each measurement. For the first irradiation the package is assembled without the sample. After the first irradiation, the inpile package is disassembled and then reassembled with the fuel sample. As described in Chapter IV, the radiation induced noise can be eliminated by a comparison of the data obtained during the two irradiations.

The buildup series experiments consisted of a fuel sample in a pressure cell fitted with a dummy transducer. The pressure cell was instrumented with one strain bridge and two thermocouples

located in the bottom of the graphite crucible. Since the only information to be obtained from the buildup experiments was the fission energy deposited in the sample, no radiation noise experiments were performed during that series. The thermocouple, strain gage, and reactor power data from these experiments were only used to gain experience in the recording and processing of the transducer data.

Neutron transport calculations using the two-dimensional, multi-energy-group, TWOTRAN code (La70) were used to predict the energy deposition to be expected for a particular combination of sample enrichment and polyethylene moderator thickness. A series of irradiations were then performed using that combination and successively larger ACPR pulses until a maximum pulse had been performed. Then another series was begun with a different enrichment and/or polyethylene thickness. Each series began with a pulse size that was predicted to yield 300 cal/gm fission energy deposition or 75 percent of the previous maximum energy deposition, whichever was greater. Subsequent experiments in the series were intended to yield energy depositions that were 75 cal/gm larger than that attained in the previous experiment. Fission product inventories were performed following each buildup experiment to determine the fission energy deposition. The FPI data was then used to supplement the neutron transport calculations in the prediction of subsequent experiments.

The vapor pressure measurements consisted of several series of four irradiations each. In each series, two assemblies were

each irradiated twice: once without and once with a fuel sample. One assembly contained a Kaman pressure transducer for the direct measurement of the pressure history. In the second assembly, an instrumented dummy transducer was used to determine heat losses to the transducer. The data from the two irradiations without fuel samples were used for radiation noise correction of the data from the two fueled experiments using the procedures described in Chapter IV. Each assembly contained two strain bridges on the pressure cell and six thermocouples in the graphite crucible.

CHAPTER IV

DATA REDUCTION AND ANALYSIS

The functional relationship between the energy content of a fuel sample and its vapor pressure was determined from a point by point comparison of pressure and energy content histories recorded during a reactor transient. This section describes the techniques used to obtain these histories from the recorded instrumentation signals and the fission product inventory data described previously. These techniques include the digitization of the recorded signals and conversion to measured parameters (pressure, temperature, or reactor power). The methods used to correct the recorded signals for radiation induced noise and to eliminate spurious high frequency noise by low pass digital filtering techniques are described. The inverse heat conduction technique used to determine surface heat fluxes from the thermocouple measurements is discussed. Finally, the formulation of the energy input and loss histories and the details of the comparisons with the pressure history are described.

NOTATION

Throughout this chapter, reference is made to sets of data and to the individual elements of those sets. The convention was adopted to use capital letters (perhaps with subscripts) to refer to the entire set and lower case letters with subscripts to refer to the individual elements. For example

$$X_i = \{x_{i,1}, x_{i,2}, \dots, x_{i,j}, \dots, x_{i,N}\} \quad (1)$$

where X_i is a set of N samples, $x_{i,j}$ is the value of X_i at time $(j-1)\Delta t$, and Δt is the ADC sample interval. The origin of time is a fiducial recorded on the magnetic tape corresponding to the time when reactor power exceeded 1 kW. The ADC start signal was derived from the fiducial.

DIGITIZATION AND CONVERSION

The reduction and analysis of the experimental data was accomplished using digital computers. Hence, the first step involved digitizing the recorded analog data using the Sandia Data Acquisition and Display System (DADS) (Po71). This system is shown in a block diagram in Figure IV-1. The amplifier shown was used to drive the 600 feet of cable between the FM recorder and the DADS. The analog to digital converter (ADC) used has a minimum resolution of 2.4414 mV at its input. Hence, the amplifier also served to increase the amplitude of the recorder output from a maximum of 0.5 volts to approximately 3 volts; thus, the precision of the digitized result was improved. The ADC can digitize data at a maximum rate of 100 kHz, although most of the data used in these experiments was digitized at 6250 Hz.

The need to know the gains of the various amplifiers in the recording and reproduction systems was eliminated by recording positive and negative voltages on tape prior to recording the instrumentation signals. These signals were used to calibrate each data channel as described below.

Let C_i be the magnitude of the input calibration voltage for the i^{th} channel and $V_{cp,i}$ and $V_{cn,i}$ be the average value of

LOW BAY INSTRUMENTATION CONSOLE

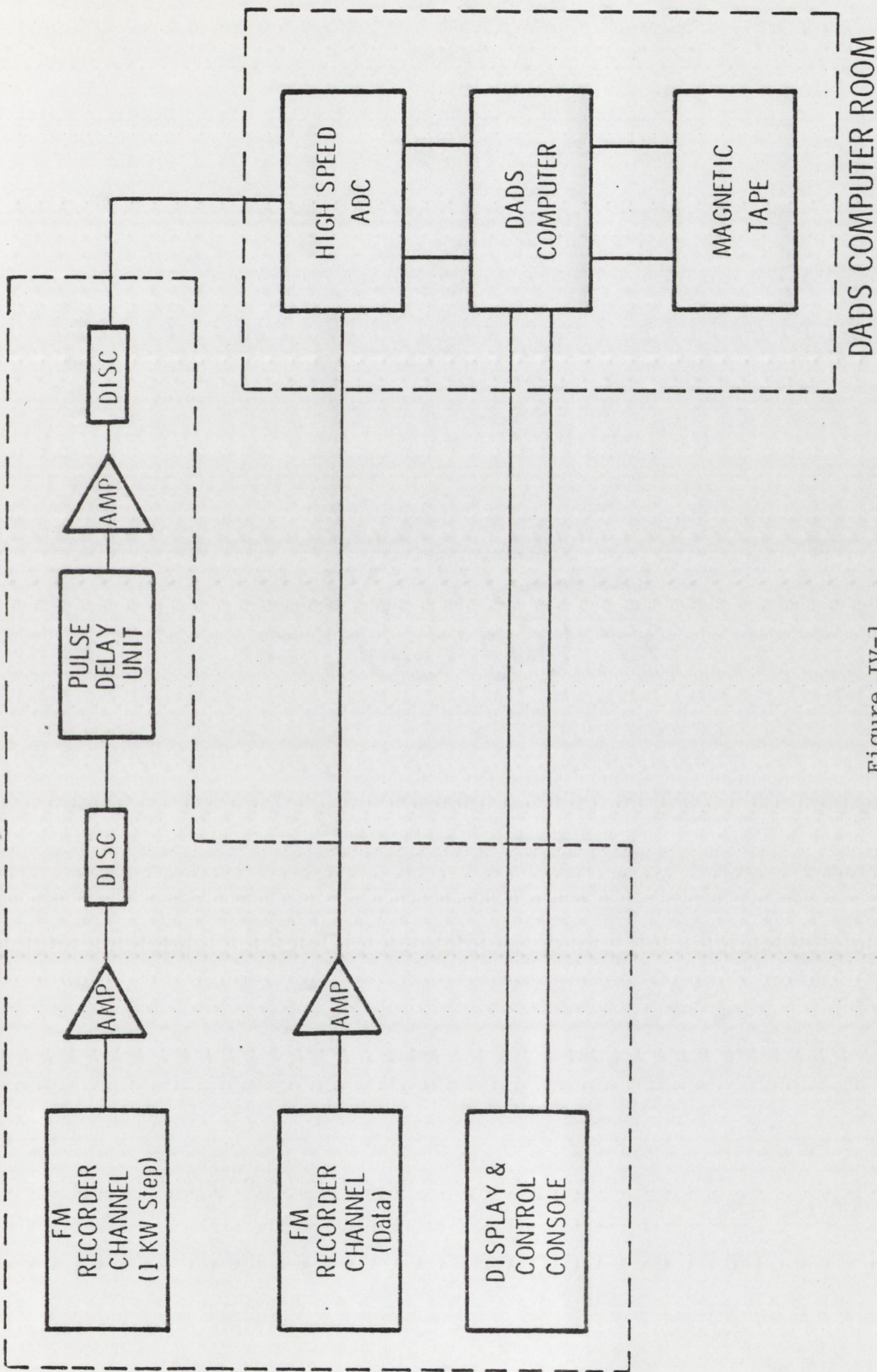


Figure IV-1
Block Diagram of Data Reproduction System

the reproduced voltages measured by the DADS ADC for the positive and negative calibration signals for the i^{th} channel. ($V_{\text{cp},i}$ and $V_{\text{cn},i}$ are averages of fifty ADC samples.) Two parameters were computed from the calibration data which permitted determination of the true input voltages. These are a zero offset, OFFSET_i , and a tape factor, TF_i . These are defined as:

$$\text{OFFSET}_i = \frac{V_{\text{cp},i} + V_{\text{cn},i}}{2} \quad (2)$$

and

$$\text{TF}_i = \frac{2C_i}{V_{\text{cp},i} - V_{\text{cn},i}} \quad (3)$$

If S_i is the set of experimental signal voltages and V_{si} is the set of reproduced signal voltages measured by the DADS ADC for the i^{th} data channel, true experimental data signal can be derived as

$$s_{i,j} = (v_{\text{si},j} - \text{OFFSET}_i) \times \text{TF}_i \quad (4)$$

For pressure and temperature channels the conversion from voltage (S_i) to pressure or temperature data (D_i) is accomplished by means of a calibration polynomial, $P_i(V)$, for each transducer or thermocouple type. That is:

$$d_{i,j} = P_i(s_{i,j}) = A_{0,i} + A_{1,i} s_{i,j} + A_{2,i} s_{i,j}^2 + \dots \quad (5)$$

where ($A_{0,i}$, $A_{1,i}$, $A_{2,i}$, ...) are the coefficients in the polynomial P_i .

The recorded reactor power signal was derived from a self-powered neutron detector in the ACPR core through a logarithmic amplifier. The output of that amplifier was adjusted so that its magnitude (in volts) was the base-10 logarithm of reactor power (RP) expressed in megawatts (i.e., 4 V = 10,000 mW). Since the logarithm of zero is not defined electronically or mathematically and the minimum input sensitivity of the logarithmic amplifier corresponded to the detector output at approximately 10 kW, it was necessary to bias the amplifier input above zero. This was accomplished by connecting a constant current source in parallel with the detector. The magnitude of the bias current used was 1×10^{-8} amp, which corresponds to approximately 0.79 mW. Hence, the experimental voltage signal for the reactor power channel, S_{12} , is defined as:

$$s_{12,j} = \log_{10} (rp_j + \text{BIAS}) \quad (6)$$

where BIAS is the reactor power equivalent of the bias current. Again, to preclude the need for exact knowledge of the bias current, the value of BIAS was determined from the experimental data. At times well before the reactor pulse, RP is essentially zero. Hence, if SB is the average of several elements of S_{12} corresponding to those early times, then:

$$SB \cong \log_{10} (0 + \text{BIAS}) = \log_{10} (\text{BIAS}) \quad (7)$$

Hence:

$$\text{BIAS} = 10^{\text{SB}} \quad (8)$$

Therefore, the reactor power history, RP, can be defined by:

$$\text{rp}_j = 10^{\text{s}_{12,j}} - \text{BIAS} \quad (9)$$

The integral of reactor power, IP, which is the basis for the energy input history, was derived from the reactor power history, RP, as:

$$\text{ip}_i = \frac{1}{2} \sum_{j=1}^i (\text{rp}_j + \text{rp}_{j-1}) \Delta t \quad (10)$$

where IP_i is the integral after time $(i-1)\Delta t$ and RP_j is the reactor power at time $(j-1)\Delta t$.

RADIATION NOISE CORRECTION AND DIGITAL FILTERING TECHNIQUES

A radiation induced signal was observed on the output of every channel of instrumentation. For the pressure transducers and the thermocouples, the radiation signal was found to be identical for a given device during successive irradiations.

To eliminate these noise signals the following procedure was used. Each assembly was irradiated twice: once without and once with the fuel sample. The instrumentation signals recorded during the first irradiation represent the radiation induced signals alone. Those from the second pulse are the sum of the radiation induced noise and the signal produced by the heating

of the fuel sample. Because of small errors in the settings on the electronics used to derive the "1 kW" fiducial, that signal can occur at slightly different times relative to the peak of reactor power for pulses that are otherwise identical. The digitized data from two experiments can be shifted so that the peaks of reactor power are coincident for both pulses.

To perform the radiation noise correction, the data from each channel from the experiment without fuel are shifted in time as necessary and subtracted point by point from the corresponding data from the fueled experiment. This procedure is demonstrated for a typical thermocouple channel in the first three frames of Figure IV-2. Frame (A) displays the uncorrected data from the fueled experiment; frame (B) shows the radiation induced noise signal; and frame (C) shows the corrected result.

For the strain gages, the radiation induced signal was not the same during successive irradiations. Further, the noise signal on the strain gages channels was much larger than the expected strain signal due to internal pressurization. Thus, the pressure signal could not be deduced from the strain gage output. This loss of information was not important, however, since the strain data were redundant to the pressure transducer.

As shown in frame (C) of Figure IV-2, after the radiation noise correction, a considerable amount of high frequency noise remains in the data, arising from random radiation induced noise, electronic noise from the amplifiers and tape recorder in the data acquisition system, and from electromagnetic noise induced

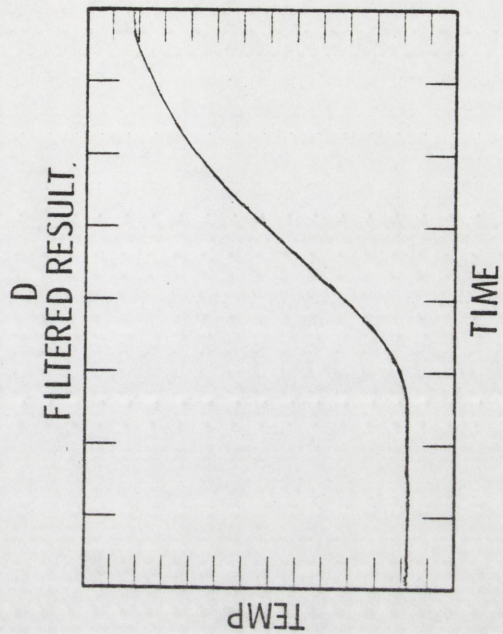
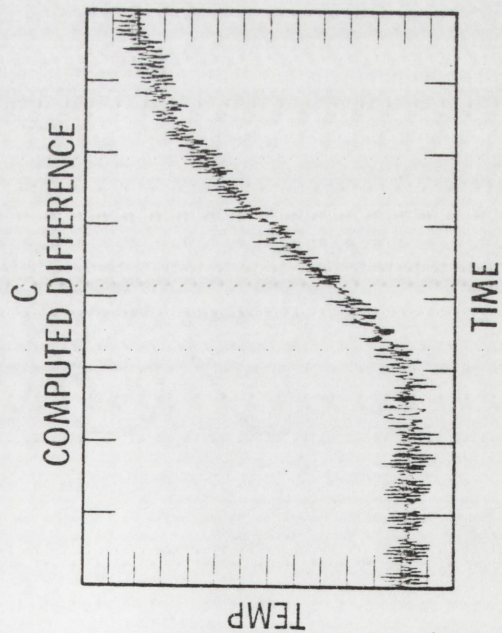
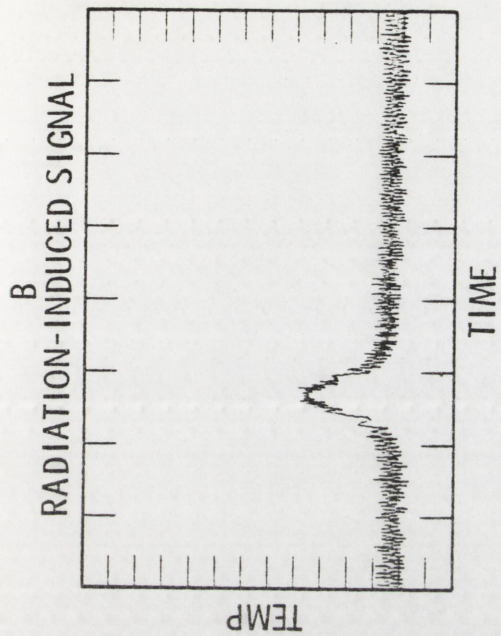
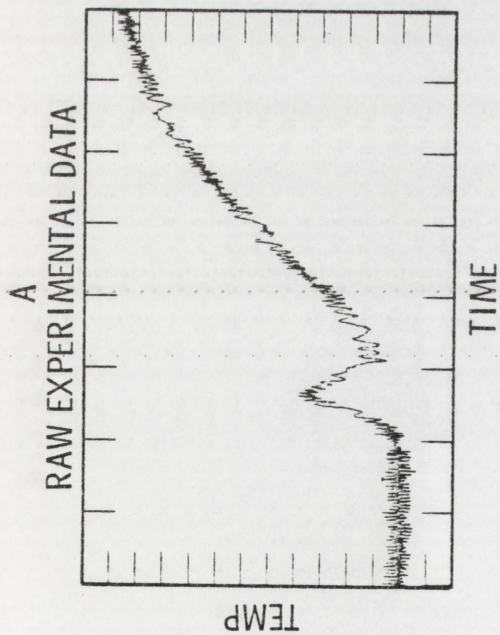


Figure IV-2
Results of Radiation Noise Correction and
Filtering Techniques for Typical Thermocouple Data

on the long cables. In order to obtain useful data traces, it is necessary to eliminate this high frequency noise. This was accomplished using low pass digital filtering techniques described by Stearns (St75). A detailed description of the filter used for this data reduction is shown in Appendix F. Frame (D) of Figure IV-2 shows the filtered result for the radiation noise corrected thermocouple data.

In practice, the radiation noise corrections for thermocouple and pressure transducer data were performed first and the results were then filtered. For the reactor power data, the logarithmic data was filtered before the linear power history was computed and integrated.

One final correction was needed for the pressure transducer data. In several of the experiments a net bias was noted in the pressure data after the radiation noise correction had been made. This resulted from zero shifts in the transducer due to changes in the cable configuration and from the fact that the unfueled experiments contained 1 atm of helium and the fueled experiments were initially evacuated. This bias was eliminated by averaging the first 50 samples of the filtered result and subtracting that value from each element of the data set. This resulted in the final pressure history for the experiment.

ENERGY INPUT HISTORIES

Since it was not possible to measure energy content directly, the energy histories were inferred from a combination of experiment data. The energy content was estimated from the energy

input to sample and energy losses from the fuel as functions of time.

Energy is deposited in the fuel samples by fission and by absorption of gamma radiation. The rate at which energy is deposited in the sample is proportional to reactor power; hence, the integral of the energy deposition in the sample is proportional to the integral of reactor power. The power integral, IP, can be normalized to the total energy deposited in the sample, yielding an energy input history.

The total integral of energy deposited in the sample is the sum of two components: 1) fission energy deposition (E_f), and 2) gamma absorption (E_γ). The total fission energy deposition during the experiment (E_f) was determined after the irradiation by the Lanthanum-140 fission product inventory technique described in Appendix E. The total energy from gamma absorption (E_γ) can be estimated from the gamma energy absorbed in Cobalt glass, as described in the ACPR Experimenter's Manual (BM74). Assuming an average gamma energy of 1 MeV, the result for UO_2 is 0.045 cal/gm-mJ or 4.8 cal/gm for a maximum ACPR pulse.

Typical ACPR reactor power pulses are shown in Figure IV-3. As shown in Figure IV-4, 75 to 85 percent of the total energy is associated with the prompt pulse; the balance is associated with the pulse tail. A detailed analysis of recorded power signals from the three size pulses used in these experiments provided more precise estimates of the fraction of the total energy release that can be associated with the prompt pulse. These are

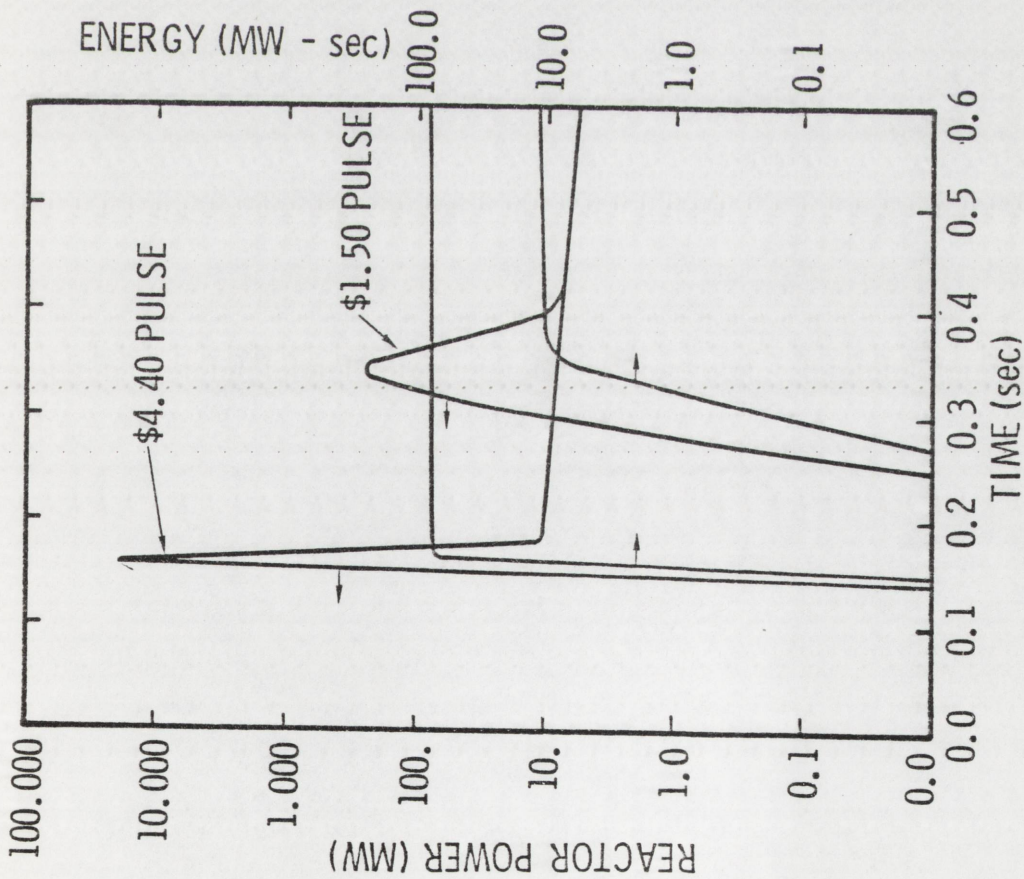


Figure IV-3

Typical ACPR Pulse Shapes
and Corresponding Pulse Integrals

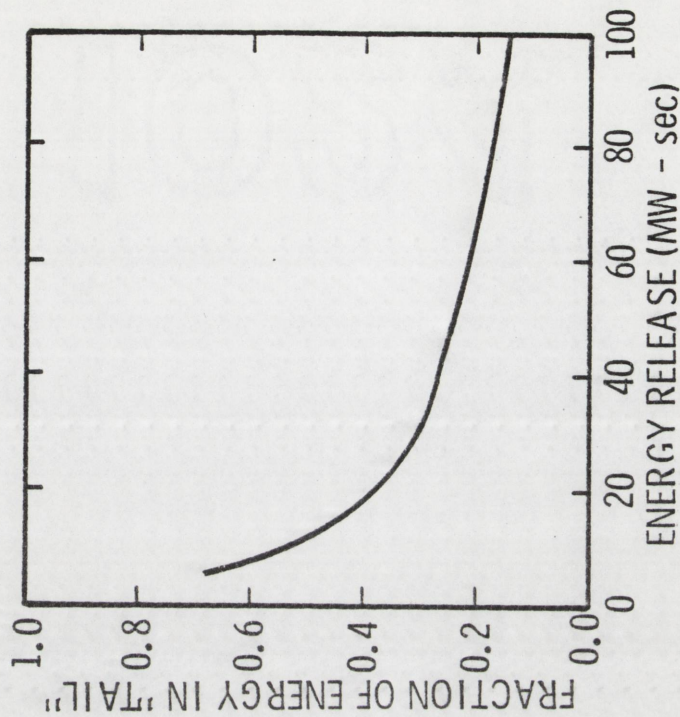


Figure IV-4

Fraction of Energy in Pulse Tail
Vs. Total Pulse Energy Release (BM74)

summarized in Table IV-1. Such values correspond to times approximately 50 msec after the peak of reactor power. If this fraction is denoted as EFRAC and if the integral of reactor power, IP, contains N points, (ip_1, ip_2, \dots, ip_N), the average energy input history, E_{avg} , can be defined as follows:

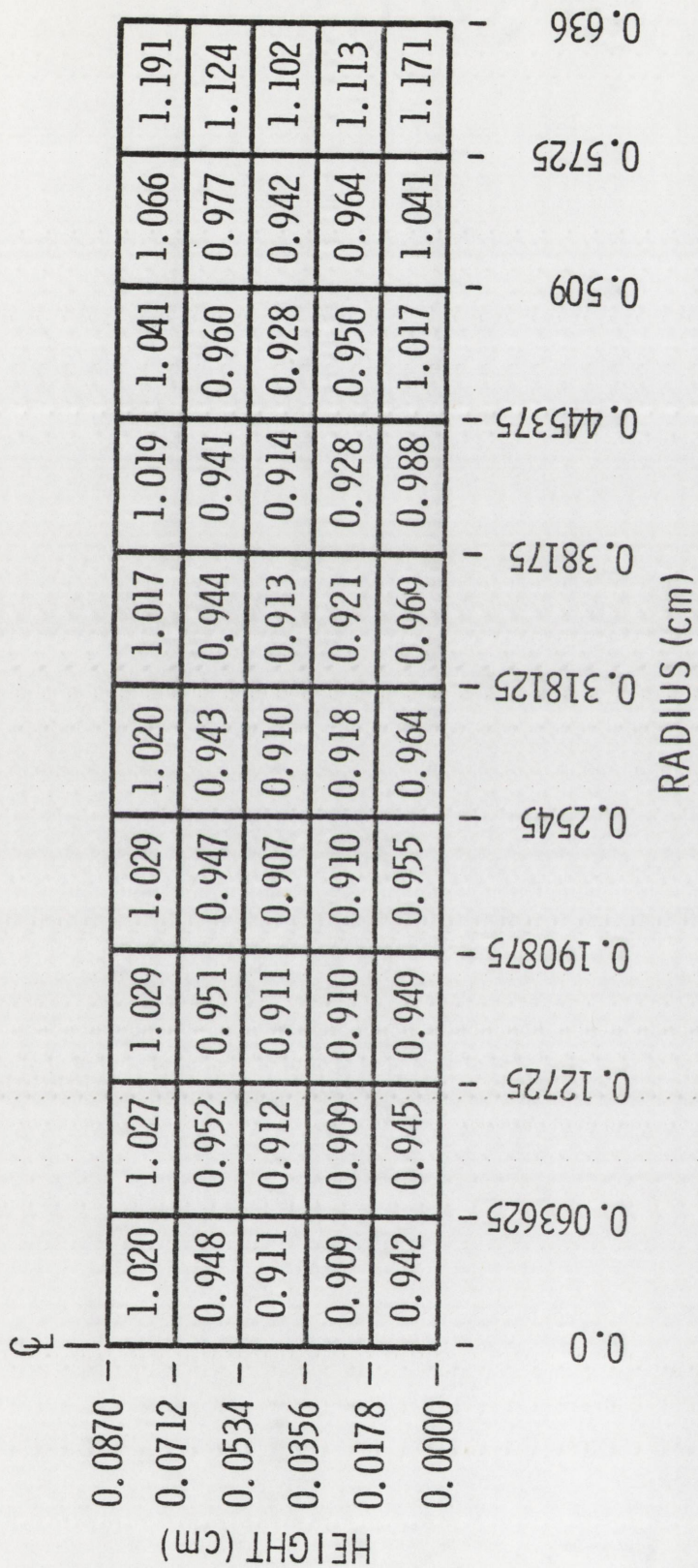
$$e_{avg,j} = \frac{(E_f + E_\gamma) \times EFRAC \times ip_j}{ip_N} \quad (11)$$

The fuel samples used in these experiments were enriched UO_2 , and were irradiated in a thermal neutron flux. As a result, the fission density profiles are not uniform due to self-shielding in the sample. The fission density distribution can be estimated from neutron transport calculations. The experiment geometry and ACPR core were modeled in detail using the TWOTRAN two dimensional neutron transport code (La70). The relative fission density distribution for a 30 percent enriched sample is shown in Figure IV-5. The values are normalized to an average fission

TABLE IV-1

Fraction of Total Energy Release
Associated with Prompt Pulse

Reactor Pulse Yield (mJ)	Fraction of Total Release in Prompt Pulse
94	0.79
97	0.80
106	0.83



TOTAL VOLUME = 0.113 CM³ AVERAGE = 1.0 PEAK-TO-MIN = 1.31

Figure IV-5
Relative Fission Density for 30 Percent Enriched
UO₂ Irradiated in ACPR with 2.75 cm Polyethylene

density of 1.00. Note that the peak-to-average fission density ratio (PTA) is 1.19.

A peak energy deposition history (E_p) may now be defined as:

$$e_{p,j} = e_{avg,j} \times PTA \quad (12)$$

ENERGY LOSS HISTORY

The total time of significant heating of the sample is approximately 20 msec. During this time heat is lost from the sample to the graphite crucible, as evidenced by the temperature rise measured by the thermocouples in the graphite. These heat losses from the fuel sample to the crucible were estimated using the inverse heat conduction technique (IHC) developed by Beck (Be68). This technique which permits the calculation of surface heat fluxes from a single transient temperature history measured in the interior of a heat conducting solid, involves the numerical inversion of a convolution integral.

The temperature history at an interior point x_1 in a solid due to a time variant surface heat flux can be described by Duhamel's Theorem (Ca59) in the form

$$T(x_1, t) - T_i = \int_0^t \dot{q}(0, \lambda) \frac{\partial \phi(x_1, t-\lambda)}{\partial t} d\lambda \quad (13)$$

where $T(x_1, t)$ is the transient temperature history at x_1 in a one-dimensional solid due to the time-variable surface heat flux

$\dot{q}(0,t)$ and $\phi(x_1,t)$ is the temperature response at x_1 for a unit rise in the surface heat flux.

The techniques used for the numerical inversion of equation (13) are described in Appendix G. The result is a heat flux history $(\dot{Q} = \{\dot{q}_1, \dot{q}_2, \dots, \dot{q}_j, \dots, \dot{q}_k\})$ where \dot{q}_j is the average heat flux over the interval $(j-1)\Delta t_1$ to $j\Delta t_1$ where Δt_1 is the IHC time step. As is described below, Δt_1 is, in general, larger than the ADC sample interval Δt . As described in Appendix G, the heat flux at each time step is determined from the solution of a set of linear equations which involve the experimental temperatures for the current time step and r future time steps, the calculated heat fluxes for all previous time steps, and the response functions $\phi(x_1,t)$.

The response functions $\phi(x_1,t)$ were computed numerically using the Chrysler Improved Numerical Differencing Analyzer for Third Generation Computers (Le67) (CINDA-3G). A one-dimensional representation of the graphite crucible was modeled using CINDA with a unit heat flux imposed on one surface and an adiabatic boundary condition at the other. The assumption of an adiabatic boundary condition was valid because of the presence of a small gap between the crucible and the pressure cell and the very small temperature increase at that boundary during the time of interest. Similarly, the use of a one-dimensional representation is justified because of the proximity of the thermocouples to the inside surface (0.38 mm) compared to the surface dimensions (12 mm diameter) and the short times involved. The response function

is derived from the temperature history at the nominal thermocouple location in the CINDA problem.

The questions of stability and accuracy arises with respect to this inverse heat conduction technique. Beck (Be68) discusses these ideas in some detail; only the conclusions will be presented here. First, as in all numerical heat transfer calculations, there is an inherent stability criterion described by the Fourier Modulus

$$\tau = \frac{\alpha \Delta t}{L^2} \quad (14)$$

where α is the thermal diffusivity, Δt is the time step, and L is a characteristic dimension (in this case, the depth of the thermocouple). For the inverse conduction problem, as opposed to a normal conduction problem, stability requires that the Fourier Modulus be greater than some value, $\tau \geq \tau_{\min}$. This requires that the thermocouples be near the surface and that relatively large time steps be used. In practice, time steps of approximately 1 msec were used with the thermocouples located 0.38 mm from the surface. The order of the expansion of the heat flux (i.e., η ; see Appendix G) and the number of future temperatures (i.e., r ; see Appendix G) both affect the stability and accuracy of the result. In general, larger values of η yield smaller errors in \dot{Q} , but less stability. The use of more future temperatures increases stability, but introduces larger uncertainties in \dot{Q} . For the analysis in the EEOS experiments, a constant approximation was used for the heat flux ($\eta=0$) with

one or two future temperatures.

This simple linear inverse heat conduction technique requires the use of constant material properties. This assumption was not good for the graphite used for the crucible over the wide range of temperatures seen in the experiment. In addition, the exact position of the thermocouple is known only to within ± 0.05 mm. The effects of these two experimental problems on the computed heat fluxes were investigated in sensitivity studies of the technique using actual experimental temperature data as input.

The constant material properties used for computing the response functions were chosen to correspond to an "average" graphite temperature. Figure IV-6 displays heat fluxes computed from the same experimental temperature history for "average" temperatures of 773 K, 1273 K, and 1773 K. It is noted that as the "average" temperature increases, the product of density and specific heat increases while the thermal conductivity decreases (see Appendix A). The effect of these changes in material properties is to cause the computed heat flux to rise more quickly to a higher value as the "average" temperature increases. The integrals of the three heat fluxes, which are related to the energy loss histories, are shown in Figure IV-7. These integrals differ by as much as a factor of two at early times, but converge to nearly the same value at 65 msec.

The computed heat fluxes can be used as input to a normal heat conduction problem to compute temperature histories at various points in the solid. One check on the validity of the

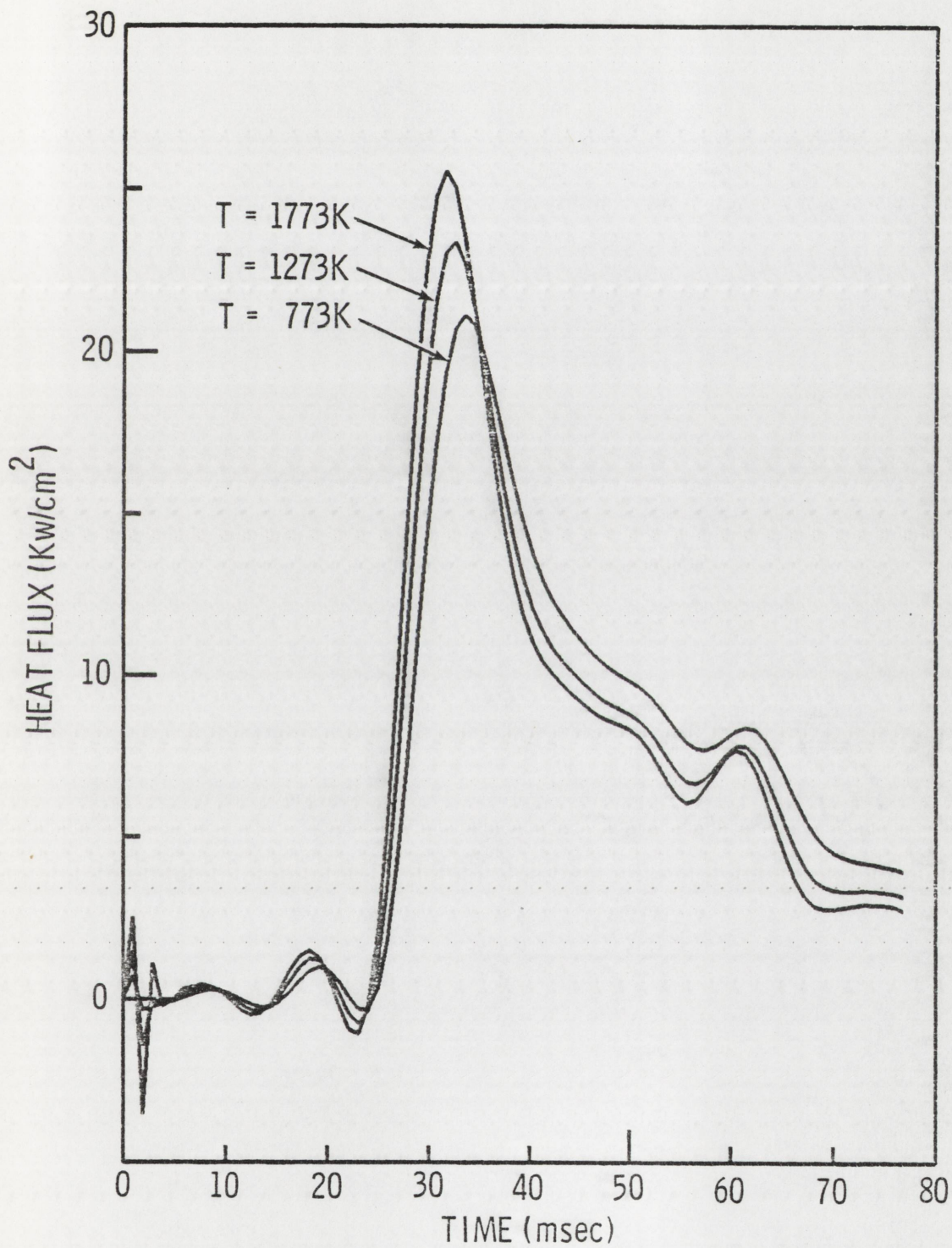


Figure IV-6

Heat Flux Histories Predicted by IHC Technique
for Three "Average Temperatures"

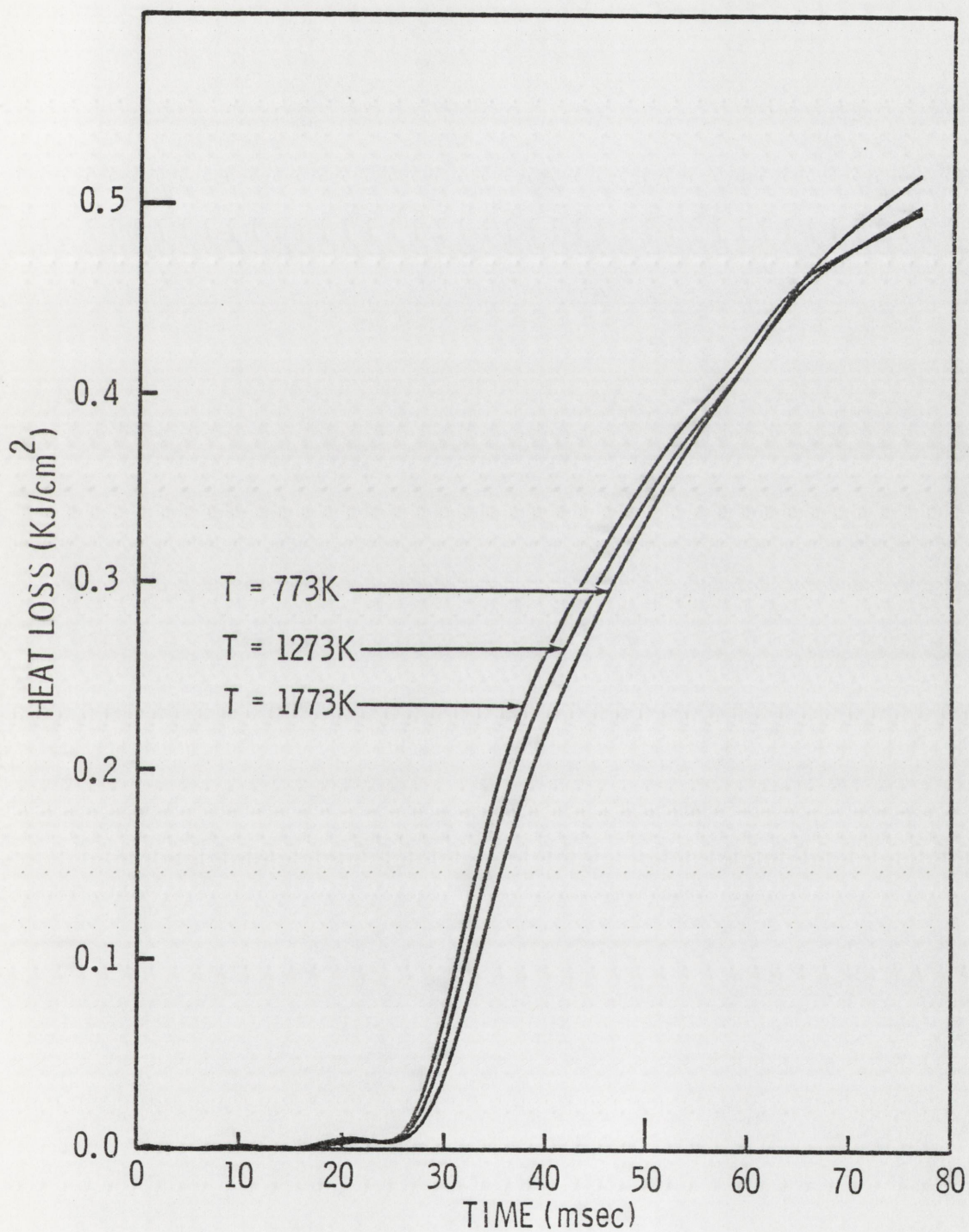


Figure IV-7

Heat Flux Integrals Predicted by IHC Technique
for Three "Average Temperatures"

heat flux estimate is to compute the temperature history at the nominal thermocouple location from the computed heat flux when the solid is modeled using temperature variant material properties and then compare that temperature history with the experimental input data. This was done for the three heat fluxes shown in Figure IV-6. The results are shown in Figure IV-8 with the experimental data. Of the three histories shown, the one for a 1773 K average temperature most closely approximates the experimental data. The differences at early times were due to an error bias in the thermocouple data.

The location of the thermocouples in the graphite also affects the computation of the surface heat flux. To investigate such effects, surface heat fluxes were computed from an experimental temperature history using response functions for three positions in the solid. These positions corresponded to the nominal thermocouple location and to positions 0.05 mm closer to the surface and 0.05 mm farther from the surface. An average temperature of 1273 K was used for all three cases. The calculated heat fluxes and the corresponding integrals are shown in Figures IV-9 and IV-10. As would be expected, smaller surface heat fluxes, occurring at later times, are predicted as the location of the experimental temperature history is moved toward the surface. The deviation of ± 0.05 mm in the thermocouple location yielded variations as large as ± 30 percent in the integrated heat flux.

The surface heat flux histories, computed for the several

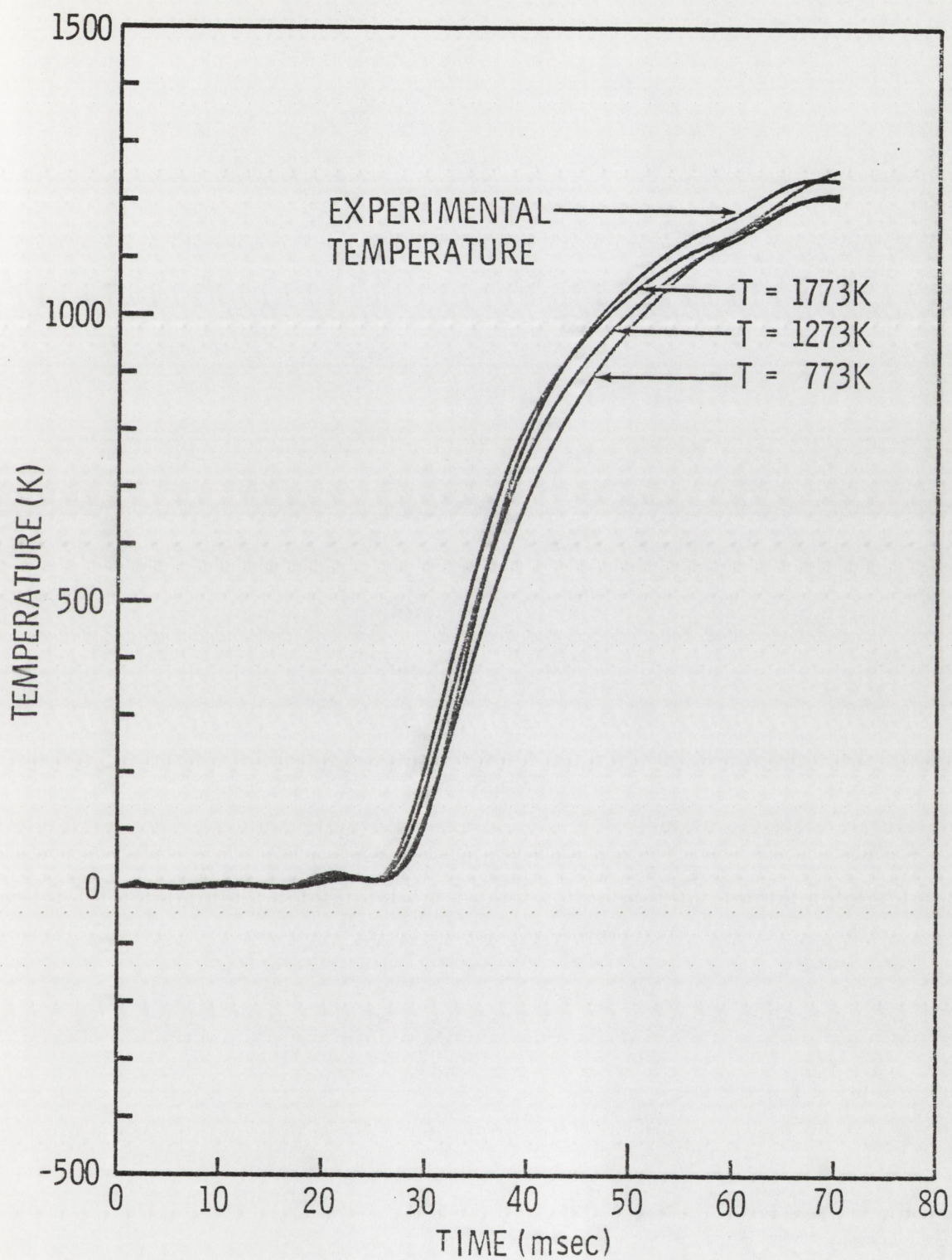


Figure IV-8

Experimental Temperature and Calculated Temperatures
at Thermocouple Location

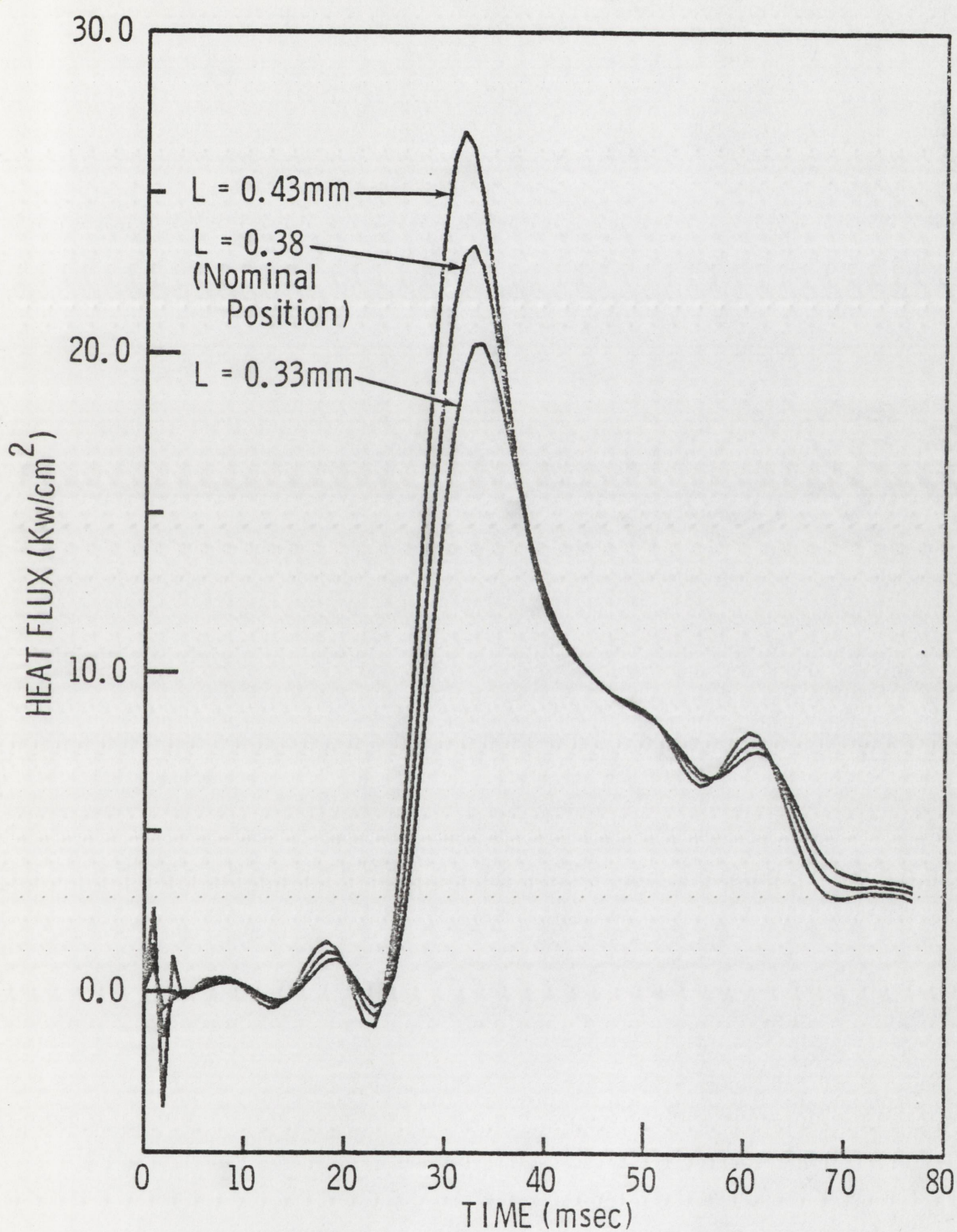


Figure IV-9

Heat Flux Histories Predicted by IHC Technique
for Three Thermocouple Locations

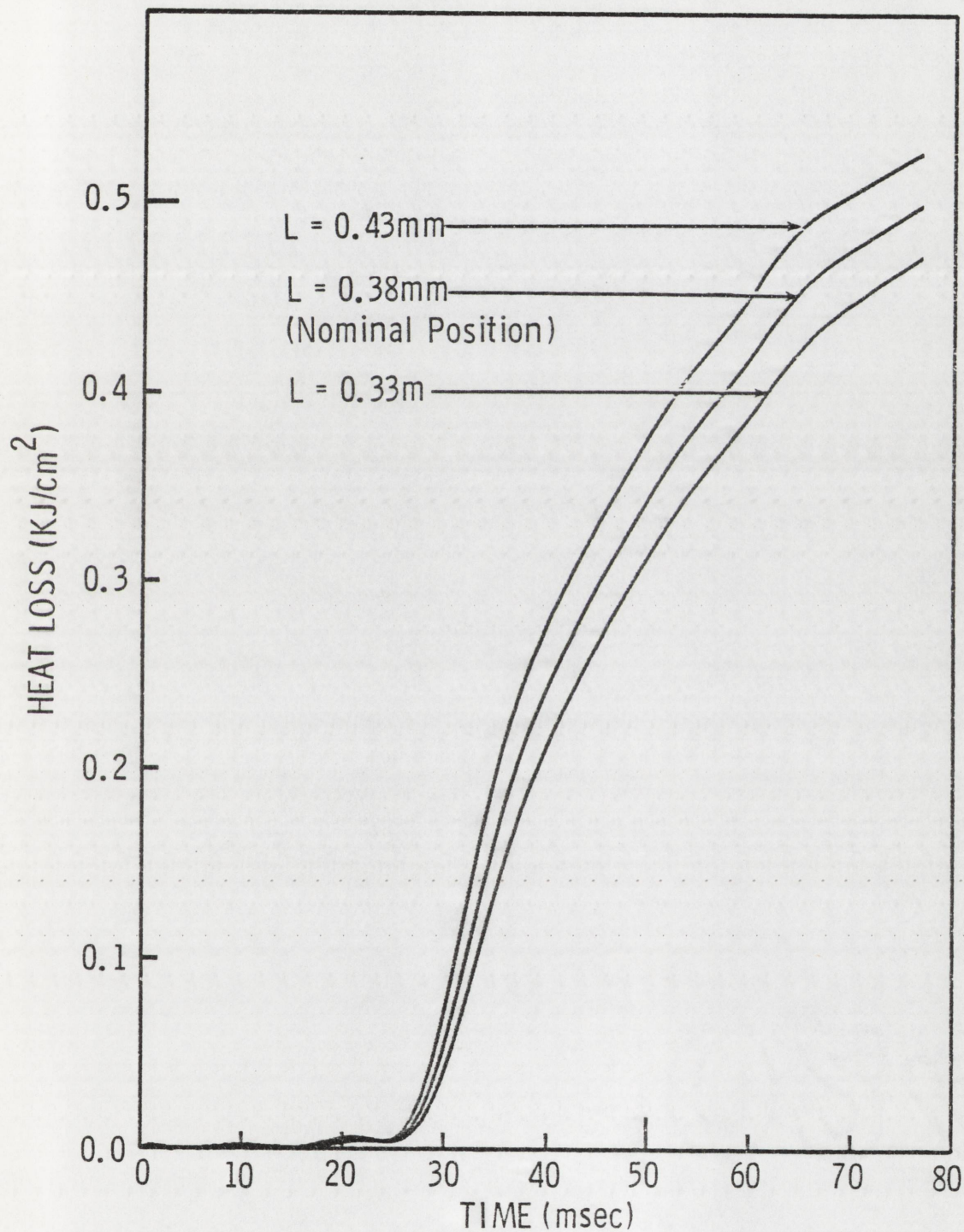


Figure IV-10

Heat Flux Integrals Predicted by IHC Technique
for Three Thermocouple Locations

thermocouples located in the graphite crucible and instrumented dummy transducer, were integrated in time and summed over the surface area to yield the energy loss history, E_{loss} , for the experiment.

A corrected average energy content history (E_{ac}) was computed as the net difference between E_{avg} and E_{loss} . Thus:

$$e_{\text{ac},j} = e_{\text{avg},j} - e_{\text{loss},j} \quad (15)$$

PRESSURE-ENERGY FUNCTIONAL RELATIONSHIPS

The first part of this chapter described the methods for obtaining pressure histories, peak energy content (E_{peak}), and corrected average energy content (E_{ac}) histories from the analog experimental data. However, the intent of the EEOS experiments was to develop functional relationships between pressure and the energy content of the fuel. Thus, the several data histories developed previously must be combined to yield the vapor pressure relationship.

Several complex phenomena occur in the fuel volume during these experiments. These included mass transport, heat transport, phase transformations, and chemical dissociation. All observations of the system during the experiments were made from outside the fuel region. Any modeling of the fuel during the transient would require knowledge of material properties which does not exist and an a priori knowledge of the equation of state of

the fuel. Therefore, a detailed description of the energy distribution within the fuel sample as a function of time is not possible. However, because of the nonuniform fission density distribution which was peaked at the surface of the sample and the significant heat losses from the sample, a detailed knowledge of that time-dependent energy distribution is essential in order to precisely describe the functional relationship between vapor pressure and energy content. It was possible, however, to extract upper and lower bounds to the vapor pressure equation from the data obtained in these experiments.

The measured pressure can be assumed to correspond to the vapor pressure of the portions of the sample with the highest energy content at each instant of time. The peak energy content history (E_{peak}) is an upper bound on the maximum energy content at each time increment, since it describes the maximum energy deposition to the fuel while neglecting heat transfer from and within the sample. E_{ac} describes the energy content averaged over the entire sample accounting for losses from the sample. Since E_{ac} represents an average, some portion of the sample must have energy content greater than or equal to the value $e_{\text{ac},j}$ for each time $(j-1)\Delta t$. Thus, E_{ac} represents a lower bound on the maximum energy content for each time increment.

Now consider the values of pressure (P), and E_{peak} at time $(j-1)\Delta t$; i.e., p_j and $e_{\text{peak},j}$. They comprise a coordinate pair (p_j, e_{peak}) on the upper energy bound of the vapor pressure equation (B_u). This bound is the set of such pairs for all

time steps; that is:

$$B_u = \{(p_1, e_{\text{peak},1}), (p_2, e_{\text{peak},2}), \dots, (p_j, e_{\text{peak},j}), \dots, (p_N, e_{\text{peak},N})\} \quad (16)$$

Similarly, the values of pressure (P) and E_{ac} at time $(j-1)\Delta t$, i.e., $(p_j, e_{ac,j})$, represent a coordinate pair on the lower energy bound (B_L) of the vapor pressure equation. Thus:

$$B_L = \{(p_1, e_{ac,1}), p_2, e_{ac,2}), \dots, (p_j, e_{ac,j}), (p_j, e_{ac,j}), \dots, (p_N, e_{\text{peak},N})\} \quad (17)$$

Within the experimental uncertainties, which are described in the next chapter (see also Appendix J), the bounds derived from different series of experiments should be identical for those states common to each series. This is demonstrated in the next chapter.

CHAPTER V

EXPERIMENT RESULTS AND DISCUSSION

This chapter summarizes the experiments performed to develop and refine the Effective Equation of State (EEOS) technique and to demonstrate the applicability of these methods for urania. The first section is concerned with the group of buildup experiments. This is followed by a description of the results from the vapor pressure measurement experiments and the development of experimental bounds for vapor pressure of $\text{UO}_{2.08}$. A brief discussion of chemical thermodynamics applicable to these experiments is presented. Finally, a comparison of the experimental results from these experiments is made with other experimental results and analytical formulations.

BUILDUP EXPERIMENTS

At the time these experiments were proposed, no experiment intended to vaporize or even melt reactor fuel had been performed in the ACPR. Several series of experiments (Cr75, Sc74) had been performed on urania below its melting point with energy depositions less than 1250 J/g from room temperature. Since the EEOS experiments were intended to investigate higher regions of energy depositions in UO_2 than previous experiments in ACPR, a slow, conservative step-by-step set of experiments was performed to map the fission energy deposition attainable in urania samples for various combinations of sample enrichment, polyethylene neutron moderator thickness, and reactor pulse sizes.

The first of these experiments was intended to yield fission energy deposition of 1250 J/g. However, because of normalization errors in the initial transport calculations used to predict the energy deposition, the buildup program began at approximately 610 J/g. The results of the buildup experiments are shown graphically in Figure V-1. The measured fission energy deposition determined by fission product inventory is shown as function of the reciprocal of the reactor pulse width at half maximum power (PWHM). The points indicate experimental measurements. The numbers next to each point are ACPR operation numbers. Dotted lines are used to describe experimental trends and the solid lines represent refined transport calculation estimates derived using the TWOTRAN (La70) two-dimensional transport code.

Note that five points (operations 7234, 7235, 7256, 7314, and 7316) fall below the trends predicted by other experimental data. These discrepancies were traced to a systematic error in the fission product inventories used to estimate energy deposition. That error was an incomplete dead time correction in the counting system used to measure the Lanthanum-140 activity. The uranium-235 fission product gamma ray spectrum contains a large fraction of low energy gammas. The multi-channel pulse height analyzer system used for these measurements is designed to correct the system clock for dead time associated with the analog to digital converter (ADC) and the computer memory system. When only a small portion of the gamma spectrum is of interest (as in the case of the fission product inventory), the input discriminators on the

SOLID LINES ARE TWOTRAN RESULTS.
SYMBOLS ARE EXPERIMENTAL DATA.

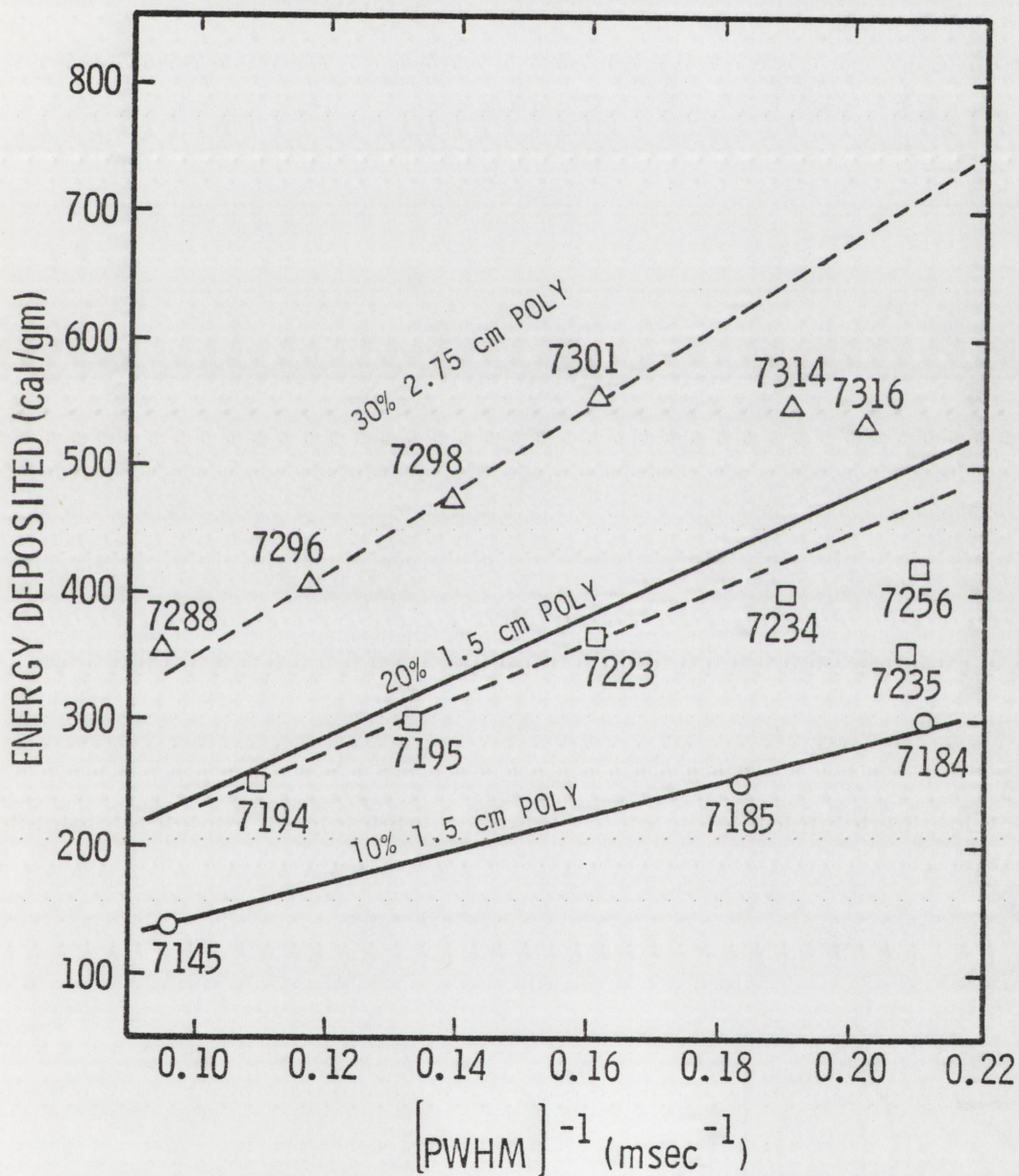


Figure V-1
Results of EEOS Buildup Experiments

ADC can be set to preclude conversion of pulses outside the selected interval. This discrimination process is very fast, but does involve a small dead time that is not included in the system dead time correction. If a large fraction of pulses is rejected (as in the case of a high activity fission product sample counted with a high lower-discriminator setting), a significant dead time error results. This effect yields a measured activity that is too low. After this error was identified, subsequent samples were counted by including much of the total spectrum within the discriminator window. The dashed lines in Figure V-1 were good estimates of the fission energy depositions attainable for the several configurations. Since these measurements were made, the configuration of the ACPR cavity was changed, resulting in a decrease in energy deposition for a given pulse size of approximately 10 percent. This change involved replacing the solid stainless steel lower reflector plug with a hollow aluminum structure; the net effect being increased axial leakage.

From the buildup experiments and subsequent pressure measurement experiments, it became apparent that the strain gage bridges included in each experiment did not yield useful data from which pressure histories could be deduced. While large signal changes were observed at the time of the reactor pulse in experiments containing fuel samples, it was found that similar signals were produced during experiments that did not contain fuel and, hence, produced no internal pressure. Further, it was observed that when the same unstrained strain bridge was irradiated during

successive reactor transients, the recorded signal changed from pulse to pulse. Thus, the radiation noise correction procedure described previously could not be used successfully. Therefore, since the strain gages were unreliable, the buildup experiments yielded no qualitative pressure information and the only information obtained was a map of attainable energy depositions as shown in Figure V-1.

VAPOR-PRESSURE EXPERIMENTS

After the completion of the buildup experiments, six series of experiments were performed to measure the vapor pressure and characterize the energy content of the sample during the reactor transient. The last five of the six series yielded valid vapor pressure information and were designated "EEOS-UO₂-X", for X = 1,2,3,4,5. The first series, which was the first experiment to contain a pressure transducer, did not yield pressure information but did demonstrate the need for a thermal buffer between the fuel sample and the face of the pressure transducer.

In that first transducer experiment (ACPR 7301) a 30 w/o enriched sample was irradiated in a pressure cell containing a Kaman pressure transducer (described previously) in which the face of the sensing diaphragm was directly exposed to the heated sample. The pressure cell was surrounded by a 27.5 mm thick polyethylene moderator. A total fission energy deposition of 2320 J/g was obtained during a 6.2 msec PWHM ACPR transient. A pressure between 3. and 5. MPa should have been measured. Instead, a large negative transient signal was observed.

This effect was attributed to a differential thermal expansion in the pressure sensing diaphragm resulting from a steep temperature gradient produced by rapid transfer of heat from the fuel sample to the exposed face of the transducer. This thermal stress resulted in motion of the diaphragm in the direction opposite to motion resulting from pressure, hence, the large negative result.

Although it was not possible to eliminate this effect, it is possible to delay its occurrence by 10-20 msec. To accomplish this, a graphite disc was placed between the face of the transducer and the fuel sample. Clearly, as the graphite thickness is increased, the delay becomes longer. However, increasing the thickness reduces the transducer sensitivity, changing its calibration. A graphite disc of 1.1 mm was found to be sufficient to produce the desired delay with a decrease of approximately 15 percent in transducer sensitivity. (This change in sensitivity was observed by determining the transducer output for several known pressures without the graphite disc. The graphite disc was then cemented to the transducer diaphragm, and the calibration procedure was repeated. A comparison of the slopes of the two calibration curves showed the decrease in sensitivity.) In order to have sufficient free volume in the original pressure cell design, a thinner graphite disc (0.38 mm) was used in EOS-UO2-1. The pressure cell design used in subsequent experiments was modified to accommodate the thicker buffer disc.

Since the inclusion of a graphite disc changed the transducer sensitivity, it was necessary to recalibrate each transducer.

Since a static gas pressure system was used to perform this calibration, it was necessary to bond the graphite disc to the transducer diaphragm. A high temperature epoxy was used for this purpose. (See Appendix A.)

The five series of vapor pressure experiments are summarized in Table V-1. Each complete series consisted of four irradiations, two pressure cell assemblies each irradiated twice. One assembly contained a pressure transducer that was irradiated without fuel to determine radiation-induced signals and then with a fuel sample to determine temperature histories at locations in the graphite crucible and to determine the pressure history. The second assembly contained a mockup of the pressure transducer with thermocouples located in the graphite disc. The two irradiations of this assembly yielded radiation noise data and temperature histories both in the graphite crucible and in the graphite buffer disc. Series EEOS-UO2-1 and EEOS-UO2-4 included only the pressure measurement experiments. The five series of experiments described in Table V-1 all involved 30 w/o enriched samples irradiated with polyethylene moderators 27.5 mm thick.

Representative pressure histories from the five series of vapor pressure experiments are shown in Figure V-2. As shown in Table V-1, EEOS-UO2-1 and EEOS-UO2-2, which were irradiated during similar transients, yielded different energy depositions. This was a result of the change in reactor configuration previously described. The difference in energy deposition is apparent in frames (A) and (B) of Figure V-2 with the higher

TABLE V-1

Summary of EOS Pressure Measurement Experiments

Series Designation	ACPR Operation Numbers *	Pulse Width at Half Maximum (msec)	Reactor Yield (mJ)	Sample Energy Deposition (J/g)	Fraction of Energy in Pulse	Transducer Buffer Disc Thickness (mm)	Pressure Cell Free Volume (mm ³)
EOS-U02-1	A 7323	5.3	94.	2720.	0.79	0.38	250.
	B 7332						
	C None						
	D None						
EOS-U02-2	A 7766	5.3	94.	2466.	0.79	1.10	300.
	B 7768						
	C 7781						
	D 7788						
EOS-U02-3	A 7836	5.2	97.	2641.	0.80	1.10	300.
	B 7863						
	C 7842						
	D 7866						
EOS-U02-4	A 7948	4.9	106.	2720.	0.83	1.10	300.
	B 7930						
	C None						
	D None						
EOS-U02-5	A 8075	4.9	106.	2720.	0.83	1.10	450.
	B 8080						
	C 8038						
	D 8047						

A - Radiation Noise Experiment for Pressure Transducer Experiment.
 B - Pressure Transducer Experiment.
 C - Radiation Noise Experiment for Instrumented Plug Experiment.
 D - Instrumented Plug Experiment.

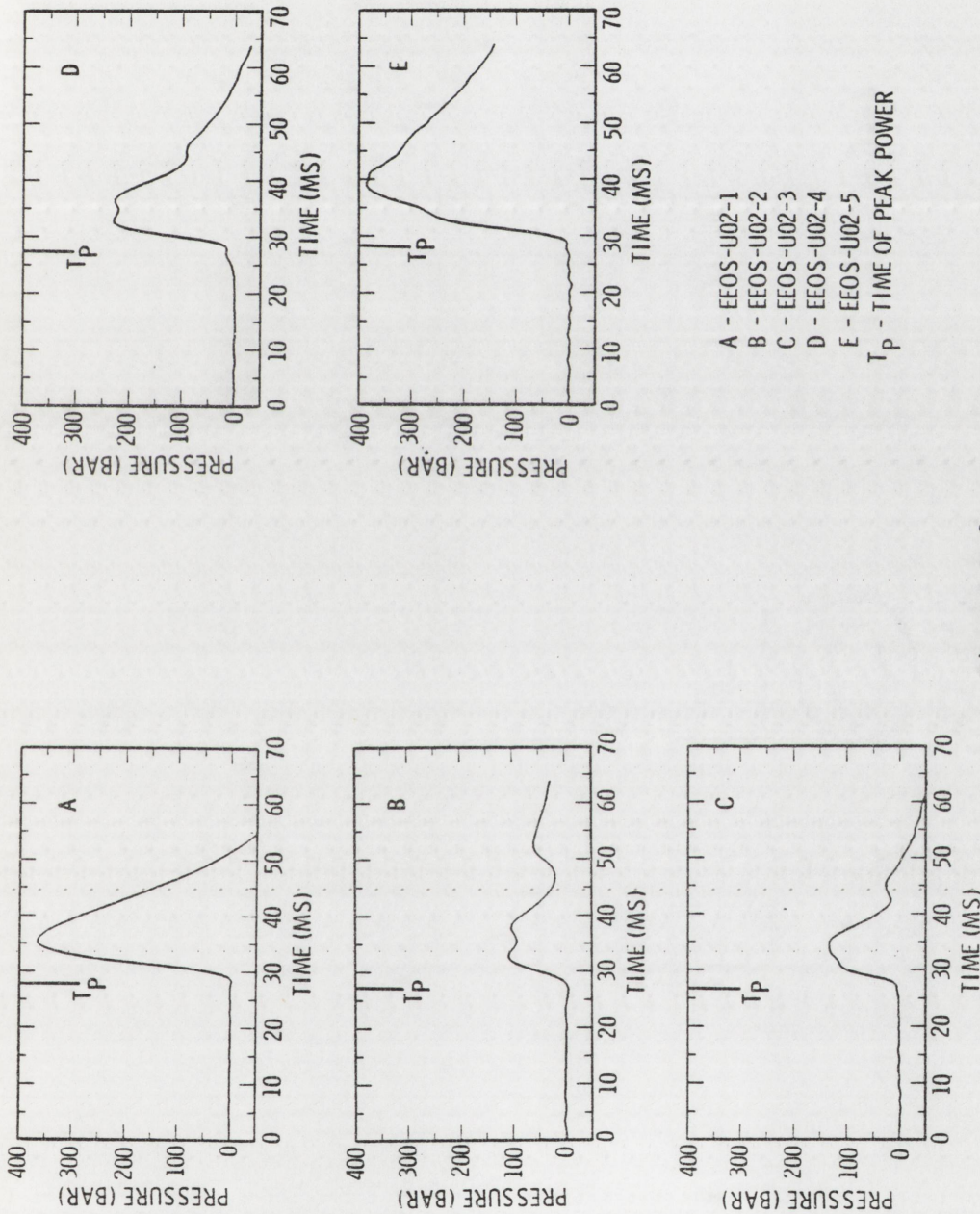


Figure V-2
Summary of Pressure Histories
from EOS Vapor Pressure Measurements

pressure corresponding to the higher energy deposition.

A comparison of the experimental parameters for EEOS-UO2-4 and EEOS-UO2-5 listed in Table V-1 shows that the only difference is the free volume of the pressure cell which should have only a small effect on the measured pressure. It is apparent from frames (D) and (E) of Figure V-2 that the measured pressure histories were quite different in the two experiments. As will be discussed later, it is apparent that the pressure cell in EEOS-UO2-2 accidentally contained a gas atmosphere around the fuel sample instead of a vacuum as in the other experiments. The presence of a non-condensable gas in the pressure cell would cause a higher pressure as it is heated than would be measured in an evacuated pressure cell. Further, the presence of gas would retard heat transfer from the vapor and, hence, sustain the pressure longer and perhaps increase its peak magnitude while energy is being added to the system. Both of these effects are apparent by comparing frames (D) and (E) in Figure V-2.

From the pressure histories, it is clear that while the graphite buffer disc does retard the transient thermal effects in the pressure transducer, it does not eliminate them, as the pressure histories all ultimately go negative. The negative transient was strongest in EEOS-UO2-1 (frame (A)). Since that experiment contained a thinner buffer disc than the other four, the thermally induced transient should be more pronounced at an earlier time as was observed.

The pressure histories obtained in EEOS-UO2-2,3,4,5 exhibited varying degrees of fine structure, i.e., small relative pressure maxima. This fine structure can be lumped into two groups:

the first occurring at or near the peak of the pressure event, the second occurring 15-25 msec after the time of peak reactor power (T_p). Since the presence of the graphite buffer disc did reduce the transducer sensitivity, any phenomenon that would affect the stiffness of that disc or the characteristics of the bond between the disc and the transducer would alter the calibration (output voltage vs. pressure relationship) of the transducer. Heat would reduce the strength of the graphite, and high pressures could fracture the disc reducing its stiffness. The net result would be a net increase in transducer sensitivity. Hence, for a given source pressure, the transducer output would yield a higher indicated pressure as the characteristics of the disc changed. This effect is the probable cause of the structure at the peak of the pressure event.

The pressure peaks that occur 15-25 msec after the main peak are attributed to the thermal decomposition and resulting vapor pressure of the adhesive used to bond the disc to the transducer. At the time of these later pressure events, the temperature at the bond increased to 1300 K, which is well above maximum operating temperature characteristics quoted by the epoxy manufacturer (560 K).

The pressure history from EEOS-U02-1 does not exhibit the finer structure described above. There are several explanations for this. First, the thinner buffer disc had a much smaller effect on the transducer sensitivity than in the other experiments and, hence, changes in the characteristic of the disc would have little

effect on the transducer output. Secondly, a different adhesive was used in this first experiment. Finally, the large thermally induced negative transient occurred early enough to mask the effects described above.

The pressure and several energy histories from the five series of experiments which were used to deduce the bounds on the vapor pressure relationship are displayed in Figures V-3 through V-7. Since the pressure data were recorded at two different gains, and reactor power histories (and, hence, energy histories) were available from each reactor pulse comprising each series, several combinations of pressure and energy histories can be obtained for each series. As a result of errors and uncertainties in radiation noise corrections, filtering, and other processing steps, not all possible combinations were deemed valid and included. Four energy histories are shown for EEOS-UO2-2,3,4, and 5 series. For EEOS-UO2-1, insufficient data was obtained to derive the loss history (E_{loss}) and the corrected average energy content history (E_{ac}). The average energy content history (E_{avg}) was derived directly from the integrated reactor power history and fission product inventory according to the methods discussed in the previous chapter. The peak energy content history (E_{peak}) was derived from E_{avg} . A heat flux history was derived from the valid temperature data measured by inside thermocouples (those located nominally 0.38 mm from the inside surface of the crucible and buffer disc). The energy loss history (E_{loss}) for each series was computed by integrating the heat flux histories for that

experiment in time and over the inside surface area of the pressure cell free volume. The corrected average energy content history (E_{ac}) was obtained as the net difference between E_{avg} and E_{loss} . In Figures V-3 through V-7, the information below the pressure traces defines the origin of the pressure and reactor power data.

No instrumented plug experiment was performed for series EEOS-UO2-4. However, because of the similar energy deposition in the two series, it was assumed that the heat transfer to the face of the transducer was the same in EEOS-UO2-4 and EEOS-UO2-5. Hence, the heat fluxes to the transducer face in EEOS-UO2-5 were used to compute E_{loss} in EEOS-UO2-4. Although the pressure transducer experiment in EEOS-UO2-5 apparently contained a noncondensable atmosphere, there is no evidence of a similar defect in the instrumented plug experiment for that series. Hence, the above assumption is reasonable. Note that the energy loss histories for EEOS-UO2-2,3 and 4 are very similar in shape and magnitude.

Point by point comparisons of the pressure histories and the peak energy histories described above are shown in Figure V-8. Note the well defined trend of the data. The deviations of the EEOS-UO2-3 and 4 data at lower energies are artifacts of inaccurate radiation noise corrections. The EEOS-UO2-5 results were excluded because of the apparent accidental presence of an initial gas pressure. Earlier in this chapter several uncertainties were noted in the pressure histories, which became significantly large

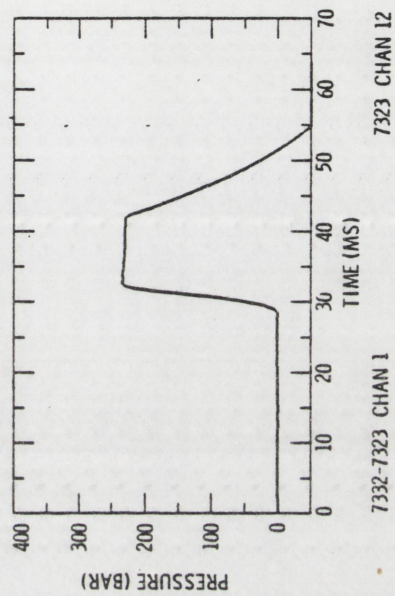
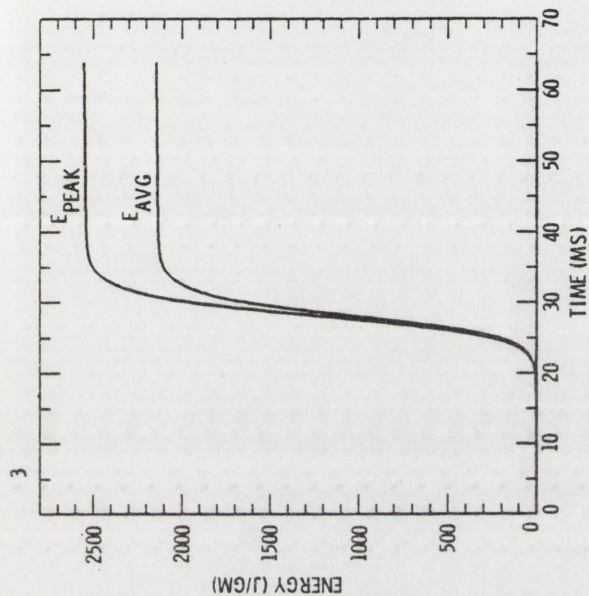
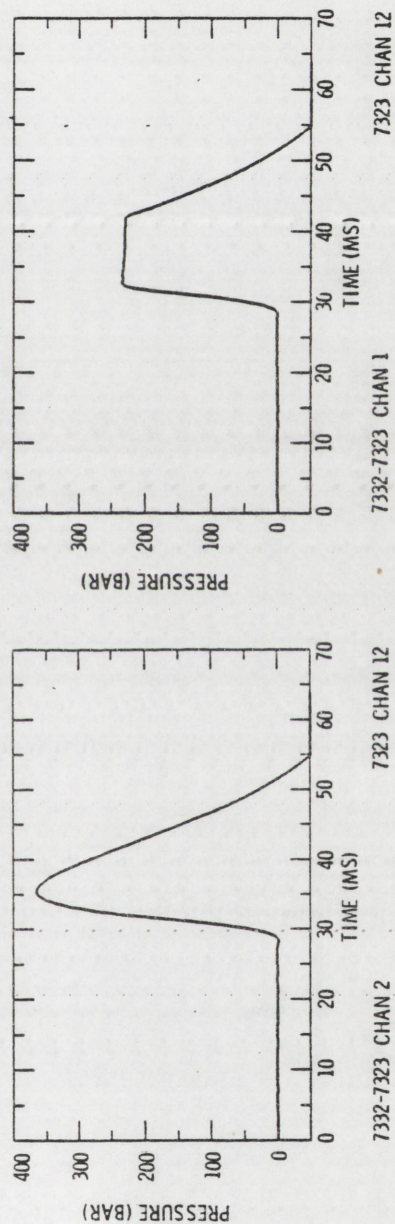
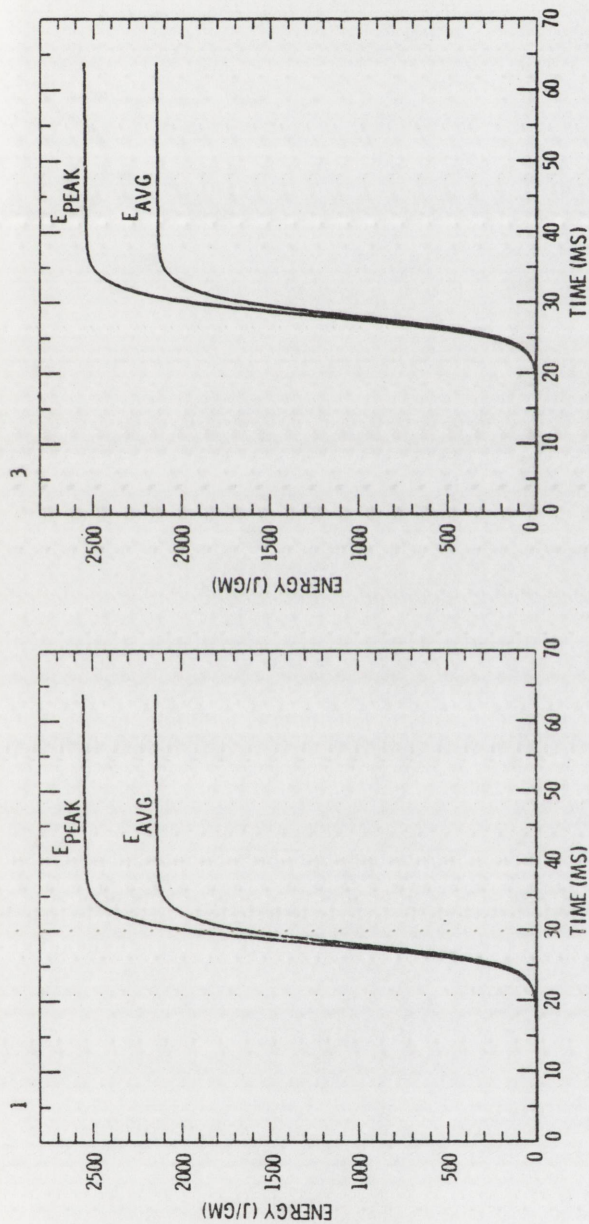
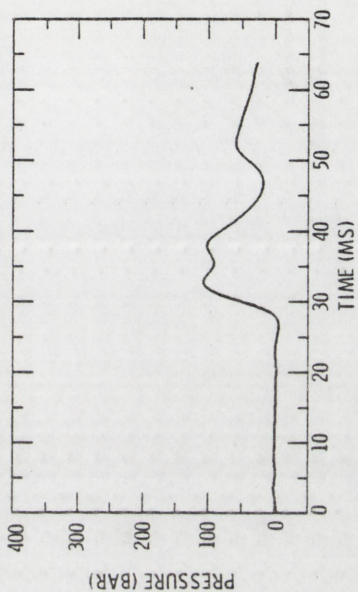
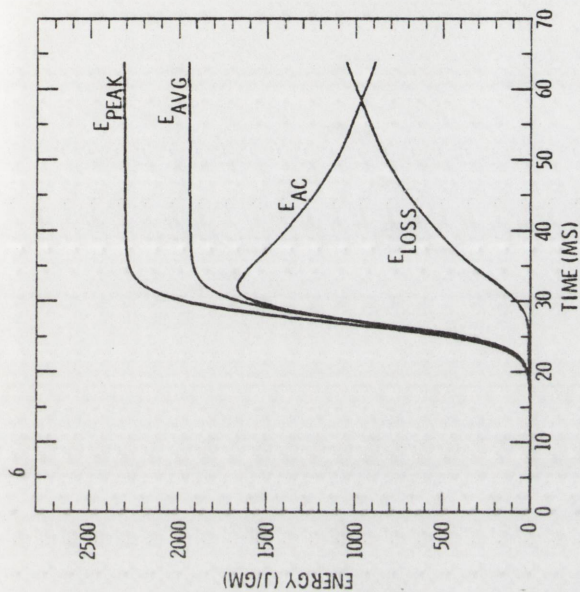
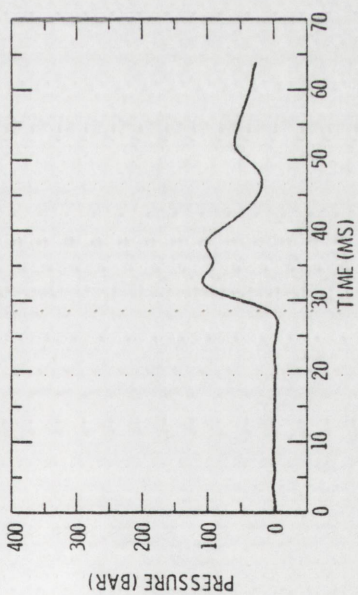
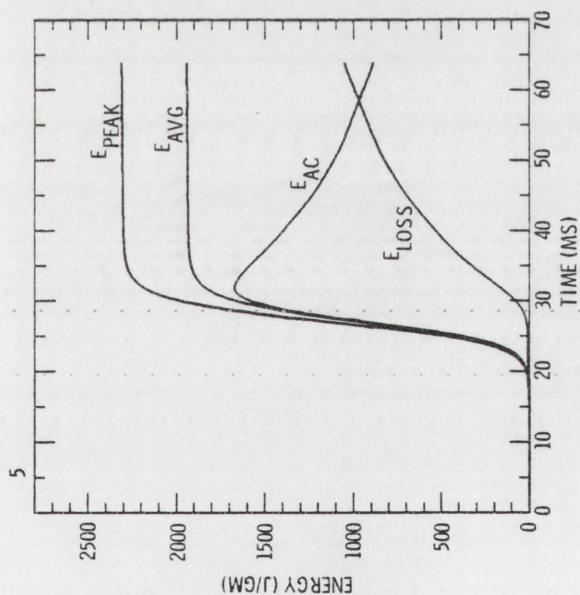


Figure V-3
Pressure and Energy Histories from EEOS-U02-1



7768 CHAN 12

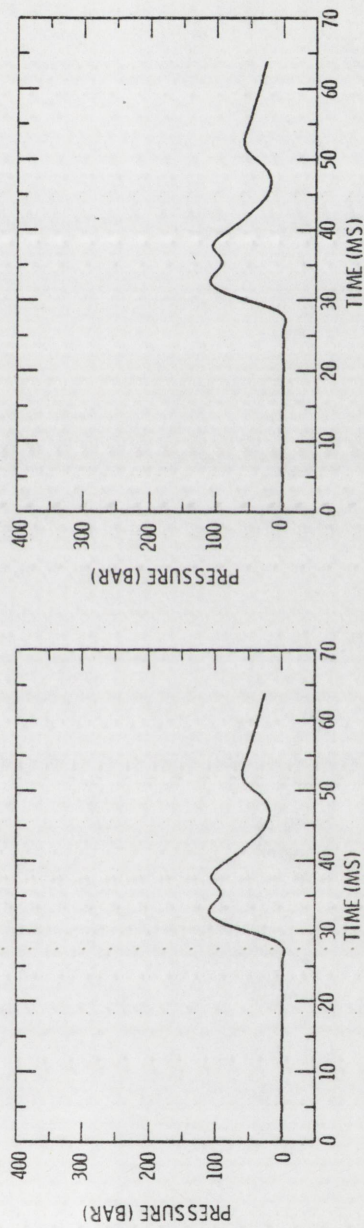
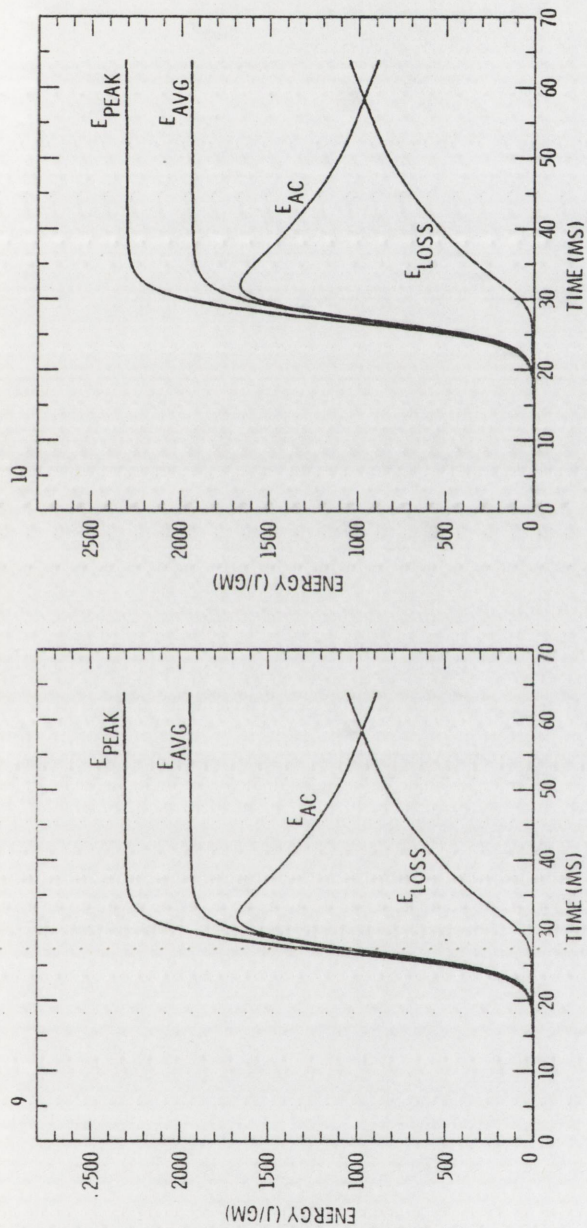


7766 CHAN 12

7768-7766 CHAN 3

Figure V-4

Pressure and Energy Histories from EEOS-UO2-2



7768-7766 CHAN 4

7766 CHAN 12

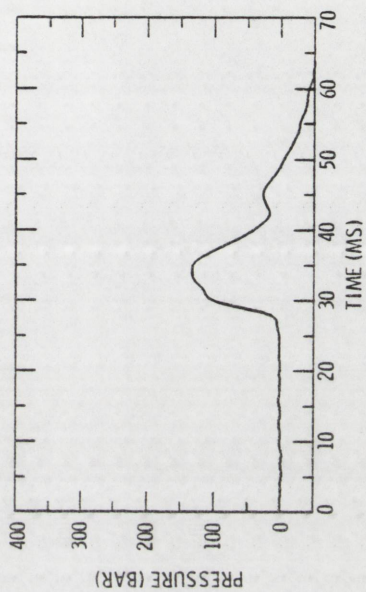
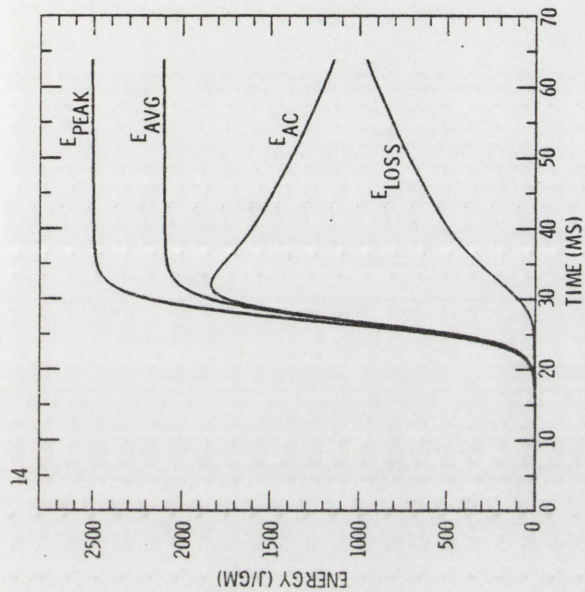
7768-7766 CHAN 4

7766 CHAN 12

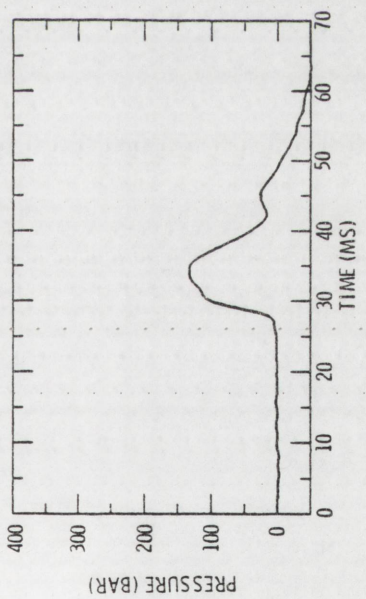
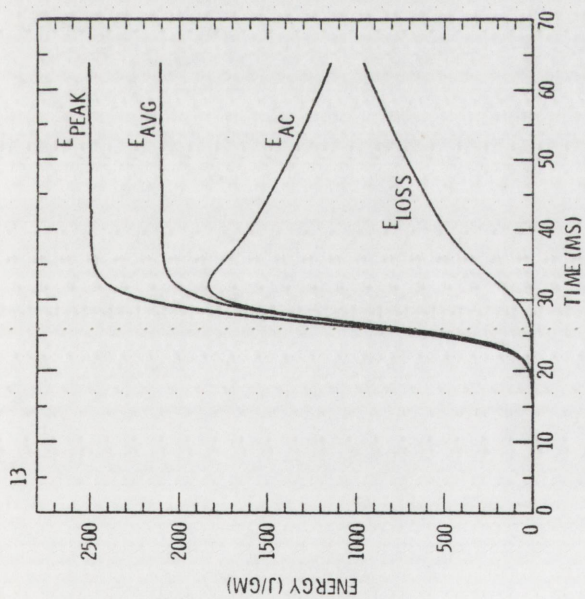
Figure V-4A

Pressure and Energy Histories from EEOS-UO2-2

(continuation)



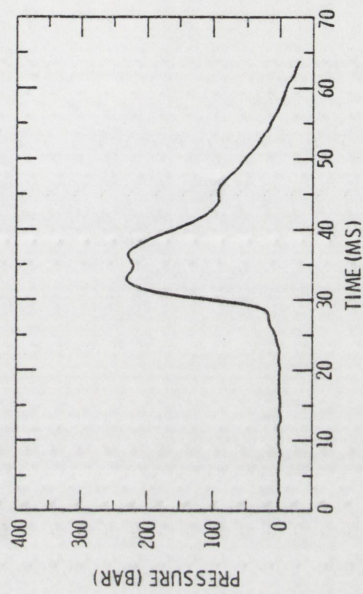
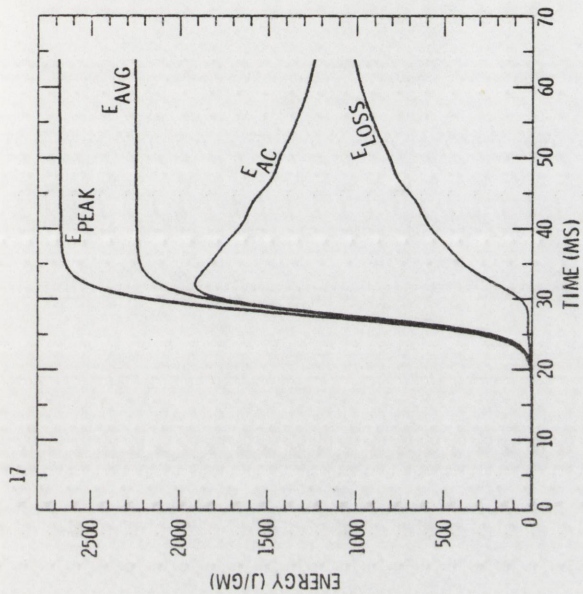
7863 CHAN 12



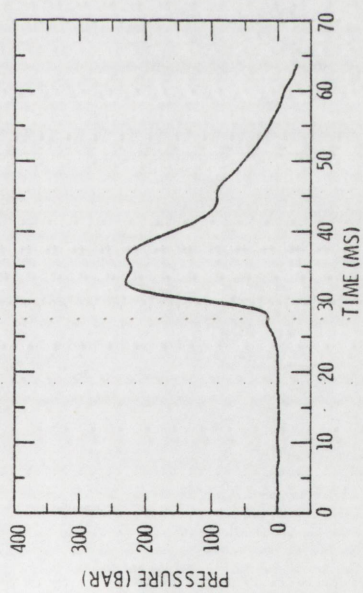
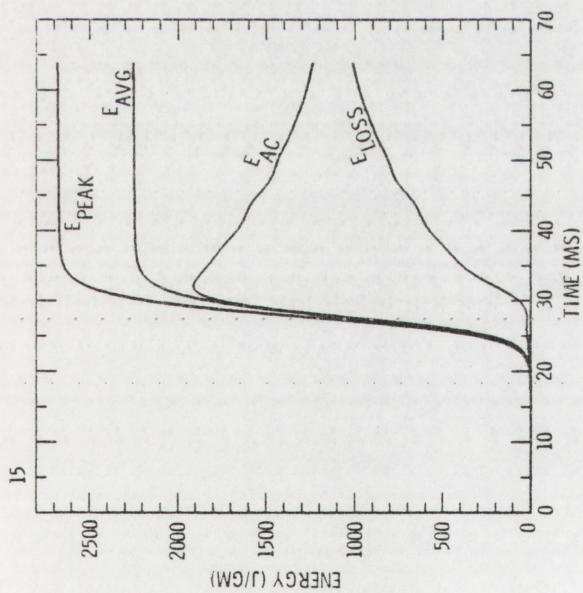
7836 CHAN 12

Figure V-5

Pressure and Energy Histories from EOS-UO2-3



7948 CHAN 12



7948-7930 CHAN 3

7930 CHAN 12

7948-7930 CHAN 3

Figure V-6

Pressure and Energy Histories from EEOS-UO2-4

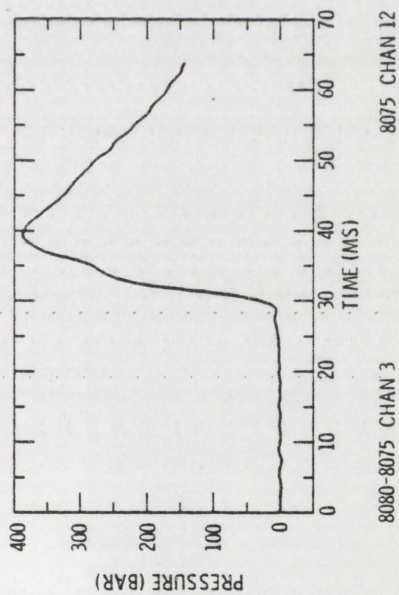
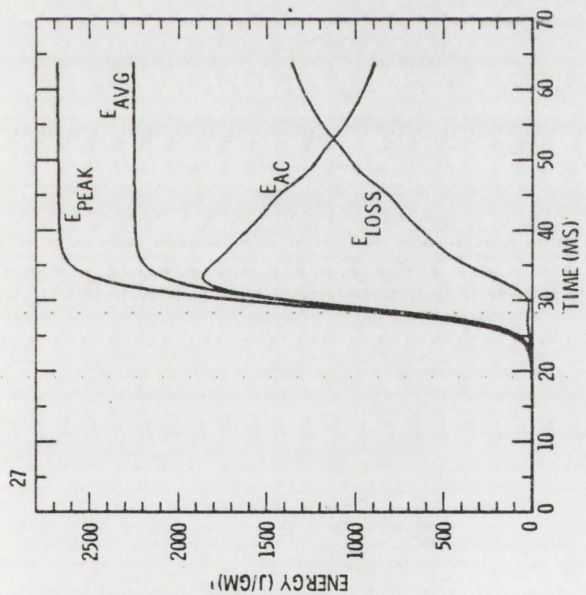
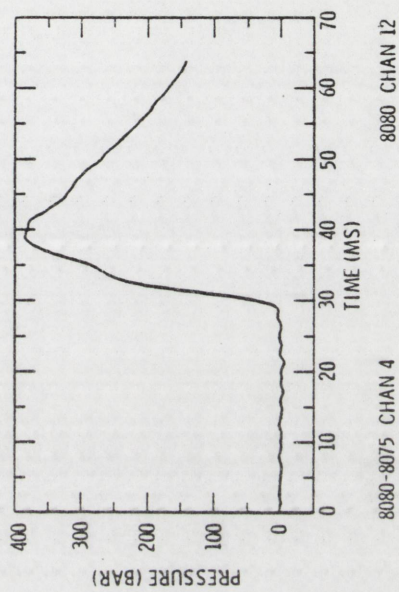
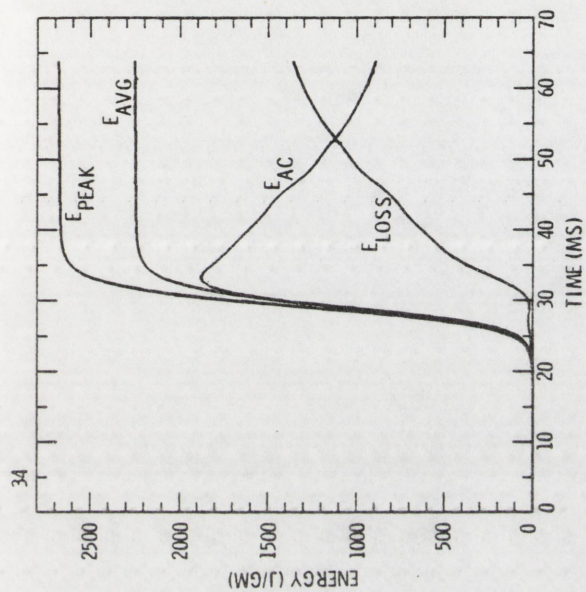


Figure V-7
Pressure and Energy Histories from EOS-UO2-5

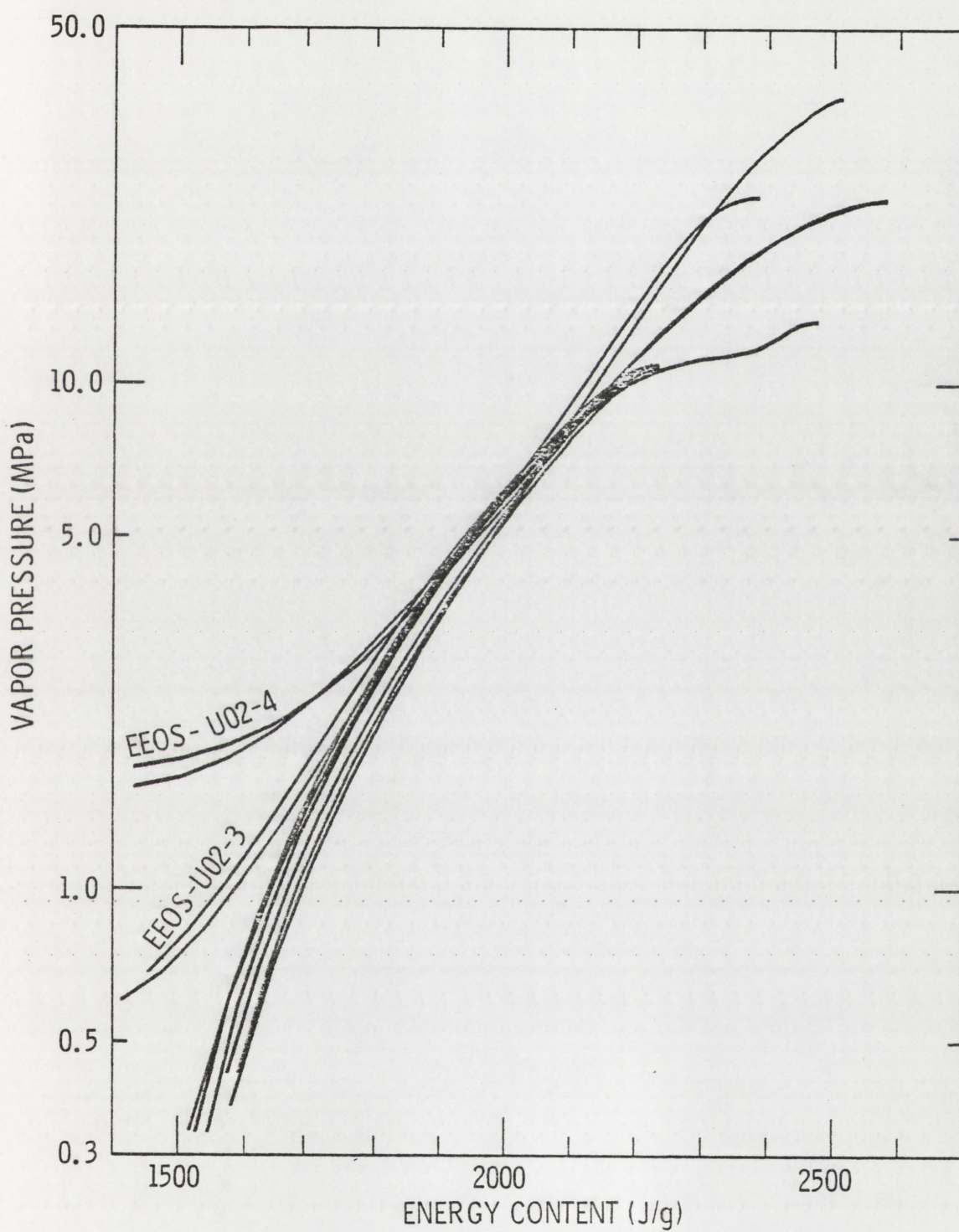


Figure V-8

Pressure Vs. Energy Relationships Using Pressure
and Peak Energy Data from EOS-UO2-1,2,3,4

after the pressure peak. As a result of these, only the data from the leading edge of the pressure pulse in each series was used to derive the pressure vs. energy relationships. Figure V-9 displays similar pressure vs. energy relationships derived from comparisons of the pressure histories and corrected average energy content histories from EEOS-UO2-2,3,4.

From the composites of the pressure-energy results of the several experimental series shown in Figures V-8 and V-9, bounds on the vapor pressure were derived for the urania material used in these experiments. These bounds are shown in Figure V-10. The solid portion of the trace of the upper energy bound is an envelope for the curves in Figure V-8. Because of the limited range of energy depositions attainable in the ACPR, insufficient data was obtained to define this bound above approximately 2000 J/g. Two possible extensions of this bound are indicated in the figure.

The lower energy bound on the vapor pressure was obtained as a best estimate of the curves in Figure V-9. Because of the inherent uncertainties in the inverse heat conduction technique as employed in these experiments which yield uncertainties in E_{loss} and, hence, E_{ac} , a best estimate was employed, rather than an envelope to the composite data.

The free volume surrounding the sample in the pressure cell was to be evacuated during the experiments. As described in Chapter III, the cell was alternately evacuated and backfilled with helium to dilute and purge oxygen from the cell. After the last evacuation, the cell was sealed. In the EEOS-UO2-5 pressure

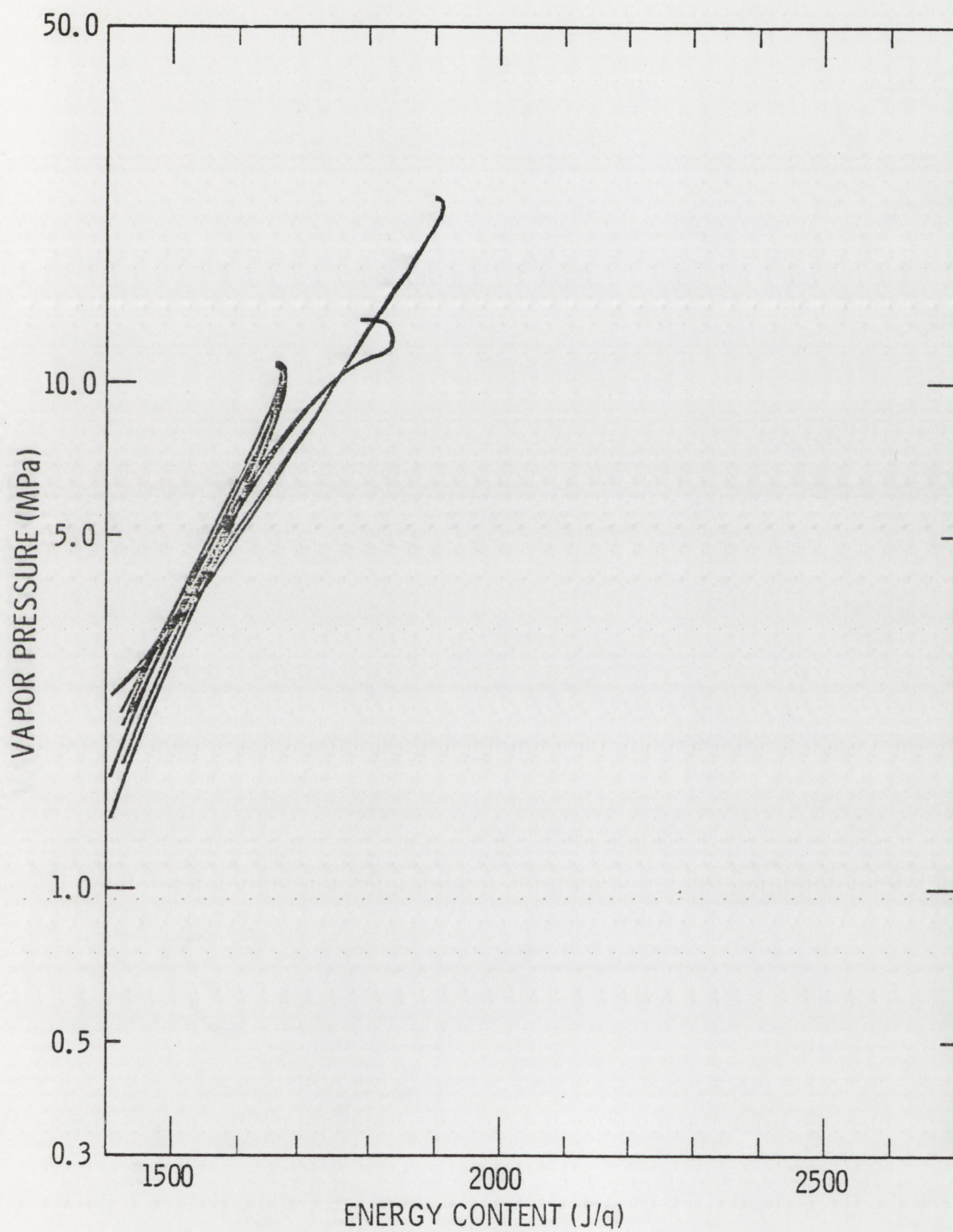


Figure V-9

Pressure Vs. Energy Relationships Using Pressure
and Corrected Average Energy Data from EOS-UO2-2,3,4

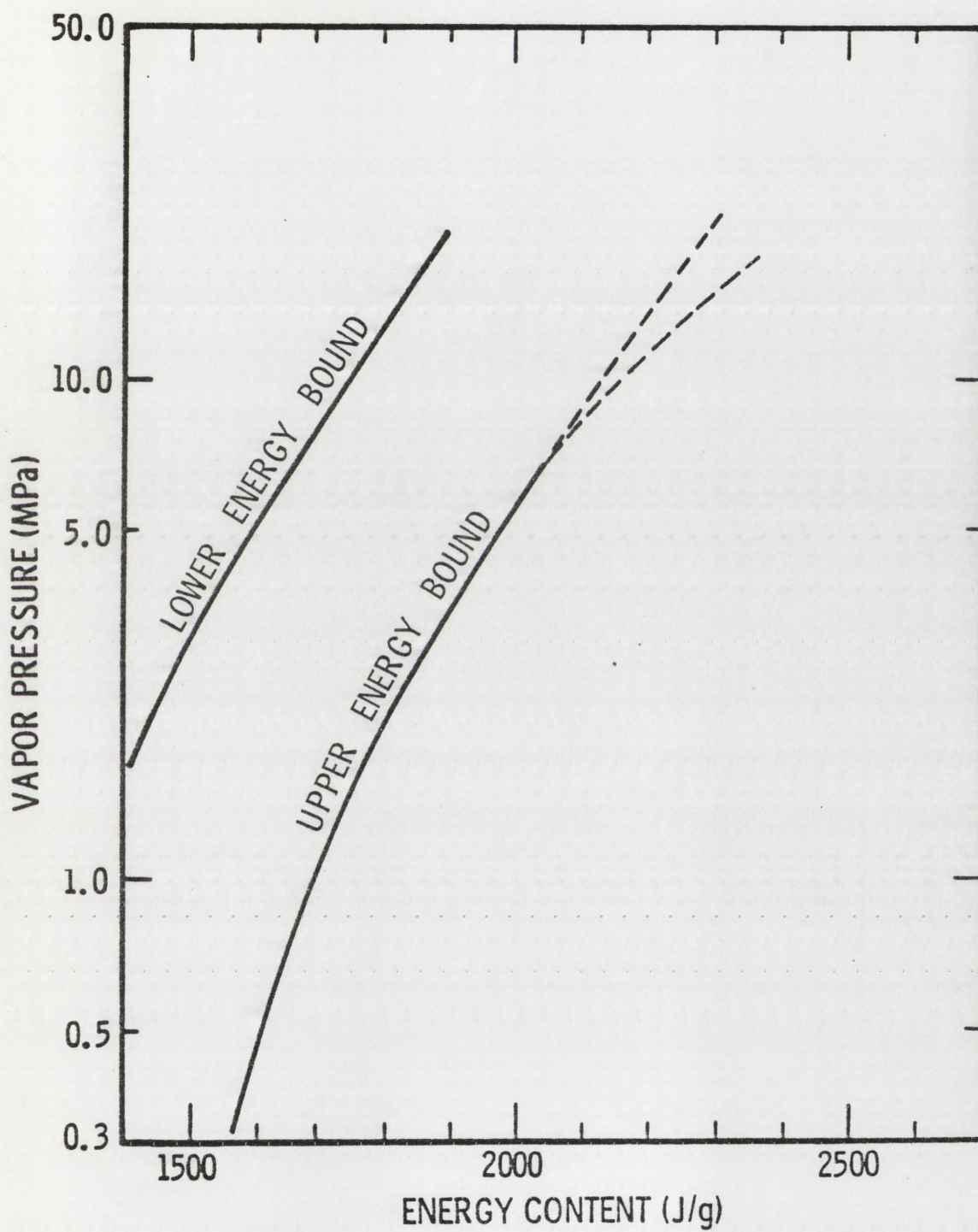


Figure V-10
Upper and Lower Bounds on Vapor Pressure of $\text{UO}_{2.08}$

transducer experiment, the cell was apparently incorrectly sealed with a helium atmosphere inside.

It is possible to demonstrate the presence of the helium atmosphere in that experiment and to estimate its initial pressure from a comparison of the upper bound results from that series and the corresponding pressure vs. peak energy result from EEOS-UO2-4. This comparison is shown in Figure V-11. If it is assumed that the pressure transducer experiment in series 4 was evacuated and that the experiments were otherwise similar between the two series, then the pressure difference between the two curves in Figure V-11 can be attributed to heating the noncondensable gas. These differences are shown in Figure V-11 and tabulated in Table V-2. From the derivation of the peak energy content the average energy content was derived. The use of the heat capacity model described later in this chapter yields estimates of the average system temperature corresponding to those energies. Finally, the initial gas pressure was estimated by assuming ideal gas behavior. These estimates are approximately 0.25 MPa for most of the points. The pressure cells were backfilled with helium at 0.1 to 0.2 MPa gage pressure. If the cell had been sealed in the helium environment, an initial gas pressure of 0.18 to 0.28 MPa absolute could result, consistent with the estimates derived above.

ESTIMATES OF ERRORS

As in any experimental measurement, there were quantifiable uncertainties in each of the experimental measurements and the results derived from that data. Estimates of these errors are

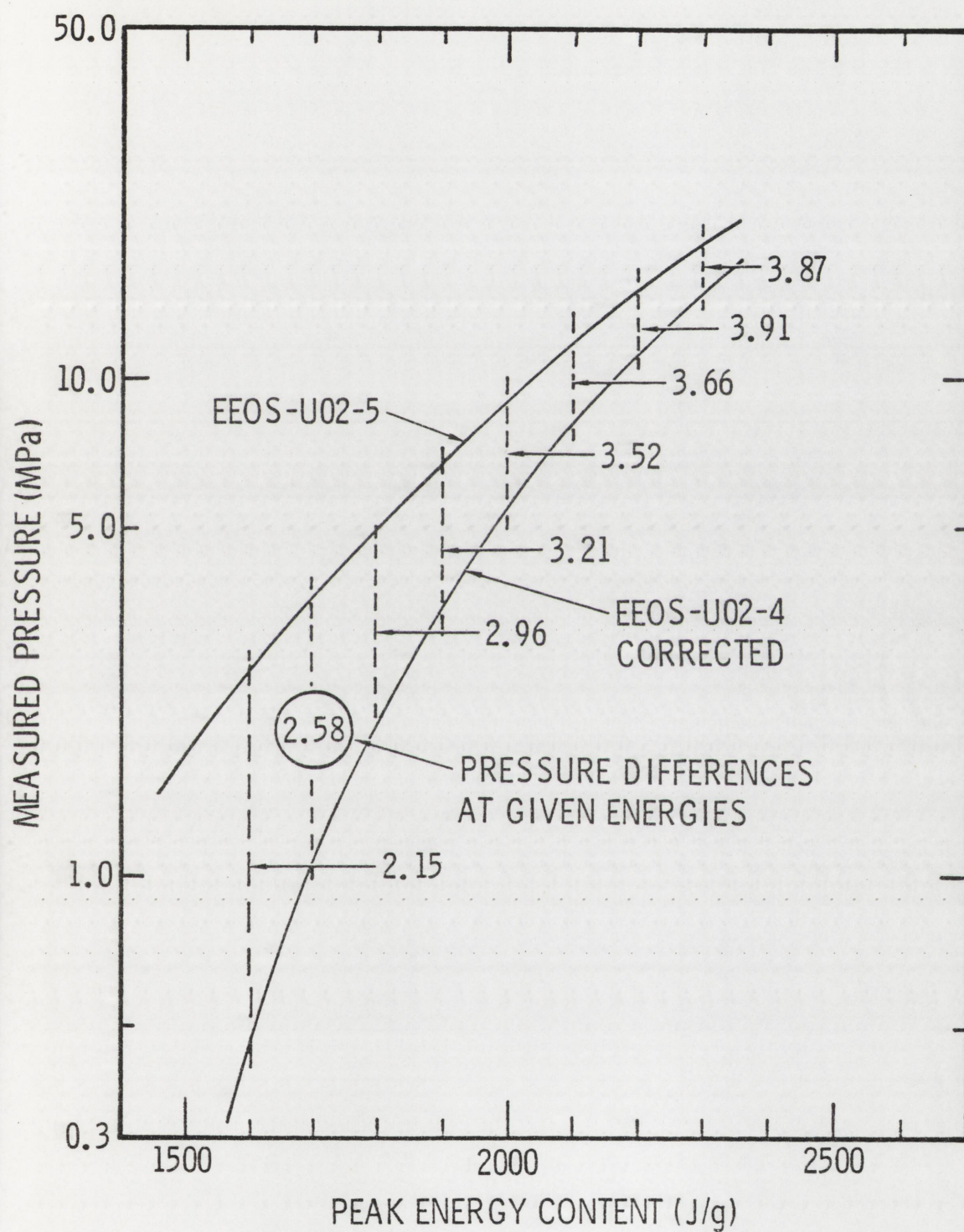


Figure V-11
Comparison of Pressure Vs. Peak Energy Relationships

TABLE V-2

Computation of Initial Pressure Condition in EOS-UO2-5 Pressure Experiment
from Pressure vs. Peak Energy Relationships

Peak Energy Content (J/g)	Average Energy Content (a) (J/g)	Average Temperature (b) (K)	Pressure Difference at Peak Energy (c) (MPa)	Computed Initial Pressure at 293K (d) (MPa)
1600.	1345.	3410.	2.15	.185
1700.	1429.	3558.	2.58	.212
1800.	1513.	3726.	2.96	.233
1900.	1597.	3894.	3.21	.242
2000.	1681.	4062.	3.52	.254
2100.	1765.	4230.	3.66	.254
2200.	1849.	4398.	3.81	.254
2300.	1933.	4566.	3.91	.251
2400.	2017.	4734.	3.87	.240

(a) (Average Energy Content) = (Peak Energy Content) ÷ 1.19.

(b) Computed using Average Energy Content and the Specific Heat Model described above based on experimental data.

(c) See Figure

(d) Computed from Ideal gas law assuming constant volume and a vacuum in EOS-UO2-4.

$$\text{(Computed Initial Pressure at 293K)} = \frac{293 \cdot x \text{ (Pressure Difference at Peak Energy)}}{\text{(Average Temperature)}}$$

summarized in Table V-3. The detailed assessment of these errors is given in Appendix I. The net uncertainties in several parameters were time dependent. In particular, the uncertainty in the measured pressure increased with time after the peak of the reactor power, as described previously, and the net percent uncertainty in the energy loss terms was largest at the time of the reactor pulse and decreased thereafter. The final energy bounds were determined from data obtained during the rise of the pressure signal (a total interval of 2-5 msec). The uncertainties in the several parameters during this interval are the values displayed in Table V-3.

The uncertainty in pressure is that attributed to the transducer calibration. The error in the fission product inventory value is dominated by the uncertainty in the integration of the photo peak and in the source-detector counting efficiency term. These uncertainties were estimated through the use of a standard Cobalt-60 source counted using the same techniques used for the ^{140}La counting. (See Appendix E.)

The largest uncertainties are associated with the energy loss determination. As described with respect to the sensitivity study of the inverse heat conduction technique in the previous chapter, small uncertainties in the exact thermocouple location yield sizable uncertainties in the calculated heat flux. Also, fractional variations in the measured temperature histories are reflected as variations of similar magnitude in the calculated heat flux. These two sources of error are not totally independent

TABLE V-3

Estimated Errors in Measured and Derived Parameters

Parameter	Estimated Error During Time Interval of Interest
Relative Sampling Time	$\pm 40 \mu\text{sec}$
Pressure	$\pm 10 \%$
Average Energy Input	$\pm 4.3\%$
Power Integral Shape	$\pm 1 \%$
Fission Product Inventory	$\pm 4 \%$
Fraction of Energy in Pulse	$\pm 1 \%$
Peak Energy Content	$\pm 6.6\%$
Average Energy Input	$\pm 4.3\%$
Peak to Average Ratio	$\pm 5.0\%$
Energy Loss	$\pm 50 \%$
Effect of T.C. Location	$\pm 30 \%$
Uncertainty in Measured Temperature	$\pm 40 \%$
Corrected Average Energy Content	$\pm 10 \%$
Average Energy Input	$\pm 4.3\%$
Energy Loss	$\pm 50 \%$

of each other. While errors may exist in the temperature measurements due to heat transfer between the graphite and the thermocouples, they are minimized for correctly installed thermocouples by changes in the graphite geometry during the application of the internal pressure. Thus, the gaps between the thermocouple and the graphite tend to close during the experiment. The other source of error in the temperature measurement is the location with respect to its nominal location. Thus, the stated net error may be too large as it was derived by treating the two error sources as independent.

The energy loss term affects the corrected average energy content term in an additive way. Thus, the magnitude of the error, not the percentage error, is significant. During the 2-5 msec interval of interest, the magnitude of the loss term (<100 J/g) is small compared to the average energy input terms (approximately 2000 J/g). Thus, its large percentage uncertainty has a much smaller net effect on the uncertainty in the resultant corrected average energy content as shown in the table.

The net errors in pressure, peak energy content, and corrected average energy content are displayed in Figure V-12 as error bars at several points on the upper and lower energy bounds. A comparison of this figure with Figures V-8 and V-9 shows that the scatter in the results from the several series of experiments is well within these error bars.

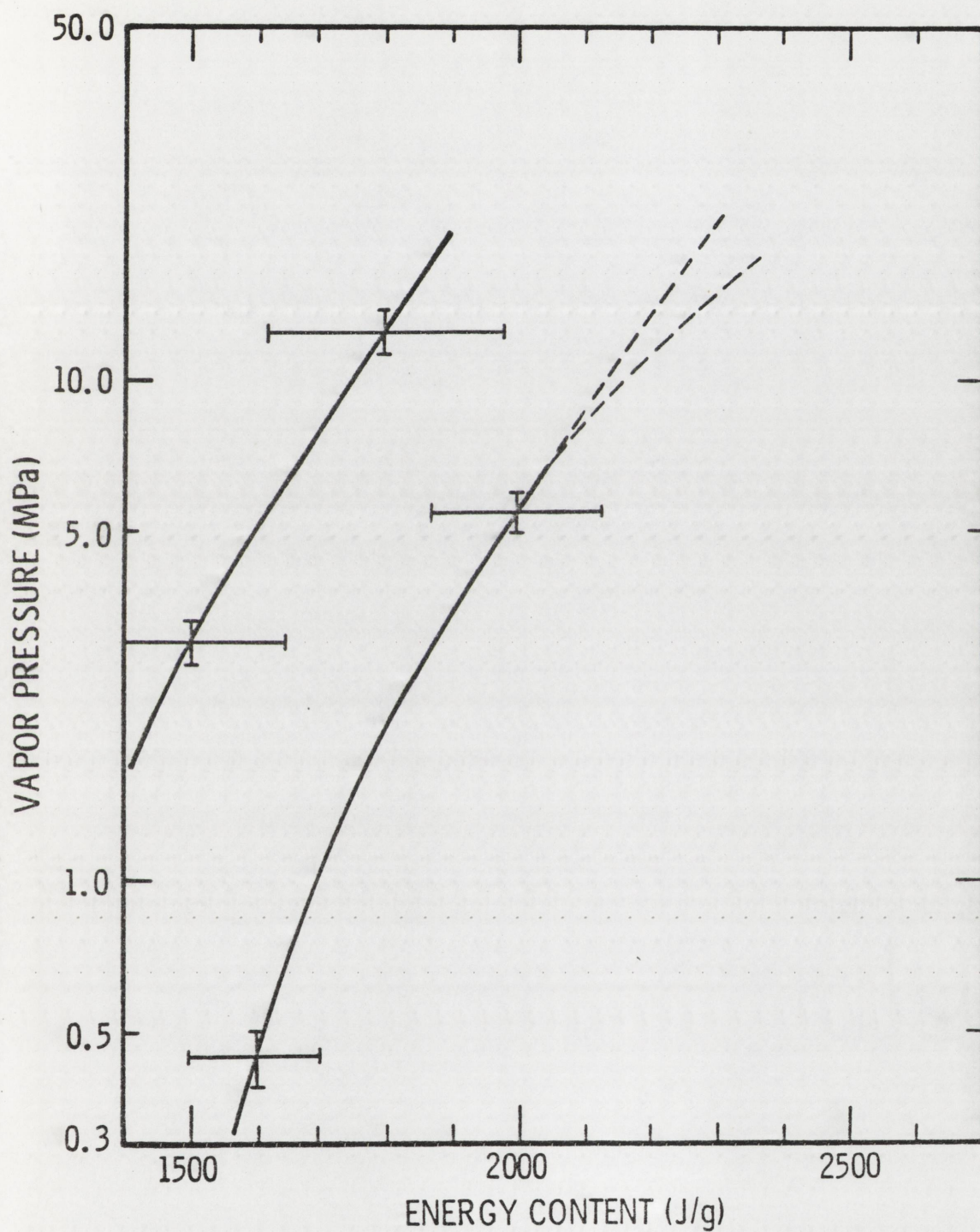
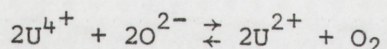


Figure V-12
Net Experimental Uncertainties in Energy Bounds
on the Vapor Pressure of $\text{UO}_{2.08}$

VAPOR PRESSURE ESTIMATES BASED ON CHEMICAL EQUILIBRIUM

Techniques have been developed by Blackburn (Bl73) and extended by Gabelnich and Chasanov (Ga72) and Breitung (Br75) to interpolate and extrapolate measured vapor pressure data. These techniques are based on the law of mass action and thermodynamic data. Blackburn (Bl73) applied this model to predict oxygen pressures over urania. Breitung (Br75) and Gabelnich and Chasanov (Ga72) extended these techniques to predict total pressure over reactor fuels to include mixed oxides and fission products.

To develop the Blackburn Model, separate expressions are formulated for hyperstoichiometric and hypostoichiometric UO_2 . These two sets of equations are then combined to describe an entire range of oxygen to metal (O/M) ratios. For substoichiometric UO_2 it was assumed that the following equilibrium relationship exists:



where the superscripts indicate the valence states of the ions.

For this equilibrium the following expression can be written

$$\ln P_{\text{O}_2} = 2 \ln \frac{n_{\text{U}^{4+}}}{n_{\text{U}^{2+}}} + 2 \ln n_{\text{O}^{2-}} + \ln K_1 \quad (1)$$

where $n_{\text{U}^{4+}}$, $n_{\text{U}^{2+}}$, $n_{\text{O}^{2-}}$ are the numbers of moles per mole of U of U^{4+} , U^{2+} , O^{2-} and K_1 includes the activity coefficients and equilibrium constant. The exclusion of the U^{3+} state was based

on the experimental work of Tetenbaum and Hunt (Te68). The equilibrium constant K_1 was evaluated by comparing equation (1) with a Gibbs-Duhem equation

$$d \ln a_U = - \frac{n_{O^{2-}}}{n_U} d \ln P_{O_2} \quad (2)$$

and by assuming the uranium activity a_U to be 1 at the metal rich phase boundary. If x denotes the oxygen deficiency of the UO_{2-x} then

$$\ln P_{O_2} \Big|_{x=0} + \ln a_U \Big|_{x=0} = \frac{\Delta G_f^0(UO_2)}{RT} \quad (3)$$

where $\Delta G_f^0(UO_2)$ is the Gibbs free energy of formation of UO_2 .

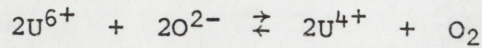
When these are combined with expressions for the metal rich phase boundary composition, it can be shown that

$$\ln K_1 = - \frac{156600}{T} + 27.2 \quad (4)$$

Equations (2) and (4) can be combined to yield

$$\frac{n_{U^{4+}}}{n_{U^{2+}}} = \frac{P_{O_2}^{1/2}}{n_{O^{2-}}} \exp(78300/T - 13.6) \quad (5)$$

For oxygen rich UO_{2+y} the following equilibrium is assumed to exist:



which yields the expression

$$\ln P_{\text{O}_2} = 2 \ln \frac{n_{\text{U}^{6+}}}{n_{\text{U}^{4+}}} + 2 \ln n_{\text{O}^{2-}} + \ln K_2 \quad (6)$$

To evaluate the constant K_2 , the following relationships were noted:

$$d \ln a_{\text{UO}_2} = - \frac{n_{\text{O}_2}}{n_{\text{UO}_2}} d \ln P_{\text{O}_2} \quad (7)$$

At $y = 0$ the UO_2 activity $a_{\text{UO}_2} = 1$. At the oxygen-rich boundary UO_{2+y_s}

$$\ln P_{\text{O}_2} \Big|_{y_s} + 8 \ln a_{\text{UO}_2} \Big|_{y_s} = \frac{2\Delta G_f^0(\text{U}_4\text{O}_9) - 8\Delta G_f^0(\text{UO}_2)}{RT} \quad (8)$$

When these are combined with expressions for the oxygen-rich phase boundary and the free energy difference, it can be shown that

$$\ln K_2 = - \frac{32900}{T} + 10.2 \quad (9)$$

Equations (6) and (9) can be combined to yield

$$\frac{n_{U^{6+}}}{n_{U^{4+}}} = \frac{P_{O_2}^{\frac{1}{2}}}{n_{O^{2-}}} \exp (16500/T - 5.1) \quad (10)$$

In addition to equations (5) and (10), two more relations are needed to compute the molar concentrations of the various ions. First, the sum of the uranium ion molar concentrations must be one:

$$n_{U^{2+}} + n_{U^{4+}} + n_{U^{6+}} = 1 \quad (11)$$

and for electrical neutrality

$$n_{O^{2-}} = 3n_{U^{6+}} + 2n_{U^{4+}} + n_{U^{2+}} \quad (12)$$

Thus, a set of four equations in six unknowns was derived. By choosing two variables (temperature, T , and oxygen ion concentration, $n_{O^{2-}}$), the other variables can be computed.

Finally, the partial pressures of the various uranium species can be computed by assuming the mixture of species acts as an ideal mixture of pure materials.

Thus,

$$\begin{aligned}
 P_{\text{UO}} &= a_{\text{U}} \left(P_{\text{O}_2} \right)^{\frac{1}{2}} \exp \left(-\Delta G_{\text{f}}^{\circ} \left(\text{UO}, \text{g} \right) / RT \right) \\
 P_{\text{UO}_2} &= a_{\text{U}} P_{\text{O}_2} \exp \left(-\Delta G_{\text{f}}^{\circ} \left(\text{UO}_2, \text{g} \right) / RT \right) \\
 P_{\text{UO}_3} &= a_{\text{UO}_2} \left(P_{\text{O}_2} \right)^{\frac{1}{2}} \exp \left[\left(\Delta G_{\text{f}}^{\circ} \left(\text{UO}_2, \text{s} \right) - \Delta G_{\text{f}}^{\circ} \left(\text{UO}_3, \text{g} \right) \right) / RT \right]
 \end{aligned} \tag{13}$$

Using expressions found in the literature for the activities and free energies, Blackburn (B173) found:

$$\begin{aligned}
 P_{\text{UO}} &= n_{\text{U}^{2+}} \exp \left(\frac{-47300}{T} + 10.8 \right) \\
 P_{\text{UO}_2} &= n_{\text{U}^{4+}} \exp \left(\frac{-69300}{T} + 18.7 \right) \\
 P_{\text{UO}_3} &= n_{\text{U}^{6+}} \exp \left(\frac{-45200}{T} + 16.2 \right)
 \end{aligned} \tag{14}$$

Finally, the total pressure was computed as the sum of the partial pressures. That is:

$$P_{\text{TOT}} = P_{\text{O}_2} + P_{\text{UO}} + P_{\text{UO}_2} + P_{\text{UO}_3} \tag{15}$$

The partial pressure of free uranium P_{U} is so small as to be ignored.

Physical chemical formulations of expressions for vapor pressure must be derived in terms of temperature. The results of the ACPR Effective Equation of State experiments were formulated as pressure vs. energy. Hence, any comparison of the analytical formulations and most other experimental results with these results necessarily requires the use of a specific heat model to relate temperature and energy content. As described in Appendix J it can be demonstrated that for these experiments, a model for specific heat at constant pressure is appropriate. The model used in this analysis is an approximation to measured values (Ch73). This model includes an average heat capacity of 0.33 J/g K below melt and 0.50 J/g K above melt with a 276 J/g heat of fusion. The melt temperature was taken to be 3115 K.

A specific heat at constant volume formulation has been used in the ANL Equation of State formulation in the VENUS Code (Sh70). This model, developed by Menzies (Me66), is an average value of 0.437 J/g K which includes the heat of fusion.

The differences between these specific models is shown in Figure V-13 with respect to two equation of state models for UO₂. The first equation of state model is the so-called ANL Equation of State model used in the VENUS Code (Sh70). This model can be described by:

$$P(\text{bar}) = 10^{-6} \exp \left[69.979 - 76800/T - 4.34 \ln T \right] \quad (16)$$

for T in K. The second model is an extrapolation of

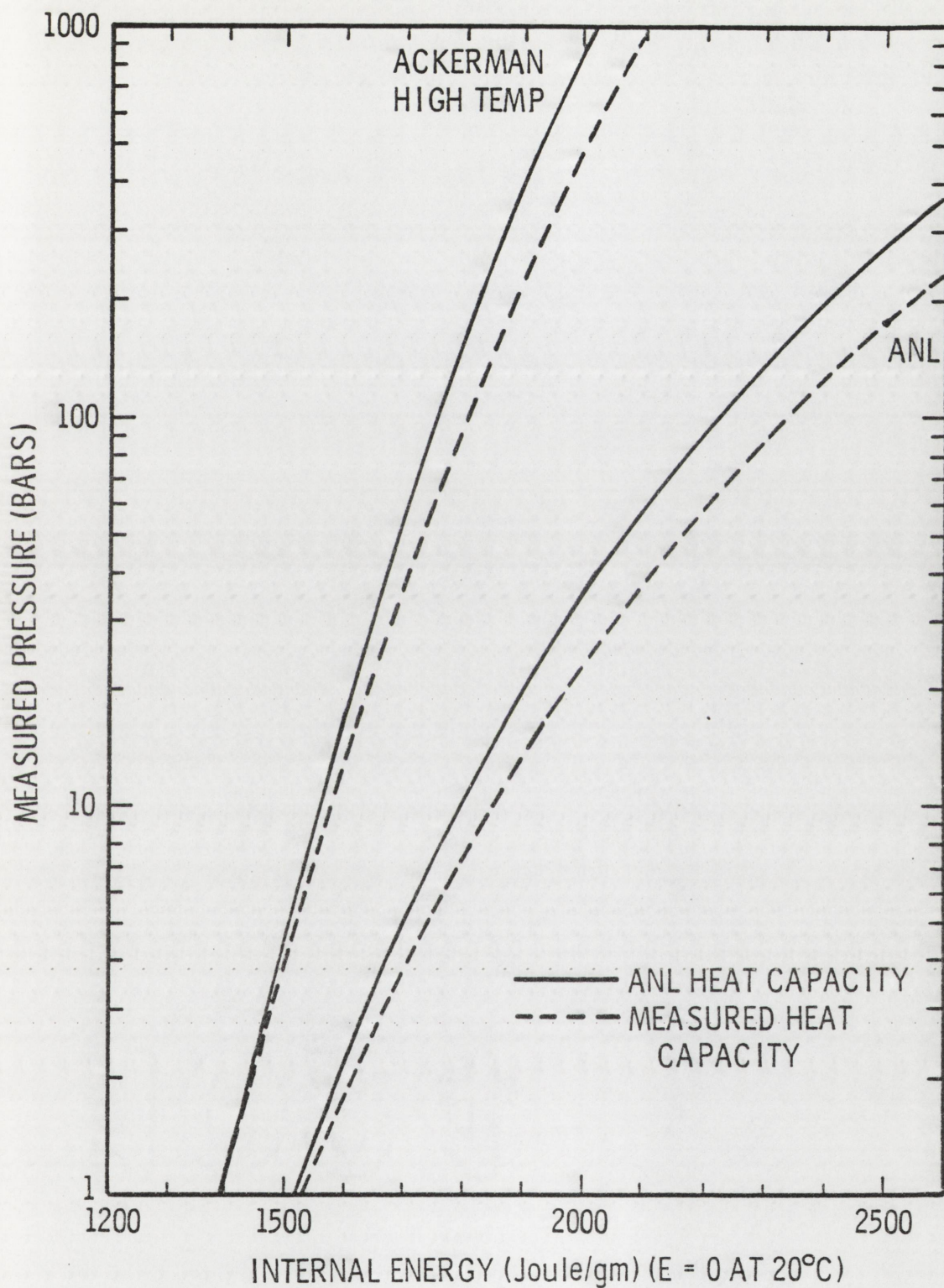


Figure V-13
Comparison of Two Vapor Pressure Models
Using Two Specific Heat Models

Ackermann's (Ac56) high temperature effusion data. This can be described as

$$P(\text{bar}) = 10^{-6} \exp (37.63 - 82880/T) \quad (17)$$

for T in K.

Since $(C_p - C_v)$ is positive the C_p model based on experimental measurements yields lower temperatures and, hence, lower pressures for a given internal energy than does the ANL C_v model.

The two empirical heat capacity models given above do not describe the variation in specific heat as a function of stoichiometry that would be expected from differences in dissociation of the various species. Further, the above models describe the steady state. They do not account for the transient effects that are postulated to exist due to the finite time for some sensible heat to be dissipated by dissociation or defect formation (Be77). While these limitations on the empirical C_p model have been noted, that formulation was used to translate equation of state models from the temperature domain to formulations in terms of energy.

The specific heat at constant pressure formulation given above was used to translate the Blackburn model (Bl73) into energy coordinates. Blackburn (Bl73) indicated uncertainties in the partial pressures predicted by equations (14) were as large as 23 percent. These uncertainties were attributed to approximations made in the derivation of equations (14). However, while the

absolute magnitude of the pressures predicted from the Blackburn model remain uncertain, the trends and relative relationships are probably valid.

Figures V-14 through V-17 display various results from equations (5), (10), (11), (12), (14), and (15), using the specific heat model to derive the energy coordinate. In Figure V-14 the variation with energy content of the total vapor pressure of species in equilibrium with UO_x for various oxygen to metal (O/M) ratios are displayed. The same data is presented in a different form in Figure V-15 as the variation of total vapor pressure with O/M ratio for several values of energy content. These results indicate that as the O/M ratio increases, the total vapor pressure increases for a given energy content. This trend is more pronounced for hyperstoichiometric urania than for hypostoichiometric urania, as would be expected. Further, the fractional change in pressure from one O/M ratio to another is larger at lower energy content and decreases as the energy content increases.

Figure V-16 shows the variation with energy of the partial and total pressures of the species in equilibrium with urania of two O/M ratios, i.e., $\text{UO}_{2.00}$ and $\text{UO}_{2.08}$. For an energy content of 2000 J/g, the variation of total and partial pressures with stoichiometry of urania is shown in Figure V-17. It is noted that the partial pressure of UO_2 is nearly independent of the stoichiometry of the urania. The partial pressures of UO_3 and O_2 increase with stoichiometry while the partial pressure of UO decreases. At higher temperatures, the dominant species in the

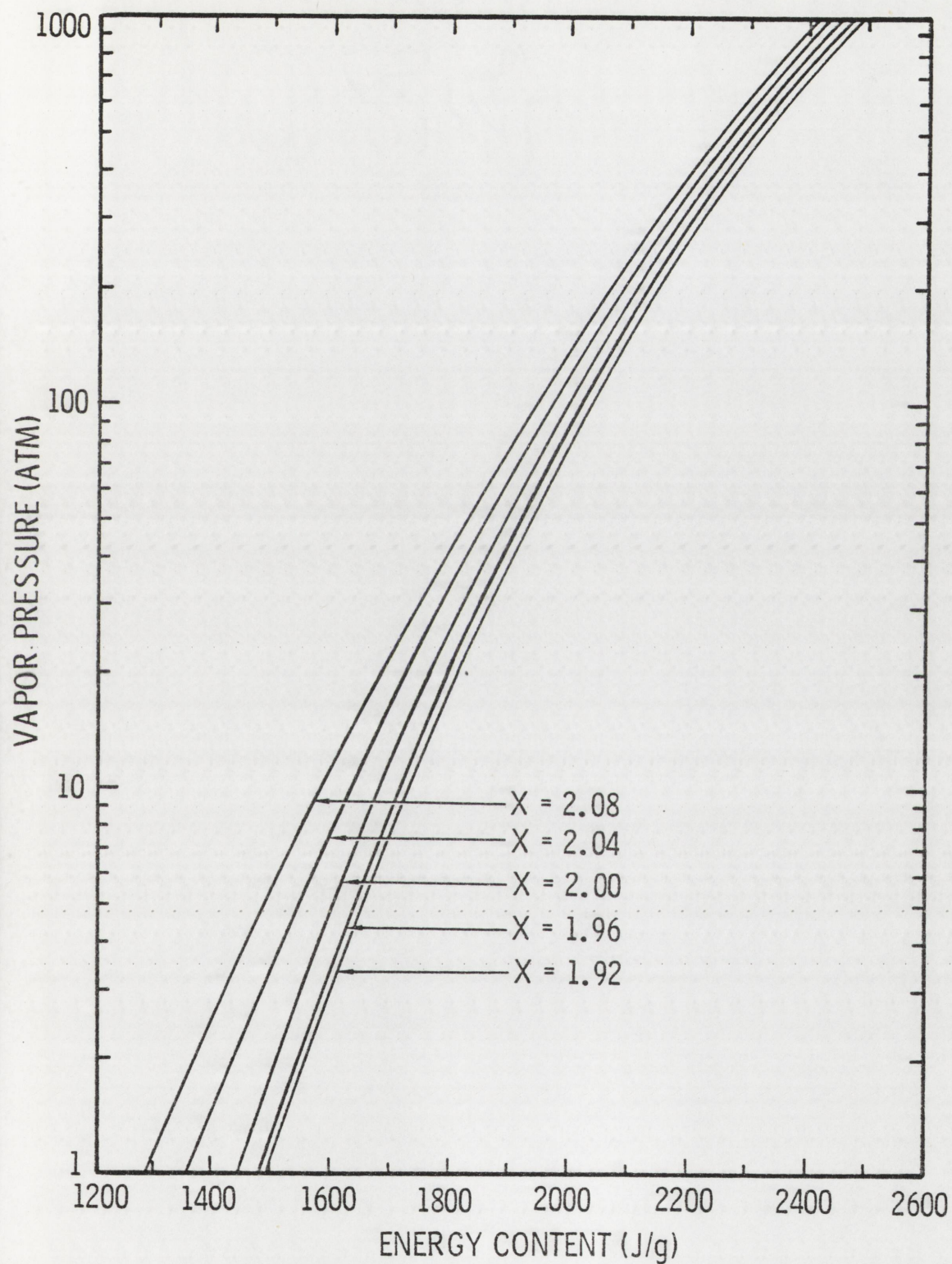


Figure V-14

Vapor Pressures for UO_x Predicted by Blackburn Model (B173)

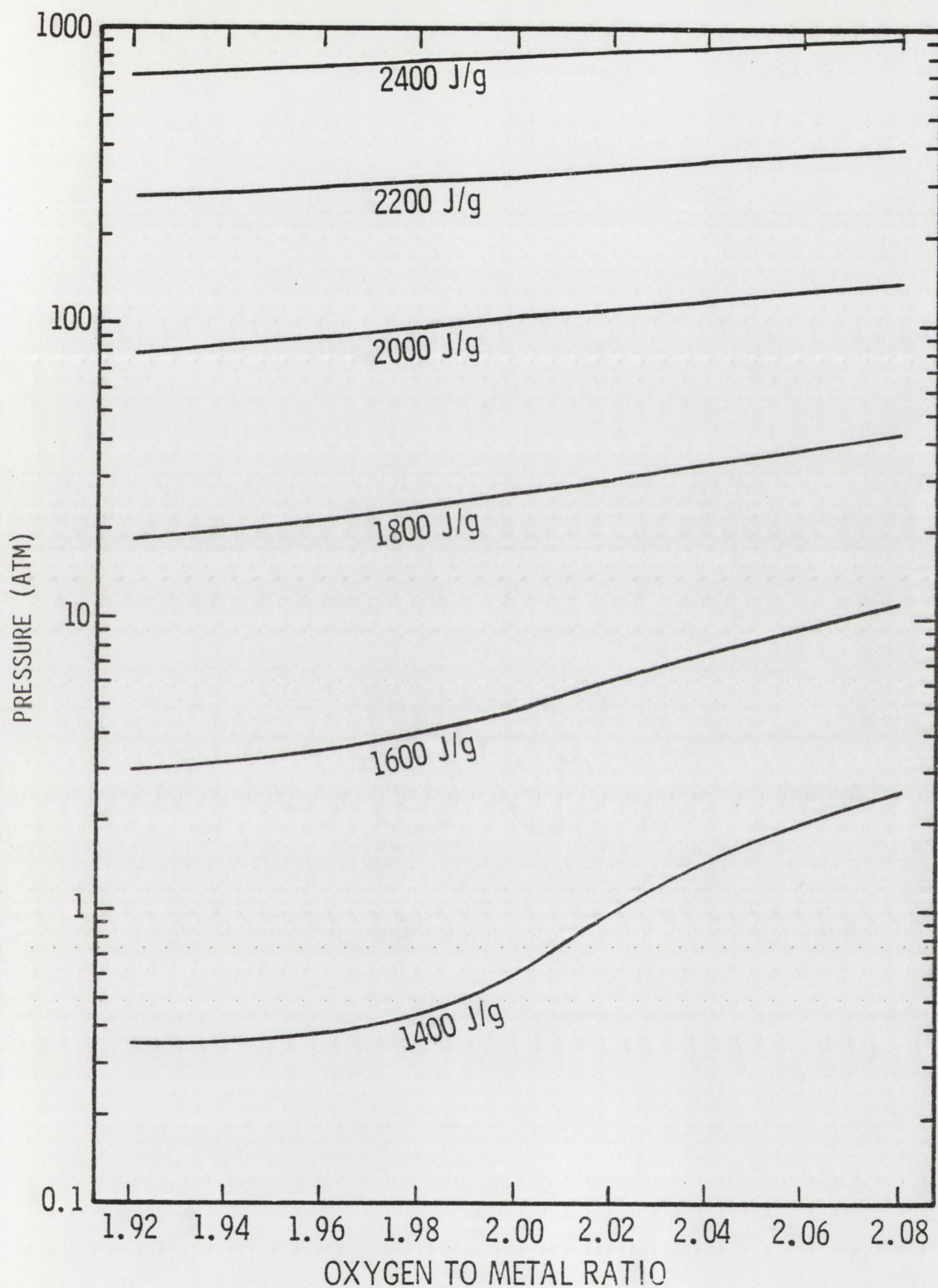


Figure V-15

Total Pressure over Urania as a Function of
Oxygen to Metal Ratio Predicted by Blackburn Model (B173)

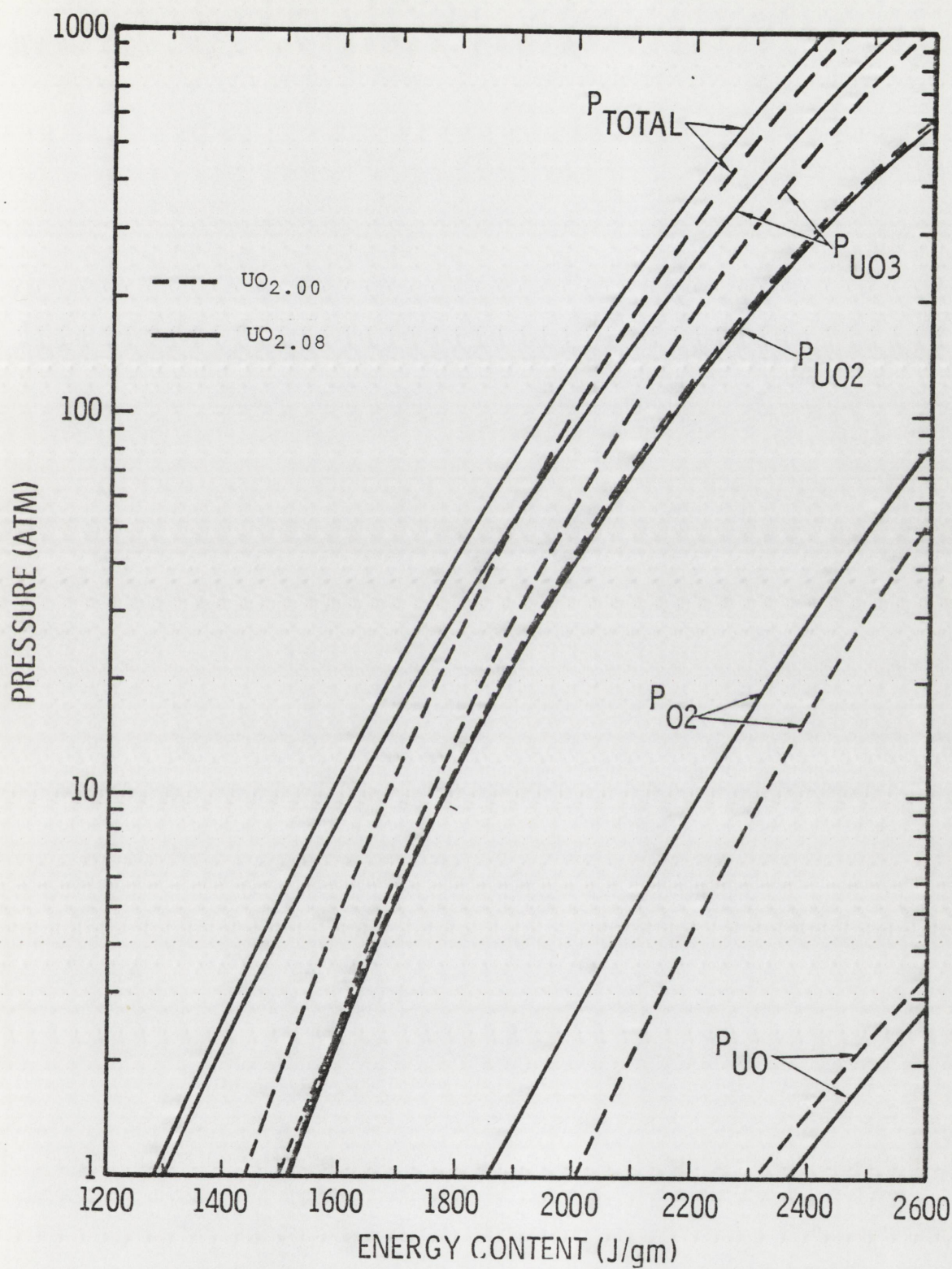


Figure V-16

Partial Pressures of Species over Urania

Predicted by Blackburn Model

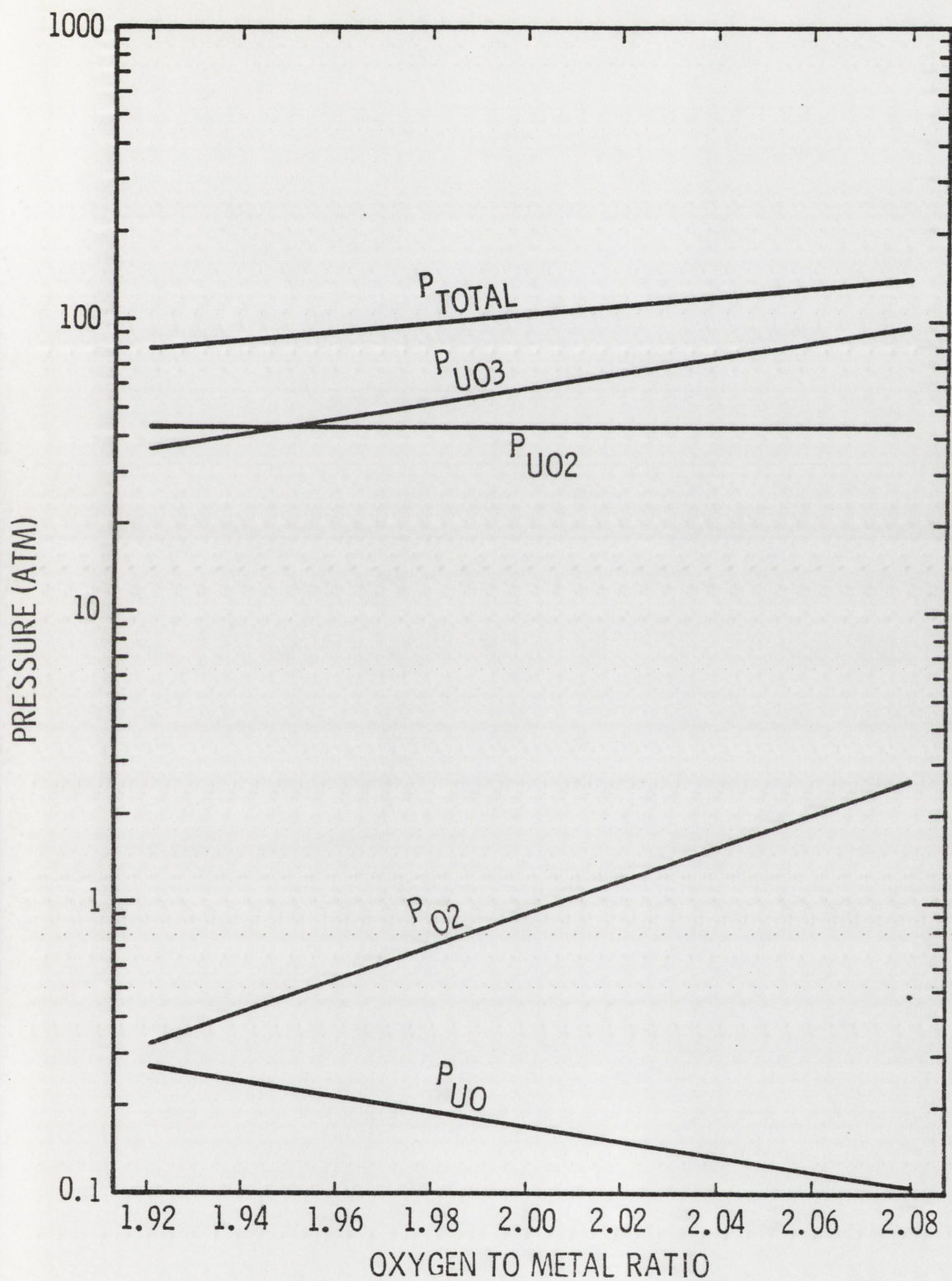


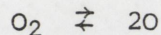
Figure V-17

Total and Partial Pressures of Species over Urania
as a Function of Oxygen to Metal Ratio for Energy
Content of 2000 J/g Predicted by Blackburn Model

vapor is UO_3 .

At higher temperatures the oxygen also dissociates to yield elemental oxygen as described by Gabelnich and Chasanov (Ga72).

That is:



While this reaction has only minimal effects on the vapor pressure, this dissociation has implications with regard to heat transport in the vapor (Ti77).

It is important to remember that the results described above are total and partial pressures of vapor in equilibrium with a surface of composition UO_x . However, since the vapor tends to be oxygen rich with respect to the sample, the surface rapidly becomes deficient in oxygen. Breitung (Br75) described this effect and its implications on vapor pressure measurements. The surface composition is determined by the net flow of oxygen into the vapor phase and by the diffusion flow to the evaporating surface from within the sample. This is shown schematically in Figure V-18, which shows the evaporating surface moving into the sample with velocity V determined by the uranium flow into the vapor $j_{\text{U}}^{\text{gas}}$ and the uranium density ρ_{U} in the sample. This system can be solved for the oxygen concentration as a function of position from the evaporating surface. The result is shown qualitatively in Figure V-19. Note that after sufficient time t_3 , the oxygen profile no longer changes. Subsequent evaporation merely causes the depleted zone to be displaced as the evaporating

surface moves into the sample. For this type of steady-state evaporation to exist, it is necessary that the ratio of the oxygen diffusion coefficient in the sample and the evaporation front velocity be small with respect to the sample thickness (i.e., $D/V \ll l$). This is called forced congruent vaporization and is shown schematically in Figure V-20. Note that once the steady-state oxygen concentration profile is established, the oxygen to metal ratio (O/M) in the vapor in equilibrium with the evaporating surface must be the same as the O/M ratio in the bulk sample. At the pressures of interest for accident analysis (i.e., greater than 1 atm), the mean free paths in the vapor are small (less than 1 μm). Thus, the probability of an evaporating molecule being back-scattered is large; and, hence, thermodynamic equilibrium between the surface and the adjacent vapor layer is insured.

If the D/V ratio is large, implying low evaporation rates, the steady state described above cannot exist. Here the diffusion of oxygen is sufficient to maintain a homogeneous oxygen concentration within the sample which decreases with evaporation time. The vapor above the surface is therefore in equilibrium with the entire sample. Hence, this type of vaporization is called equilibrium evaporation and is shown schematically in Figure V-21.

A certain amount of time is required to establish the steady state oxygen profile. Breitung (Br75) estimates this time to be approximately 1 msec at 4000 K for evaporation rates expected during the transient laser heating experiments and that the

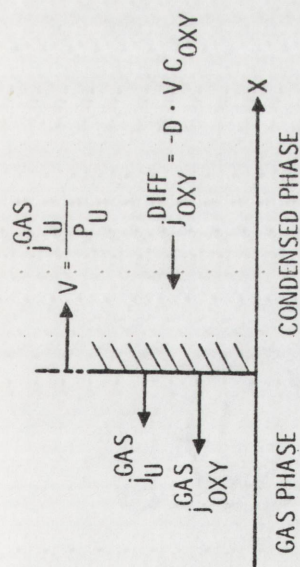


Figure V-18

Species Flows in Evaporating Urania (Br75)

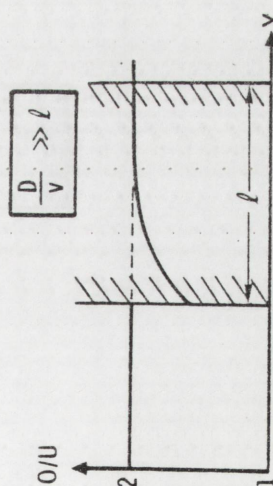


Figure V-20

Forced Congruent Evaporation of UO_2 (Br75)

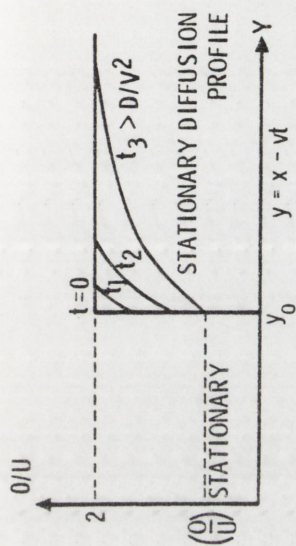


Figure V-19

Oxygen Concentration Profile
in Evaporating Urania (Br75)

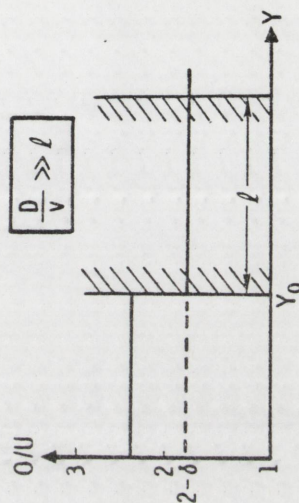


Figure V-21

Equilibrium Evaporation of UO_2 (Br75)

surface stoichiometry changes by 90 percent of its steady-state change in 100 μ sec. (At 4000 K, Breitung (Br75) estimated that a 1 μ m thickness evaporates in 100 μ sec.) The transient heating techniques used to investigate the high temperature, high energy states of interest in accident analysis tend toward the forced congruent evaporation mode, while the low temperature transpiration and effusion experiments are classic examples of equilibrium evaporation.

The vapor pressure in the case of equilibrium evaporation may differ considerably from that of forced congruent evaporation. Breitung (Br75) investigated these differences using techniques similar to those of Blackburn (Bl73) based on equilibrium chemical thermodynamics. These results are shown in Figure V-22 for $\text{UO}_{2.00}$. It is noted that the pressures for the two types of evaporation are similar at lower temperatures; but, at high temperatures the pressures during forced congruent evaporation are larger than those from equilibrium evaporation. This difference becomes larger as the temperature increases. The effects of different sets of thermodynamic data are also demonstrated in Figure V-22. It is noted that while the total pressures predicted from the two sets of data are systematically different, the relationship between the pressures due to the two types of evaporation remains the same.

COMPARISON WITH OTHER RESULTS

The results obtained in the EEOS experiments were compared with the other high temperature data described in Chapter II.

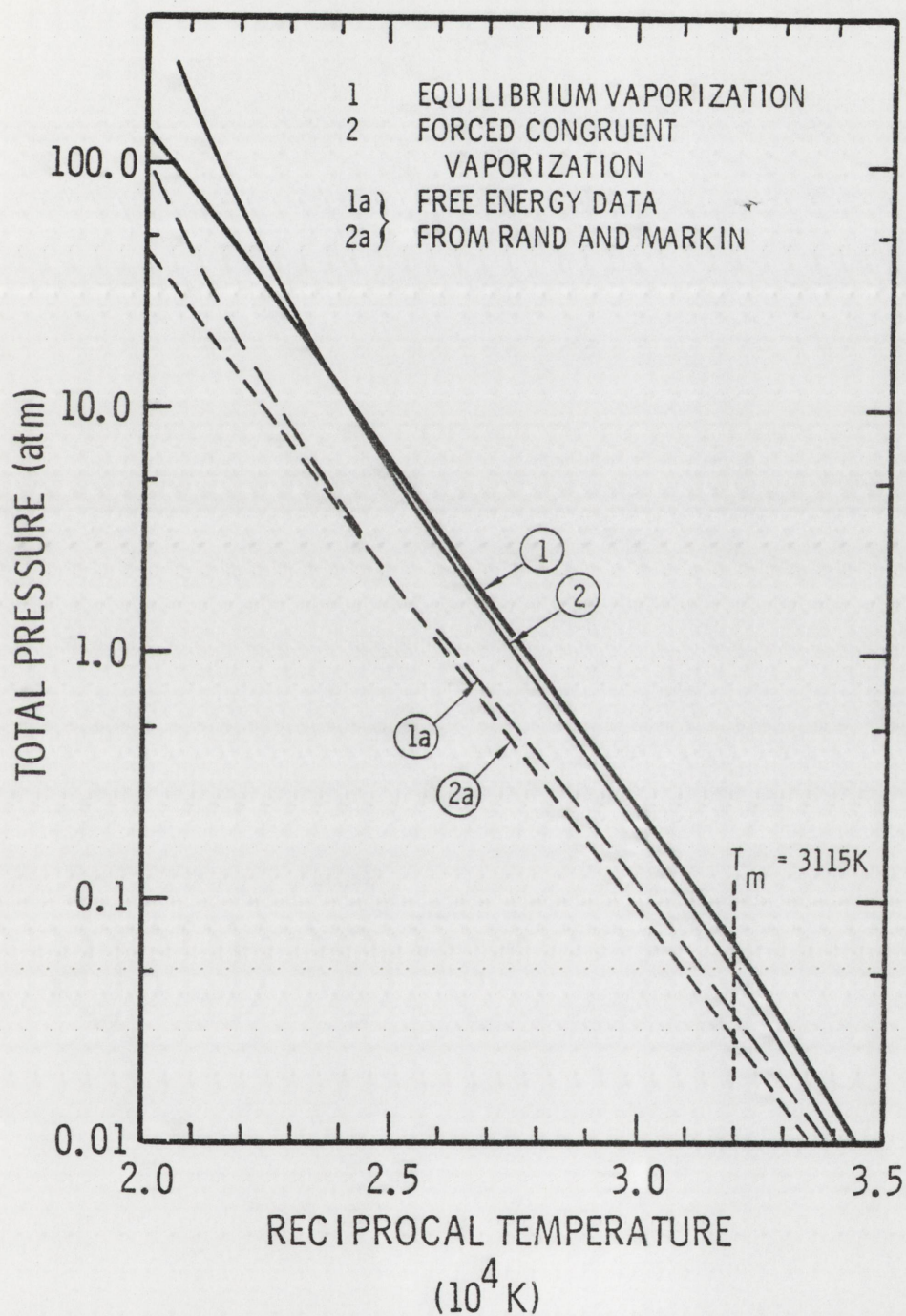


Figure V-22

Total Vapor Pressure Above $\text{UO}_{2.00}$ for Equilibrium
 and Forced Congruent Vaporization (Br75)

Comparisons were also made with the vapor pressure formulations of the VENUS (Sh70) ANL EOS, with an extrapolation of Ackermann's high temperature data (Ac56), and with the results of the Blackburn formulation (Bl73) described in the previous section. In all cases, the specific heat at constant pressure model described on page 140 was used to relate temperature and energy content.

In Figure V-23 the experimental data of Benson (Be76), Bober (Bo75-1), and Ohse (Oh76) are shown with the upper and lower energy bounds from the EEOS experiments. The closest comparison is with the data of Benson's electron beam experiments (Be76). The urania used in those experiments was nearly identical to the samples used in the EEOS experiments, both with an oxygen-to-uranium (O/U) ratio of 2.08. Further, Benson's (Be76) data is formulated as vapor pressure as a function of internal energy; thus, the comparison is not limited by the validity of a specific heat model. From Figure V-23 it is noted that Benson's (Be76) data is bounded by the EEOS results and that his data parallels the upper energy bound. Most of Ohse's data (Oh76) also is bounded by the EEOS results. Only the data obtained by Bober, et al., (Bo75-1) falls outside the EEOS bounds for the vapor pressure over $\text{UO}_{2.08}$. It must be noted that the specific heat model that was used is not based on experimental measurements over the region of energy and temperature in which it was applied. Thus, the translation of temperature to energy may not be precise. The same limitation applies to comparisons

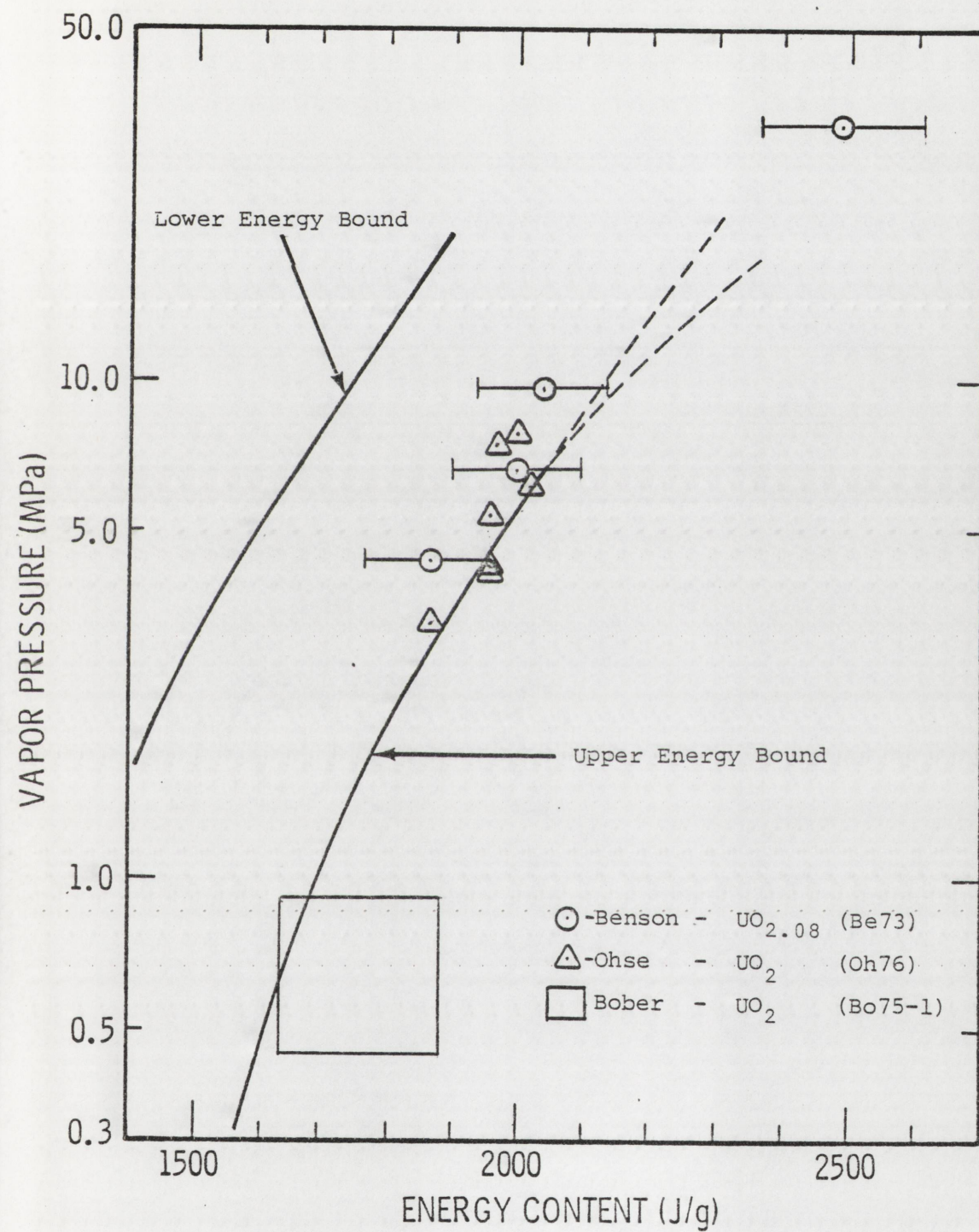


Figure V-23
Comparison of EEOS Results with Other Experimental Data

with the analytical formulations. Neither Bober (Bo75-1, Bo75-2) nor Ohse (Oh75, Oh76) specified the O/U ratio of the samples used in their experiments. Ohse (Oh76) does state that his samples were heated to above the melting point and held at that temperature so that the sample stoichiometry would approach its equilibrium value. As was discussed in the previous section, Breitung (Br75) showed that the stationary evaporation O/U ratio is lower than the original sample stoichiometry. The Blackburn results (Bl73) show that lower O/U ratios of the evaporating surface yield lower total vapor pressures. The comparison of Benson's (Be76) results and the EEOS results with the Ohse (Oh76) and Bober results (Bo75-1) may demonstrate that trend. The comparison of Figure V-23 with the estimated experimental uncertainties shown in Figure V-12 shows that nearly all of the high temperature experimental data falls within those error limits.

A comparison of the EEOS results with two widely referenced extrapolations of low temperature measurements on UO_2 is shown in Figure V-24. The two vapor pressure relationships are the VENUS ANL EOS (Sh70) and a fit to the Ackermann high temperature (AHT) data (Ac56). It is noted that, in the range of pressure and energy content shown in the figure, the ANL EOS predicts lower pressures than those indicated by the EEOS results, differing by a nearly constant factor of 2 from the upper energy bound. The AHT data is bounded by the EEOS results for most of the region shown. However, at high pressures, the AHT formulation predicts much higher pressures than indicated by the EEOS results.

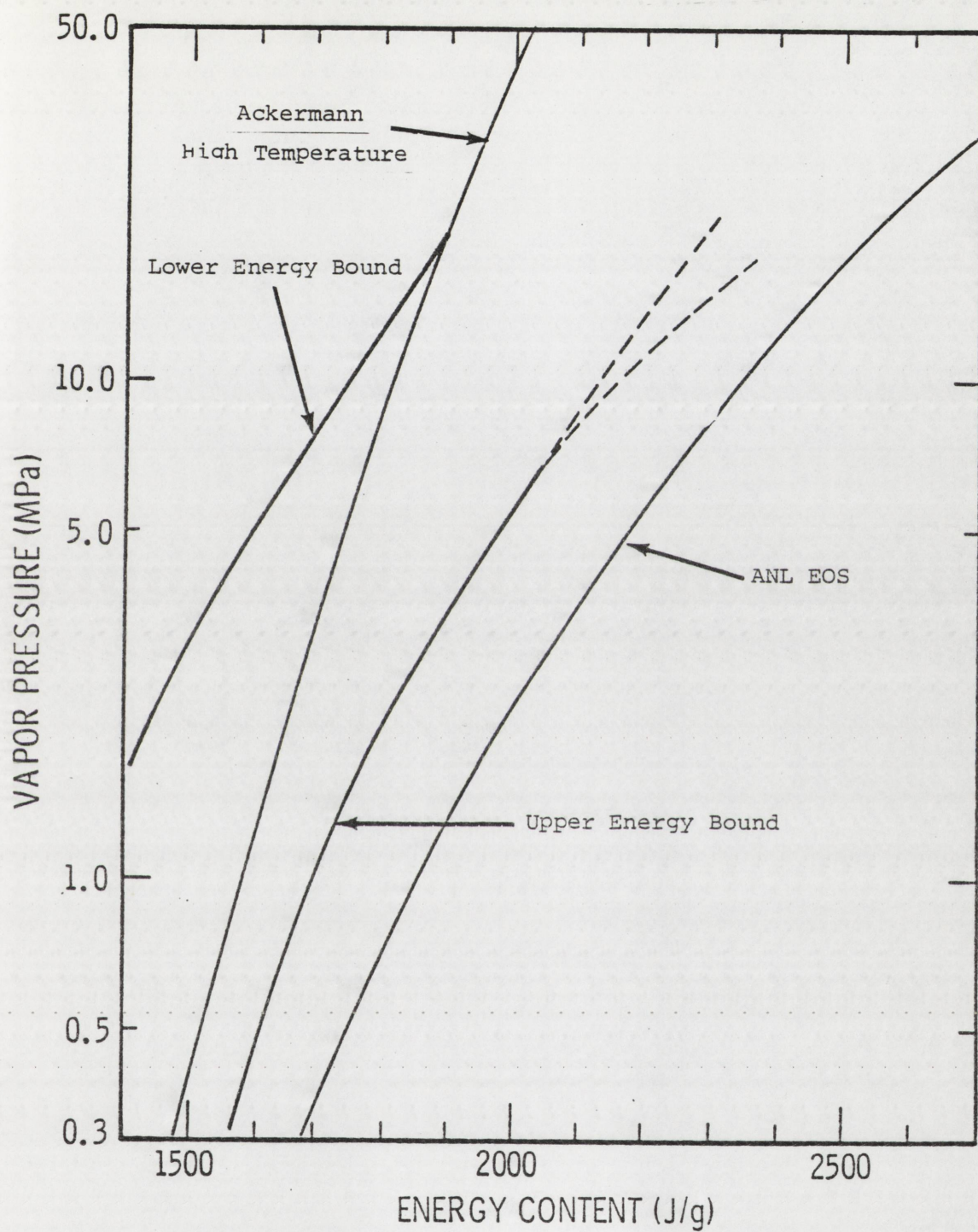


Figure V-24
Comparison of EOS Results with
Extrapolations of Low Temperature Data

A final comparison is made between the EEOS vapor pressure bounds and the Blackburn (B173) results that were derived previously. (See Figure V-25.) Results of that equilibrium chemical thermodynamics method are shown for O/U ratios of 1.92, 2.00, and 2.08. At low values of energy content, the Blackburn (B173) results parallel the upper energy bound, while at high energy content, they more nearly approximate the lower energy bound of the EEOS data. This trend is to be expected since in the EEOS experiment higher energy implies longer times and, hence, larger heat losses from the sample. Therefore, the peak energy content of the EEOS sample will be defined by the upper energy bound at early times during the experiment and by the lower energy bound at later times, and will be contained between those bounds at intermediate times. The experimental uncertainties in the EEOS measurements are large enough to preclude any detailed differentiation between samples of different stoichiometry.

POSTMORTEM

One pressure cell that had been used in a high energy experiment similar to the EEOS-UO2-5 series was disassembled to determine the final disposition of the fuel sample. After the four cap screws and retainer plate were removed, it was discovered that the pressure transducer, Inconel insert and graphite crucible (see Figure III-7) were tightly bonded together. The Inconel pressure cell was removed by shearing the thermocouples which held it to the graphite crucible. The crucible was finally separated by forcing wedges between the Inconel insert and the

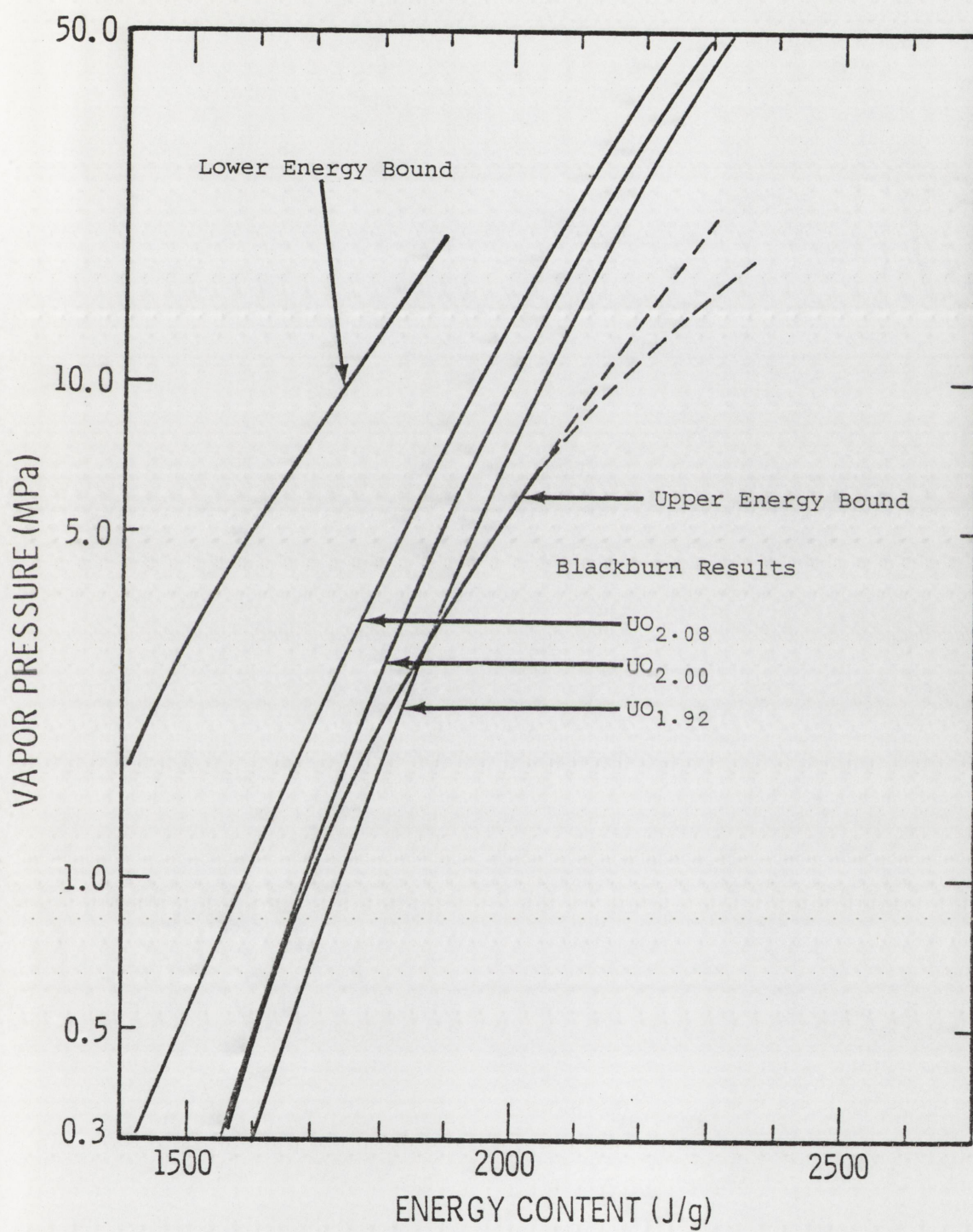


Figure V-25
Comparison of EEOS Results with Blackburn Results

crucible. A longitudinal crack developed in the cylindrical side of the crucible as it separated from the transducer. The bottom of the crucible separated from the remainder of the crucible along fractures as shown in Figure V-26. The graphite buffer disc remained bonded to the graphite crucible as shown in Figure V-26. The various components appeared to be bonded together with UO_2 deposited in the gaps between them.

A photo micrograph of the crucible fracture surface is shown in Figure V-27. The surface is covered with UO_2 , indicating that fracture was formed by the tensile failure of the graphite in the corners during deformation due to the high internal pressure. The UO_2 was then extruded into that crack. The UO_2 layer does not extend to the outside edge, indicating that the fracture was not complete until broken upon disassembly.

Figure V-28 is a photo micrograph of the inside surface of the graphite buffer disc. It displays the rough texture of the UO_2 deposited on that surface.

Much of the UO_2 appeared as loose debris which was piled on the bottom of the graphite crucible when it separated during disassembly. This debris is shown in the low magnification photo micrograph in Figure V-29. Some of this loose debris was formed during the experiment. However, much of it was produced by fracturing larger pieces during subsequent handling. Higher magnification of the debris shows it to be of three types. In Figure V-30 small spheres (approximately 0.02 mm diameter) of UO_2 are seen (indicated by arrows). Those were probably frozen

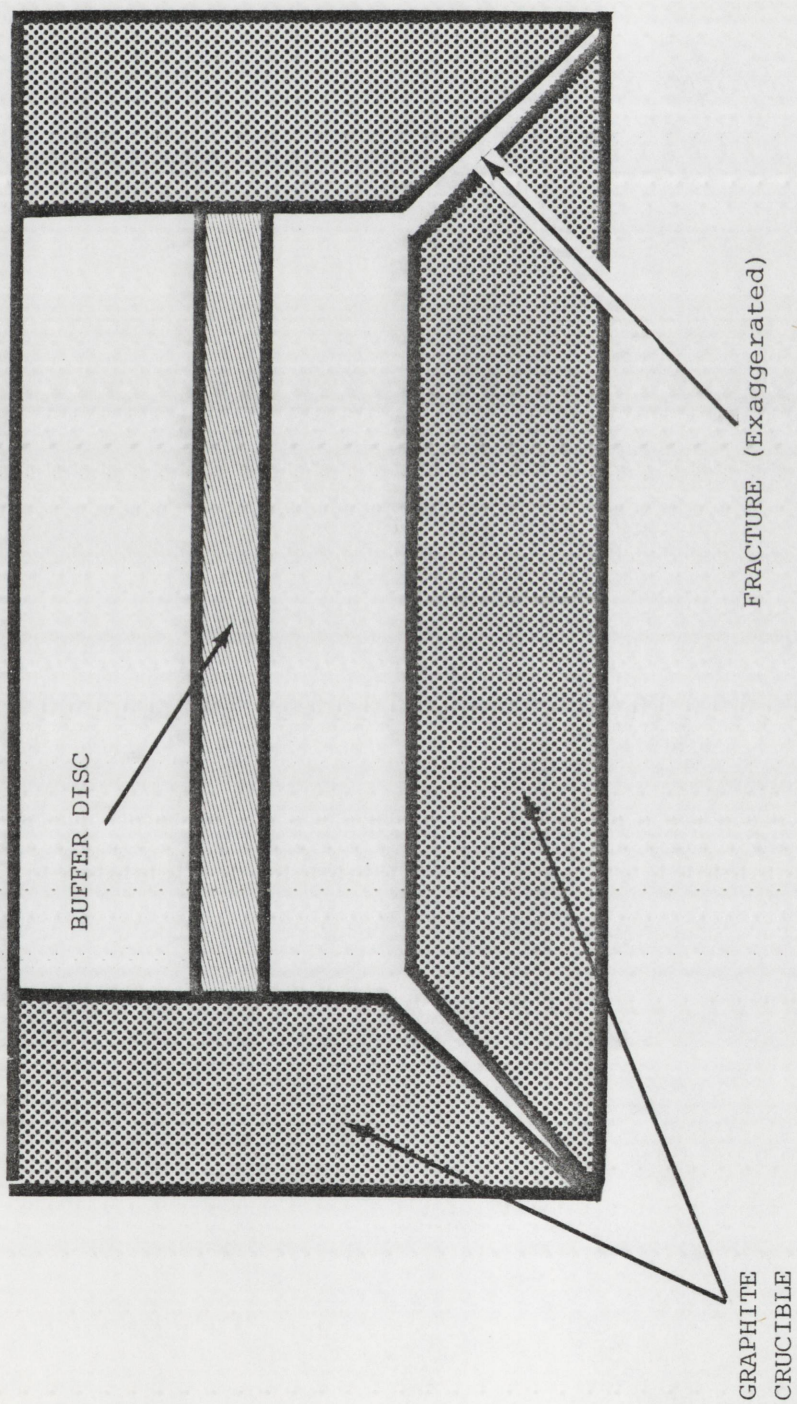


Figure V-26
Sketch of Postmortem Graphite Crucible

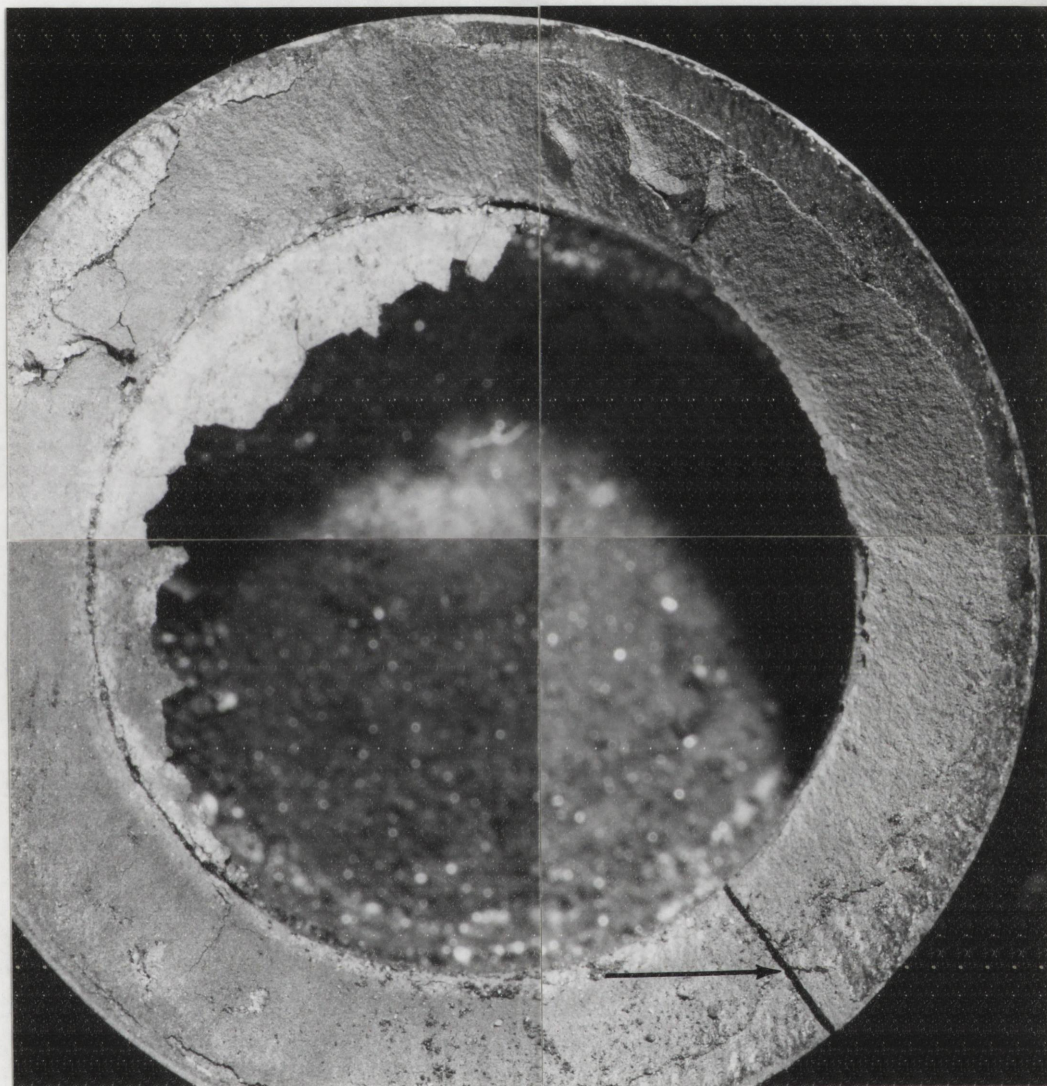


Figure V-27
Photo Micrograph of Crucible Fracture Surface

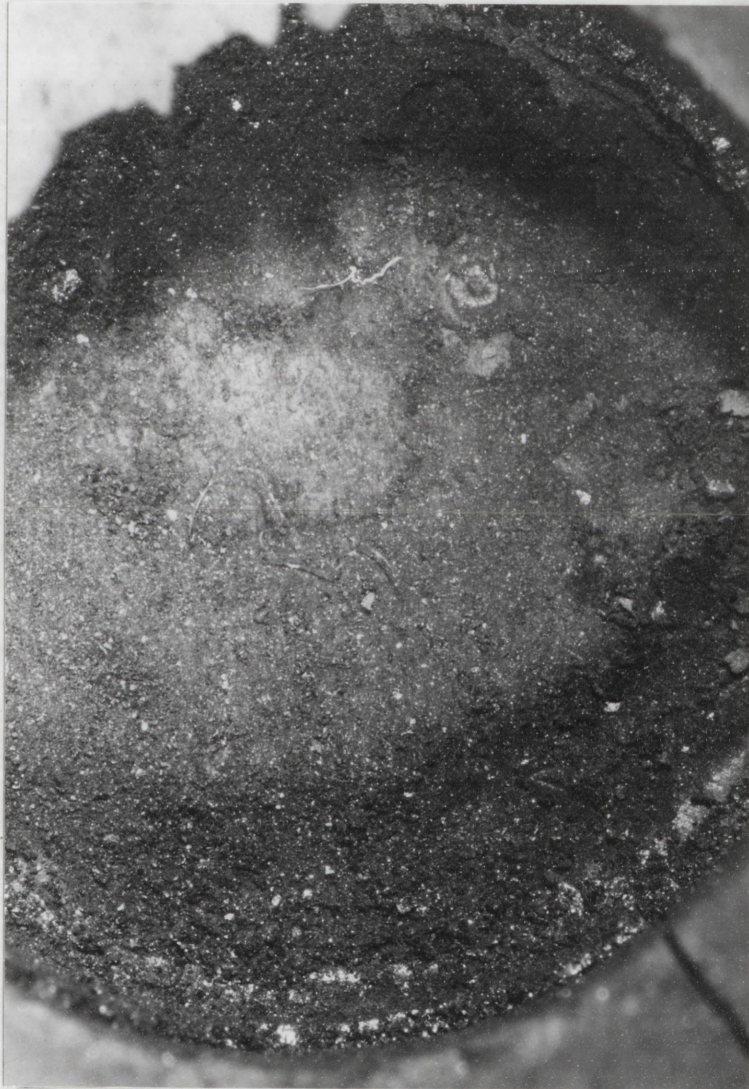


Figure V-28
Photo Micrograph of Surface of Transducer Buffer Disc

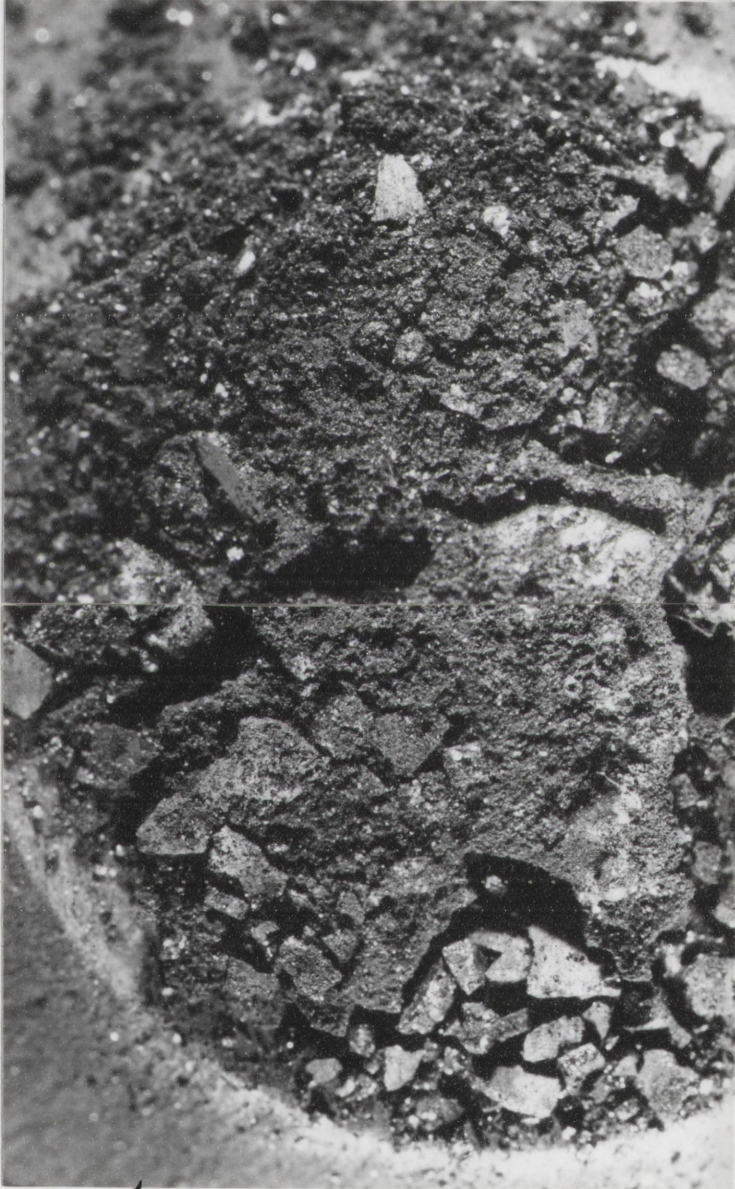


Figure V-29
Photo Micrograph of Loose Debris
on Bottom of Postmortem Crucible

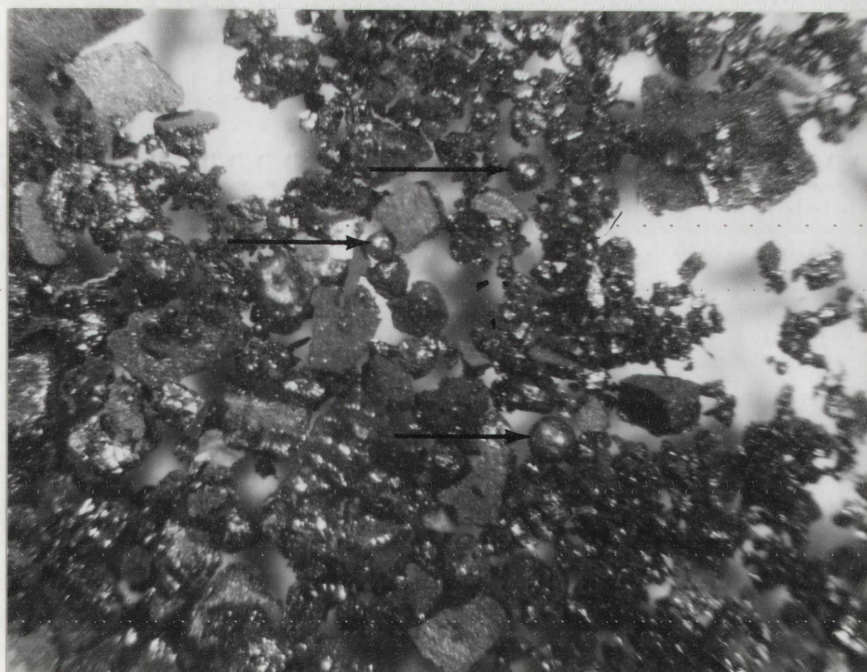


Figure V-30

Photo Micrograph Showing Spherical Debris

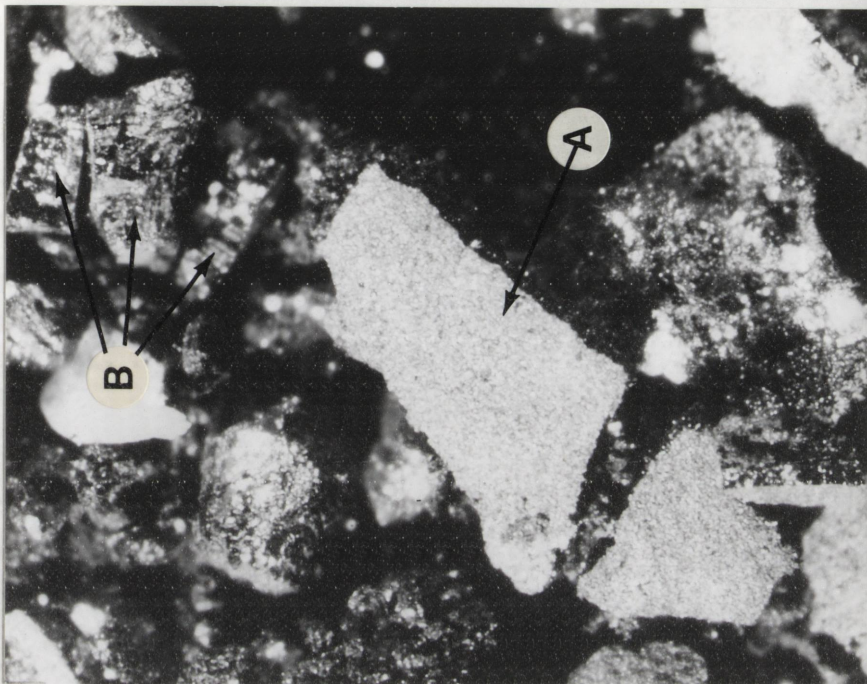


Figure V-31

Photo Micrograph Showing Porous and Dense Debris

from the vapor in free fall during the experiment. Figure V-31 displays the other two types. One (marked A) is a very low density, pumice-like solid; the other (marked B in the photo micrograph) is a dense, glass-like solid. The flat regular surfaces indicate that this debris formed on the surfaces of crucible and/or buffer disc, but the exact origin cannot be defined.

The crucible was mounted in plastic, cut diametrically, and polished. The resulting cross-section is shown in Figure V-32. Four regions, marked with arrows, are of particular interest. The right edge of the buffer disc (marked A in Figure V-32) is bonded with UO_2 to the crucible as shown in Figures V-33 and V-34. A fracture in the buffer disc is noted which also contains UO_2 . The UO_2 deposited at the left edge of the buffer disc (indicated by B in Figure V-32) is shown in Figure V-35. It is noted that very fine macrograin structure is seen in the UO_2 that is in contact with the crucible while much larger grains are seen toward the free surface indicating much more rapid freezing at the wall.

In Figure V-36, a large piece of debris (marked C in Figure V-32) is seen. That debris was from the bottom surface of the crucible, and, before the crucible was mounted, was still attached to the crucible as shown in the upper left of Figure V-27. From Figure V-36, it is noted that the flat surface of the debris, which was in contact with the bottom of the crucible, is solid and dense. The other surface is porous and bubbly. That structure is indicative of vapor bubbles.

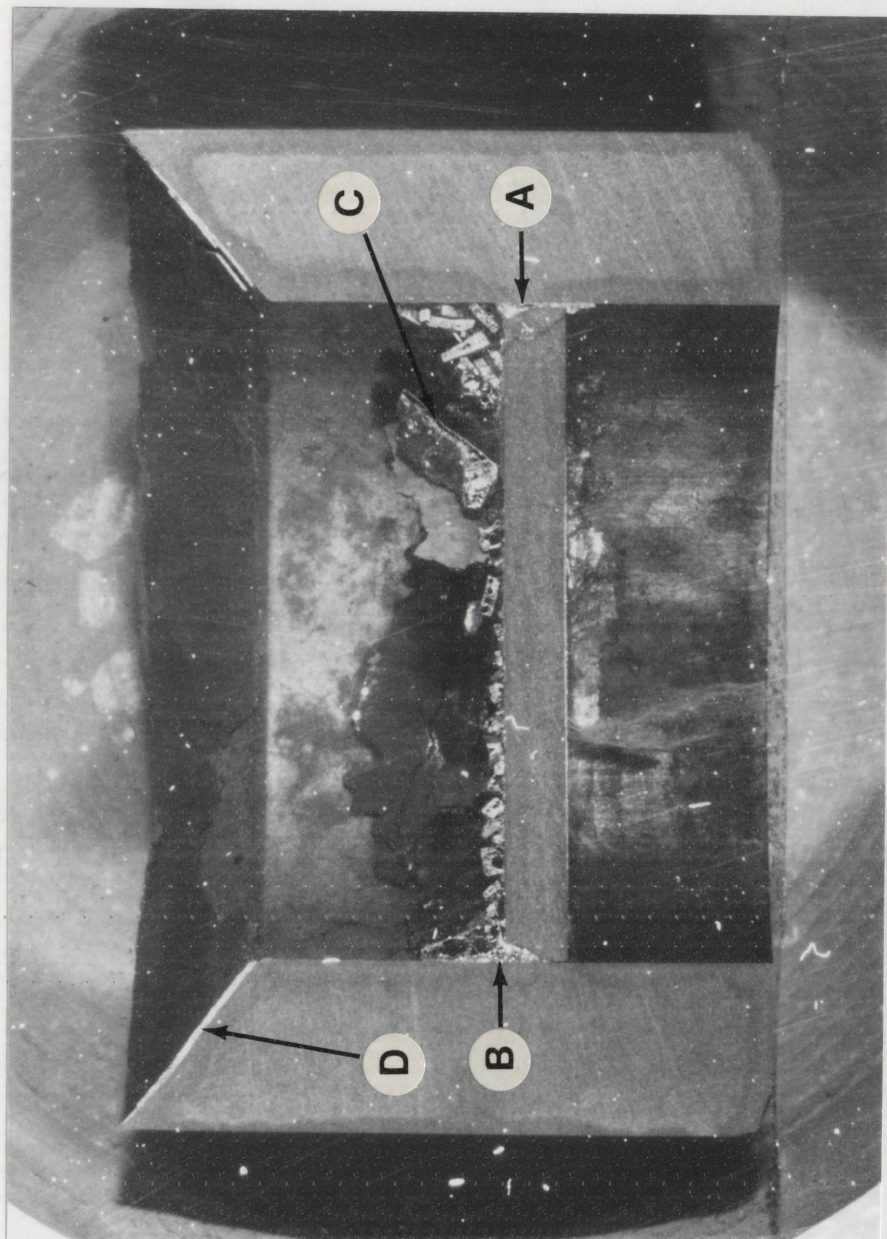


Figure V-32
Cross-Section of Postmortem Graphite Crucible



Figure V-33

Photo Micrograph of Right Edge of Buffer Disc

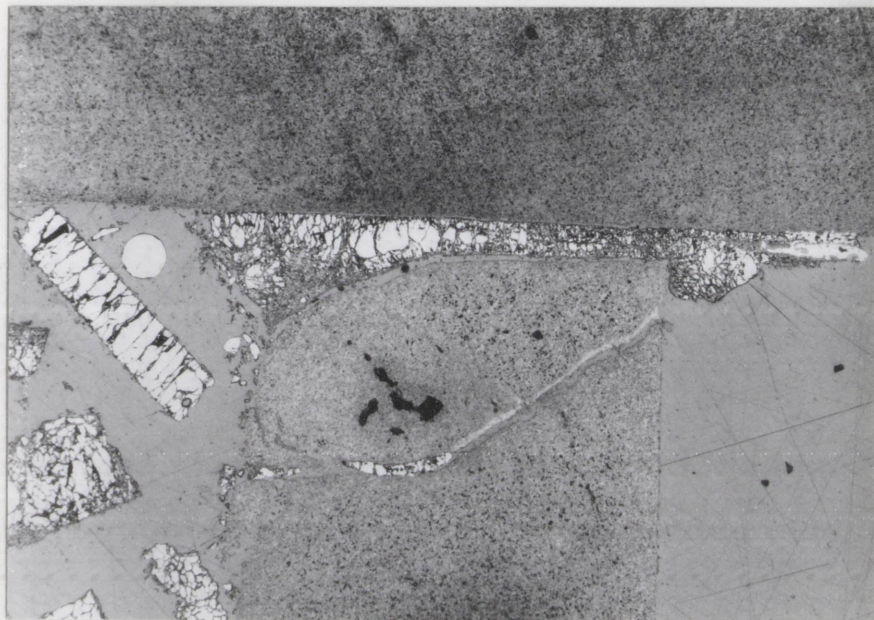


Figure V-34

Photo Micrograph of Right Edge of Buffer Disc

(Bright Illumination)

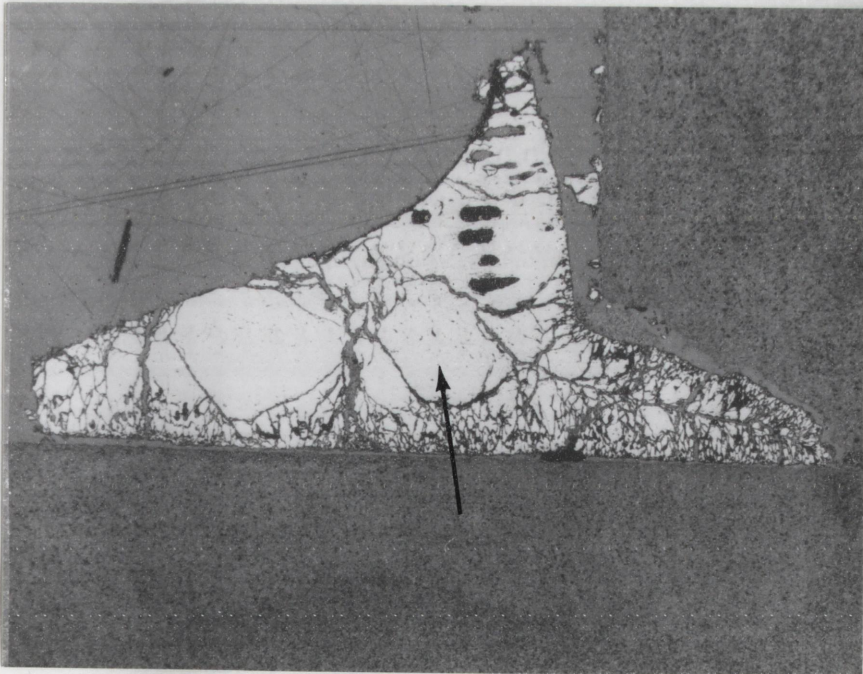


Figure V-35
 Photo Micrograph of Left Edge of Buffer Disc
 (Bright Illumination)

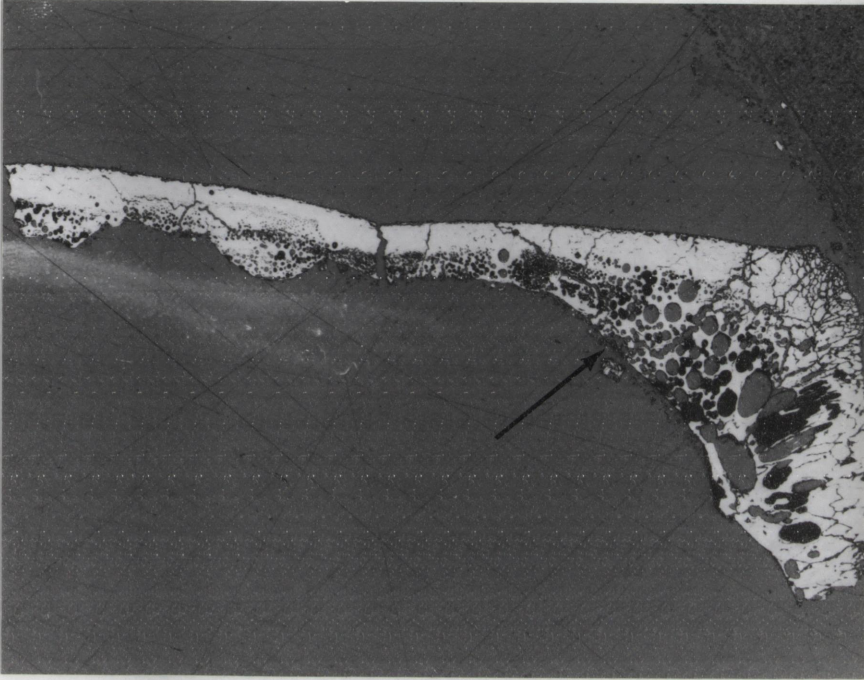


Figure V-36
 Photo Micrograph of Large Debris
 (Bright Illumination)

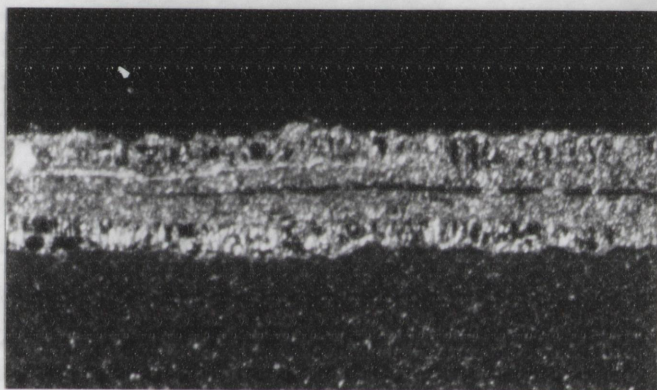
Figure V-37 shows three portions of the UO_2 layer on the fracture surface (indicated by D in Figure V-32). In frame (A), the inside end of the fracture is shown, and frame (C) is the outside edge. The layer is approximately 0.07 mm thick at the inside. Note that the layer displays a symmetry about its centerline, indicative of simultaneous freezing from both surfaces. The fine grain structure is indicative of rapid freezing.

Most of the UO_2 debris appear in various shades of gray. However, some of the debris exhibit bright yellow and rust colors. Figure V-38 is a photo micrograph of the large grain indicated with the arrow in Figure V-35. The tiny inclusions within the small grains are yellow. Figure V-39 shows small spherical structures on the surface of the large debris shown in Figure V-36. These structures, which were on the inside free surface of that debris, are rust colored. These colored materials may be indicative of oxides of uranium other than UO_2 . The determination of the composition of these and other debris is beyond the scope of this work.

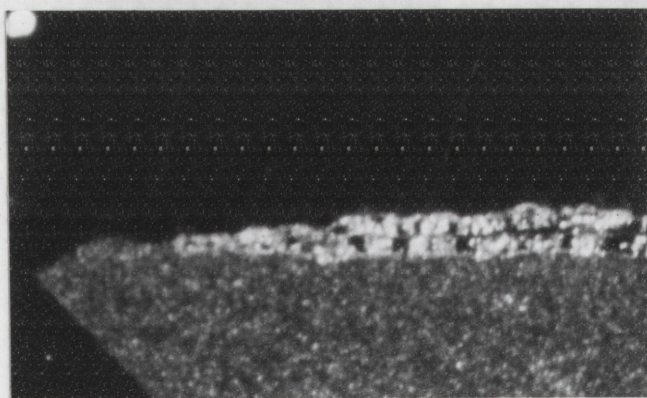
Finally, none of the postmortem examinations detected any attack of the graphite crucible. The rounded edges of the buffer disc as shown in Figures V-33, V-34, and V-35 are indicative of the original buffer disc geometry as indicated by the arrow in Figure V-40.



A



B



C

Figure V-37
Photo Micrograph of UO_2 on Fracture Surface

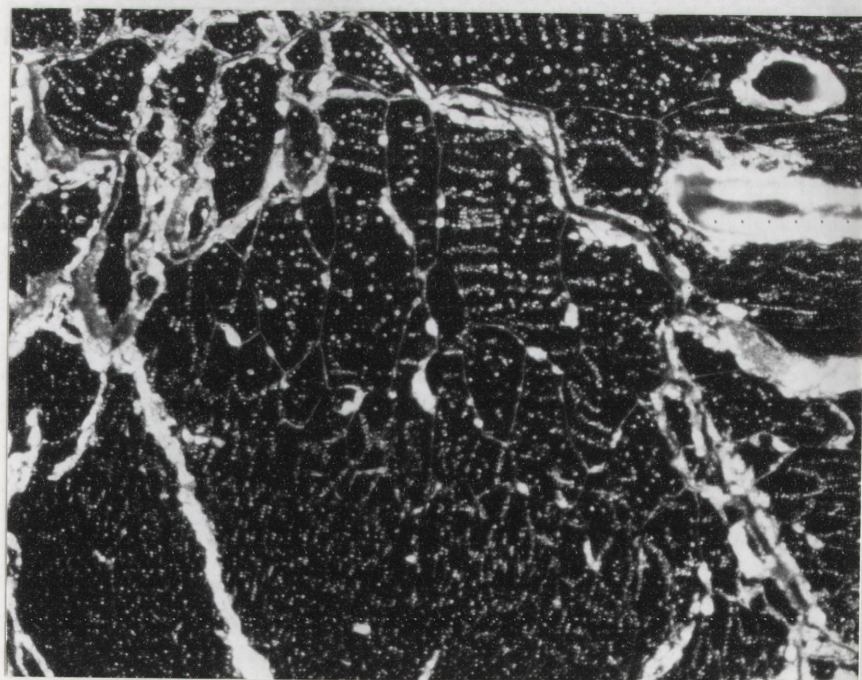


Figure V-38

Photo Micrograph of Colored Inclusions

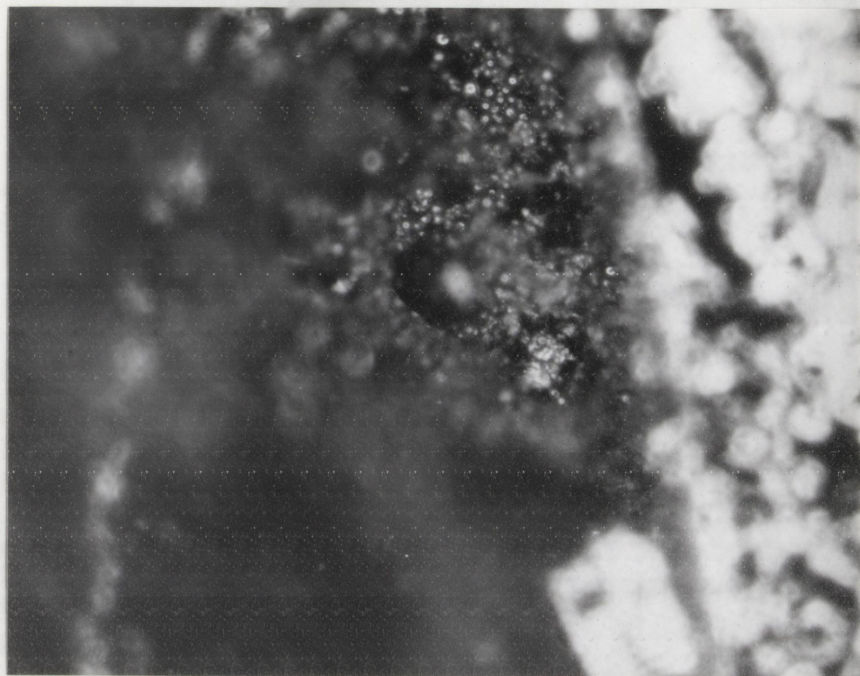


Figure V-39

Photo Micrograph of Colored Spherical Debris



Figure V-40
Kaman Pressure Transducer with Buffer Disc

CHAPTER VI

CONCLUSIONS AND RECOMMENDATIONS

A new technique was developed to measure the vapor pressure of reactor fuels at high temperature and pressure. This technique involves pulse fission heating of the sample to the desired energy states with heating rates comparable to those expected during a severe LMFBR transient. Since the pressure measured may be due to several dissociated fuel species and fission products, and since the evolution of the pressure may be time dependent, the term Effective Equation of State (EEOS) was used to describe these experiments. The results of these experiments are expressed as vapor pressure as a function of sample energy content.

A pressure transducer is used to monitor the pressure in a sealed graphite-lined volume containing the fuel sample during an ACPR transient. The energy input history to the sample is derived from the reactor power history, fission product inventory measurements, and neutron transport calculations. Energy losses from the sample are determined by linear inverse heat conduction techniques using temperature histories derived from thermocouples located in the walls of the confining pressure cell. Because of nonuniformities in the distribution of fission energy deposition within the sample and because of the energy losses from the sample, it is not possible to define a unique energy content history. It is possible, however, to define bounds on the energy content. Bounds on the vapor pressure (formulated as pressure as a

function of energy content) are derived through a point by point comparison of the pressure history with the bounds on energy content.

The EEOS technique was used to determine the vapor pressure of high purity uranium dioxide with an oxygen-to-metal ratio of 2.08. Energy depositions of up to 2720 J/g relative to room temperature were obtained, resulting in measured pressures in excess of 38 MPa. Bounds on the vapor pressure of $\text{UO}_{2.08}$ were found to be:

$$P(\text{MPa}) = \exp \left[(10.004 \pm 1.497) - \frac{(13.365 \pm 2.535)}{E(\text{kJ})} \right]$$

(upper pressure bound for $1.4 \text{ kJ} \leq E \leq 1.9 \text{ kJ}$), and

$$P(\text{MPa}) = \exp \left[(10.894 \pm .198) - \frac{(18.298 \pm .386)}{E(\text{kJ})} \right]$$

(lower pressure bound for $1.6 \text{ kJ} \leq E \leq 2.0 \text{ kJ}$). These results bound previous high temperature data reported by other investigators.

It was noted that the results of these and other transient experiments may be time and/or rate dependent because of dissociation and time dependent heat capacity phenomena.

The comparison of pressure versus temperature relationships with the results of these EEOS experiments requires a knowledge of a specific heat relationship for the fuel material. Experimental specific heat data do not exist for the region of interest. Thus, translation of temperature to energy involves some uncertainty.

Therefore, a need exists for such specific heat data.

The separation between the derived energy bounds is determined by the peak-to-average fission density ratio and by the energy losses from the sample. Thus, in the experiments performed on $\text{UO}_{2.08}$, those bounds are separated by at least a factor of 1.19. A more uniform energy deposition profile would narrow the separation between the bounds derived in the EEOS experiments. Since, as shown in Figure IV-5, the fission density is peaked to the outside circumference of the fuel sample, it may be possible to shield the outside surface without perturbing the neutron fluence incident on the flat surfaces of the sample. This should reduce the peak-to-average ratio, but would also reduce the average energy deposition in the sample. These possibilities should be investigated.

Two limitations on the inverse heat conduction technique used to determine heat losses from the sample were noted. First, knowledge of the exact location of the thermocouple junction within the graphite crucible is important. Radiographic or other techniques need to be developed to make that determination for the assembled pressure cell. The second limitation is the requirement of the use of constant material properties in the analysis in the linear inverse heat conduction techniques. Non-linear techniques can be developed to permit the use of temperature dependent properties.

More detailed postmortem studies should be performed to characterize the species present and their distribution in the debris.

The most important recommendation is that the technique now be applied to other reactor fuels to expand the knowledge available for safety analysis. The inpile technique with double radiological containment is well suited for measurements on plutonium bearing fuels and pre-irradiated fuels containing fission products. To perform such experiments, the experimental package may need minor modification to facilitate assembly and disassembly in a glove box line. A dry, inert atmosphere, as would be present in a glove box line, is necessary for handling the nitride and carbide fuels. While glove box assembly and contamination control would slow the experimental process, no other problems are foreseen.

APPENDIX A
SELECTED MECHANICAL AND THERMOPHYSICAL
PROPERTIES OF MATERIALS

TABLE A-1

Selected Properties of Uranium Dioxide

Property	Value	Reference
Melting Point	3115 K	(Mi70)
Enthalpy of solid at 3115 K	1121 K	(Mi70)
Heat of fusion	278±4 J/g	(Le76)
Heat of vaporization	1700±200 J/g	(Le76)

TABLE A-2

Thermophysical and Mechanical Properties of Uranium Dioxide (Cr75)

Temperature (C)	ρ (gm/cc)	C_p (cal/gm-C)	$\rho * C_p$ (cal/cc-C)	k (cal/sec-cm-C)
0	10.43	.0536	0.559	.0184
100	10.42	.0621	0.647	.0165
200	10.41	.0655	0.693	.0143
300	10.40	.0693	0.720	.0128
500	10.36	.0726	0.753	.0102
700	10.33	.0748	0.772	.0084
900	10.28	.0765	0.786	.0067
1200	10.18	.0792	0.806	.0056
1600	10.01	.0858	0.859	.0054
2000	9.79	.1020	0.998	.0088
2400	9.50	.1321	1.256	.0131
2600	9.34	.1525	1.425	.0151
2841	9.13	.1876	1.649	.0174
2842	8.74	.1225	1.071	.0174
3000	8.59	.1225	1.052	.0191
3500	8.14	.1225	0.997	--

TABLE A-3

Room Temperature Properties of AXF Graphite⁽¹⁾

Property	Value	Unit
Density	1.80-1.88	g/cc
Coefficient of Thermal Expansion	7.9×10^{-6}	C ⁻¹
Thermal Conductivity	1.126	w/cm-C
Compressive Strength	20,000	psi
Sublimation Temperature	3800	K.
Structure	Isotropic ⁽²⁾	

⁽¹⁾ Poco Graphite, Inc. - Subsidiary of Union Oil of California,
P. O. Box 2121, Decatur, Texas.

⁽²⁾ Property deviation with direction of measurement is less than
1±.03 in any dimension.

TABLE A-4
Thermophysical Properties of AXF Graphite⁽¹⁾

Temperature (C)	ρ (2) (gm/cc)	C_p (3) (J/g-C)	ρC_p (J/cc-C)	k (4) (w/cm-C)
0	1.841	.33	.61	1.15
200	1.832	.35	.64	.96
400	1.824	.38	.69	.77
600	1.815	.41	.74	.63
1000	1.798	.45	.81	.47
1300	1.786	.48	.85	.41
1600	1.774	.49	.87	.37
2000	1.757	.51	.90	.34
2600	1.733	.53	.92	.31
3000	1.717	.54	.93	.25

⁽¹⁾ Properties used for inverse heat conduction analysis - temperature dependence derived from room temperature data and average graphite properties.

⁽²⁾ Derived from room temperature density and thermal expansion (See Table

⁽³⁾ Average properties for ATJ graphite (To67).

⁽⁴⁾ Average properties for ATJ graphite (Ho72).

TABLE A-5

Selected Properties For Inconel-718 (Ma74)

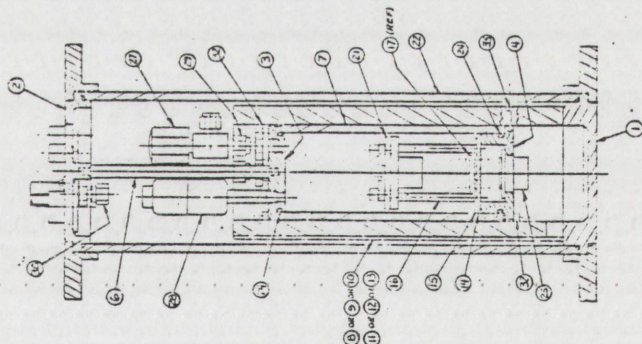
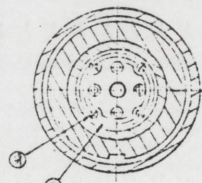
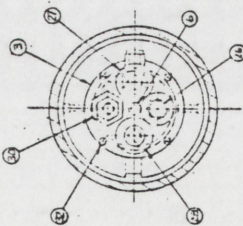
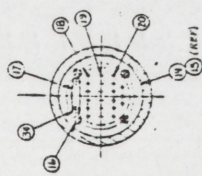
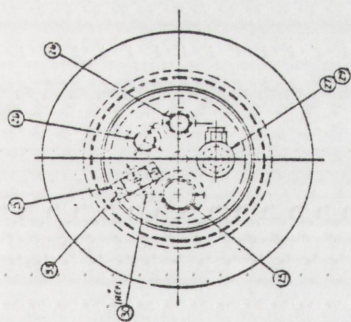
Property	Value	Unit
Melting Range	1260-1336	C
Density	8.2	g/cc
Specific Heat	.104	cal/gm-c
Coefficient of Thermal Expansion		
at 20 C	6.7×10^{-6}	C ⁻¹
at 500 C	8.2×10^{-6}	C ⁻¹
Thermal Conductivity		
at 20 C	.025	cal/sec-cm-C
at 500 C	.036	cal/sec-cm-C
Yield Strength		
at 20 C	170	ksi
at 500 C	140	ksi

APPENDIX B

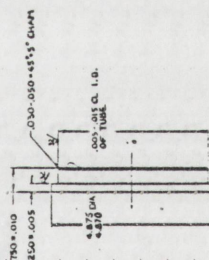
MECHANICAL DRAWINGS OF EXPERIMENTAL COMPONENTS

NOTES
4. HANDLING TO BE SHOWN BY THE

1	2	3	4	5	6	7	8	9	10	11	12	13	14	15	16	17	18	19	20	21	22	23	24	25	26	27	28	29	30	31	32	33	34	35	36	37	38	39	40	41	42	43	44	45	46	47	48	49	50	51	52	53	54	55	56	57	58	59	60	61	62	63	64	65	66	67	68	69	70	71	72	73	74	75	76	77	78	79	80	81	82	83	84	85	86	87	88	89	90	91	92	93	94	95	96	97	98	99	100
---	---	---	---	---	---	---	---	---	----	----	----	----	----	----	----	----	----	----	----	----	----	----	----	----	----	----	----	----	----	----	----	----	----	----	----	----	----	----	----	----	----	----	----	----	----	----	----	----	----	----	----	----	----	----	----	----	----	----	----	----	----	----	----	----	----	----	----	----	----	----	----	----	----	----	----	----	----	----	----	----	----	----	----	----	----	----	----	----	----	----	----	----	----	----	----	----	----	----	-----

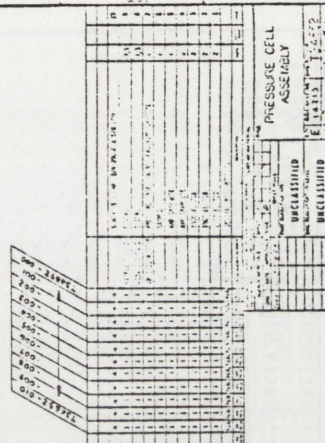


1	2	3	4	5	6	7	8	9	10	11	12	13	14	15	16	17	18	19	20	21	22	23	24	25	26	27	28	29	30	31	32	33	34	35	36	37	38	39	40	41	42	43	44	45	46	47	48	49	50	51	52	53	54	55	56	57	58	59	60	61	62	63	64	65	66	67	68	69	70	71	72	73	74	75	76	77	78	79	80	81	82	83	84	85	86	87	88	89	90	91	92	93	94	95	96	97	98	99	100
---	---	---	---	---	---	---	---	---	----	----	----	----	----	----	----	----	----	----	----	----	----	----	----	----	----	----	----	----	----	----	----	----	----	----	----	----	----	----	----	----	----	----	----	----	----	----	----	----	----	----	----	----	----	----	----	----	----	----	----	----	----	----	----	----	----	----	----	----	----	----	----	----	----	----	----	----	----	----	----	----	----	----	----	----	----	----	----	----	----	----	----	----	----	----	----	----	----	----	-----

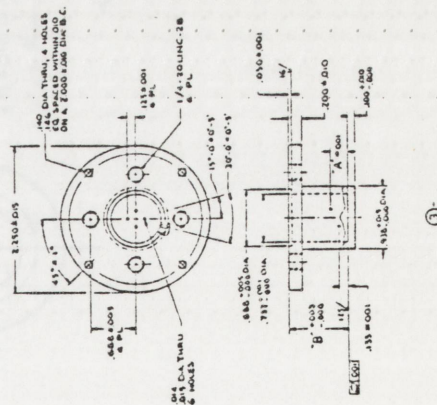
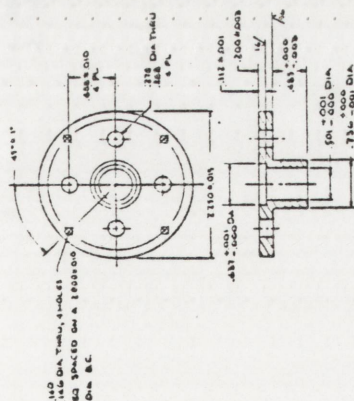
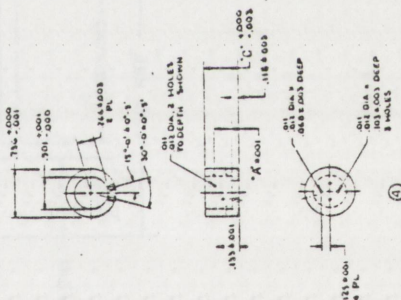
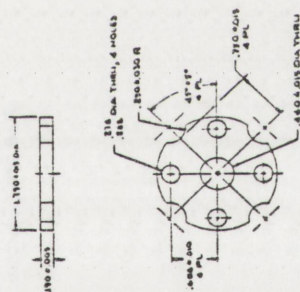
[illegible]

166

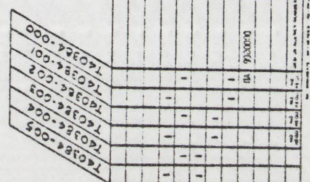
1. PARTS NOTED BY DR. S. J. J.
2. PARTS NOTED BY DR. S. J. J.
3. PARTS NOTED BY DR. S. J. J.
4. PARTS NOTED BY DR. S. J. J.



PART NO.	A	B	C	D	E	F	G	H	I	J	K	L	M	N	O	P	Q	R	S	T	U	V	W	X	Y	Z	
1234567890	1	2	3	4	5	6	7	8	9	10	11	12	13	14	15	16	17	18	19	20	21	22	23	24	25	26	27
2345678901	2	3	4	5	6	7	8	9	10	11	12	13	14	15	16	17	18	19	20	21	22	23	24	25	26	27	28
3456789012	3	4	5	6	7	8	9	10	11	12	13	14	15	16	17	18	19	20	21	22	23	24	25	26	27	28	29
4567890123	4	5	6	7	8	9	10	11	12	13	14	15	16	17	18	19	20	21	22	23	24	25	26	27	28	29	30
5678901234	5	6	7	8	9	10	11	12	13	14	15	16	17	18	19	20	21	22	23	24	25	26	27	28	29	30	31
6789012345	6	7	8	9	10	11	12	13	14	15	16	17	18	19	20	21	22	23	24	25	26	27	28	29	30	31	32
7890123456	7	8	9	10	11	12	13	14	15	16	17	18	19	20	21	22	23	24	25	26	27	28	29	30	31	32	33
8901234567	8	9	10	11	12	13	14	15	16	17	18	19	20	21	22	23	24	25	26	27	28	29	30	31	32	33	34
9012345678	9	10	11	12	13	14	15	16	17	18	19	20	21	22	23	24	25	26	27	28	29	30	31	32	33	34	35
0123456789	10	11	12	13	14	15	16	17	18	19	20	21	22	23	24	25	26	27	28	29	30	31	32	33	34	35	36
1234567890	11	12	13	14	15	16	17	18	19	20	21	22	23	24	25	26	27	28	29	30	31	32	33	34	35	36	37
2345678901	12	13	14	15	16	17	18	19	20	21	22	23	24	25	26	27	28	29	30	31	32	33	34	35	36	37	38
3456789012	13	14	15	16	17	18	19	20	21	22	23	24	25	26	27	28	29	30	31	32	33	34	35	36	37	38	39
4567890123	14	15	16	17	18	19	20	21	22	23	24	25	26	27	28	29	30	31	32	33	34	35	36	37	38	39	40
5678901234	15	16	17	18	19	20	21	22	23	24	25	26	27	28	29	30	31	32	33	34	35	36	37	38	39	40	41
6789012345	16	17	18	19	20	21	22	23	24	25	26	27	28	29	30	31	32	33	34	35	36	37	38	39	40	41	42
7890123456	17	18	19	20	21	22	23	24	25	26	27	28	29	3													

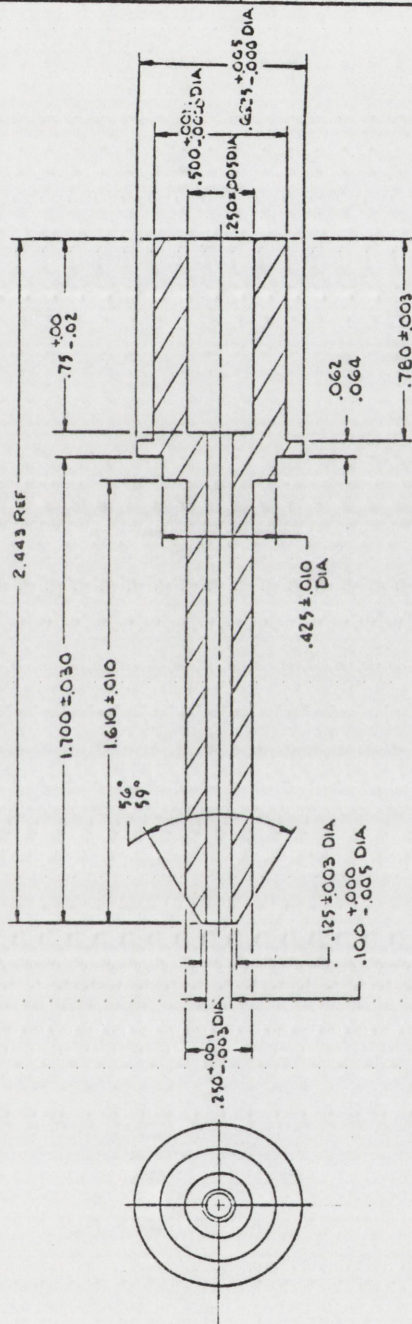


ADMISSIONS	BONUS	COMMISSION	PART NO.
710	.100	.1173	T40324-000
710	.115	.1173	T40324-001
723	.100	.1186	T40324-002
723	.115	.1186	T40324-003
740	.100	.1203	T40328-004
740	.115	.1203	T40328-005



DATE	12/12/12	TIME	14:21:15	DATE	12/12/12	TIME	14:21:15
EEO5 INSTRUMENTED DUMMY TRANSDUCER				140384			
UNCLASSIFIED (When Classification Exp.)				UNCLASSIFIED			
TITLE				EEO5 INSTRUMENTED DUMMY TRANSDUCER			

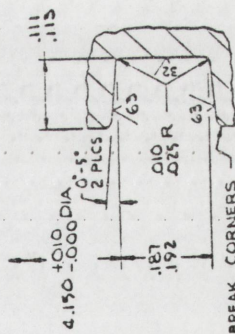
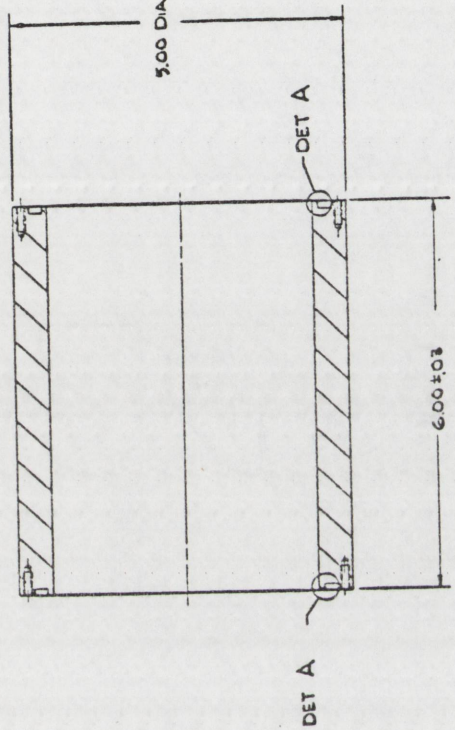
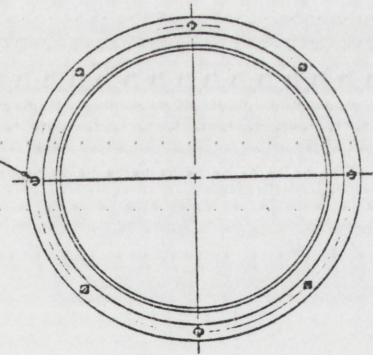
1. GENERAL REQUIREMENTS PER 9900000.
2. MATERIAL: INCONEL X-750 BAR.



EPOS PRESSURE CELL TEST FIXTURE	
UNCLASSIFIED	UNCLASSIFIED
14213	T36049

1. GENERAL REQUIREMENT PER 9900000.
2. MATERIAL - ALUMINUM TUBING 5000 0.0

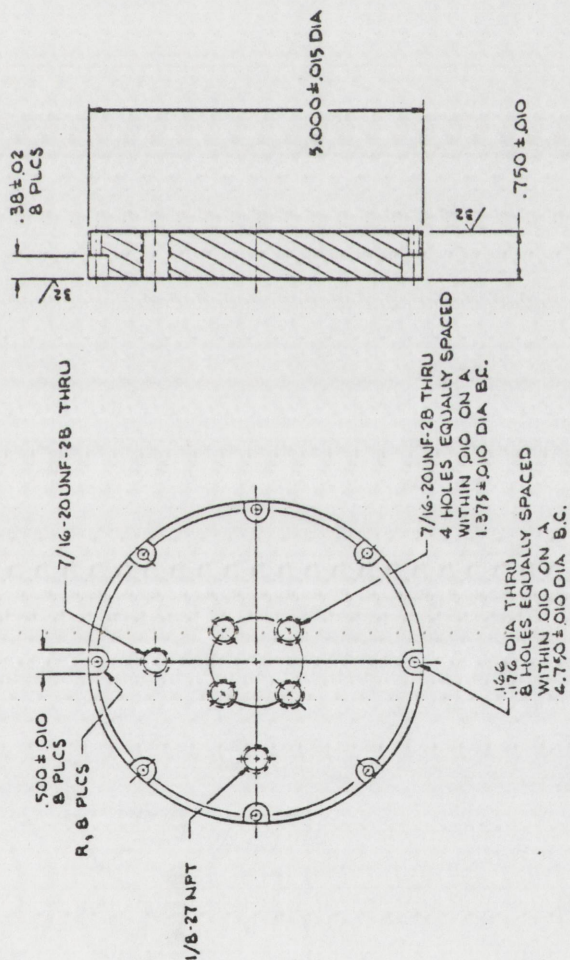
6-32 UNC-2B X .37 ± 0.06 DEEP
8 HOLES EQUALLY SPACED
WITHIN .010 ON A 4.750 ± 0.010
DIA B.C., EACH END



BREAK CORNERS
APPROX .005 R
2 PLCS
DET A
SCALE - NONE

PROJECT APPROVED		DATE		BY		TITLE	
222		22 12		T T		UNCLASSIFIED	
UNCLASSIFIED		UNCLASSIFIED		UNCLASSIFIED		UNCLASSIFIED	
CASE		T36550-000		A		A	
EEO'S PICTURE		14213		T36550		T36550	

1. GENERAL REQUIREMENTS PER 9900000.
2. MATERIAL - LUCITE PLATE .75 THICK.

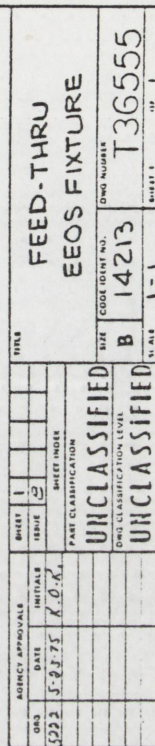


PART APPROVALS		DESIGN		DRAWING		CHECK		DATE		BY		DATE		BY	
DATE		DATE		DATE		DATE		DATE		DATE		DATE		DATE	
UNCLASSIFIED		UNCLASSIFIED		UNCLASSIFIED		UNCLASSIFIED		UNCLASSIFIED		UNCLASSIFIED		UNCLASSIFIED		UNCLASSIFIED	
TOP		ELOS FIXTURE		C 14213		T36551		1		1		1		1	

- [illegible]



- | OFFICE ATTACHE
PASSPORT CONTROL NO. | REFERENCE | | | | | |
|--|-----------|---|-------------|---------|------|--------|
| | ITEM | DESCRIPTION | PREPARED BY | DATE | CHRG | AMOUNT |
| T36555-000 | A | ROACH 9652/REIL 5222 | | 6-5-75 | | |
| | B | ADDED 1/6 FINISH MAKE
REIL, 5222; 5 BEECEE, 9652 | | 6-28-76 | | |



APPENDIX C

DESCRIPTIONS OF COMMERCIAL PRESSURE CELL COMPONENTS

"C"-SEALS

The metallic "C"-seals used in these experiments were manufactured by Pressure Science Incorporated, Beltsville, Maryland, 20705. The smaller seal, associated with the pressure transducer, was nickel plated (PN 612X55-0008). The larger seal, associated with the Inconel insert, was silver plated (PN 612R51-0012-2).

THERMOCOUPLES

The thermocouples used in these were manufactured by Omega Engineering, Inc., Stamford, Connecticut, 06907. They were Chromel-Alumel thermocouples sheathed with Inconel 600. The sheath diameter was 0.010 in. and the individual wires were 0.0015 in. diameter. Both grounded junctions (PN SCAIN-010G-6-RR) and exposed junctions (PN SCAIN-010E-6-RP) were used.

STRAIN GAGES

The strain gages used in these experiments were a "T"-rosette type (PN FAET-12D-12S6ET) manufactured by BLH Electronics, Walham, Massachusetts, 02154.

ADHESIVES

Two types of adhesive were used to bond strain gages and the graphite buffer disc. For experiments through EEOS-UO2-1, Eastman-910 cement with catalyst was used. In subsequent experiments, EPY-550 filled epoxy was used. Both were obtained from BLH Electronics, Walham, Massachusetts, 02154.

KAMAN PRESSURE TRANSDUCER

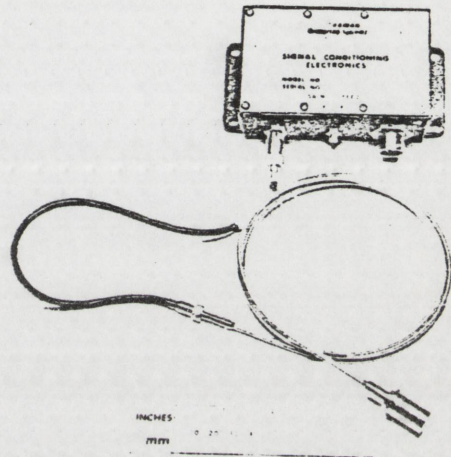
The pressure transducers used in these experiments were manufactured by Kaman Sciences Corporation, Colorado Springs, Colorado. The transducers were model numbers KP-1911-A5000P-CO5 and KP-1911-A5000P-C1.23. The difference in the two models is the length of the metallic sheathed cable. The manufacturer's description of the transducer is given on the following pages.

HIGH TEMPERATURE PRESSURE MEASURING SYSTEMS

KP-1910 SERIES

FEATURES

- COMPLETE SYSTEM: Sensor, Cabling and Electronics.
- SENSOR OPERATES TO OVER 540°C (1000°F)
- STATIC TO HIGH FREQUENCY RESPONSE
- EXCELLENT RESOLUTION and LINEARITY
- SMALL TOTAL ERROR BAND
- HERMETIC CORROSION RESISTANT DESIGN



DESCRIPTION

KAMAN'S KP-1910 SERIES PRESSURE MEASURING SYSTEM is a fully integrated transducer system consisting of sensor, cabling, and signal conditioning electronics. The output voltage is proportional to the applied static and dynamic pressure. The system is available with absolute calibration as a standard model. Gage and differential systems are optional as are special pressure and acoustical ranges.

The sensor and cabling are constructed to operate reliably to over 540°C (1000°F) and they can be submersed in the media. Mounting can be accomplished mechanically or by welding to optional adapters. Inside, the sensor has active and reference sensing elements to compensate for extraneous quasi-steady state effects such as temperature and radiation. The optional differential pressure model has a tube exiting from the rear of the sensor for supplying a gaseous reference pressure; whereas, the gage pressure sensor has a vent for atmospheric reference.

The single cable between sensor and electronics has two sections: the high temperature metallic sheathed cable plus a short, flexible section. The transition connector is designed to be rugged and to simplify bulkhead penetrations as well as being suitable for panel mounting. The metallic sheathed cable is available in incremental lengths up to 12 meters (40 feet).

The signal conditioning electronics is solid state consisting of an oscillator-demodulator that is used to excite the sensor and demodulate the return signal. Adjustment of "zero" and "gain" is provided. The sensing portion of the system should be considered as a discrete unit that consists of a sensor, the cabling and a small circuit card within the electronics housing. These discrete sensing units are interchangeable with other oscillator-demodulators.

TYPICAL APPLICATIONS

Measuring pressure continuously from -75°C (-100°F) to 540°C (1000°F) without cooling is routine for the KP-1910 Series Pressure Measuring Systems.

EQUIPMENT	PROCESS
Steam and Gas Turbines	Chemical
Jet and Rocket Engines	Plastic
Reactors: Liquid metal, Water and Gas Coolant Loops (Can be fabricated to U.S. AEC Reactor Development Technology Standards).	Petrochemical
Laboratory	Rubber
	Steam (KP-1912)
	Pressurized Water (KP-1912)
	Liquid Metals
	Combustion

The standard (Model KP-1911) is compatible with most media including liquid sodium, plastics, petroleum products, and most other gases and liquids. The sensor is alloy 718 (AMS 5662) and the cable is alloy 600 (AMS 5580). The Model KP-1912 is especially designed for usage in water and steam environments. The sensor is alloy 625 (AMS 5666) and the cable is alloy 600 (AMS 5580).

OPERATING PRINCIPLE

The measuring system utilizes a principle of impedance variation which is caused by eddy currents induced in the conductive diaphragm. The electromagnetic coupling between the coil and the diaphragm is dependent upon their common separation distance which is proportional to pressure on the diaphragm. In the functional system, a pair of coils is used in a patented manner such that temperature and radiation effects are essentially cancelled.

The cabling is used to transmit the signal to and from the sensor while withstanding the thermal gradient between sensor and electronics. The associated signal conditioning consists of an oscillator, amplifiers, and a demodulator that provides an analog output signal directly proportional to pressure.

SPECIFICATIONS *

	KP-1911	KP-1912
MATERIAL SENSOR METAL SHEATHED CABLE	Alloy 718 (AMS 5662) Alloy 600 (AMS 5580)	Alloy 625 (AMS 5666) Alloy 600 (AMS 5580)
PRESSURE PRESSURE RANGES, FULL SCALE (See Table II) Absolute Gage (Optional)** Differential - 1000 psi max. working press. (Optional)** PROOF PRESSURE (Short term at operating temperature)	5 to 5000 psi 5 to 5000 psi ±5 to ±1000 psi 150% for 5 to 500 psi FS 110% above 500 psi FS	5 to 1000 psi 5 to 1000 psi ±5 to ±1000 psi 150% for 5 to 100 psi FS 110% above 100 psi FS CONTACT KAMAN for HIGHER RANGES
TEMPERATURE OPERATING TEMPERATURE RANGE Sensor and Metal Sheathed Cable Connector on Metal Sheathed Cable Soft Cable and Connector Electronics CALIBRATED TEMPERATURES Sensor: Standard Optional SURVIVAL TEMPERATURE RANGE Sensor and Metal Sheathed Cable STORAGE TEMPERATURE Sensor and Metal Sheathed Cable Connector on Metal Sheathed Cable Soft Cable and Connector Electronics RATE OF TEMPERATURE CHANGE FOR SURVIVAL Sensor RATE OF TEMP. CHANGE for SPECIFIED THERMAL ZERO or SENSITIVITY SHIFTS Sensor THERMAL ZERO SHIFT (25°C o max. operating temp.) Sensor Electronics THERMAL SENSITIVITY SHIFT Sensor Electronics	-75°C to 540°C (-100°F to 1000°F) -75°C to 150°C (-100°F to 300°F) -55°C to 105°C (-67°F to 220°F) 0°C to 55°C (32°F to 132°F) 25°C (77°F) 25°C, 270°C & 540°C (77°F, 500°F & 1000°F) or to customer's requirements with computer analysis of calibration data -196°C to 650°C (Short term) -75°C to 540°C (-100°F to 1000°F) -75°C to 150°C (-100°F to 300°F) -55°C to 105°C (-67°F to 220°F) -55°C to 105°C (-67°F to 220°F) 900°C/sec (1652°F/sec) max 0.5°C/sec (0.9°F/sec) max Less than ± 0.02% FSO/°C Less than ± 0.04% FSO/°C Less than ± 0.02%/°C Less than ± 0.04%/°C	-75°C to 540°C (-100°F to 1000°F) -75°C to 150°C (-100°F to 300°F) -55°C to 105°C (-67°F to 220°F) 0°C to 55°C (32°F to 132°F) 25°C (77°F) 25°C, 270°C & 540°C (77°F, 500°F & 1000°F) or to customer's requirements with computer analysis of calibration data -196°C to 650°C (Short term) -75°C to 540°C (-100°F to 1000°F) -75°C to 150°C (-100°F to 300°F) -55°C to 105°C (-67°F to 220°F) -55°C to 105°C (-67°F to 220°F) 900°C/sec (1652°F/sec) max 0.5°C/sec (0.9°F/sec) max Less than ± 0.02% FSO/°C Less than ± 0.04% FSO/°C Less than ± 0.02%/°C Less than ± 0.04%/°C
SYSTEM PERFORMANCE FREQUENCY RESPONSE Sensor (Pressure range dependent) Electronics: Standard Optional LINEARITY, Least Squares REPEATABILITY @ 25°C (77°F) HYSTERESIS @ 25°C (77°F) THRESHOLD OUTPUT NOISE @ Standard Output Voltage OUTPUT VOLTAGE, ANALOG Standard: Absolute and Gage Differential Optional: Absolute and Gage Differential All OUTPUT IMPEDANCE OUTPUT CURRENT (Short circuit protected)	See Table II Zero to 10 kHz (-3dB point) Zero to 50 kHz (-3dB point) Within ± 1% FSO Within 0.1% FSO typical 0.5% FSO typical Less than 0.15% FS Pressure Less than 0.5 mV rms 0 to 1 Vdc -1 to 1 Vdc 0 to 2, 0 to 5 or 0 to 10 Vdc -2 to 2 or -5 to 5 Vdc Up to 19 V between -9 to 10 Vdc 5 Ohms max 15 mA max	See Table II Zero to 10 kHz (-3dB point) Zero to 50 kHz (-3dB point) Within ± 1% FSO Within 0.1% FSO typical 0.5% FSO typical Less than 0.15% FS Pressure Less than 0.5 mV rms 0 to 1 Vdc -1 to 1 Vdc 0 to 2, 0 to 5 or 0 to 10 Vdc -2 to 2 or -5 to 5 Vdc Up to 19 V between -9 to 10 Vdc 5 Ohms max 15 mA max
POWER SUPPLY REQUIREMENTS*** VOLTAGE VOLTAGE REGULATION CURRENT	Plus and minus 15 Vdc ± 1/2 Vdc 55 mA typical	Plus and minus 15 Vdc ± 1/2 Vdc 55 mA typical

* In accordance with the Instrument Society of America standard no. ISA S37.1, dated 1969. FSO = Full Scale Output.

** The reference pressure media for the sensor is recommended to be clean air or inert gas with less than 5% relative humidity.

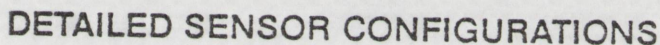
*** See Options for KAMAN Power Supply.

TABLE I PRESSURE CONVERSION FACTORS

	(A) atm	(D) dyne/cm ²	(I) in. of water	(C) cm of Hg	(K) kgf/m ²	(N) N/m ²	(P) psi	(F) lb/ft ²	(B) bars
1 atmosphere	1	1.013x10 ⁶	408.8	76.00	1.033x10 ⁵	1.013x10 ⁵	14.70	2116	1.013
1 dyne/cm ²	9.869x10 ⁻⁷	1	4.015x10 ⁻⁵	7.501x10 ⁻⁵	1.020x10 ⁻⁵	0.1	1.450x10 ⁻⁵	2.089x10 ⁻⁵	10 ⁻⁷
1 inch of water at 4° C	2.458x10 ⁻²	2491	1	0.1868	25.40	249.1	3.613x10 ⁻²	5.202	2.491x10 ⁻²
1 cm of mercury at 0° C	1.316x10 ⁻¹	1.333x10 ⁵	5.353	1	135.9	1333	0.1934	27.86	1.333x10 ⁻¹
1 kilogram-force per m ²	9.678x10 ⁻³	98.07	3.937x10 ⁻²	7.356x10 ⁻²	1	9.807	1.422x10 ⁻²	0.2048	9.804x10 ⁻³
1 newton per m ² (1 pascal)	9.869x10 ⁻⁷	10	4.015x10 ⁻⁵	7.501x10 ⁻⁵	0.1020	1	1.450x10 ⁻⁵	2.089x10 ⁻⁵	10 ⁻⁷
1 lb per in. ²	6.803x10 ⁻²	6.895x10 ⁴	27.68	5.171	7.031x10 ³	6.895x10 ³	1	144	6.897x10 ⁻²
1 lb per ft ²	4.725x10 ⁻³	478.8	0.1922	3.591x10 ⁻²	4.882	47.88	6.944x10 ⁻³	1	4.787x10 ⁻³
1 bar	0.9869	10 ⁶	401.5	75.01	1.020x10 ⁵	10 ⁵	14.50	2.089x10 ³	1

EXAMPLE: 1 Atmosphere = 1.013 x 10⁶ Dynes/cm²

DIMENSIONS ARE MAXIMUM LIMIT IN INCHES (MILLIMETERS)



DIMENSIONS ARE MAXIMUM LIMIT IN INCHES (MILLIMETERS)

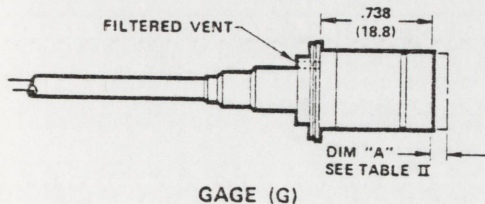
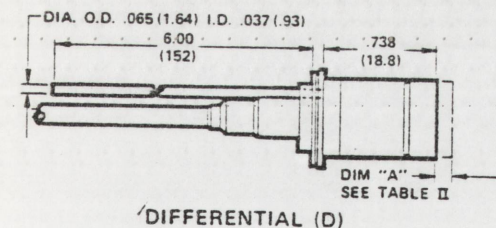
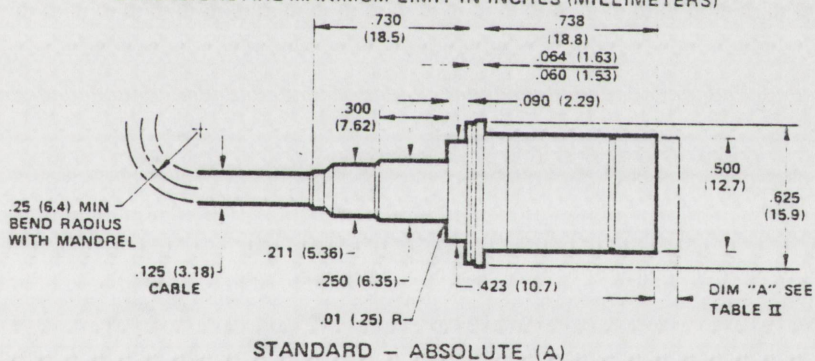
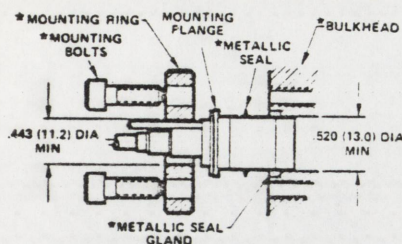


TABLE II
PRESSURE RANGE VS DIMENSION "A"
AND FREQUENCY RESPONSE

STANDARD PULL SCALE PRESSURE RANGE	DIMENSION "A"				AVERAGE FREQUENCY RESPONSE PER 1/2 25°C TO 540°C	
	KP-1911		KP-1912		KP-1911	KP-1912
	NOTES	WELL-TEMPERATURE	NOTES	WELL-TEMPERATURE		
5	.003	.076	.003	.076	1460	1340
10	.004	.102	.004	.102	2100	1910
20	.005	.127	.005	.127	2870	2680
50	.007	.178	.007	.178	4350	4160
100	.009	.229	.008	.203	5860	5800
200	.011	.279	.012	.305	8330	8940
500	.015	.381	.018	.457	12770	16550
1000	.019	.483	.026	.660	16280	25114
2000	.026	.660	HIGHER RANGES SPECIALLY DESIGNED UPON REQUEST		26200	
3000	.032	.813			34900	
5000	.042	1.067			45990	

SUGGESTED MOUNTING

DIMENSIONS ARE MAXIMUM LIMIT IN INCHES (MILLIMETERS)



STANDARD MOUNTING (SM)

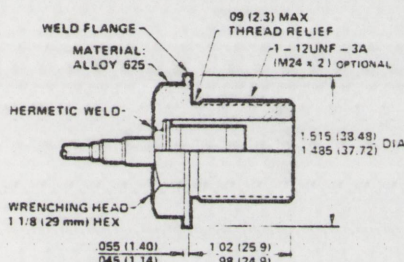
* SUPPLIED BY CUSTOMER

STANDARD SENSOR MOUNTING CONSIDERATIONS

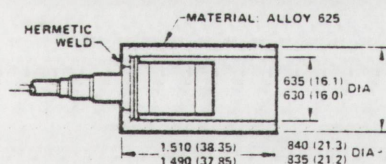
The design factors affecting the selection of the mounting components are temperature, pressure, and compatibility with the pressure media. Dimensions and surface finishes should be in accordance with the recommendations of the seal manufacturer. Names of the possible suppliers of metallic seals can be furnished upon request.

SENSOR MOUNTING OPTIONS

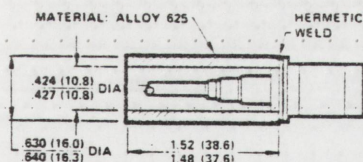
DIMENSIONS ARE MAXIMUM LIMIT IN INCHES (MILLIMETERS)



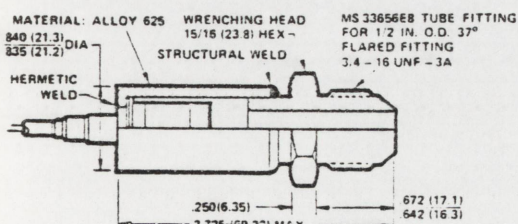
THREADED MOUNTING (TM)



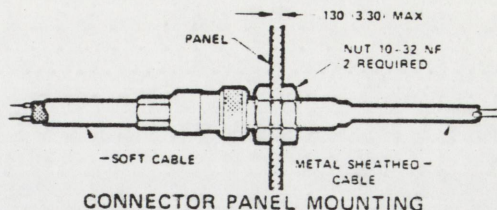
FORWARD WELD MOUNTING (FW)



REAR WELD MOUNTING (RW)



TUBE FITTING MOUNTING (TF)



CONNECTOR PANEL MOUNTING

OPTIONS

Non-Standard pressure ranges between limits shown in Table II. Calibrated temperatures (see specifications). Computer analysis of calibration data is supplied.

Convert calibration data from psi to other units from Table I. Sensor Mounting Options.

Increased length of High Temperature Metal Sheathed Cable up to 40 feet maximum (see Model Number Index Key).

Increased length of Soft Cable up to 30 feet maximum.

Maximum length of all cable is 42 feet.

Change bandwidth of electronics (affects output noise).

Increase output voltage (see specifications).

Change "zero" voltage point to any specified static pressure.

Synchronization of electronics to prevent system "cross talk".

Power Supply P-3200 or P-3300 with digital readout, to provide regulated + and -15 Vdc output for up to 6 systems.

Standard input voltage is 120Vac. If 240Vac is required add suffix A (e.g. P-3200A). Specification sheets are available.

Power and output cable: 10 feet (part no. 850874-010).

Material Certification Documentation.

U.S. AEC Reactor Development Technology standard C-6-3T.

Improved specifications may be attainable depending upon exact environmental conditions (i.e. lower operating temperature, narrower calibrated temperature band, etc.).

Available on other Kaman Pressure Measuring Systems:

Bench, Rack Mounted, or Aerospace electronics.

Soft Cable lengths up to 1000 feet between sensor and electronics.

ORDERING INFORMATION

Specify by model number and desired option.

MODEL NUMBER INDEX KEY

KP-19XX-XXXX-XX-CXX	
KAMAN	METAL SHEATHED CABLE LENGTH
PRESSURE	05 = 5 ft = 1.524 m
HIGH TEMPERATURE	10 = 10 ft = 3.048 m
SENSOR MATERIAL	15 = 15 ft = 4.572 m
11 = Alloy 718	20 = 20 ft = 6.096 m
12 = Alloy 625	30 = 30 ft = 9.144 m
TYPE OF SENSOR	40 = 40 ft = 12.190 m
A = ABSOLUTE*	
D = DIFFERENTIAL	
G = GAGE	
PRESSURE RANGE	
05 = 5	
10 = 10	
200 = 200	
etc.	
See Table II for standard ranges.	
PRESSURE UNIT	
P = psi*	
	* Denotes Standard Product
	MOUNTING CONFIGURATION
	SM = STANDARD MOUNT*
	FW = FORWARD WELD
	RW = REAR WELD
	TF = TUBE FITTING
	TM = THREADED MOUNT
	CS = CUSTOMER SPECIAL
	(Attach details with inquiry)

All specifications are subject to change without notice.



KAMAN SCIENCES CORPORATION
A KAMAN COMPANY

1500 Garden of the Gods Rd. • Telephone (303) 598-5880 • Telex 452412

Mailing Address: P. O. Box 7463 • Colorado Springs, Colorado 80933

Printed in the U.S.A.

APPENDIX D

DETAILED EXPERIMENT PROCEDURES

The following procedures were used for the preparation of each experiment. The components of the pressure cell were chemically cleaned of oil and grease. The pressure cell was assembled, and the thermocouples were inserted through the Inconel cup and into the appropriate holes in the graphite crucible. Soft silver solder was used to seal the thermocouples to the Inconel cup by heating the pressure cell on a hot plate. In experiments with fewer than six thermocouples, unused holes were sealed over with silver solder. The pressure cells were cleaned with water and dried in an oven.

Strain gages were attached to the outside cylindrical portion of the pressure cell between thermocouple locations using high temperature epoxy adhesive according to the manufacturer's instructions. Gages for the unstrained portion of the strain bridge were bonded to stainless steel shim stock. After heat curing of the epoxy, four-conductor 36-gauge ribbon cable was used to connect the strain gages to the terminal board. Leads were soldered to the active and passive gages. The pressure cell was then placed on the four support rods of the bottom lid and loosely attached with nuts. The shim stock holding the passive strain gage was cantilevered from one of the support rods with tape. Thermocouple and strain gage leads were soldered to the terminal board on the bottom lid. Strain relief was provided for

the thermocouples by means of a clamp to the terminal board and by taping to the support rods. The strain gage leads were taped to the pressure cell, shim stock, and support rods. The installation was checked by measuring the resistance of leads to each other and to the pressure cell.

The nuts were then removed from the support rods, and the Inconel insert portion of the pressure cell was removed. The sealing surfaces were cleaned with alcohol and dried. The metallic "C-seal" was installed between the Inconel cup and insert, and the nuts on the four support rods were securely tightened.

For experiments containing instrumented dummy transducers, the thermocouples were inserted through the Inconel plug and into appropriate holes in the graphite disc. The graphite and thermocouples were sealed to the plug with the same high temperature epoxy that was used for the strain gages. After curing, excess cement was removed from the edges with a fine file. The thermocouple leads were then soldered to the upper terminal board.

Preparation of Kaman transducers involved honing the welds in the transducer body down to less than .501" diameter to permit its assembly into the pressure cell insert. The graphite buffer disc was bonded using the same techniques described for the instrumented dummy transducer.

The pressure cell was attached to a pressure system by means of a test fixture which took the place of a pressure transducer. (See drawing in Appendix B.) The modified pressure transducer, if used, was installed in the same pressure system. The output

voltages from the strain bridge amplifier (gain = x100), and from the pressure transducer were calibrated against a pressure gage from 0 psig to 1900 psig. The pressure transducers were subsequently calibrated to at least 5000 psig by the Sandia Transducer Laboratory. Least squares fits of pressure as a function of output voltages were performed. The resulting equations were used in the subsequent processing of the experimental data via the Sandia DADS system to convert strain voltage and transducer voltage to pressure.

For experiments containing fuel samples, the sealing surfaces of the pressure cell and pressure transducer (or dummy transducer) were cleaned with alcohol and dried. The correct sample was removed from the safe, and placed in the pressure cell. Appropriate entries were made and witnessed in the "EEOS Fuel Log Book" to verify the sample used. The "C-seal," transducer (or dummy transducer), retaining plate, and four high strength cap screws were installed. The screws were not tightened but were left about two turns loose. A bracket and elastic band were attached to the transducer (or dummy transducer) to hold it off the "C-seal." The assembled pressure cell was then placed in the loading fixture (See drawings in Appendix B) with the wrench feed-throughs of the fixture engaging the four cap screws. The metallic cable of the pressure transducer, if present, was sealed through the upper lid of the loading fixture, as were the wrench feed-throughs, by means of O-ring seals. The loading fixture and, hence, the fueled region of the pressure cell were

purged of air by alternately evacuating and backfilling with dry helium. The fixture was evacuated to approximately 1×10^{-4} torr and the pressure cell was sealed by tightening the four cap screws via the wrench feed-throughs. The vacuum was monitored by means of a thermocouple vacuum gage in the upper lid of the loading fixture.

The sealed pressure cell was then removed from the loading fixture and installed in the inner containment. If a Kaman pressure transducer was used, the metallic sheathed cable was routed through seals in the upper lids of the inner and outer containers. If an instrumented dummy transducer was used, the cable from the upper lid of the inner container was attached to the upper terminal board. Eight socket head cap screws anchored the bottom lid and pressure cell to the inner container. This containment was purged of air by alternately evacuating and backfilling with dry helium. After being overpressured with helium to approximately 30 psig, the container was leak checked by immersing in denatured ethanol and observing for bubbles. After a successful leak test, the inner can was dried and evacuated, and its valve was closed and capped.

If used, a polyethylene moderator sleeve was installed over the inner can and fastened with two screws. The cable from the bottom lid of the inner can was connected, and the cable was taped to the outside of the polyethylene. This assembly was then placed in the outer container; additional polyethylene moderator, if used, was placed over the outer container, and the container

was sealed. The outer can was purged of air and leak tested as above. The helium pressure was bled down to atmospheric pressure, and the valve was closed and capped. Excess metallic sheathed cable from the pressure transducer was coiled above the outer lid and the end was attached to a strain relief bracket. The continuity of the instrumentation leads was again checked.

Each channel of the data acquisition system was functionally checked from the poolside console by means of a standard voltage source. The thermocouple reference junction temperature and strain gage supply battery voltage were checked. The cables were then attached and the experiment package was lowered into the reactor. The reactor upper reflector plug was lowered to 36 inches. Continuity of the instrumentation was again checked, and the appropriate cables were attached to the reference junctions, strain gage supply battery and zero bias circuit, and pressure transducer electronics. Each channel of instrumentation was checked by noting the signal at the input to the amplifiers in the data acquisition system and at the input to the tape recorder. Positive, negative, and zero calibration voltages were recorded on the FM tape recorder by disconnecting the signal inputs to the amplifiers and attaching the calibration signals. Calibration voltages were chosen to equal or slightly exceed the maximum anticipated data signal for each instrumentation channel. Amplifier gains were adjusted so that the input to the FM tape recorder was ± 0.5 volts when the calibration voltages were attached to the amplifier inputs.

After calibration the system was returned to its normal configuration to record the experimental data. A copy of the page of "EEOS Fuel Log Book" for the sample being irradiated which documented the loading of the sample and the performance of the leak tests was given to the ACPR operations personnel to certify the loading procedure. The experiment was irradiated in the desired ACPR transient while the instrumentation signals were recorded on the FM Analog tape recorder and on an oscillograph.

After irradiation, the experimental package was left in the ACPR loading tube for about 1 day to decay to acceptable levels. The experiment was then removed from the reactor and stored in the ACPR experiment handling area for an additional 1-4 days until the radiation levels at the surface of the container were 100-300 millirad/hour. The containment was disassembled in the reverse order of assembly by first purging with helium and evacuating with the vacuum exhaust vented into a fume exhaust hood. The sealed pressure cell was removed from the support rods and placed in a polyethylene bag. The containment and terminal board were cleaned with alcohol and acetone and stored in shielded areas for future experiments.

The fission energy deposition in the sample was determined by Lanthanum-140 fission product inventory techniques. (See Appendix E.) The pressure cell was not opened prior to counting to preclude any loss of material. After fission product inventory, the fuel was recovered by opening the pressure cell in a fume hood. The recorded signals were digitized and converted to

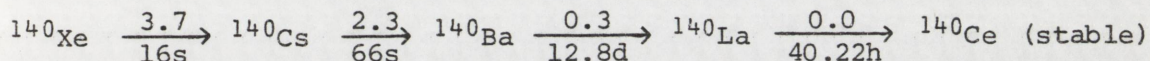
measured parameters (temperature, pressure, etc.) via the Sandia DADS, using the strain gage and pressure transducer calibrations determined above, published tables of thermocouple data, and reactor log power calibrations.

APPENDIX E

FISSION ENERGY DEPOSITION MEASUREMENT BY

^{140}Ba - ^{140}La FISSION PRODUCT INVENTORY ANALYSIS

The fission product decay chain of importance is



where, for example, the direct fission yield of ^{140}Cs is 2.3 percent (Co65) and its half-life is 66 seconds (Le68). A gamma-ray spectrometer can be used to determine the amount of ^{140}La and, hence, ^{140}Ba , in an irradiated sample containing uranium at any time t . Once the number of ^{140}Ba atoms is known for time $t = 0$, the fission energy released in pellet can be determined. This section outlines the ^{140}Ba - ^{140}La fission product inventory analysis utilized during these UO_2 EOS experiments.

Essentially all of the ^{140}Xe and ^{140}Cs will decay into ^{140}Ba within a very short time, compared with the ^{140}Ba half-life, after irradiation. Thus, it is assumed that the total fission yield (6.3 percent) of the decay chain is ^{140}Ba . (When the following derivation includes all isotopes of the decay chain, the energy deposition computed from that formulation differs by less than .01 percent from the results given here for samples counted more than 1 week after irradiation.) Thus, after several days a parent-daughter decay relationship between ^{140}Ba and ^{140}La is established. Solving the radioactive decay equations in the

usual manner gives

$$N_{\text{La}}(t) = \frac{\lambda_{\text{Ba}}}{\lambda_{\text{La}} - \lambda_{\text{Ba}}} N_{\text{Ba}}^0 \left(e^{-\lambda_{\text{Ba}} t} - e^{-\lambda_{\text{La}} t} \right) + N_{\text{La}}^0 e^{-\lambda_{\text{La}} t} \quad (1)$$

where $N_{\text{La}}(t)$ is the number of ^{140}La atoms as a function of time t ; after irradiation, N_{Ba}^0 and N_{La}^0 are the number of ^{140}Ba and ^{140}La atoms, respectively, at time $t = 0$, and λ_{Ba} and λ_{La} are the disintegration constants of ^{140}Ba and ^{140}La , respectively. As indicated by the decay chain, no direct fission yield of ^{140}La has been measured, so the second term in equation (1) is zero, giving

$$N_{\text{La}}(t) = \frac{\lambda_{\text{Ba}}}{\lambda_{\text{La}} - \lambda_{\text{Ba}}} N_{\text{Ba}}^0 \left(e^{-\lambda_{\text{Ba}} t} - e^{-\lambda_{\text{La}} t} \right) \quad (2)$$

The activity of the lanthanum at any time t is

$$A_{\text{La}}(t) = \lambda_{\text{La}} N_{\text{La}}(t) \quad (3)$$

At time $t = 0$, the barium activity is given by

$$A_{\text{Ba}}^0 = \lambda_{\text{Ba}} N_{\text{Ba}}^0 \quad (4)$$

Substituting equations (2) and (4) into (3) and rearranging terms yields

$$A_{\text{La}}(t) = \frac{A_{\text{Ba}}^0 e^{-\lambda_{\text{Ba}} t}}{1 - \frac{\lambda_{\text{Ba}}}{\lambda_{\text{La}}}} \left[1 - e^{(\lambda_{\text{Ba}} - \lambda_{\text{La}})t} \right] \quad (5)$$

Rewriting equation (5) gives

$$A_{Ba}^0 = \lambda_{Ba} N_{Ba}^0 = A_{La}(t) \left(1 - \frac{\lambda_{Ba}}{\lambda_{La}}\right) e^{\lambda_{Ba} t} / \left(1 - e^{(\lambda_{Ba} - \lambda_{La})t}\right) \quad (6)$$

and

$$N_{Ba}^0 = \frac{A_{La}(t) \left(1 - \frac{\lambda_{Ba}}{\lambda_{La}}\right) e^{\lambda_{Ba} t}}{\lambda_{Ba} \left(1 - e^{(\lambda_{Ba} - \lambda_{La})t}\right)} \quad (7)$$

The decay constants for lanthanum and barium are 0.41361 and 0.054152 days⁻¹, respectively. Substituting these values into equation (7) yields

$$N_{Ba}^0 = A_{La}(t) \times (2.311 \times 10^4) \frac{e^{0.054152t}}{1 - e^{-0.35946t}} \quad (8)$$

where $A_{La}(t)$ is disintegrations per minute and t equals the time in days after irradiation.

The absolute disintegration rate $A_{La}(t)$ is given by (He64)

$$A_{La}(t) = \frac{N_P}{T(E) P d} \quad (9)$$

where N_P is the total number of gamma rays per minute recorded in the photopeak, $T(E)$ is the total absolute detection efficiency for the source-detector geometry used, P is the peak-to-total ratio as defined by Heath (He64) and d is the probability of decay for the gamma ray being counted. The ^{140}La 1.598 MeV

gamma ray was detected by a 3" x 3" NaI crystal, implying that $P = 0.312 \pm .003$ (He64). Probability of decay d by the measured mode is 0.960 (Le68). Substituting these values and equation (9) into equation (8) gives

$$N_{Ba}^O = \frac{N_P}{T(E)} \times (7.716 \times 10^4) \frac{e^{0.054152t}}{1 - e^{-0.35946t}} \quad (10)$$

Since the cumulative fission yield of ^{140}Ba is 6.3 percent and there are 6.62×10^{-12} calories per fission (Di61) retained in the UO_2 , the energy E deposited in a UO_2 pellet weighing W_t grams is

$$E = \frac{N_{Ba}^O}{W_t} \times \frac{6.62 \times 10^{-12}}{0.063} \frac{\text{calories}}{\text{gram}} \quad (11)$$

and using equation (10) yields

$$E = \frac{N_P}{W_t T(E)} \times (8.108 \times 10^{-6}) \frac{e^{0.054152t}}{1 - e^{-0.35946t}} \quad (12)$$

The area under the photopeak N_P was determined by an automated numerical integration of the gamma ray spectrum. The photopeak was defined by the linear extrapolation of its slopes on each side from its half maximum to zero and including the area bounded by those extrapolations and the measured peak. The samples were counted for sufficient time to yield at least 10^5 counts in the photopeak. Thus, the uncertainties due to the

statistical nature of radioactive decay were less than .03 percent. However, other uncertainties exist because of the method of integration and errors in measuring the source-to-detector distance upon which $T(E)$ depends. To determine the uncertainty in $N_p/T(E)$, a Co-60 standard source was counted using the same techniques as were used for the fuel samples. The results of a large number (~50) of such measurements yielded measured activities within ± 3.7 percent of known sample activity. This value was assigned to the uncertainty in $N_p/T(E)$.

The uncertainties in the other terms in equations (7), (9), and (11) are shown in Table E-1. These values were obtained either from literature sources or estimated for measured parameters (t and Wt). For values of t greater than 10 days, the uncertainties in the values of the two exponential terms are found to be .4 percent for the numerator and .01 percent for the denominator. Since all terms then appear in products or quotients, the net fractional error in E derived from equation (12) is the square root of the sum of the squares of the uncertainties in the various terms. Using the values shown in Table E-1, along with those derived above, we find that the probable error in E from equation (12) is ± 4.0 percent.

TABLE E-1

Summary of Errors Associated With Fission Product Inventory

Parameter	Nominal Value	Uncertainty	Fractional Error
$T_{1/2\text{Ba}} (\lambda_{\text{Ba}})$	12.8 days	.1 days	.8 %
$T_{1/2\text{La}} (\lambda_{\text{La}})$	40.22 hours	.02 hours	.04 %
t	10 days	5 min.	.03 %
P	.312	.003	.1 %
d	.960	.001	.1 %
Yield	.063	.0005	.8 %
wt	.99 grams	10 μg	.001 %
$N_{\text{P}}/T(\text{E})$	10^4 counts/min.	---	3.7 %

APPENDIX F

DIGITAL FILTERING TECHNIQUE

Low pass digital filtering techniques described by Stearns (St75) were used to eliminate high frequency noise from the digitized experimental data. The digital filter employed is described in this section.

The recursive algorithm (St75) for a digital filter states that the output of a digital filter at time step (m) can be described as a weighted sum of past and future input samples and past output samples. That is

$$g_m = \sum_{n=-N}^N b_n f_{m-n} - \sum_{n=1}^N a_n g_{m-n} \quad (1)$$

or

$$\sum_{n=0}^N a_n g_{m-n} = \sum_{n=-N}^N b_n f_{m-n} \quad (2)$$

where $a_0 \equiv 1$

(f_n) is the input data set

(g_n) is the output data set.

The properties of the filter transfer function are determined by the weighting coefficients (a_n) and (b_n) .

The low pass filter used for the data in these experiments was based on an analog Butterworth filter design. The power gain function for a Butterworth low pass filter is shown in Figure F-1.

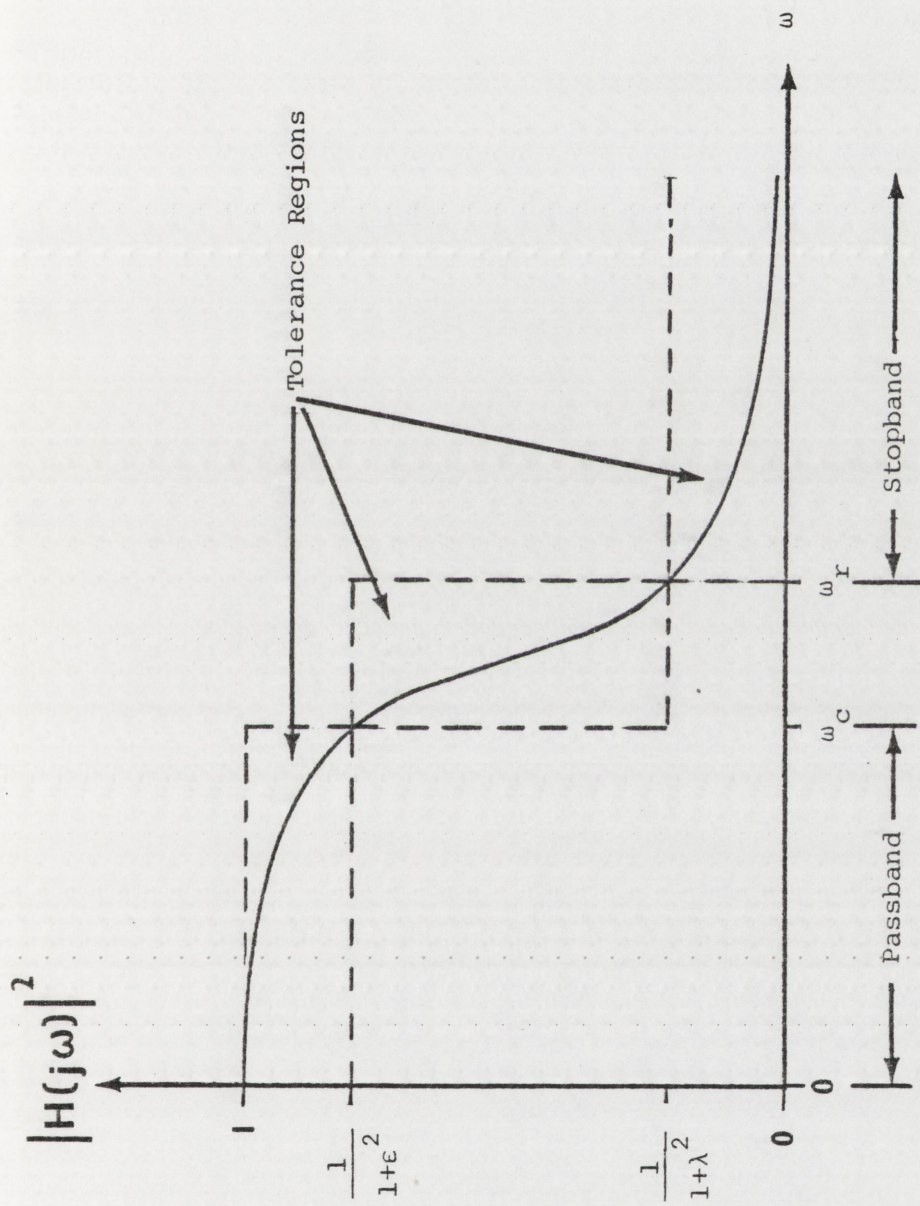


Figure F-1
Butterworth Filter Power Gain Characteristics

The most efficient filter design is obtained by the cascade of a number of filter elements as shown in Figure F-2. The output of one filter section becomes the input for the next. The more stages in the filter, the steeper the power gain function becomes; i.e., the sharper the filter cutoff.

It can be shown for a Butterworth that if f_m^n and g_m^n are the input and output of the n^{th} filter section at time $m\Delta T$ (where ΔT is the time step), then:

$$g_m^n = A_n (f_m^n + 2f_{m-1}^n + f_{m-2}^n) - B_n g_{m-1}^n - C_n g_{m-2}^n$$

where:

$$A_n = R^2/X$$

$$B_n = 2(1 - R^2)/X$$

$$C_n = (1 + R^2 + 2R \cos \theta_n)/X$$

$$X = 1 + R^2 - 2R \cos \theta_n$$

$$R = \omega_c^1 \epsilon^{-\frac{1}{2}N_s}$$

$$\theta_n = \left[2(n + N_s) - 1 \right] \pi / 4N_s$$

$$\omega_c^1 = \tan (f_c \pi \Delta T)$$

$$f_c = \text{cutoff frequency (Hz)}$$

$$N_s = \text{Number of stages}$$

$$\epsilon = \text{defined in Figure F-1}$$

(3)

Note that:

$$f_m^1 = f_m$$

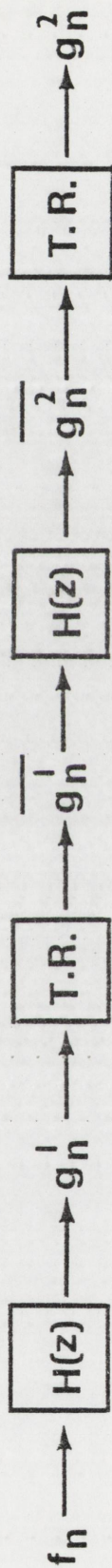
$$f_m^n = g_m^{n-1} \text{ for } n = 2, N_s - 1$$

$$g_m = g_m^{N_s}$$

(4)



Figure F-2
Block Diagram of Filter with N_s Stages



TR = Time Reversal

Figure F-3
Zero Phase Shift Filter Using Time Reversal

The application of a digital filter to these experiments involved some additional considerations. A digital filter, like an analog filter, introduces a frequency dependent phase shift. This phase shift distorts the temporal content of the data set which is unacceptable in this application. The phase shift can be eliminated by invoking the concept of time reversal. This procedure is shown schematically in Figure F-3. If the data set f_n has N elements, the concept of time reversal involves defining a new data set \bar{f}_n such that:

$$\bar{f}_n = f_{N-n+1} \quad \text{for } n=1, N \quad (5)$$

As shown in the figure, the data set f_n is filtered yielding a data set g_n^1 which has been distorted by a phase shift. This result is reversed in time to yield \bar{g}_n^1 which is then filtered to yield \bar{g}_n^2 which now has no phase shift but is still reversed in time. A time reversal of \bar{g}_n^2 yields g_n^2 which has the correct temporal content. The cascading of these two filters again enhances the overall power gain function.

In the digital filter techniques, it is assumed that the input function is continuous. However, the finite records obtained from the experiments are discontinuous at the end points. These discontinuities, if filtered, introduce "ringing" in the filtered output which is false data. This problem is eliminated by forming a larger data set by the addition of data to each end of the original set to bring the ends continuously to zero. This is shown schematically in Figure F-4. If $V_L + V_u$ are the average values

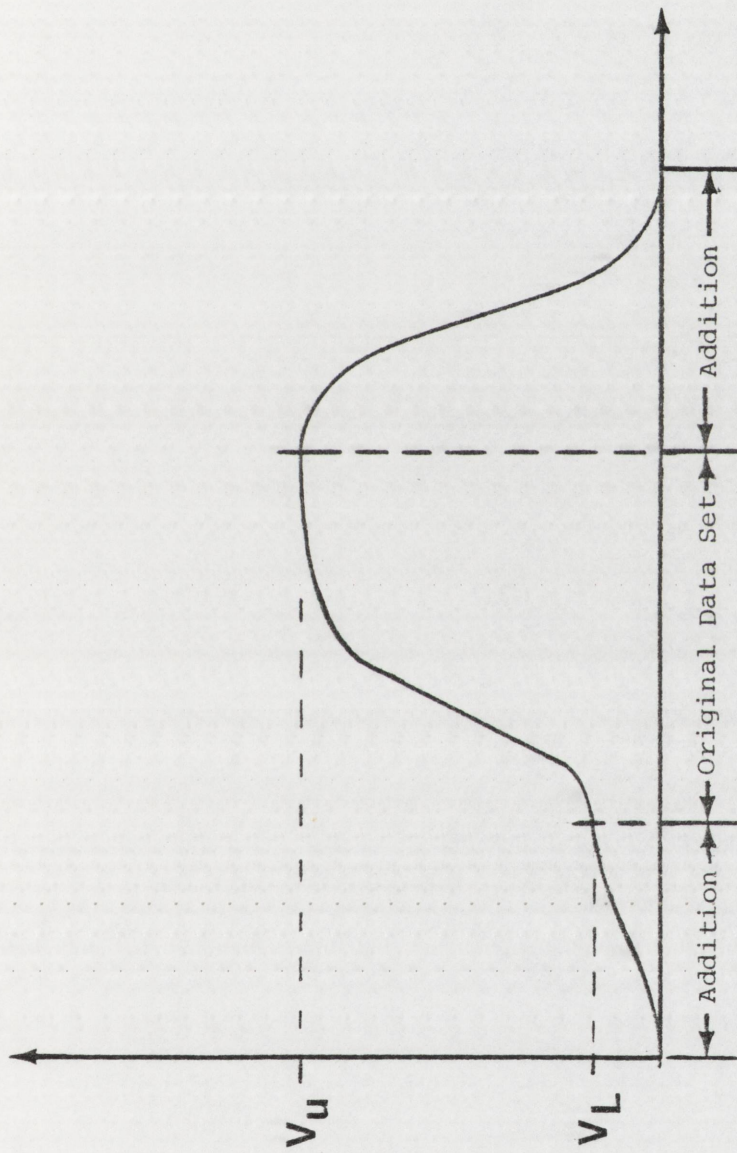


Figure F-4
Larger Data Set Formed to Eliminate Discontinuities

of the two ends of the data set f_n with N points, then the new data set (\bar{f}_n) is formed as follows:

$$\left. \begin{aligned} \bar{f}_n &= v_L \left(\frac{1 - \cos\left(\frac{\pi(n-1)}{250}\right)}{2} \right) && \text{for } n=1, 250 \\ \bar{f}_n &= f_{(n-250)} && \text{for } n=251, 250 + N \\ \bar{f}_n &= v_u \left(\frac{1 - \cos\left(\frac{\pi(500 + N - n)}{250}\right)}{2} \right) && \text{for } n=251 + N, 500 + N \\ \bar{f}_n &= 0 && \text{for } n=500 + N, 1000 \end{aligned} \right\} (6)$$

This larger data set is then filtered and the result is extracted from the filtered result \bar{g}_n as follows:

$$g_n = \bar{g}_{(250 + n)} \quad (7)$$

For the reduction of the EEOS data, two identical three-stage Butterworth filters, coupled with time reversal, were used. The filters were designed to attenuate the cutoff frequency f_c by a factor of 2 (i.e., $\epsilon = 1$).

APPENDIX G

INVERSE HEAT CONDUCTION TECHNIQUES

A technique was developed by Beck (Be68) to estimate heat fluxes at the surface of a heat-conducting solid from a transient temperature history measured at an interior point within the solid. This inverse heat conduction technique, which involves the numerical inversion of a convolution integral, is described in this section.

The temperature history at an interior point x_1 in a solid, due to a time variant surface heat flux, can be described by Duhamel's theorem in the form

$$T(x_1, t) - T_i = \int_0^t \dot{q}(0, \lambda) \frac{\partial \phi(x_1, t - \lambda)}{\partial t} d\lambda \quad (1)$$

where $T(x_1, t)$ is the transient temperature history at x_1 in a one-dimensional solid due to the time-variable surface heat flux $\dot{q}(0, t)$. $\phi(x_1, t)$ is the temperature response at x_1 for a unit rise in the surface heat flux. Equation (1) can be evaluated numerically as shown below for time $t = M\Delta T$

$$T_M = \sum_{n=0}^{M-1} \dot{q}_n \Delta \phi_{M-n} + \dot{q}_M \Delta \phi_0 \quad \text{where } \dot{q}_0 = 0 \quad (2)$$

The notation used is:

$$T_M = T(x_1, t) = T(x_1, M\Delta t) \quad (2a)$$

$$\begin{aligned}\frac{\Delta\phi_{m-n}}{\Delta t} &= \frac{\phi(x_1, (M-n+1)\Delta t) - \phi(x_1, (M-n)\Delta t)}{\Delta t} \\ &\approx \frac{\partial\phi(x_1, (M-n+\frac{1}{2})\Delta t)}{\partial t}\end{aligned}\quad (2b)$$

$$\dot{q}_n = \dot{q}(x_0, (n-\frac{1}{2})\Delta t) \quad (2c)$$

Temperatures at times $M\Delta t$, $(M+1)\Delta t$, ..., $(M+j)\Delta t$ can be given as

$$\begin{aligned}T_M &= \sum_{n=0}^{M-1} \dot{q}_n \Delta\phi_{M-n} + \dot{q}_M \Delta\phi_0 \quad (\dot{q}_0 \equiv 0) \\ T_{M+1} &= \sum_{n=0}^{M-1} \dot{q}_n \Delta\phi_{M-n+1} + \dot{q}_M \Delta\phi_1 + \dot{q}_{M+1} \Delta\phi_0 \\ &\vdots \\ T_{M+j} &= \sum_{n=0}^{M-1} \dot{q}_n \Delta\phi_{M-n+j} + \dot{q}_M \Delta\phi_j + \dot{q}_{M+1} \Delta\phi_{j-1} + \cdots + \dot{q}_{M+j} \Delta\phi_0\end{aligned}\quad (3)$$

The heat flux at time $(M+i-\frac{1}{2})\Delta t$ may be expressed as:

$$\dot{q}_{M+i} = A_0 + A_1 i + A_2 i^2 + \cdots + A_n i^n \quad (4)$$

Thus:

$$A_0 = \dot{q}_M \quad (4a)$$

A least squares technique can now be employed to evaluate the heat flux. If we assume the maximum value of j in equation (3) is r , then it is required that

$$F_r = \sum_{j=0}^r (T_{M+j} - T_{e,M+j})^2 \quad (5)$$

be made a minimum with respect to the coefficients A_0, A_1, \dots, A_η in (4). $T_{e,M+j}$ is the experimentally measured temperature at point x_1 at time $(M+j)\Delta t$. For a least squares solution to exist, it was required that $r \geq \eta + 1$.

Equations (3) and (4) can be combined to yield:

$$\left. \begin{aligned} T_{M+j} &= \sum_0^{M-1} \dot{q}_n \Delta \phi_{M-n+j} \\ &+ C_{0j} A_0 + C_{1j} A_1 + \dots + C_{\eta j} A_\eta \end{aligned} \right\} \quad (6)$$

where

$$C_{Pj} = \sum_{\ell=0}^j \ell^P \Delta \phi_{j-\ell} \quad (0^0 \equiv 1) \quad (6a)$$

Differentiating equation (5) with respect to A_P and equating to zero yields:

$$\begin{aligned} \frac{\partial F_r}{\partial A_P} = 0 &= 2 \sum_{j=0}^r \left[(T_{M+j} - T_{e,M+j}) \frac{\partial T_{M+j}}{\partial A_P} \right] \\ &+ 2 \sum_{j=0}^r \left[(T_{M+j} - T_{e_1 M+j}) \frac{\partial T_{e_1 M+j}}{\partial A_P} \right] \end{aligned} \quad (7)$$

From equation (6) note that

$$\frac{\partial T_{M+j}}{\partial A_P} = C_{Pj} \quad (8)$$

Thus, a set of linear equations is formed:

$$\sum_{j=0}^r (T_{M+j} - T_{e,M+j}) C_{Pj} = 0 \quad \text{for } P = 0, 1, 2, \dots, \eta \quad (9)$$

Equations (6) and (9) can be combined and rearranged to yield:

$$\sum_{j=0}^r T_{e,M+j} C_{Pj} - \sum_{n=0}^{M-1} q_n \sum_{j=0}^r \Delta \phi_{M-n+j} C_{Pj} =$$

$$\sum_{j=0}^r (C_{0j} C_{Pj} A_0 + C_{1j} C_{Pj} A_1 + \dots + C_{\eta j} C_{Pj} A_\eta) \quad (10)$$

$$\text{for } P = 0, 1, 2, \dots, \eta$$

This set of equations can be written as follows:

$$\beta_{r,0P} A_0 + \beta_{r,1P} A_1 + \dots + \beta_{r,\eta P} A_\eta = S_{rP} \quad (11)$$

$$\text{for } P = 0, 1, 2, \dots, \eta$$

where

$$\beta_{r,SP} = \beta_{r,PS} = \sum_{j=0}^P C_{Sj} C_{Pj} \begin{cases} S = 0,1,\dots,\eta \\ P = 0,1,\dots,\eta \end{cases} \quad (11a)$$

$$S_{rP} = \sum_{j=0}^r T_{e,M+j} C_{Pj} - \sum_{n=0}^{M-1} \dot{q}_n \sum_{j=0}^r \Delta\phi_{M-n+j} C_{Pj} \quad (11b)$$

Finally, recall that $A_0 = \dot{q}_M$. Thus, for every time step $M\Delta T$, it is only necessary to solve equations (11) for A_0 . This set of equations involve experimental temperatures for the current time step and r future time steps, the calculated surface heat fluxes for all previous time steps, and the response functions $\Delta\phi_{M-n}$.

APPENDIX H

REPRESENTATIVE DATA FROM ONE EXPERIMENT

On the following pages, the radiation-corrected, filtered data from the vapor pressure measurement series, EEOS-UO2-3, are tabulated. As can be seen in Table H-1, most of the data contains experimental biases. The biases were eliminated in subsequent data processing by averaging the first 50 data values in each set and subtracting that value from all values in that data set. No bias is associated with the power integral data. The designations, "inner" and "outer," in the table headings for thermocouple data refer to the depth of the thermocouple. "Inner" thermocouples were located .38 mm from the inside graphite surface; "outer" thermocouples were located 1.27 mm from that surface. The other data required for reduction of these data histories are given in Table V-1.

TABLE H-1
 FILTERED EXPERIMENT DATA HISTORIES FROM ACPR NO. 7463 CORRECTED FOR RADIATION INDUCED SIGNALS BY
 DATA FROM ACPR NO. 7836 FOR SAMPLE 30-10

ELAPSED TIME (SEC)	PRESSURE		THERMOCOUPLE		THERMOCOUPLE		THERMOCOUPLE		THERMOCOUPLE		THERMOCOUPLE		THERMOCOUPLE	
	TRANSDUCER HIGH GAIN (PSI)	TRANSDUCER LOW GAIN (PSI)	BOTTOM OUTER (DEG C)	BOTTOM INNER-1 (DEG C)	BOTTOM INNER-2 (DEG C)	SIDE UPPER (DEG C)	SIDE LOWER (DEG C)	TOP INNER-1 (DEG C)	TOP INNER-2 (DEG C)	TOP INNER-3 (DEG C)	TOP INNER-4 (DEG C)	TOP INNER-5 (DEG C)	TOP INNER-6 (DEG C)	TOP INNER-7 (DEG C)
0.	-.46594E+02	-.46594E+02	.10509E+02	.10509E+02	.10509E+02	.10509E+02	.10509E+02	.10509E+02	.10509E+02	.10509E+02	.10509E+02	.10509E+02	.10509E+02	.10509E+02
.16000L-03	-.47032E+02	-.47032E+02	.10612E+02	.10612E+02	.10612E+02	.10612E+02	.10612E+02	.10612E+02	.10612E+02	.10612E+02	.10612E+02	.10612E+02	.10612E+02	.10612E+02
.32000L-03	-.47760E+02	-.47760E+02	.10718E+02	.10718E+02	.10718E+02	.10718E+02	.10718E+02	.10718E+02	.10718E+02	.10718E+02	.10718E+02	.10718E+02	.10718E+02	.10718E+02
.48000L-03	-.48735E+02	-.48735E+02	.10827E+02	.10827E+02	.10827E+02	.10827E+02	.10827E+02	.10827E+02	.10827E+02	.10827E+02	.10827E+02	.10827E+02	.10827E+02	.10827E+02
.64000L-03	-.49863E+02	-.49863E+02	.10938E+02	.10938E+02	.10938E+02	.10938E+02	.10938E+02	.10938E+02	.10938E+02	.10938E+02	.10938E+02	.10938E+02	.10938E+02	.10938E+02
.80000L-03	-.51010E+02	-.51010E+02	.11052E+02	.11052E+02	.11052E+02	.11052E+02	.11052E+02	.11052E+02	.11052E+02	.11052E+02	.11052E+02	.11052E+02	.11052E+02	.11052E+02
.96000L-03	-.52028E+02	-.52028E+02	.11169E+02	.11169E+02	.11169E+02	.11169E+02	.11169E+02	.11169E+02	.11169E+02	.11169E+02	.11169E+02	.11169E+02	.11169E+02	.11169E+02
.11200L-02	-.52781E+02	-.52781E+02	.11288E+02	.11288E+02	.11288E+02	.11288E+02	.11288E+02	.11288E+02	.11288E+02	.11288E+02	.11288E+02	.11288E+02	.11288E+02	.11288E+02
.12800L-02	-.53168E+02	-.53168E+02	.11409E+02	.11409E+02	.11409E+02	.11409E+02	.11409E+02	.11409E+02	.11409E+02	.11409E+02	.11409E+02	.11409E+02	.11409E+02	.11409E+02
.14400L-02	-.53150E+02	-.53150E+02	.11532E+02	.11532E+02	.11532E+02	.11532E+02	.11532E+02	.11532E+02	.11532E+02	.11532E+02	.11532E+02	.11532E+02	.11532E+02	.11532E+02
.16000L-02	-.52757E+02	-.52757E+02	.11657E+02	.11657E+02	.11657E+02	.11657E+02	.11657E+02	.11657E+02	.11657E+02	.11657E+02	.11657E+02	.11657E+02	.11657E+02	.11657E+02
.17600L-02	-.52079E+02	-.52079E+02	.11784E+02	.11784E+02	.11784E+02	.11784E+02	.11784E+02	.11784E+02	.11784E+02	.11784E+02	.11784E+02	.11784E+02	.11784E+02	.11784E+02
.19200L-02	-.51250E+02	-.51250E+02	.11913E+02	.11913E+02	.11913E+02	.11913E+02	.11913E+02	.11913E+02	.11913E+02	.11913E+02	.11913E+02	.11913E+02	.11913E+02	.11913E+02
.20800L-02	-.50414E+02	-.50414E+02	.12043E+02	.12043E+02	.12043E+02	.12043E+02	.12043E+02	.12043E+02	.12043E+02	.12043E+02	.12043E+02	.12043E+02	.12043E+02	.12043E+02
.22400L-02	-.49692E+02	-.49692E+02	.12175E+02	.12175E+02	.12175E+02	.12175E+02	.12175E+02	.12175E+02	.12175E+02	.12175E+02	.12175E+02	.12175E+02	.12175E+02	.12175E+02
.24000L-02	-.49156E+02	-.49156E+02	.12308E+02	.12308E+02	.12308E+02	.12308E+02	.12308E+02	.12308E+02	.12308E+02	.12308E+02	.12308E+02	.12308E+02	.12308E+02	.12308E+02
.25600L-02	-.48814E+02	-.48814E+02	.12442E+02	.12442E+02	.12442E+02	.12442E+02	.12442E+02	.12442E+02	.12442E+02	.12442E+02	.12442E+02	.12442E+02	.12442E+02	.12442E+02
.27200L-02	-.48617E+02	-.48617E+02	.12577E+02	.12577E+02	.12577E+02	.12577E+02	.12577E+02	.12577E+02	.12577E+02	.12577E+02	.12577E+02	.12577E+02	.12577E+02	.12577E+02
.28800L-02	-.48476E+02	-.48476E+02	.12713E+02	.12713E+02	.12713E+02	.12713E+02	.12713E+02	.12713E+02	.12713E+02	.12713E+02	.12713E+02	.12713E+02	.12713E+02	.12713E+02
.30400L-02	-.48297E+02	-.48297E+02	.12849E+02	.12849E+02	.12849E+02	.12849E+02	.12849E+02	.12849E+02	.12849E+02	.12849E+02	.12849E+02	.12849E+02	.12849E+02	.12849E+02
.32000L-02	-.48001E+02	-.48001E+02	.12986E+02	.12986E+02	.12986E+02	.12986E+02	.12986E+02	.12986E+02	.12986E+02	.12986E+02	.12986E+02	.12986E+02	.12986E+02	.12986E+02
.33600L-02	-.47553E+02	-.47553E+02	.13123E+02	.13123E+02	.13123E+02	.13123E+02	.13123E+02	.13123E+02	.13123E+02	.13123E+02	.13123E+02	.13123E+02	.13123E+02	.13123E+02
.35200L-02	-.46959E+02	-.46959E+02	.13261E+02	.13261E+02	.13261E+02	.13261E+02	.13261E+02	.13261E+02	.13261E+02	.13261E+02	.13261E+02	.13261E+02	.13261E+02	.13261E+02
.36800L-02	-.46256E+02	-.46256E+02	.13398E+02	.13398E+02	.13398E+02	.13398E+02	.13398E+02	.13398E+02	.13398E+02	.13398E+02	.13398E+02	.13398E+02	.13398E+02	.13398E+02
.38400L-02	-.45494E+02	-.45494E+02	.13535E+02	.13535E+02	.13535E+02	.13535E+02	.13535E+02	.13535E+02	.13535E+02	.13535E+02	.13535E+02	.13535E+02	.13535E+02	.13535E+02
.40000L-02	-.44710E+02	-.44710E+02	.13671E+02	.13671E+02	.13671E+02	.13671E+02	.13671E+02	.13671E+02	.13671E+02	.13671E+02	.13671E+02	.13671E+02	.13671E+02	.13671E+02
.41600L-02	-.43918E+02	-.43918E+02	.13807E+02	.13807E+02	.13807E+02	.13807E+02	.13807E+02	.13807E+02	.13807E+02	.13807E+02	.13807E+02	.13807E+02	.13807E+02	.13807E+02
.43200L-02	-.43099E+02	-.43099E+02	.13942E+02	.13942E+02	.13942E+02	.13942E+02	.13942E+02	.13942E+02	.13942E+02	.13942E+02	.13942E+02	.13942E+02	.13942E+02	.13942E+02
.44800L-02	-.42217E+02	-.42217E+02	.14076E+02	.14076E+02	.14076E+02	.14076E+02	.14076E+02	.14076E+02	.14076E+02	.14076E+02	.14076E+02	.14076E+02	.14076E+02	.14076E+02
.46400L-02	-.41235E+02	-.41235E+02	.14209E+02	.14209E+02	.14209E+02	.14209E+02	.14209E+02	.14209E+02	.14209E+02	.14209E+02	.14209E+02	.14209E+02	.14209E+02	.14209E+02
.48000L-02	-.40138E+02	-.40138E+02	.14340E+02	.14340E+02	.14340E+02	.14340E+02	.14340E+02	.14340E+02	.14340E+02	.14340E+02	.14340E+02	.14340E+02	.14340E+02	.14340E+02
.49600L-02	-.38951E+02	-.38951E+02	.14470E+02	.14470E+02	.14470E+02	.14470E+02	.14470E+02	.14470E+02	.14470E+02	.14470E+02	.14470E+02	.14470E+02	.14470E+02	.14470E+02
.51200L-02	-.37746E+02	-.37746E+02	.14598E+02	.14598E+02	.14598E+02	.14598E+02	.14598E+02	.14598E+02	.14598E+02	.14598E+02	.14598E+02	.14598E+02	.14598E+02	.14598E+02
.52800L-02	-.36638E+02	-.36638E+02	.14724E+02	.14724E+02	.14724E+02	.14724E+02	.14724E+02	.14724E+02	.14724E+02	.14724E+02	.14724E+02	.14724E+02	.14724E+02	.14724E+02
.54400L-02	-.35766E+02	-.35766E+02	.14848E+02	.14848E+02	.14848E+02	.14848E+02	.14848E+02	.14848E+02	.14848E+02	.14848E+02	.14848E+02	.14848E+02	.14848E+02	.14848E+02

TABLE n-1 (CONTINUED)
 FILTERED EXPERIMENT DATA HISTORIES FROM ACPR NO. 7863 CORRECTED FOR RADIATION INDUCED SIGNALS BY
 DATA FROM ACPR NO. 7836 FOR SAMPLE 30-10

ELAPSED TIME (SFC)	PRESSURE TRANSDUCER HIGH GAIN (PSI)	PRESSURE TRANSDUCER LOW GAIN (PSI)	THERMOCOUPLE BOTTOM OUTER (DEG C)	THERMOCOUPLE BOTTOM INNER-1 (DEG C)	THERMOCOUPLE BOTTOM INNER-2 (DEG C)	THERMOCOUPLE SIDE UPPER (DEG C)	THERMOCOUPLE SIDE LOWER (DEG C)
.56000E-02	-.35272E+02	-.35272E+02	.14969E+02	.14969E+02	.14969E+02	.14969E+02	.14969E+02
.57600E-02	-.35269E+02	-.35269E+02	.15089E+02	.15089E+02	.15089E+02	.15089E+02	.15089E+02
.59200E-02	-.35817E+02	-.35817E+02	.15205E+02	.15205E+02	.15205E+02	.15205E+02	.15205E+02
.60800E-02	-.36904E+02	-.36904E+02	.15319E+02	.15319E+02	.15319E+02	.15319E+02	.15319E+02
.62400E-02	-.38438E+02	-.38438E+02	.15430E+02	.15430E+02	.15430E+02	.15430E+02	.15430E+02
.64000E-02	-.40254E+02	-.40254E+02	.15539E+02	.15539E+02	.15539E+02	.15539E+02	.15539E+02
.65600E-02	-.42134E+02	-.42134E+02	.15644E+02	.15644E+02	.15644E+02	.15644E+02	.15644E+02
.67200E-02	-.43840E+02	-.43840E+02	.15746E+02	.15746E+02	.15746E+02	.15746E+02	.15746E+02
.68800E-02	-.45152E+02	-.45152E+02	.15844E+02	.15844E+02	.15844E+02	.15844E+02	.15844E+02
.70400E-02	-.45900E+02	-.45900E+02	.15939E+02	.15939E+02	.15939E+02	.15939E+02	.15939E+02
.72000E-02	-.45994E+02	-.45994E+02	.16031E+02	.16031E+02	.16031E+02	.16031E+02	.16031E+02
.73600E-02	-.45439E+02	-.45439E+02	.16119E+02	.16119E+02	.16119E+02	.16119E+02	.16119E+02
.75200E-02	-.44329E+02	-.44329E+02	.16203E+02	.16203E+02	.16203E+02	.16203E+02	.16203E+02
.76800E-02	-.42826E+02	-.42826E+02	.16284E+02	.16284E+02	.16284E+02	.16284E+02	.16284E+02
.78400E-02	-.41135E+02	-.41135E+02	.16361E+02	.16361E+02	.16361E+02	.16361E+02	.16361E+02
.80000E-02	-.39458E+02	-.39458E+02	.16434E+02	.16434E+02	.16434E+02	.16434E+02	.16434E+02
.81600E-02	-.37970E+02	-.37970E+02	.16503E+02	.16503E+02	.16503E+02	.16503E+02	.16503E+02
.83200E-02	-.36789E+02	-.36789E+02	.16568E+02	.16568E+02	.16568E+02	.16568E+02	.16568E+02
.84800E-02	-.35970E+02	-.35970E+02	.16630E+02	.16630E+02	.16630E+02	.16630E+02	.16630E+02
.86400E-02	-.35505E+02	-.35505E+02	.16687E+02	.16687E+02	.16687E+02	.16687E+02	.16687E+02
.88000E-02	-.35336E+02	-.35336E+02	.16741E+02	.16741E+02	.16741E+02	.16741E+02	.16741E+02
.89600E-02	-.35380E+02	-.35380E+02	.16791E+02	.16791E+02	.16791E+02	.16791E+02	.16791E+02
.91199E-02	-.35542E+02	-.35542E+02	.16837E+02	.16837E+02	.16837E+02	.16837E+02	.16837E+02
.92799E-02	-.35741E+02	-.35741E+02	.16880E+02	.16880E+02	.16880E+02	.16880E+02	.16880E+02
.94399E-02	-.35919E+02	-.35919E+02	.16919E+02	.16919E+02	.16919E+02	.16919E+02	.16919E+02
.96000E-02	-.36048E+02	-.36048E+02	.16954E+02	.16954E+02	.16954E+02	.16954E+02	.16954E+02
.97599E-02	-.36128E+02	-.36128E+02	.16986E+02	.16986E+02	.16986E+02	.16986E+02	.16986E+02
.99199E-02	-.36181E+02	-.36181E+02	.17014E+02	.17014E+02	.17014E+02	.17014E+02	.17014E+02
.10080E-01	-.36245E+02	-.36245E+02	.17039E+02	.17039E+02	.17039E+02	.17039E+02	.17039E+02
.10240E-01	-.36362E+02	-.36362E+02	.17061E+02	.17061E+02	.17061E+02	.17061E+02	.17061E+02
.10400E-01	-.36563E+02	-.36563E+02	.17080E+02	.17080E+02	.17080E+02	.17080E+02	.17080E+02
.10560E-01	-.36867E+02	-.36867E+02	.17096E+02	.17096E+02	.17096E+02	.17096E+02	.17096E+02
.10720E-01	-.37273E+02	-.37273E+02	.17109E+02	.17109E+02	.17109E+02	.17109E+02	.17109E+02
.10880E-01	-.37764E+02	-.37764E+02	.17120E+02	.17120E+02	.17120E+02	.17120E+02	.17120E+02
.11040E-01	-.38306E+02	-.38306E+02	.17128E+02	.17128E+02	.17128E+02	.17128E+02	.17128E+02

TABLE H-1 (CONTINUED)
 FILTERED EXPERIMENT DATA HISTORIES FROM ACPR NO. 7863 CORRECTED FOR RADIATION INDUCED SIGNALS BY
 DATA FROM ACPR NO. 7836 FOR SAMPLE 30-10

ELAPSED TIME (SEC)	PRESSURE TRANSDUCER HIGH GAIN (PSI)	PRESSURE TRANSDUCER LOW GAIN (PSI)	THERMOCOUPLE BOTTOM OUTER (DEG C)	THERMOCOUPLE BOTTOM INNER-1 (DEG C)	THERMOCOUPLE BOTTOM INNER-2 (DEG C)	THERMOCOUPLE SIDE UPPER (DEG C)	THERMOCOUPLE SIDE LOWER (DEG C)
.11200E-01	-.38868E+02	-.38868E+02	.17134E+02	.17134E+02	.17134E+02	.17134E+02	.17134E+02
.11360E-01	-.39422E+02	-.39422E+02	.17138E+02	.17138E+02	.17138E+02	.17138E+02	.17138E+02
.11520E-01	-.39956E+02	-.39956E+02	.17139E+02	.17139E+02	.17139E+02	.17139E+02	.17139E+02
.11680E-01	-.40475E+02	-.40475E+02	.17139E+02	.17139E+02	.17139E+02	.17139E+02	.17139E+02
.11840E-01	-.40993E+02	-.40993E+02	.17138E+02	.17138E+02	.17138E+02	.17138E+02	.17138E+02
.12000E-01	-.41522E+02	-.41522E+02	.17134E+02	.17134E+02	.17134E+02	.17134E+02	.17134E+02
.12160E-01	-.42066E+02	-.42066E+02	.17130E+02	.17130E+02	.17130E+02	.17130E+02	.17130E+02
.12320E-01	-.42612E+02	-.42612E+02	.17125E+02	.17125E+02	.17125E+02	.17125E+02	.17125E+02
.12480E-01	-.43132E+02	-.43132E+02	.17119E+02	.17119E+02	.17119E+02	.17119E+02	.17119E+02
.12640E-01	-.43597E+02	-.43597E+02	.17112E+02	.17112E+02	.17112E+02	.17112E+02	.17112E+02
.12800E-01	-.43983E+02	-.43983E+02	.17106E+02	.17106E+02	.17106E+02	.17106E+02	.17106E+02
.12960E-01	-.44288E+02	-.44288E+02	.17098E+02	.17098E+02	.17098E+02	.17098E+02	.17098E+02
.13120E-01	-.44531E+02	-.44531E+02	.17091E+02	.17091E+02	.17091E+02	.17091E+02	.17091E+02
.13280E-01	-.44746E+02	-.44746E+02	.17084E+02	.17084E+02	.17084E+02	.17084E+02	.17084E+02
.13440E-01	-.44967E+02	-.44967E+02	.17078E+02	.17078E+02	.17078E+02	.17078E+02	.17078E+02
.13600E-01	-.45207E+02	-.45207E+02	.17072E+02	.17072E+02	.17072E+02	.17072E+02	.17072E+02
.13760E-01	-.45447E+02	-.45447E+02	.17067E+02	.17067E+02	.17067E+02	.17067E+02	.17067E+02
.13920E-01	-.45625E+02	-.45625E+02	.17063E+02	.17063E+02	.17063E+02	.17063E+02	.17063E+02
.14080E-01	-.45651E+02	-.45651E+02	.17060E+02	.17060E+02	.17060E+02	.17060E+02	.17060E+02
.14240E-01	-.45421E+02	-.45421E+02	.17058E+02	.17058E+02	.17058E+02	.17058E+02	.17058E+02
.14400E-01	-.44851E+02	-.44851E+02	.17058E+02	.17058E+02	.17058E+02	.17058E+02	.17058E+02
.14560E-01	-.43903E+02	-.43903E+02	.17060E+02	.17060E+02	.17060E+02	.17060E+02	.17060E+02
.14720E-01	-.42605E+02	-.42605E+02	.17063E+02	.17063E+02	.17063E+02	.17063E+02	.17063E+02
.14880E-01	-.41062E+02	-.41062E+02	.17069E+02	.17069E+02	.17069E+02	.17069E+02	.17069E+02
.15040E-01	-.39442E+02	-.39442E+02	.17076E+02	.17076E+02	.17076E+02	.17076E+02	.17076E+02
.15200E-01	-.37957E+02	-.37957E+02	.17086E+02	.17086E+02	.17086E+02	.17086E+02	.17086E+02
.15360E-01	-.36826E+02	-.36826E+02	.17098E+02	.17098E+02	.17098E+02	.17098E+02	.17098E+02
.15520E-01	-.36246E+02	-.36246E+02	.17113E+02	.17113E+02	.17113E+02	.17113E+02	.17113E+02
.15680E-01	-.36350E+02	-.36350E+02	.17131E+02	.17131E+02	.17131E+02	.17131E+02	.17131E+02
.15840E-01	-.37188E+02	-.37188E+02	.17151E+02	.17151E+02	.17151E+02	.17151E+02	.17151E+02
.16000E-01	-.38712E+02	-.38712E+02	.17174E+02	.17174E+02	.17174E+02	.17174E+02	.17174E+02
.16160E-01	-.40780E+02	-.40780E+02	.17199E+02	.17199E+02	.17199E+02	.17199E+02	.17199E+02
.16320E-01	-.43170E+02	-.43170E+02	.17228E+02	.17228E+02	.17228E+02	.17228E+02	.17228E+02
.16480E-01	-.45617E+02	-.45617E+02	.17260E+02	.17260E+02	.17260E+02	.17260E+02	.17260E+02
.16640E-01	-.47849E+02	-.47849E+02	.17294E+02	.17294E+02	.17294E+02	.17294E+02	.17294E+02

TABLE M-1 (CONTINUED)
 FILTERED EXPERIMENT DATA HISTORIES FROM ACPR NO. 7A63 CORRECTED FOR RADIATION INDUCED SIGNALS BY
 DATA FROM ACPR NO. 7836 FOR SAMPLE 30-10

ELAPSED TIME (SEC)	PRESSURE TRANSDUCER HIGH GAIN (PSI)	PRESSURE TRANSDUCER LOW GAIN (PSI)	THERMOCOUPLE BOTTOM OUTER (DEG C)	THERMOCOUPLE BOTTOM INNER-1 (DEG C)	THERMOCOUPLE BOTTOM INNER-2 (DEG C)	THERMOCOUPLE SIDE UPPER (DEG C)	THERMOCOUPLE SIDE LOWER (DEG C)
.16800E-01	-.49630E+02	-.49630E+02	.17332E+02	.17332E+02	.17332E+02	.17332E+02	.17332E+02
.16960E-01	-.50803E+02	-.50803E+02	.17372E+02	.17372E+02	.17372E+02	.17372E+02	.17372E+02
.17120E-01	-.51311E+02	-.51311E+02	.17416E+02	.17416E+02	.17416E+02	.17416E+02	.17416E+02
.17280E-01	-.51210E+02	-.51210E+02	.17462E+02	.17462E+02	.17462E+02	.17462E+02	.17462E+02
.17440E-01	-.50654E+02	-.50654E+02	.17512E+02	.17512E+02	.17512E+02	.17512E+02	.17512E+02
.17600E-01	-.49861E+02	-.49861E+02	.17564E+02	.17564E+02	.17564E+02	.17564E+02	.17564E+02
.17760E-01	-.49072E+02	-.49072E+02	.17620E+02	.17620E+02	.17620E+02	.17620E+02	.17620E+02
.17920E-01	-.48504E+02	-.48504E+02	.17678E+02	.17678E+02	.17678E+02	.17678E+02	.17678E+02
.18080E-01	-.48308E+02	-.48308E+02	.17739E+02	.17739E+02	.17739E+02	.17739E+02	.17739E+02
.18240E-01	-.48545E+02	-.48545E+02	.17803E+02	.17803E+02	.17803E+02	.17803E+02	.17803E+02
.18400E-01	-.49179E+02	-.49179E+02	.17869E+02	.17869E+02	.17869E+02	.17869E+02	.17869E+02
.18560E-01	-.50088E+02	-.50088E+02	.17937E+02	.17937E+02	.17937E+02	.17937E+02	.17937E+02
.18720E-01	-.51096E+02	-.51096E+02	.18009E+02	.18009E+02	.18009E+02	.18009E+02	.18009E+02
.18880E-01	-.52009E+02	-.52009E+02	.18082E+02	.18082E+02	.18082E+02	.18082E+02	.18082E+02
.19040E-01	-.52659E+02	-.52659E+02	.18157E+02	.18157E+02	.18157E+02	.18157E+02	.18157E+02
.19200E-01	-.52938E+02	-.52938E+02	.18235E+02	.18235E+02	.18235E+02	.18235E+02	.18235E+02
.19360E-01	-.52821E+02	-.52821E+02	.18314E+02	.18314E+02	.18314E+02	.18314E+02	.18314E+02
.19520E-01	-.52375E+02	-.52375E+02	.18394E+02	.18394E+02	.18394E+02	.18394E+02	.18394E+02
.19640E-01	-.51743E+02	-.51743E+02	.18477E+02	.18477E+02	.18477E+02	.18477E+02	.18477E+02
.19840E-01	-.51118E+02	-.51118E+02	.18561E+02	.18561E+02	.18561E+02	.18561E+02	.18561E+02
.20000E-01	-.50698E+02	-.50698E+02	.18645E+02	.18645E+02	.18645E+02	.18645E+02	.18645E+02
.20160E-01	-.50645E+02	-.50645E+02	.18731E+02	.18731E+02	.18731E+02	.18731E+02	.18731E+02
.20320E-01	-.51040E+02	-.51040E+02	.18818E+02	.18818E+02	.18818E+02	.18818E+02	.18818E+02
.20480E-01	-.51863E+02	-.51863E+02	.18905E+02	.18905E+02	.18905E+02	.18905E+02	.18905E+02
.20640E-01	-.52991E+02	-.52991E+02	.18993E+02	.18993E+02	.18993E+02	.18993E+02	.18993E+02
.20800E-01	-.54213E+02	-.54213E+02	.19081E+02	.19081E+02	.19081E+02	.19081E+02	.19081E+02
.20960E-01	-.55275E+02	-.55275E+02	.19169E+02	.19169E+02	.19169E+02	.19169E+02	.19169E+02
.21120E-01	-.55933E+02	-.55933E+02	.19257E+02	.19257E+02	.19257E+02	.19257E+02	.19257E+02
.21280E-01	-.55996E+02	-.55996E+02	.19345E+02	.19345E+02	.19345E+02	.19345E+02	.19345E+02
.21440E-01	-.55373E+02	-.55373E+02	.19433E+02	.19433E+02	.19433E+02	.19433E+02	.19433E+02
.21600E-01	-.54086E+02	-.54086E+02	.19519E+02	.19519E+02	.19519E+02	.19519E+02	.19519E+02
.21760E-01	-.52263E+02	-.52263E+02	.19605E+02	.19605E+02	.19605E+02	.19605E+02	.19605E+02
.21920E-01	-.50115E+02	-.50115E+02	.19690E+02	.19690E+02	.19690E+02	.19690E+02	.19690E+02
.22080E-01	-.47895E+02	-.47895E+02	.19774E+02	.19774E+02	.19774E+02	.19774E+02	.19774E+02
.22240E-01	-.45851E+02	-.45851E+02	.19856E+02	.19856E+02	.19856E+02	.19856E+02	.19856E+02

TABLE H-1 (CONTINUED)

FILTERED EXPERIMENT DATA HISTORIES FROM ACPR NO. 7863 CORRECTED FOR RADIATION INDUCED SIGNALS BY DATA FROM ACPR NO. 7836 FOR SAMPLE 30-10

ELAPSED TIME (SEC)	PRESSURE TRANSDUCER HIGH GAIN (PSI)		PRESSURE TRANSDUCER LOW GAIN (PSI)		THERMOCOUPLE BOTTOM OUTER (DEG C)		THERMOCOUPLE BOTTOM INNER-1 (DEG C)		THERMOCOUPLE BOTTOM INNER-2 (DEG C)		THERMOCOUPLE SIDE UPPER (DEG C)		THERMOCOUPLE SIDE LOWER (DEG C)	
22400E-01	-	44191E+02	-	44191E+02	1937E+02	1937E+02	1937E+02	1937E+02	1937E+02	1937E+02	1937E+02	1937E+02	1937E+02	1937E+02
22560E-01	-	43056E+02	-	43056E+02	20016E+02	20016E+02	20016E+02	20016E+02	20016E+02	20016E+02	20016E+02	20016E+02	20016E+02	20016E+02
22720E-01	-	42510E+02	-	42510E+02	20093E+02	20093E+02	20093E+02	20093E+02	20093E+02	20093E+02	20093E+02	20093E+02	20093E+02	20093E+02
22880E-01	-	42540E+02	-	42540E+02	20169E+02	20169E+02	20169E+02	20169E+02	20169E+02	20169E+02	20169E+02	20169E+02	20169E+02	20169E+02
23040E-01	-	43067E+02	-	43067E+02	20242E+02	20242E+02	20242E+02	20242E+02	20242E+02	20242E+02	20242E+02	20242E+02	20242E+02	20242E+02
23200E-01	-	43966E+02	-	43966E+02	20313E+02	20313E+02	20313E+02	20313E+02	20313E+02	20313E+02	20313E+02	20313E+02	20313E+02	20313E+02
23360E-01	-	45081E+02	-	45081E+02	20382E+02	20382E+02	20382E+02	20382E+02	20382E+02	20382E+02	20382E+02	20382E+02	20382E+02	20382E+02
23520E-01	-	46247E+02	-	46247E+02	20449E+02	20449E+02	20449E+02	20449E+02	20449E+02	20449E+02	20449E+02	20449E+02	20449E+02	20449E+02
23679E-01	-	47304E+02	-	47304E+02	20513E+02	20513E+02	20513E+02	20513E+02	20513E+02	20513E+02	20513E+02	20513E+02	20513E+02	20513E+02
23840E-01	-	48117E+02	-	48117E+02	20574E+02	20574E+02	20574E+02	20574E+02	20574E+02	20574E+02	20574E+02	20574E+02	20574E+02	20574E+02
23999E-01	-	48583E+02	-	48583E+02	20633E+02	20633E+02	20633E+02	20633E+02	20633E+02	20633E+02	20633E+02	20633E+02	20633E+02	20633E+02
24160E-01	-	48647E+02	-	48647E+02	20689E+02	20689E+02	20689E+02	20689E+02	20689E+02	20689E+02	20689E+02	20689E+02	20689E+02	20689E+02
24320E-01	-	48300E+02	-	48300E+02	20743E+02	20743E+02	20743E+02	20743E+02	20743E+02	20743E+02	20743E+02	20743E+02	20743E+02	20743E+02
24479E-01	-	47580E+02	-	47580E+02	20793E+02	20793E+02	20793E+02	20793E+02	20793E+02	20793E+02	20793E+02	20793E+02	20793E+02	20793E+02
24640E-01	-	46563E+02	-	46563E+02	20841E+02	20841E+02	20841E+02	20841E+02	20841E+02	20841E+02	20841E+02	20841E+02	20841E+02	20841E+02
24799E-01	-	45353E+02	-	45353E+02	20886E+02	20886E+02	20886E+02	20886E+02	20886E+02	20886E+02	20886E+02	20886E+02	20886E+02	20886E+02
24960E-01	-	44044E+02	-	44044E+02	20928E+02	20928E+02	20928E+02	20928E+02	20928E+02	20928E+02	20928E+02	20928E+02	20928E+02	20928E+02
25119E-01	-	42801E+02	-	42801E+02	20968E+02	20968E+02	20968E+02	20968E+02	20968E+02	20968E+02	20968E+02	20968E+02	20968E+02	20968E+02
25280E-01	-	41647E+02	-	41647E+02	21005E+02	21005E+02	21005E+02	21005E+02	21005E+02	21005E+02	21005E+02	21005E+02	21005E+02	21005E+02
25439E-01	-	40645E+02	-	40645E+02	21039E+02	21039E+02	21039E+02	21039E+02	21039E+02	21039E+02	21039E+02	21039E+02	21039E+02	21039E+02
25599E-01	-	39796E+02	-	39796E+02	21070E+02	21070E+02	21070E+02	21070E+02	21070E+02	21070E+02	21070E+02	21070E+02	21070E+02	21070E+02
25760E-01	-	39060E+02	-	39060E+02	21099E+02	21099E+02	21099E+02	21099E+02	21099E+02	21099E+02	21099E+02	21099E+02	21099E+02	21099E+02
25919E-01	-	38371E+02	-	38371E+02	21125E+02	21125E+02	21125E+02	21125E+02	21125E+02	21125E+02	21125E+02	21125E+02	21125E+02	21125E+02
26079E-01	-	37666E+02	-	37666E+02	21149E+02	21149E+02	21149E+02	21149E+02	21149E+02	21149E+02	21149E+02	21149E+02	21149E+02	21149E+02
26239E-01	-	36914E+02	-	36914E+02	21171E+02	21171E+02	21171E+02	21171E+02	21171E+02	21171E+02	21171E+02	21171E+02	21171E+02	21171E+02
26399E-01	-	36150E+02	-	36150E+02	21191E+02	21191E+02	21191E+02	21191E+02	21191E+02	21191E+02	21191E+02	21191E+02	21191E+02	21191E+02
26559E-01	-	35491E+02	-	35491E+02	21208E+02	21208E+02	21208E+02	21208E+02	21208E+02	21208E+02	21208E+02	21208E+02	21208E+02	21208E+02
26719E-01	-	35140E+02	-	35140E+02	21224E+02	21224E+02	21224E+02	21224E+02	21224E+02	21224E+02	21224E+02	21224E+02	21224E+02	21224E+02
26879E-01	-	35374E+02	-	35374E+02	21238E+02	21238E+02	21238E+02	21238E+02	21238E+02	21238E+02	21238E+02	21238E+02	21238E+02	21238E+02
27039E-01	-	36493E+02	-	36493E+02	21250E+02	21250E+02	21250E+02	21250E+02	21250E+02	21250E+02	21250E+02	21250E+02	21250E+02	21250E+02
27199E-01	-	38764E+02	-	38764E+02	21261E+02	21261E+02	21261E+02	21261E+02	21261E+02	21261E+02	21261E+02	21261E+02	21261E+02	21261E+02
27359E-01	-	42345E+02	-	42345E+02	21271E+02	21271E+02	21271E+02	21271E+02	21271E+02	21271E+02	21271E+02	21271E+02	21271E+02	21271E+02
27519E-01	-	47204E+02	-	47204E+02	21279E+02	21279E+02	21279E+02	21279E+02	21279E+02	21279E+02	21279E+02	21279E+02	21279E+02	21279E+02
27679E-01	-	53034E+02	-	53034E+02	21287E+02	21287E+02	21287E+02	21287E+02	21287E+02	21287E+02	21287E+02	21287E+02	21287E+02	21287E+02
27839E-01	-	59191E+02	-	59191E+02	21295E+02	21295E+02	21295E+02	21295E+02	21295E+02	21295E+02	21295E+02	21295E+02	21295E+02	21295E+02

TABLE H-1 (CONTINUED)
 FILTERED EXPERIMENT DATA HISTORIES FROM ACPR NO. 7463 CORRECTED FOR RADIATION INDUCED SIGNALS BY
 DATA FROM ACPR NO. 7836 FOR SAMPLE 30-10

ELAPSED TIME (SEC)	PRESSURE		PRESSURE		THERMOCOUPLE		THERMOCOUPLE		THERMOCOUPLE		THERMOCOUPLE		THERMOCOUPLE		THERMOCOUPLE	
	TRANSDUCER HIGH GAIN (PSI)	TRANSDUCER LOW GAIN (PSI)	TRANSDUCER HIGH GAIN (PSI)	TRANSDUCER LOW GAIN (PSI)	TOP OUTER (DEG C)	TOP INNER-1 (DEG C)	TOP INNER-2 (DEG C)	TOP INNER-3 (DEG C)	TOP INNER-4 (DEG C)	TOP INNER-5 (DEG C)	TOP INNER-6 (DEG C)	TOP INNER-7 (DEG C)	TOP INNER-8 (DEG C)	TOP INNER-9 (DEG C)	TOP INNER-10 (DEG C)	TOP INNER-11 (DEG C)
27999E-01	-64648E+02	-64648E+02	-64648E+02	-64648E+02	21302E+02	21302E+02	21302E+02	21302E+02	21302E+02	21302E+02	21302E+02	21302E+02	21302E+02	21302E+02	21302E+02	21302E+02
28159E-01	-68000E+02	-68000E+02	-68000E+02	-68000E+02	21309E+02	21309E+02	21309E+02	21309E+02	21309E+02	21309E+02	21309E+02	21309E+02	21309E+02	21309E+02	21309E+02	21309E+02
28319E-01	-67511E+02	-67511E+02	-67511E+02	-67511E+02	21316E+02	21316E+02	21316E+02	21316E+02	21316E+02	21316E+02	21316E+02	21316E+02	21316E+02	21316E+02	21316E+02	21316E+02
28479E-01	-61226E+02	-61226E+02	-61226E+02	-61226E+02	21323E+02	21323E+02	21323E+02	21323E+02	21323E+02	21323E+02	21323E+02	21323E+02	21323E+02	21323E+02	21323E+02	21323E+02
28639E-01	-47121E+02	-47121E+02	-47121E+02	-47121E+02	21331E+02	21331E+02	21331E+02	21331E+02	21331E+02	21331E+02	21331E+02	21331E+02	21331E+02	21331E+02	21331E+02	21331E+02
28799E-01	-23243E+02	-23243E+02	-23243E+02	-23243E+02	21340E+02	21340E+02	21340E+02	21340E+02	21340E+02	21340E+02	21340E+02	21340E+02	21340E+02	21340E+02	21340E+02	21340E+02
28959E-01	11930E+02	11930E+02	11930E+02	11930E+02	21351E+02	21351E+02	21351E+02	21351E+02	21351E+02	21351E+02	21351E+02	21351E+02	21351E+02	21351E+02	21351E+02	21351E+02
29119E-01	59768E+02	59768E+02	59768E+02	59768E+02	21362E+02	21362E+02	21362E+02	21362E+02	21362E+02	21362E+02	21362E+02	21362E+02	21362E+02	21362E+02	21362E+02	21362E+02
29279E-01	12105E+03	12105E+03	12105E+03	12105E+03	21375E+02	21375E+02	21375E+02	21375E+02	21375E+02	21375E+02	21375E+02	21375E+02	21375E+02	21375E+02	21375E+02	21375E+02
29439E-01	19624E+03	19624E+03	19624E+03	19624E+03	21391E+02	21391E+02	21391E+02	21391E+02	21391E+02	21391E+02	21391E+02	21391E+02	21391E+02	21391E+02	21391E+02	21391E+02
29599E-01	28552E+03	28552E+03	28552E+03	28552E+03	21409E+02	21409E+02	21409E+02	21409E+02	21409E+02	21409E+02	21409E+02	21409E+02	21409E+02	21409E+02	21409E+02	21409E+02
29759E-01	38902E+03	38902E+03	38902E+03	38902E+03	21429E+02	21429E+02	21429E+02	21429E+02	21429E+02	21429E+02	21429E+02	21429E+02	21429E+02	21429E+02	21429E+02	21429E+02
29919E-01	50697E+03	50697E+03	50697E+03	50697E+03	21452E+02	21452E+02	21452E+02	21452E+02	21452E+02	21452E+02	21452E+02	21452E+02	21452E+02	21452E+02	21452E+02	21452E+02
30079E-01	63976E+03	63976E+03	63976E+03	63976E+03	21478E+02	21478E+02	21478E+02	21478E+02	21478E+02	21478E+02	21478E+02	21478E+02	21478E+02	21478E+02	21478E+02	21478E+02
30239E-01	78799E+03	78799E+03	78799E+03	78799E+03	21508E+02	21508E+02	21508E+02	21508E+02	21508E+02	21508E+02	21508E+02	21508E+02	21508E+02	21508E+02	21508E+02	21508E+02
30399E-01	95229E+03	95229E+03	95229E+03	95229E+03	21541E+02	21541E+02	21541E+02	21541E+02	21541E+02	21541E+02	21541E+02	21541E+02	21541E+02	21541E+02	21541E+02	21541E+02
30559E-01	11331E+04	11331E+04	11331E+04	11331E+04	21579E+02	21579E+02	21579E+02	21579E+02	21579E+02	21579E+02	21579E+02	21579E+02	21579E+02	21579E+02	21579E+02	21579E+02
30719E-01	13305E+04	13305E+04	13305E+04	13305E+04	21620E+02	21620E+02	21620E+02	21620E+02	21620E+02	21620E+02	21620E+02	21620E+02	21620E+02	21620E+02	21620E+02	21620E+02
30879E-01	15437E+04	15437E+04	15437E+04	15437E+04	21667E+02	21667E+02	21667E+02	21667E+02	21667E+02	21667E+02	21667E+02	21667E+02	21667E+02	21667E+02	21667E+02	21667E+02
31039E-01	17710E+04	17710E+04	17710E+04	17710E+04	21718E+02	21718E+02	21718E+02	21718E+02	21718E+02	21718E+02	21718E+02	21718E+02	21718E+02	21718E+02	21718E+02	21718E+02
31199E-01	20096E+04	20096E+04	20096E+04	20096E+04	21774E+02	21774E+02	21774E+02	21774E+02	21774E+02	21774E+02	21774E+02	21774E+02	21774E+02	21774E+02	21774E+02	21774E+02
31359E-01	22558E+04	22558E+04	22558E+04	22558E+04	21836E+02	21836E+02	21836E+02	21836E+02	21836E+02	21836E+02	21836E+02	21836E+02	21836E+02	21836E+02	21836E+02	21836E+02
31519E-01	25052E+04	25052E+04	25052E+04	25052E+04	21904E+02	21904E+02	21904E+02	21904E+02	21904E+02	21904E+02	21904E+02	21904E+02	21904E+02	21904E+02	21904E+02	21904E+02
31679E-01	27531E+04	27531E+04	27531E+04	27531E+04	21977E+02	21977E+02	21977E+02	21977E+02	21977E+02	21977E+02	21977E+02	21977E+02	21977E+02	21977E+02	21977E+02	21977E+02
31839E-01	29947E+04	29947E+04	29947E+04	29947E+04	22057E+02	22057E+02	22057E+02	22057E+02	22057E+02	22057E+02	22057E+02	22057E+02	22057E+02	22057E+02	22057E+02	22057E+02
31999E-01	32259E+04	32259E+04	32259E+04	32259E+04	22144E+02	22144E+02	22144E+02	22144E+02	22144E+02	22144E+02	22144E+02	22144E+02	22144E+02	22144E+02	22144E+02	22144E+02
32159E-01	34436E+04	34436E+04	34436E+04	34436E+04	22237E+02	22237E+02	22237E+02	22237E+02	22237E+02	22237E+02	22237E+02	22237E+02	22237E+02	22237E+02	22237E+02	22237E+02
32319E-01	36456E+04	36456E+04	36456E+04	36456E+04	22337E+02	22337E+02	22337E+02	22337E+02	22337E+02	22337E+02	22337E+02	22337E+02	22337E+02	22337E+02	22337E+02	22337E+02
32479E-01	38310E+04	38310E+04	38310E+04	38310E+04	22444E+02	22444E+02	22444E+02	22444E+02	22444E+02	22444E+02	22444E+02	22444E+02	22444E+02	22444E+02	22444E+02	22444E+02
32639E-01	40001E+04	40001E+04	40001E+04	40001E+04	22559E+02	22559E+02	22559E+02	22559E+02	22559E+02	22559E+02	22559E+02	22559E+02	22559E+02	22559E+02	22559E+02	22559E+02
32799E-01	41538E+04	41538E+04	41538E+04	41538E+04	22682E+02	22682E+02	22682E+02	22682E+02	22682E+02	22682E+02	22682E+02	22682E+02	22682E+02	22682E+02	22682E+02	22682E+02
32959E-01	42937E+04	42937E+04	42937E+04	42937E+04	22813E+02	22813E+02	22813E+02	22813E+02	22813E+02	22813E+02	22813E+02	22813E+02	22813E+02	22813E+02	22813E+02	22813E+02
33119E-01	44215E+04	44215E+04	44215E+04	44215E+04	22952E+02	22952E+02	22952E+02	22952E+02	22952E+02	22952E+02	22952E+02	22952E+02	22952E+02	22952E+02	22952E+02	22952E+02
33279E-01	45387E+04	45387E+04	45387E+04	45387E+04	23099E+02	23099E+02	23099E+02	23099E+02	23099E+02	23099E+02	23099E+02	23099E+02	23099E+02	23099E+02	23099E+02	23099E+02
33439E-01	46465E+04	46465E+04	46465E+04	46465E+04	23255E+02	23255E+02	23255E+02	23255E+02	23255E+02	23255E+02	23255E+02	23255E+02	23255E+02	23255E+02	23255E+02	23255E+02

TABLE M-1 (CONTINUED)
 FILTERED EXPERIMENT DATA HISTORIES FROM ACPR NO. 7863 CORRECTED FOR RADIATION INDUCED SIGNALS BY
 DATA FROM ACPR NO. 7836 FOR SAMPLE 30-10

ELAPSED TIME (SEC)	PRESSURE TRANSDUCER		THERMOCOUPLE BOTTOM OUTER (DEG C)		THERMOCOUPLE BOTTOM INNER-1 (DEG C)		THERMOCOUPLE BOTTOM INNER-2 (DEG C)		THERMOCOUPLE SIDE UPPER (DEG C)		THERMOCOUPLE SIDE LOWER (DEG C)	
	HIGH GAIN (PSI)	LOW GAIN (PSI)										
33599L-01	47455E+04	47455E+04	23420F+02	23420E+02	23420E+02	23420E+02	23420E+02	23420E+02	23420E+02	23420E+02	23420E+02	23420E+02
33759L-01	48361F+04	48361E+04	23594E+02	23594E+02	23594E+02	23594E+02	23594E+02	23594E+02	23594E+02	23594E+02	23594E+02	23594E+02
33919L-01	49180E+04	49180E+04	23777F+02	23777E+02	23777E+02	23777E+02	23777E+02	23777E+02	23777E+02	23777E+02	23777E+02	23777E+02
34079L-01	49911E+04	49911E+04	23969E+02	23969E+02	23969E+02	23969E+02	23969E+02	23969E+02	23969E+02	23969E+02	23969E+02	23969E+02
34239L-01	50550E+04	50550E+04	24171E+02	24171E+02	24171E+02	24171E+02	24171E+02	24171E+02	24171E+02	24171E+02	24171E+02	24171E+02
34399L-01	51094E+04	51094E+04	24382F+02	24382E+02	24382E+02	24382E+02	24382E+02	24382E+02	24382E+02	24382E+02	24382E+02	24382E+02
34559L-01	51545E+04	51545E+04	24603E+02	24603E+02	24603E+02	24603E+02	24603E+02	24603E+02	24603E+02	24603E+02	24603E+02	24603E+02
34719L-01	51904E+04	51904E+04	24835E+02	24835E+02	24835E+02	24835E+02	24835E+02	24835E+02	24835E+02	24835E+02	24835E+02	24835E+02
34879L-01	52177E+04	52177E+04	25076E+02	25076E+02	25076E+02	25076E+02	25076E+02	25076E+02	25076E+02	25076E+02	25076E+02	25076E+02
35039L-01	52368E+04	52368E+04	25327F+02	25327E+02	25327E+02	25327E+02	25327E+02	25327E+02	25327E+02	25327E+02	25327E+02	25327E+02
35199L-01	52484E+04	52484E+04	25589F+02	25589E+02	25589E+02	25589E+02	25589E+02	25589E+02	25589E+02	25589E+02	25589E+02	25589E+02
35359L-01	52534F+04	52534E+04	25861F+02	25861E+02	25861E+02	25861E+02	25861E+02	25861E+02	25861E+02	25861E+02	25861E+02	25861E+02
35519L-01	52523E+04	52523E+04	26143E+02	26143E+02	26143E+02	26143E+02	26143E+02	26143E+02	26143E+02	26143E+02	26143E+02	26143E+02
35679L-01	52458E+04	52458E+04	26436E+02	26436E+02	26436E+02	26436E+02	26436E+02	26436E+02	26436E+02	26436E+02	26436E+02	26436E+02
35839L-01	52345E+04	52345E+04	26740F+02	26740E+02	26740E+02	26740E+02	26740E+02	26740E+02	26740E+02	26740E+02	26740E+02	26740E+02
35999L-01	52190E+04	52190E+04	27055E+02	27055E+02	27055E+02	27055E+02	27055E+02	27055E+02	27055E+02	27055E+02	27055E+02	27055E+02
36159L-01	51998E+04	51998E+04	27380F+02	27380E+02	27380E+02	27380E+02	27380E+02	27380E+02	27380E+02	27380E+02	27380E+02	27380E+02
36319L-01	51774E+04	51774E+04	27716E+02	27716E+02	27716E+02	27716E+02	27716E+02	27716E+02	27716E+02	27716E+02	27716E+02	27716E+02
36479L-01	51523E+04	51523E+04	28063E+02	28063E+02	28063E+02	28063E+02	28063E+02	28063E+02	28063E+02	28063E+02	28063E+02	28063E+02
36639L-01	51248E+04	51248E+04	28421E+02	28421E+02	28421E+02	28421E+02	28421E+02	28421E+02	28421E+02	28421E+02	28421E+02	28421E+02
36799L-01	50950E+04	50950E+04	28789E+02	28789E+02	28789E+02	28789E+02	28789E+02	28789E+02	28789E+02	28789E+02	28789E+02	28789E+02
36959L-01	50631E+04	50631E+04	29169E+02	29169E+02	29169E+02	29169E+02	29169E+02	29169E+02	29169E+02	29169E+02	29169E+02	29169E+02
37119L-01	50290E+04	50290E+04	29560E+02	29560E+02	29560E+02	29560E+02	29560E+02	29560E+02	29560E+02	29560E+02	29560E+02	29560E+02
37279L-01	49925E+04	49925E+04	29962E+02	29962E+02	29962E+02	29962E+02	29962E+02	29962E+02	29962E+02	29962E+02	29962E+02	29962E+02
37439L-01	49535E+04	49535E+04	30375E+02	30375E+02	30375E+02	30375E+02	30375E+02	30375E+02	30375E+02	30375E+02	30375E+02	30375E+02
37599L-01	49120E+04	49120E+04	30799E+02	30799E+02	30799E+02	30799E+02	30799E+02	30799E+02	30799E+02	30799E+02	30799E+02	30799E+02
37759L-01	48679E+04	48679E+04	31234E+02	31234E+02	31234E+02	31234E+02	31234E+02	31234E+02	31234E+02	31234E+02	31234E+02	31234E+02
37919L-01	48214E+04	48214E+04	31680E+02	31680E+02	31680E+02	31680E+02	31680E+02	31680E+02	31680E+02	31680E+02	31680E+02	31680E+02
38079E-01	47726E+04	47726E+04	32137E+02	32137E+02	32137E+02	32137E+02	32137E+02	32137E+02	32137E+02	32137E+02	32137E+02	32137E+02
38239E-01	47218E+04	47218E+04	32605E+02	32605E+02	32605E+02	32605E+02	32605E+02	32605E+02	32605E+02	32605E+02	32605E+02	32605E+02
38399E-01	46693E+04	46693E+04	33084E+02	33084E+02	33084E+02	33084E+02	33084E+02	33084E+02	33084E+02	33084E+02	33084E+02	33084E+02
38559E-01	46152E+04	46152E+04	33574E+02	33574E+02	33574E+02	33574E+02	33574E+02	33574E+02	33574E+02	33574E+02	33574E+02	33574E+02
38719E-01	45598E+04	45598E+04	34075E+02	34075E+02	34075E+02	34075E+02	34075E+02	34075E+02	34075E+02	34075E+02	34075E+02	34075E+02
38879E-01	45032E+04	45032E+04	34588E+02	34588E+02	34588E+02	34588E+02	34588E+02	34588E+02	34588E+02	34588E+02	34588E+02	34588E+02
39039E-01	44455E+04	44455E+04	35111E+02	35111E+02	35111E+02	35111E+02	35111E+02	35111E+02	35111E+02	35111E+02	35111E+02	35111E+02

TABLE 4-1 (CONTINUED)
 FILTERED EXPERIMENT DATA HISTORIES FROM ACPR NO. 7836 CORRECTED FOR RADIATION INDUCED SIGNALS BY
 DATA FROM ACPR NO. 7836 FOR SAMPLE 30-10

ELAPSED TIME (SEC)	PRESSURE TRANSDUCER HIGH GAIN (PSI)	PRESSURE TRANSDUCER LOW GAIN (PSI)	THERMOCOUPLE BOTTOM OUTER (DEG C)	THERMOCOUPLE ROTTOM INNER-1 (DEG C)	THERMOCOUPLE ROTTOM INNER-2 (DEG C)	THERMOCOUPLE SIDE UPPER (DEG C)	THERMOCOUPLE SIDE LOWER (DEG C)
.39199E-01	.43867E+04	.43867E+04	.35645E+02	.35645E+02	.35645E+02	.35645E+02	.35645E+02
.39359E-01	.43269E+04	.43269E+04	.36190E+02	.36190E+02	.36190E+02	.36190E+02	.36190E+02
.39519E-01	.42662E+04	.42662E+04	.36746E+02	.36746E+02	.36746E+02	.36746E+02	.36746E+02
.39679E-01	.42046E+04	.42046E+04	.37313E+02	.37313E+02	.37313E+02	.37313E+02	.37313E+02
.39839E-01	.41421E+04	.41421E+04	.37891E+02	.37891E+02	.37891E+02	.37891E+02	.37891E+02
.39999E-01	.40790E+04	.40790E+04	.38480E+02	.38480E+02	.38480E+02	.38480E+02	.38480E+02
.40159E-01	.40152E+04	.40152E+04	.39080E+02	.39080E+02	.39080E+02	.39080E+02	.39080E+02
.40319E-01	.39509E+04	.39509E+04	.39691E+02	.39691E+02	.39691E+02	.39691E+02	.39691E+02
.40479E-01	.38861E+04	.38861E+04	.40312E+02	.40312E+02	.40312E+02	.40312E+02	.40312E+02
.40639E-01	.38209E+04	.38209E+04	.40944E+02	.40944E+02	.40944E+02	.40944E+02	.40944E+02
.40799E-01	.37553E+04	.37553E+04	.41587E+02	.41587E+02	.41587E+02	.41587E+02	.41587E+02
.40959E-01	.36894E+04	.36894E+04	.42241E+02	.42241E+02	.42241E+02	.42241E+02	.42241E+02
.41119E-01	.36232E+04	.36232E+04	.42906E+02	.42906E+02	.42906E+02	.42906E+02	.42906E+02
.41279E-01	.35569E+04	.35569E+04	.43581E+02	.43581E+02	.43581E+02	.43581E+02	.43581E+02
.41439E-01	.34906E+04	.34906E+04	.44267E+02	.44267E+02	.44267E+02	.44267E+02	.44267E+02
.41599E-01	.34245E+04	.34245E+04	.44964E+02	.44964E+02	.44964E+02	.44964E+02	.44964E+02
.41759E-01	.33586E+04	.33586E+04	.45672E+02	.45672E+02	.45672E+02	.45672E+02	.45672E+02
.41919E-01	.32931E+04	.32931E+04	.46391E+02	.46391E+02	.46391E+02	.46391E+02	.46391E+02
.42079E-01	.32281E+04	.32281E+04	.47120E+02	.47120E+02	.47120E+02	.47120E+02	.47120E+02
.42239E-01	.31635E+04	.31635E+04	.47860E+02	.47860E+02	.47860E+02	.47860E+02	.47860E+02
.42399E-01	.30994E+04	.30994E+04	.48611E+02	.48611E+02	.48611E+02	.48611E+02	.48611E+02
.42559E-01	.30355E+04	.30355E+04	.49372E+02	.49372E+02	.49372E+02	.49372E+02	.49372E+02
.42719E-01	.29717E+04	.29717E+04	.50145E+02	.50145E+02	.50145E+02	.50145E+02	.50145E+02
.42879E-01	.29078E+04	.29078E+04	.50928E+02	.50928E+02	.50928E+02	.50928E+02	.50928E+02
.43039E-01	.28436E+04	.28436E+04	.51722E+02	.51722E+02	.51722E+02	.51722E+02	.51722E+02
.43199E-01	.27789E+04	.27789E+04	.52526E+02	.52526E+02	.52526E+02	.52526E+02	.52526E+02
.43359E-01	.27139E+04	.27139E+04	.53342E+02	.53342E+02	.53342E+02	.53342E+02	.53342E+02
.43519E-01	.26484E+04	.26484E+04	.54168E+02	.54168E+02	.54168E+02	.54168E+02	.54168E+02
.43679E-01	.25829E+04	.25829E+04	.55005E+02	.55005E+02	.55005E+02	.55005E+02	.55005E+02
.43839E-01	.25174E+04	.25174E+04	.55853E+02	.55853E+02	.55853E+02	.55853E+02	.55853E+02
.43999E-01	.24524E+04	.24524E+04	.56712E+02	.56712E+02	.56712E+02	.56712E+02	.56712E+02
.44159E-01	.23881E+04	.23881E+04	.57582E+02	.57582E+02	.57582E+02	.57582E+02	.57582E+02
.44319E-01	.23248E+04	.23248E+04	.58462E+02	.58462E+02	.58462E+02	.58462E+02	.58462E+02
.44479E-01	.22625E+04	.22625E+04	.59353E+02	.59353E+02	.59353E+02	.59353E+02	.59353E+02
.44639E-01	.22012E+04	.22012E+04	.60255E+02	.60255E+02	.60255E+02	.60255E+02	.60255E+02

TABLE H-1 (CONTINUED)
 FILTERED EXPERIMENT DATA HISTORIES FROM ACPR NO. 7863 CORRECTED FOR RADIATION INDUCED SIGNALS BY
 DATA FROM ACPR NO. 7836 FOR SAMPLE 30-10

ELAPSED TIME (SEC)	PRESSURE TRANSDUCER HIGH GAIN (PSI)	PRESSURE TRANSDUCER LOW GAIN (PSI)	THERMOCOUPLE BOTTOM OUTER (DEG C)	THERMOCOUPLE BOTTOM INNER-1 (DEG C)	THERMOCOUPLE BOTTOM INNER-2 (DEG C)	THERMOCOUPLE SIDE UPPER (DEG C)	THERMOCOUPLE SIDE LOWER (DEG C)
.44799E-01	.21408E+04	.21408E+04	.61168E+02	.61168E+02	.61168E+02	.61168E+02	.61168E+02
.44959E-01	.20808E+04	.20808E+04	.62092E+02	.62092E+02	.62092E+02	.62092E+02	.62092E+02
.45119E-01	.20210E+04	.20210E+04	.63026E+02	.63026E+02	.63026E+02	.63026E+02	.63026E+02
.45279E-01	.19610E+04	.19610E+04	.63971E+02	.63971E+02	.63971E+02	.63971E+02	.63971E+02
.45439E-01	.19005E+04	.19005E+04	.64927E+02	.64927E+02	.64927E+02	.64927E+02	.64927E+02
.45599E-01	.18394E+04	.18394E+04	.65894E+02	.65894E+02	.65894E+02	.65894E+02	.65894E+02
.45759E-01	.17777E+04	.17777E+04	.66871E+02	.66871E+02	.66871E+02	.66871E+02	.66871E+02
.45919E-01	.17155E+04	.17155E+04	.67859E+02	.67859E+02	.67859E+02	.67859E+02	.67859E+02
.46079E-01	.16531E+04	.16531E+04	.68857E+02	.68857E+02	.68857E+02	.68857E+02	.68857E+02
.46239E-01	.15908E+04	.15908E+04	.69866E+02	.69866E+02	.69866E+02	.69866E+02	.69866E+02
.46399E-01	.15289E+04	.15289E+04	.70886E+02	.70886E+02	.70886E+02	.70886E+02	.70886E+02
.46559E-01	.14676E+04	.14676E+04	.71916E+02	.71916E+02	.71916E+02	.71916E+02	.71916E+02
.46719E-01	.14071E+04	.14071E+04	.72956E+02	.72956E+02	.72956E+02	.72956E+02	.72956E+02
.46879E-01	.13476E+04	.13476E+04	.74006E+02	.74006E+02	.74006E+02	.74006E+02	.74006E+02
.47039E-01	.12891E+04	.12891E+04	.75067E+02	.75067E+02	.75067E+02	.75067E+02	.75067E+02
.47199E-01	.12315E+04	.12315E+04	.76137E+02	.76137E+02	.76137E+02	.76137E+02	.76137E+02
.47359E-01	.11748E+04	.11748E+04	.77218E+02	.77218E+02	.77218E+02	.77218E+02	.77218E+02
.47519E-01	.11191E+04	.11191E+04	.78309E+02	.78309E+02	.78309E+02	.78309E+02	.78309E+02
.47679E-01	.10642E+04	.10642E+04	.79409E+02	.79409E+02	.79409E+02	.79409E+02	.79409E+02
.47839E-01	.10103E+04	.10103E+04	.80519E+02	.80519E+02	.80519E+02	.80519E+02	.80519E+02
.47999E-01	.95738E+03	.95738E+03	.81639E+02	.81639E+02	.81639E+02	.81639E+02	.81639E+02
.48159E-01	.90538E+03	.90538E+03	.82768E+02	.82768E+02	.82768E+02	.82768E+02	.82768E+02
.48319E-01	.85427E+03	.85427E+03	.83906E+02	.83906E+02	.83906E+02	.83906E+02	.83906E+02
.48479E-01	.80396E+03	.80396E+03	.85053E+02	.85053E+02	.85053E+02	.85053E+02	.85053E+02
.48639E-01	.75432E+03	.75432E+03	.86209E+02	.86209E+02	.86209E+02	.86209E+02	.86209E+02
.48799E-01	.70520E+03	.70520E+03	.87374E+02	.87374E+02	.87374E+02	.87374E+02	.87374E+02
.48959E-01	.65648E+03	.65648E+03	.88548E+02	.88548E+02	.88548E+02	.88548E+02	.88548E+02
.49119E-01	.60808E+03	.60808E+03	.89730E+02	.89730E+02	.89730E+02	.89730E+02	.89730E+02
.49279E-01	.56002E+03	.56002E+03	.90920E+02	.90920E+02	.90920E+02	.90920E+02	.90920E+02
.49438E-01	.51236E+03	.51236E+03	.92118E+02	.92118E+02	.92118E+02	.92118E+02	.92118E+02
.49599E-01	.46523E+03	.46523E+03	.93323E+02	.93323E+02	.93323E+02	.93323E+02	.93323E+02
.49759E-01	.41875E+03	.41875E+03	.94537E+02	.94537E+02	.94537E+02	.94537E+02	.94537E+02
.49918E-01	.37307E+03	.37307E+03	.95757E+02	.95757E+02	.95757E+02	.95757E+02	.95757E+02
.50078E-01	.32825E+03	.32825E+03	.96985E+02	.96985E+02	.96985E+02	.96985E+02	.96985E+02
.50239E-01	.28431E+03	.28431E+03	.98219E+02	.98219E+02	.98219E+02	.98219E+02	.98219E+02

TABLE M-1 (CONTINUED)
 FILTERED EXPERIMENT DATA HISTORIES FROM ACPR NO. 7863 CORRECTED FOR RADIATION INDUCED SIGNALS BY
 DATA FROM ACPR NO. 7836 FOR SAMPLE 30-10

ELAPSED TIME (SEC)	PRESSURE TRANSDUCER HIGH GAIN (PSI)		PRESSURE TRANSDUCER LOW GAIN (PSI)		THERMOCOUPLE BOTTOM OUTER (DEG C)		THERMOCOUPLE BOTTOM INNER-1 (DEG C)		THERMOCOUPLE BOTTOM INNER-2 (DEG C)		THERMOCOUPLE SIDE UPPER (DEG C)		THERMOCOUPLE SIDE LOWER (DEG C)	
50399E-01	24118E+03		24118E+03		99460E+02		99460E+02		99460E+02		99460E+02		99460E+02	
50558E-01	19876E+03		19876E+03		10071E+03		10071E+03		10071E+03		10071E+03		10071E+03	
50719E-01	15688E+03		15688E+03		10196E+03		10196E+03		10196E+03		10196E+03		10196E+03	
50879E-01	11539E+03		11539E+03		10322E+03		10322E+03		10322E+03		10322E+03		10322E+03	
51038E-01	74159E+02		74159E+02		10449E+03		10449E+03		10449E+03		10449E+03		10449E+03	
51198E-01	33103E+02		33103E+02		10576E+03		10576E+03		10576E+03		10576E+03		10576E+03	
51359E-01	77916E+01		77916E+01		10703E+03		10703E+03		10703E+03		10703E+03		10703E+03	
51519E-01	48472E+02		48472E+02		10831E+03		10831E+03		10831E+03		10831E+03		10831E+03	
51678E-01	88425E+02		88425E+02		10959E+03		10959E+03		10959E+03		10959E+03		10959E+03	
51838E-01	12870E+03		12870E+03		11088E+03		11088E+03		11088E+03		11088E+03		11088E+03	
51998E-01	16793E+03		16793E+03		11218E+03		11218E+03		11218E+03		11218E+03		11218E+03	
52158E-01	20637E+03		20637E+03		11347E+03		11347E+03		11347E+03		11347E+03		11347E+03	
52318E-01	24392E+03		24392E+03		11477E+03		11477E+03		11477E+03		11477E+03		11477E+03	
52478E-01	28055E+03		28055E+03		11607E+03		11607E+03		11607E+03		11607E+03		11607E+03	
52638E-01	31628E+03		31628E+03		11738E+03		11738E+03		11738E+03		11738E+03		11738E+03	
52798E-01	35123E+03		35123E+03		11869E+03		11869E+03		11869E+03		11869E+03		11869E+03	
52958E-01	38554E+03		38554E+03		12000E+03		12000E+03		12000E+03		12000E+03		12000E+03	
53118E-01	41939E+03		41939E+03		12131E+03		12131E+03		12131E+03		12131E+03		12131E+03	
53278E-01	45295E+03		45295E+03		12263E+03		12263E+03		12263E+03		12263E+03		12263E+03	
53438E-01	48633E+03		48633E+03		12394E+03		12394E+03		12394E+03		12394E+03		12394E+03	
53598E-01	51958E+03		51958E+03		12526E+03		12526E+03		12526E+03		12526E+03		12526E+03	
53758E-01	55269E+03		55269E+03		12658E+03		12658E+03		12658E+03		12658E+03		12658E+03	
53918E-01	58556E+03		58556E+03		12790E+03		12790E+03		12790E+03		12790E+03		12790E+03	
54078E-01	61804E+03		61804E+03		12922E+03		12922E+03		12922E+03		12922E+03		12922E+03	
54238E-01	64996E+03		64996E+03		13054E+03		13054E+03		13054E+03		13054E+03		13054E+03	
54398E-01	68116E+03		68116E+03		13186E+03		13186E+03		13186E+03		13186E+03		13186E+03	
54558E-01	71153E+03		71153E+03		13318E+03		13318E+03		13318E+03		13318E+03		13318E+03	
54718E-01	74103E+03		74103E+03		13450E+03		13450E+03		13450E+03		13450E+03		13450E+03	
54878E-01	76972E+03		76972E+03		13582E+03		13582E+03		13582E+03		13582E+03		13582E+03	
55038E-01	79774E+03		79774E+03		13714E+03		13714E+03		13714E+03		13714E+03		13714E+03	
55198E-01	82530E+03		82530E+03		13846E+03		13846E+03		13846E+03		13846E+03		13846E+03	
55358E-01	85268E+03		85268E+03		13977E+03		13977E+03		13977E+03		13977E+03		13977E+03	
55518E-01	88011E+03		88011E+03		14109E+03		14109E+03		14109E+03		14109E+03		14109E+03	
55678E-01	90783E+03		90783E+03		14240E+03		14240E+03		14240E+03		14240E+03		14240E+03	
55838E-01	93599E+03		93599E+03		14372E+03		14372E+03		14372E+03		14372E+03		14372E+03	

TABLE H-1 (CONTINUED)
 FILTERED EXPERIMENT DATA HISTORIES FROM ACPR NO. 7863 CORRECTED FOR RADIATION INDUCED SIGNALS BY
 DATA FROM ACPR NO. 7836 FOR SAMPLE 30-10

ELAPSED TIME (SEC)	PRESSURE TRANSDUCER HIGH GAIN (PSI)		PRESSURE TRANSDUCER LOW GAIN (PSI)		THERMOCOUPLE BOTTOM OUTER (DEG C)		THERMOCOUPLE BOTTOM INNER-1 (DEG C)		THERMOCOUPLE ROTOM INNER-2 (DEG C)		THERMOCOUPLE SIDE UPPER (DEG C)		THERMOCOUPLE SIDE LOWER (DEG C)	
.55998E-01	--.96465E+03	--.96465E+03	--.96465E+03	--.96465E+03	.14503E+03	.14503E+03	.14503E+03	.14503E+03	.14503E+03	.14503E+03	.14503E+03	.14503E+03	.14503E+03	.14503E+03
.56158E-01	--.99377E+03	--.99377E+03	--.99377E+03	--.99377E+03	.14634E+03	.14634E+03	.14634E+03	.14634E+03	.14634E+03	.14634E+03	.14634E+03	.14634E+03	.14634E+03	.14634E+03
.56318E-01	--.10232E+04	--.10232E+04	--.10232E+04	--.10232E+04	.14765E+03	.14765E+03	.14765E+03	.14765E+03	.14765E+03	.14765E+03	.14765E+03	.14765E+03	.14765E+03	.14765E+03
.56478E-01	--.10528E+04	--.10528E+04	--.10528E+04	--.10528E+04	.14896E+03	.14896E+03	.14896E+03	.14896E+03	.14896E+03	.14896E+03	.14896E+03	.14896E+03	.14896E+03	.14896E+03
.56638E-01	--.10823E+04	--.10823E+04	--.10823E+04	--.10823E+04	.15026E+03	.15026E+03	.15026E+03	.15026E+03	.15026E+03	.15026E+03	.15026E+03	.15026E+03	.15026E+03	.15026E+03
.56798E-01	--.11113E+04	--.11113E+04	--.11113E+04	--.11113E+04	.15157E+03	.15157E+03	.15157E+03	.15157E+03	.15157E+03	.15157E+03	.15157E+03	.15157E+03	.15157E+03	.15157E+03
.56958E-01	--.11397E+04	--.11397E+04	--.11397E+04	--.11397E+04	.15287E+03	.15287E+03	.15287E+03	.15287E+03	.15287E+03	.15287E+03	.15287E+03	.15287E+03	.15287E+03	.15287E+03
.57118E-01	--.11673E+04	--.11673E+04	--.11673E+04	--.11673E+04	.15417E+03	.15417E+03	.15417E+03	.15417E+03	.15417E+03	.15417E+03	.15417E+03	.15417E+03	.15417E+03	.15417E+03
.57278E-01	--.11940E+04	--.11940E+04	--.11940E+04	--.11940E+04	.15546E+03	.15546E+03	.15546E+03	.15546E+03	.15546E+03	.15546E+03	.15546E+03	.15546E+03	.15546E+03	.15546E+03
.57438E-01	--.12199E+04	--.12199E+04	--.12199E+04	--.12199E+04	.15676E+03	.15676E+03	.15676E+03	.15676E+03	.15676E+03	.15676E+03	.15676E+03	.15676E+03	.15676E+03	.15676E+03
.57598E-01	--.12452E+04	--.12452E+04	--.12452E+04	--.12452E+04	.15805E+03	.15805E+03	.15805E+03	.15805E+03	.15805E+03	.15805E+03	.15805E+03	.15805E+03	.15805E+03	.15805E+03
.57758E-01	--.12700E+04	--.12700E+04	--.12700E+04	--.12700E+04	.15934E+03	.15934E+03	.15934E+03	.15934E+03	.15934E+03	.15934E+03	.15934E+03	.15934E+03	.15934E+03	.15934E+03
.57918E-01	--.12947E+04	--.12947E+04	--.12947E+04	--.12947E+04	.16063E+03	.16063E+03	.16063E+03	.16063E+03	.16063E+03	.16063E+03	.16063E+03	.16063E+03	.16063E+03	.16063E+03
.58078E-01	--.13197E+04	--.13197E+04	--.13197E+04	--.13197E+04	.16192E+03	.16192E+03	.16192E+03	.16192E+03	.16192E+03	.16192E+03	.16192E+03	.16192E+03	.16192E+03	.16192E+03
.58238E-01	--.13449E+04	--.13449E+04	--.13449E+04	--.13449E+04	.16320E+03	.16320E+03	.16320E+03	.16320E+03	.16320E+03	.16320E+03	.16320E+03	.16320E+03	.16320E+03	.16320E+03
.58398E-01	--.13706E+04	--.13706E+04	--.13706E+04	--.13706E+04	.16448E+03	.16448E+03	.16448E+03	.16448E+03	.16448E+03	.16448E+03	.16448E+03	.16448E+03	.16448E+03	.16448E+03
.58558E-01	--.13967E+04	--.13967E+04	--.13967E+04	--.13967E+04	.16576E+03	.16576E+03	.16576E+03	.16576E+03	.16576E+03	.16576E+03	.16576E+03	.16576E+03	.16576E+03	.16576E+03
.58718E-01	--.14231E+04	--.14231E+04	--.14231E+04	--.14231E+04	.16704E+03	.16704E+03	.16704E+03	.16704E+03	.16704E+03	.16704E+03	.16704E+03	.16704E+03	.16704E+03	.16704E+03
.58878E-01	--.14496E+04	--.14496E+04	--.14496E+04	--.14496E+04	.16831E+03	.16831E+03	.16831E+03	.16831E+03	.16831E+03	.16831E+03	.16831E+03	.16831E+03	.16831E+03	.16831E+03
.59038E-01	--.14759E+04	--.14759E+04	--.14759E+04	--.14759E+04	.16959E+03	.16959E+03	.16959E+03	.16959E+03	.16959E+03	.16959E+03	.16959E+03	.16959E+03	.16959E+03	.16959E+03
.59198E-01	--.15018E+04	--.15018E+04	--.15018E+04	--.15018E+04	.17086E+03	.17086E+03	.17086E+03	.17086E+03	.17086E+03	.17086E+03	.17086E+03	.17086E+03	.17086E+03	.17086E+03
.59358E-01	--.15272E+04	--.15272E+04	--.15272E+04	--.15272E+04	.17213E+03	.17213E+03	.17213E+03	.17213E+03	.17213E+03	.17213E+03	.17213E+03	.17213E+03	.17213E+03	.17213E+03
.59518E-01	--.15520E+04	--.15520E+04	--.15520E+04	--.15520E+04	.17340E+03	.17340E+03	.17340E+03	.17340E+03	.17340E+03	.17340E+03	.17340E+03	.17340E+03	.17340E+03	.17340E+03
.59678E-01	--.15763E+04	--.15763E+04	--.15763E+04	--.15763E+04	.17466E+03	.17466E+03	.17466E+03	.17466E+03	.17466E+03	.17466E+03	.17466E+03	.17466E+03	.17466E+03	.17466E+03
.59838E-01	--.16002E+04	--.16002E+04	--.16002E+04	--.16002E+04	.17592E+03	.17592E+03	.17592E+03	.17592E+03	.17592E+03	.17592E+03	.17592E+03	.17592E+03	.17592E+03	.17592E+03
.59998E-01	--.16238E+04	--.16238E+04	--.16238E+04	--.16238E+04	.17719E+03	.17719E+03	.17719E+03	.17719E+03	.17719E+03	.17719E+03	.17719E+03	.17719E+03	.17719E+03	.17719E+03
.60158E-01	--.16473E+04	--.16473E+04	--.16473E+04	--.16473E+04	.17845E+03	.17845E+03	.17845E+03	.17845E+03	.17845E+03	.17845E+03	.17845E+03	.17845E+03	.17845E+03	.17845E+03
.60318E-01	--.16708E+04	--.16708E+04	--.16708E+04	--.16708E+04	.17971E+03	.17971E+03	.17971E+03	.17971E+03	.17971E+03	.17971E+03	.17971E+03	.17971E+03	.17971E+03	.17971E+03
.60478E-01	--.16944E+04	--.16944E+04	--.16944E+04	--.16944E+04	.18097E+03	.18097E+03	.18097E+03	.18097E+03	.18097E+03	.18097E+03	.18097E+03	.18097E+03	.18097E+03	.18097E+03
.60638E-01	--.17182E+04	--.17182E+04	--.17182E+04	--.17182E+04	.18222E+03	.18222E+03	.18222E+03	.18222E+03	.18222E+03	.18222E+03	.18222E+03	.18222E+03	.18222E+03	.18222E+03
.60798E-01	--.17420E+04	--.17420E+04	--.17420E+04	--.17420E+04	.18348E+03	.18348E+03	.18348E+03	.18348E+03	.18348E+03	.18348E+03	.18348E+03	.18348E+03	.18348E+03	.18348E+03
.60958E-01	--.17659E+04	--.17659E+04	--.17659E+04	--.17659E+04	.18473E+03	.18473E+03	.18473E+03	.18473E+03	.18473E+03	.18473E+03	.18473E+03	.18473E+03	.18473E+03	.18473E+03
.61118E-01	--.17898E+04	--.17898E+04	--.17898E+04	--.17898E+04	.18599E+03	.18599E+03	.18599E+03	.18599E+03	.18599E+03	.18599E+03	.18599E+03	.18599E+03	.18599E+03	.18599E+03
.61278E-01	--.18136E+04	--.18136E+04	--.18136E+04	--.18136E+04	.18724E+03	.18724E+03	.18724E+03	.18724E+03	.18724E+03	.18724E+03	.18724E+03	.18724E+03	.18724E+03	.18724E+03
.61438E-01	--.18372E+04	--.18372E+04	--.18372E+04	--.18372E+04	.18849E+03	.18849E+03	.18849E+03	.18849E+03	.18849E+03	.18849E+03	.18849E+03	.18849E+03	.18849E+03	.18849E+03

TABLE H-1 (CONTINUED)
 FILTERED EXPERIMENT DATA HISTORIES FROM ACPR NO. 7863 CORRECTED FOR RADIATION INDUCED SIGNALS BY
 DATA FROM ACPR NO. 7836 FOR SAMPLE 30-10

ELAPSED TIME (SEC)	PRESSURE TRANSDUCER HIGH GAIN (PSI)	PRESSURE TRANSDUCER LOW GAIN (PSI)	THERMOCOUPLE BOTTOM INNER-1 (DEG C)	THERMOCOUPLE BOTTOM INNER-2 (DEG C)	THERMOCOUPLE SIDE UPPER (DEG C)	THERMOCOUPLE SIDE LOWER (DEG C)
.61598E-01	-.18607E+04	-.18607E+04	.18974E+03	.18974E+03	.18974E+03	.18974E+03
.61758E-01	-.18840E+04	-.18840E+04	.19100E+03	.19100E+03	.19100E+03	.19100E+03
.61918E-01	-.19072E+04	-.19072E+04	.19225E+03	.19225E+03	.19225E+03	.19225E+03
.62078E-01	-.19302E+04	-.19302E+04	.19350E+03	.19350E+03	.19350E+03	.19350E+03
.62238E-01	-.19530E+04	-.19530E+04	.19475E+03	.19475E+03	.19475E+03	.19475E+03
.62398E-01	-.19757E+04	-.19757E+04	.19600E+03	.19600E+03	.19600E+03	.19600E+03
.62558E-01	-.19982E+04	-.19982E+04	.19726E+03	.19726E+03	.19726E+03	.19726E+03
.62718E-01	-.20204E+04	-.20204E+04	.19851E+03	.19851E+03	.19851E+03	.19851E+03
.62878E-01	-.20424E+04	-.20424E+04	.19976E+03	.19976E+03	.19976E+03	.19976E+03
.63038E-01	-.20641E+04	-.20641E+04	.20102E+03	.20102E+03	.20102E+03	.20102E+03
.63198E-01	-.20855E+04	-.20855E+04	.20227E+03	.20227E+03	.20227E+03	.20227E+03
.63358E-01	-.21065E+04	-.21065E+04	.20353E+03	.20353E+03	.20353E+03	.20353E+03
.63518E-01	-.21272E+04	-.21272E+04	.20479E+03	.20479E+03	.20479E+03	.20479E+03
.63678E-01	-.21476E+04	-.21476E+04	.20605E+03	.20605E+03	.20605E+03	.20605E+03
.63838E-01	-.21676E+04	-.21676E+04	.20731E+03	.20731E+03	.20731E+03	.20731E+03
.63998E-01	-.21872E+04	-.21872E+04	.20857E+03	.20857E+03	.20857E+03	.20857E+03
.64158E-01	-.22065E+04	-.22065E+04	.20984E+03	.20984E+03	.20984E+03	.20984E+03
.64318E-01	-.22257E+04	-.22257E+04	.21110E+03	.21110E+03	.21110E+03	.21110E+03
.64478E-01	-.22448E+04	-.22448E+04	.21237E+03	.21237E+03	.21237E+03	.21237E+03
.64638E-01	-.22639E+04	-.22639E+04	.21364E+03	.21364E+03	.21364E+03	.21364E+03
.64798E-01	-.22833E+04	-.22833E+04	.21491E+03	.21491E+03	.21491E+03	.21491E+03
.64958E-01	-.23031E+04	-.23031E+04	.21619E+03	.21619E+03	.21619E+03	.21619E+03
.65118E-01	-.23233E+04	-.23233E+04	.21747E+03	.21747E+03	.21747E+03	.21747E+03
.65278E-01	-.23440E+04	-.23440E+04	.21875E+03	.21875E+03	.21875E+03	.21875E+03
.65438E-01	-.23651E+04	-.23651E+04	.22003E+03	.22003E+03	.22003E+03	.22003E+03
.65598E-01	-.23867E+04	-.23867E+04	.22132E+03	.22132E+03	.22132E+03	.22132E+03
.65758E-01	-.24085E+04	-.24085E+04	.22261E+03	.22261E+03	.22261E+03	.22261E+03
.65918E-01	-.24304E+04	-.24304E+04	.22390E+03	.22390E+03	.22390E+03	.22390E+03
.66078E-01	-.24522E+04	-.24522E+04	.22520E+03	.22520E+03	.22520E+03	.22520E+03
.66238E-01	-.24738E+04	-.24738E+04	.22650E+03	.22650E+03	.22650E+03	.22650E+03
.66398E-01	-.24950E+04	-.24950E+04	.22780E+03	.22780E+03	.22780E+03	.22780E+03
.66558E-01	-.25159E+04	-.25159E+04	.22910E+03	.22910E+03	.22910E+03	.22910E+03
.66718E-01	-.25363E+04	-.25363E+04	.23041E+03	.23041E+03	.23041E+03	.23041E+03
.66878E-01	-.25564E+04	-.25564E+04	.23173E+03	.23173E+03	.23173E+03	.23173E+03
.67038E-01	-.25761E+04	-.25761E+04	.23304E+03	.23304E+03	.23304E+03	.23304E+03

TABLE H-1 (CONCLUDED)
 FILTERED EXPERIMENT DATA HISTORIES FROM ACPR NO. 7863 CORRECTED FOR RADIATION INDUCED SIGNALS BY
 DATA FROM ACPR NO. 7836 FOR SAMPLE 30-10

ELAPSED TIME (SEC)	PRESSURE TRANSDUCER HIGH GAIN (PSI)	PRESSURE TRANSDUCER LOW GAIN (PSI)	TEMPERATURE BOTTOM OUTER (DEG C)	TEMPERATURE BOTTOM INNER-1 (DEG C)	TEMPERATURE BOTTOM INNER-2 (DEG C)	TEMPERATURE SIDE UPPER (DEG C)	TEMPERATURE SIDE LOWER (DEG C)
67197L-01	-25955E+04	-25955E+04	23436E+03	23436E+03	23436E+03	23436E+03	23436E+03
67357L-01	-26146E+04	-26146E+04	23568E+03	23568E+03	23568E+03	23568E+03	23568E+03
67517L-01	-26333E+04	-26333E+04	23701E+03	23701E+03	23701E+03	23701E+03	23701E+03
67677L-01	-26518E+04	-26518E+04	23834E+03	23834E+03	23834E+03	23834E+03	23834E+03
67837L-01	-26700E+04	-26700E+04	23967E+03	23967E+03	23967E+03	23967E+03	23967E+03
67997L-01	-26880E+04	-26880E+04	24100E+03	24100E+03	24100E+03	24100E+03	24100E+03
68157L-01	-27058E+04	-27058E+04	24234E+03	24234E+03	24234E+03	24234E+03	24234E+03
68317L-01	-27236E+04	-27236E+04	24368E+03	24368E+03	24368E+03	24368E+03	24368E+03
68477L-01	-27414E+04	-27414E+04	24502E+03	24502E+03	24502E+03	24502E+03	24502E+03
68637L-01	-27595E+04	-27595E+04	24637E+03	24637E+03	24637E+03	24637E+03	24637E+03
68797L-01	-27778E+04	-27778E+04	24772E+03	24772E+03	24772E+03	24772E+03	24772E+03
68957L-01	-27964E+04	-27964E+04	24907E+03	24907E+03	24907E+03	24907E+03	24907E+03
69117L-01	-28152E+04	-28152E+04	25042E+03	25042E+03	25042E+03	25042E+03	25042E+03
69277L-01	-28342E+04	-28342E+04	25178E+03	25178E+03	25178E+03	25178E+03	25178E+03
69437L-01	-28531E+04	-28531E+04	25314E+03	25314E+03	25314E+03	25314E+03	25314E+03
69597L-01	-28717E+04	-28717E+04	25449E+03	25449E+03	25449E+03	25449E+03	25449E+03
69757L-01	-28899E+04	-28899E+04	25585E+03	25585E+03	25585E+03	25585E+03	25585E+03
69917L-01	-29075E+04	-29075E+04	25722E+03	25722E+03	25722E+03	25722E+03	25722E+03
70077L-01	-29246E+04	-29246E+04	25858E+03	25858E+03	25858E+03	25858E+03	25858E+03
70237L-01	-29410E+04	-29410E+04	25994E+03	25994E+03	25994E+03	25994E+03	25994E+03
70397L-01	-29570E+04	-29570E+04	26130E+03	26130E+03	26130E+03	26130E+03	26130E+03
70557L-01	-29726E+04	-29726E+04	26266E+03	26266E+03	26266E+03	26266E+03	26266E+03
70717L-01	-29881E+04	-29881E+04	26402E+03	26402E+03	26402E+03	26402E+03	26402E+03
70877L-01	-30035E+04	-30035E+04	26538E+03	26538E+03	26538E+03	26538E+03	26538E+03
71037L-01	-30190E+04	-30190E+04	26674E+03	26674E+03	26674E+03	26674E+03	26674E+03
71197L-01	-30346E+04	-30346E+04	26809E+03	26809E+03	26809E+03	26809E+03	26809E+03
71357L-01	-30504E+04	-30504E+04	26945E+03	26945E+03	26945E+03	26945E+03	26945E+03
71517L-01	-30665E+04	-30665E+04	27080E+03	27080E+03	27080E+03	27080E+03	27080E+03
71677L-01	-30828E+04	-30828E+04	27214E+03	27214E+03	27214E+03	27214E+03	27214E+03
71837L-01	-30992E+04	-30992E+04	27349E+03	27349E+03	27349E+03	27349E+03	27349E+03

TABLE H-2
INTEGRATED REACTOR POWER HISTORIES FROM ACPR NO. 7836 AND ACPR NO. 7863

ELAPSED TIME (SEC)	INTEGRATED REACTOR POWER 7836 (MJ)	ELAPSED TIME (SEC)	INTEGRATED REACTOR POWER 7836 (MJ)	ELAPSED TIME (SEC)	INTEGRATED REACTOR POWER 7863 (MJ)	ELAPSED TIME (SEC)	INTEGRATED REACTOR POWER 7836 (MJ)	ELAPSED TIME (SEC)	INTEGRATED REACTOR POWER 7863 (MJ)
0.	-66755E-05	11200E-01	91967E-03	22400E-01	12081E+01	12081E+01	12081E+01	22400E-01	12081E+01
32000E-03	-87778E-05	11520E-01	11170E-02	22720E-01	15084E+01	15084E+01	15084E+01	22720E-01	15084E+01
64000E-03	-11361E-04	11840E-01	13553E-02	23040E-01	18823E+01	18823E+01	18823E+01	23040E-01	18823E+01
96000E-03	-10793E-04	12160E-01	16404E-02	23360E-01	23476E+01	23476E+01	23476E+01	23360E-01	23476E+01
12800E-02	-82983E-05	12480E-01	19779E-02	23680E-01	29265E+01	29265E+01	29265E+01	23680E-01	29265E+01
16000E-02	-53925E-05	12800E-01	23770E-02	24000E-01	36462E+01	36462E+01	36462E+01	24000E-01	36462E+01
19200E-02	-14262E-05	13120E-01	28485E-02	24320E-01	45359E+01	45359E+01	45359E+01	24320E-01	45359E+01
22400E-02	29155E-05	13440E-01	34041E-02	24640E-01	56252E+01	56252E+01	56252E+01	24640E-01	56252E+01
25600E-02	56044E-05	13760E-01	40607E-02	24960E-01	69457E+01	69457E+01	69457E+01	24960E-01	69457E+01
28800E-02	67416E-05	14080E-01	48409E-02	25280E-01	85281E+01	85281E+01	85281E+01	25280E-01	85281E+01
32000E-02	84543E-05	14400E-01	57733E-02	25600E-01	10396E+02	10396E+02	10396E+02	25600E-01	10396E+02
35200E-02	11705E-04	14720E-01	68998E-02	25920E-01	12560E+02	12560E+02	12560E+02	25920E-01	12560E+02
38400E-02	16360E-04	15040E-01	82764E-02	26240E-01	15022E+02	15022E+02	15022E+02	26240E-01	15022E+02
41600E-02	23728E-04	15360E-01	99702E-02	26560E-01	17776E+02	17776E+02	17776E+02	26560E-01	17776E+02
44800E-02	35455E-04	15680E-01	12072E-01	26880E-01	20815E+02	20815E+02	20815E+02	26880E-01	20815E+02
48000E-02	51097E-04	16000E-01	14706E-01	27200E-01	24113E+02	24113E+02	24113E+02	27200E-01	24113E+02
51200E-02	69099E-04	16320E-01	18024E-01	27520E-01	27637E+02	27637E+02	27637E+02	27520E-01	27637E+02
54400E-02	88257E-04	16640E-01	22215E-01	27840E-01	31348E+02	31348E+02	31348E+02	27840E-01	31348E+02
57600E-02	10762E-03	16960E-01	27523E-01	28160E-01	35190E+02	35190E+02	35190E+02	28160E-01	35190E+02
60800E-02	12619E-03	17280E-01	34230E-01	28480E-01	39081E+02	39081E+02	39081E+02	28480E-01	39081E+02
64000E-02	14253E-03	17600E-01	42645E-01	28800E-01	42929E+02	42929E+02	42929E+02	28800E-01	42929E+02
67200E-02	15548E-03	17920E-01	53173E-01	29120E-01	46648E+02	46648E+02	46648E+02	29120E-01	46648E+02
70400E-02	16594E-03	18240E-01	66353E-01	29440E-01	50155E+02	50155E+02	50155E+02	29440E-01	50155E+02
73600E-02	17556E-03	18560E-01	82823E-01	29760E-01	53373E+02	53373E+02	53373E+02	29760E-01	53373E+02
76800E-02	18502E-03	18880E-01	10333E+00	30080E-01	56251E+02	56251E+02	56251E+02	30080E-01	56251E+02
80000E-02	19576E-03	19200E-01	12888E+00	30400E-01	58774E+02	58774E+02	58774E+02	30400E-01	58774E+02
83200E-02	21089E-03	19520E-01	16088E+00	30720E-01	60950E+02	60950E+02	60950E+02	30720E-01	60950E+02
86400E-02	23298E-03	19840E-01	20101E+00	31040E-01	62809E+02	62809E+02	62809E+02	31040E-01	62809E+02
89600E-02	26340E-03	20160E-01	25134E+00	31360E-01	64391E+02	64391E+02	64391E+02	31360E-01	64391E+02
92800E-02	30386E-03	20480E-01	31454E+00	31680E-01	65740E+02	65740E+02	65740E+02	31680E-01	65740E+02
96000E-02	35732E-03	20800E-01	39393E+00	32000E-01	66899E+02	66899E+02	66899E+02	32000E-01	66899E+02
99200E-02	42691E-03	21120E-01	49336E+00	32320E-01	67898E+02	67898E+02	67898E+02	32320E-01	67898E+02
102400E-01	51473E-03	21440E-01	61762E+00	32640E-01	68762E+02	68762E+02	68762E+02	32640E-01	68762E+02
105600E-01	62325E-03	21760E-01	77297E+00	32960E-01	69510E+02	69510E+02	69510E+02	32960E-01	69510E+02
108800E-01	75672E-03	22080E-01	96685E+00	33280E-01	70159E+02	70159E+02	70159E+02	33280E-01	70159E+02

TABLE H-2 (CONTINUED)
INTEGRATED REACTOR POWER HISTORIES FROM ACPR NO. 7836 AND ACPR NO. 7863

ELAPSED TIME (SEC)	INTEGRATED REACTOR POWER 7836 (MJ)	INTEGRATED REACTOR POWER 7863 (MJ)	ELAPSED TIME (SEC)	INTEGRATED REACTOR POWER 7836 (MJ)	INTEGRATED REACTOR POWER 7863 (MJ)	ELAPSED TIME (SEC)	INTEGRATED REACTOR POWER 7836 (MJ)	INTEGRATED REACTOR POWER 7863 (MJ)	ELAPSED TIME (SEC)	INTEGRATED REACTOR POWER 7836 (MJ)	INTEGRATED REACTOR POWER 7863 (MJ)
33600E-01	70720E+02	70720E+02	44799E-01	73561E+02	73561E+02	55999E-01	73561E+02	73561E+02	55999E-01	73561E+02	73701E+02
33920E-01	71119E+02	71119E+02	45119E-01	73565E+02	73565E+02	56319E-01	73565E+02	73565E+02	56319E-01	73565E+02	73705E+02
34240E-01	71604E+02	71604E+02	45439E-01	73570E+02	73570E+02	56639E-01	73570E+02	73570E+02	56639E-01	73570E+02	73709E+02
34560E-01	71943E+02	71943E+02	45759E-01	73574E+02	73574E+02	56959E-01	73574E+02	73574E+02	56959E-01	73574E+02	73713E+02
34880E-01	72223E+02	72223E+02	46079E-01	73578E+02	73578E+02	57279E-01	73578E+02	73578E+02	57279E-01	73578E+02	73717E+02
35200E-01	72452E+02	72452E+02	46399E-01	73583E+02	73583E+02	57599E-01	73583E+02	73583E+02	57599E-01	73583E+02	73721E+02
35519E-01	72639E+02	72639E+02	46719E-01	73587E+02	73587E+02	57919E-01	73587E+02	73587E+02	57919E-01	73587E+02	73724E+02
35840E-01	72791E+02	72791E+02	47039E-01	73591E+02	73591E+02	58239E-01	73591E+02	73591E+02	58239E-01	73591E+02	73728E+02
36159E-01	72914E+02	72914E+02	47359E-01	73595E+02	73595E+02	58559E-01	73595E+02	73595E+02	58559E-01	73595E+02	73732E+02
36479E-01	73015E+02	73015E+02	47679E-01	73599E+02	73599E+02	58879E-01	73599E+02	73599E+02	58879E-01	73599E+02	73736E+02
36800E-01	73098E+02	73098E+02	47999E-01	73603E+02	73603E+02	59199E-01	73603E+02	73603E+02	59199E-01	73603E+02	73740E+02
37119E-01	73166E+02	73166E+02	48319E-01	73607E+02	73607E+02	59519E-01	73607E+02	73607E+02	59519E-01	73607E+02	73744E+02
37440E-01	73222E+02	73222E+02	48639E-01	73611E+02	73611E+02	59839E-01	73611E+02	73611E+02	59839E-01	73611E+02	73748E+02
37759E-01	73269E+02	73269E+02	48959E-01	73615E+02	73615E+02	60159E-01	73615E+02	73615E+02	60159E-01	73615E+02	73752E+02
38079E-01	73309E+02	73309E+02	49279E-01	73619E+02	73619E+02	60479E-01	73619E+02	73619E+02	60479E-01	73619E+02	73756E+02
38399E-01	73342E+02	73342E+02	49599E-01	73623E+02	73623E+02	60799E-01	73623E+02	73623E+02	60799E-01	73623E+02	73759E+02
38719E-01	73370E+02	73370E+02	49919E-01	73627E+02	73627E+02	61119E-01	73627E+02	73627E+02	61119E-01	73627E+02	73763E+02
39039E-01	73395E+02	73395E+02	50239E-01	73631E+02	73631E+02	61438E-01	73631E+02	73631E+02	61438E-01	73631E+02	73767E+02
39359E-01	73416E+02	73416E+02	50559E-01	73635E+02	73635E+02	61759E-01	73635E+02	73635E+02	61759E-01	73635E+02	73771E+02
39679E-01	73434E+02	73434E+02	50879E-01	73639E+02	73639E+02	62078E-01	73639E+02	73639E+02	62078E-01	73639E+02	73775E+02
39999E-01	73450E+02	73450E+02	51199E-01	73643E+02	73643E+02	62399E-01	73643E+02	73643E+02	62399E-01	73643E+02	73779E+02
40319E-01	73463E+02	73463E+02	51519E-01	73647E+02	73647E+02	62718E-01	73647E+02	73647E+02	62718E-01	73647E+02	73783E+02
40639E-01	73476E+02	73476E+02	51839E-01	73651E+02	73651E+02	63039E-01	73651E+02	73651E+02	63039E-01	73651E+02	73787E+02
40959E-01	73487E+02	73487E+02	52159E-01	73655E+02	73655E+02	63359E-01	73655E+02	73655E+02	63359E-01	73655E+02	73791E+02
41279E-01	73496E+02	73496E+02	52479E-01	73658E+02	73658E+02	63678E-01	73658E+02	73658E+02	63678E-01	73658E+02	73794E+02
41599E-01	73505E+02	73505E+02	52799E-01	73662E+02	73662E+02	63998E-01	73662E+02	73662E+02	63998E-01	73662E+02	73798E+02
41919E-01	73513E+02	73513E+02	53119E-01	73666E+02	73666E+02	64318E-01	73666E+02	73666E+02	64318E-01	73666E+02	73802E+02
42239E-01	73520E+02	73520E+02	53439E-01	73670E+02	73670E+02	64638E-01	73670E+02	73670E+02	64638E-01	73670E+02	73806E+02
42559E-01	73526E+02	73526E+02	53759E-01	73674E+02	73674E+02	64958E-01	73674E+02	73674E+02	64958E-01	73674E+02	73810E+02
42879E-01	73532E+02	73532E+02	54079E-01	73678E+02	73678E+02	65278E-01	73678E+02	73678E+02	65278E-01	73678E+02	73814E+02
43199E-01	73537E+02	73537E+02	54399E-01	73682E+02	73682E+02	65598E-01	73682E+02	73682E+02	65598E-01	73682E+02	73818E+02
43519E-01	73543E+02	73543E+02	54719E-01	73686E+02	73686E+02	65918E-01	73686E+02	73686E+02	65918E-01	73686E+02	73822E+02
43839E-01	73547E+02	73547E+02	55039E-01	73690E+02	73690E+02	66238E-01	73690E+02	73690E+02	66238E-01	73690E+02	73826E+02
44159E-01	73552E+02	73552E+02	55359E-01	73693E+02	73693E+02	66558E-01	73693E+02	73693E+02	66558E-01	73693E+02	73830E+02
44479E-01	73557E+02	73557E+02	55679E-01	73697E+02	73697E+02	66878E-01	73697E+02	73697E+02	66878E-01	73697E+02	73833E+02

TABLE H-3
 FILTERED EXPERIMENT DATA HISTORIES FROM ACPR NO. 7866 CORRECTED FOR RADIATION INDUCED SIGNALS BY
 DATA FROM ACPR NO. 7842 FOR SAMPLE 30-11

ELAPSED TIME (SFC)	THERMOCOUPLE BOTTOM OUTER (DEG C)	THERMOCOUPLE BOTTOM INNER-1 (DEG C)	THERMOCOUPLE BOTTOM INNER-2 (DEG C)	THERMOCOUPLE SIDE UPPER (DEG C)	THERMOCOUPLE SIDE LOWER (DEG C)	THERMOCOUPLE DUMMY PLUG OUTER (DEG C)	THERMOCOUPLE DUMMY PLUG INNER-1 (DEG C)	THERMOCOUPLE DUMMY PLUG INNER-2 (DEG C)
0.	.10509E+02	.10509E+02	.10509E+02	.10509E+02	.10509E+02	-.78566E+02	-.78566E+02	-.78566E+02
.16000E-03	.10612E+02	.10612E+02	.10612E+02	.10612E+02	.10612E+02	-.78481E+02	-.78481E+02	-.78481E+02
.32000E-03	.10718E+02	.10718E+02	.10718E+02	.10718E+02	.10718E+02	-.78392E+02	-.78392E+02	-.78392E+02
.48000E-03	.10827E+02	.10827E+02	.10827E+02	.10827E+02	.10827E+02	-.78300E+02	-.78300E+02	-.78300E+02
.64000E-03	.10938E+02	.10938E+02	.10938E+02	.10938E+02	.10938E+02	-.78204E+02	-.78204E+02	-.78204E+02
.80000E-03	.11052E+02	.11052E+02	.11052E+02	.11052E+02	.11052E+02	-.78105E+02	-.78105E+02	-.78105E+02
.96000E-03	.11169E+02	.11169E+02	.11169E+02	.11169E+02	.11169E+02	-.78003E+02	-.78003E+02	-.78003E+02
.11200E-02	.11288E+02	.11288E+02	.11288E+02	.11288E+02	.11288E+02	-.77899E+02	-.77899E+02	-.77899E+02
.12800E-02	.11409E+02	.11409E+02	.11409E+02	.11409E+02	.11409E+02	-.77792E+02	-.77792E+02	-.77792E+02
.14400E-02	.11532E+02	.11532E+02	.11532E+02	.11532E+02	.11532E+02	-.77683E+02	-.77683E+02	-.77683E+02
.16000E-02	.11657E+02	.11657E+02	.11657E+02	.11657E+02	.11657E+02	-.77572E+02	-.77572E+02	-.77572E+02
.17600E-02	.11784E+02	.11784E+02	.11784E+02	.11784E+02	.11784E+02	-.77459E+02	-.77459E+02	-.77459E+02
.19200E-02	.11913E+02	.11913E+02	.11913E+02	.11913E+02	.11913E+02	-.77345E+02	-.77345E+02	-.77345E+02
.20800E-02	.12043E+02	.12043E+02	.12043E+02	.12043E+02	.12043E+02	-.77229E+02	-.77229E+02	-.77229E+02
.22400E-02	.12175E+02	.12175E+02	.12175E+02	.12175E+02	.12175E+02	-.77113E+02	-.77113E+02	-.77113E+02
.24000E-02	.12308E+02	.12308E+02	.12308E+02	.12308E+02	.12308E+02	-.76995E+02	-.76995E+02	-.76995E+02
.25600E-02	.12442E+02	.12442E+02	.12442E+02	.12442E+02	.12442E+02	-.76876E+02	-.76876E+02	-.76876E+02
.27200E-02	.12577E+02	.12577E+02	.12577E+02	.12577E+02	.12577E+02	-.76758E+02	-.76758E+02	-.76758E+02
.28800E-02	.12713E+02	.12713E+02	.12713E+02	.12713E+02	.12713E+02	-.76639E+02	-.76639E+02	-.76639E+02
.30400E-02	.12849E+02	.12849E+02	.12849E+02	.12849E+02	.12849E+02	-.76519E+02	-.76519E+02	-.76519E+02
.32000E-02	.12986E+02	.12986E+02	.12986E+02	.12986E+02	.12986E+02	-.76400E+02	-.76400E+02	-.76400E+02
.33600E-02	.13123E+02	.13123E+02	.13123E+02	.13123E+02	.13123E+02	-.76281E+02	-.76281E+02	-.76281E+02
.35200E-02	.13261E+02	.13261E+02	.13261E+02	.13261E+02	.13261E+02	-.76163E+02	-.76163E+02	-.76163E+02
.36800E-02	.13398E+02	.13398E+02	.13398E+02	.13398E+02	.13398E+02	-.76045E+02	-.76045E+02	-.76045E+02
.38400E-02	.13535E+02	.13535E+02	.13535E+02	.13535E+02	.13535E+02	-.75928E+02	-.75928E+02	-.75928E+02
.40000E-02	.13671E+02	.13671E+02	.13671E+02	.13671E+02	.13671E+02	-.75811E+02	-.75811E+02	-.75811E+02
.41600E-02	.13807E+02	.13807E+02	.13807E+02	.13807E+02	.13807E+02	-.75696E+02	-.75696E+02	-.75696E+02
.43200E-02	.13942E+02	.13942E+02	.13942E+02	.13942E+02	.13942E+02	-.75582E+02	-.75582E+02	-.75582E+02
.44800E-02	.14076E+02	.14076E+02	.14076E+02	.14076E+02	.14076E+02	-.75469E+02	-.75469E+02	-.75469E+02
.46400E-02	.14209E+02	.14209E+02	.14209E+02	.14209E+02	.14209E+02	-.75358E+02	-.75358E+02	-.75358E+02
.48000E-02	.14340E+02	.14340E+02	.14340E+02	.14340E+02	.14340E+02	-.75249E+02	-.75249E+02	-.75249E+02
.49600E-02	.14470E+02	.14470E+02	.14470E+02	.14470E+02	.14470E+02	-.75141E+02	-.75141E+02	-.75141E+02
.51200E-02	.14598E+02	.14598E+02	.14598E+02	.14598E+02	.14598E+02	-.75035E+02	-.75035E+02	-.75035E+02
.52800E-02	.14724E+02	.14724E+02	.14724E+02	.14724E+02	.14724E+02	-.74931E+02	-.74931E+02	-.74931E+02
.54400E-02	.14848E+02	.14848E+02	.14848E+02	.14848E+02	.14848E+02	-.74829E+02	-.74829E+02	-.74829E+02

TABLE H-3 (CONTINUED)
 FILTERED EXPERIMENT DATA HISTORIES FROM ACPR NO. 7866 CORRECTED FOR RADIATION INDUCED SIGNALS BY
 DATA FROM ACPR NO. 7842 FOR SAMPLE 30-11

ELAPSED TIME (SEC)	THERMOCOUPLE BOTTOM OUTER (DEG C)	THERMOCOUPLE BOTTOM INNER-1 (DEG C)	THERMOCOUPLE BOTTOM INNER-2 (DEG C)	THERMOCOUPLE SIDE UPPER (DEG C)	THERMOCOUPLE SIDE LOWER (DEG C)	THERMOCOUPLE DUMMY PLUG OUTER (DEG C)	THERMOCOUPLE DUMMY PLUG INNER-1 (DEG C)	THERMOCOUPLE DUMMY PLUG INNER-2 (DEG C)
56000E-02	14969E+02	14969E+02	14969E+02	14969E+02	14969E+02	14969E+02	14969E+02	14969E+02
57600E-02	15089E+02	15089E+02	15089E+02	15089E+02	15089E+02	15089E+02	15089E+02	15089E+02
59200E-02	15205E+02	15205E+02	15205E+02	15205E+02	15205E+02	15205E+02	15205E+02	15205E+02
60800E-02	15319E+02	15319E+02	15319E+02	15319E+02	15319E+02	15319E+02	15319E+02	15319E+02
62400E-02	15430E+02	15430E+02	15430E+02	15430E+02	15430E+02	15430E+02	15430E+02	15430E+02
64000E-02	15539E+02	15539E+02	15539E+02	15539E+02	15539E+02	15539E+02	15539E+02	15539E+02
65600E-02	15644E+02	15644E+02	15644E+02	15644E+02	15644E+02	15644E+02	15644E+02	15644E+02
67200E-02	15746E+02	15746E+02	15746E+02	15746E+02	15746E+02	15746E+02	15746E+02	15746E+02
68800E-02	15844E+02	15844E+02	15844E+02	15844E+02	15844E+02	15844E+02	15844E+02	15844E+02
70400E-02	15939E+02	15939E+02	15939E+02	15939E+02	15939E+02	15939E+02	15939E+02	15939E+02
72000E-02	16031E+02	16031E+02	16031E+02	16031E+02	16031E+02	16031E+02	16031E+02	16031E+02
73600E-02	16119E+02	16119E+02	16119E+02	16119E+02	16119E+02	16119E+02	16119E+02	16119E+02
75200E-02	16203E+02	16203E+02	16203E+02	16203E+02	16203E+02	16203E+02	16203E+02	16203E+02
76800E-02	16284E+02	16284E+02	16284E+02	16284E+02	16284E+02	16284E+02	16284E+02	16284E+02
78400E-02	16361E+02	16361E+02	16361E+02	16361E+02	16361E+02	16361E+02	16361E+02	16361E+02
80000E-02	16434E+02	16434E+02	16434E+02	16434E+02	16434E+02	16434E+02	16434E+02	16434E+02
81600E-02	16503E+02	16503E+02	16503E+02	16503E+02	16503E+02	16503E+02	16503E+02	16503E+02
83200E-02	16568E+02	16568E+02	16568E+02	16568E+02	16568E+02	16568E+02	16568E+02	16568E+02
84800E-02	16630E+02	16630E+02	16630E+02	16630E+02	16630E+02	16630E+02	16630E+02	16630E+02
86400E-02	16687E+02	16687E+02	16687E+02	16687E+02	16687E+02	16687E+02	16687E+02	16687E+02
88000E-02	16741E+02	16741E+02	16741E+02	16741E+02	16741E+02	16741E+02	16741E+02	16741E+02
89600E-02	16791E+02	16791E+02	16791E+02	16791E+02	16791E+02	16791E+02	16791E+02	16791E+02
91199E-02	16837E+02	16837E+02	16837E+02	16837E+02	16837E+02	16837E+02	16837E+02	16837E+02
92799E-02	16880E+02	16880E+02	16880E+02	16880E+02	16880E+02	16880E+02	16880E+02	16880E+02
94399E-02	16919E+02	16919E+02	16919E+02	16919E+02	16919E+02	16919E+02	16919E+02	16919E+02
96000E-02	16954E+02	16954E+02	16954E+02	16954E+02	16954E+02	16954E+02	16954E+02	16954E+02
97599E-02	16986E+02	16986E+02	16986E+02	16986E+02	16986E+02	16986E+02	16986E+02	16986E+02
99199E-02	17014E+02	17014E+02	17014E+02	17014E+02	17014E+02	17014E+02	17014E+02	17014E+02
10080E-01	17039E+02	17039E+02	17039E+02	17039E+02	17039E+02	17039E+02	17039E+02	17039E+02
10240E-01	17061E+02	17061E+02	17061E+02	17061E+02	17061E+02	17061E+02	17061E+02	17061E+02
10400E-01	17080E+02	17080E+02	17080E+02	17080E+02	17080E+02	17080E+02	17080E+02	17080E+02
10560E-01	17096E+02	17096E+02	17096E+02	17096E+02	17096E+02	17096E+02	17096E+02	17096E+02
10720E-01	17109E+02	17109E+02	17109E+02	17109E+02	17109E+02	17109E+02	17109E+02	17109E+02
10880E-01	17120E+02	17120E+02	17120E+02	17120E+02	17120E+02	17120E+02	17120E+02	17120E+02
11040E-01	17128E+02	17128E+02	17128E+02	17128E+02	17128E+02	17128E+02	17128E+02	17128E+02

TABLE H-3 (CONTINUED)

FILTERED EXPERIMENT DATA HISTORIES FROM ACPR NO. 7866 CORRECTED FOR RADIATION INDUCED SIGNALS BY
DATA FROM ACPR NO. 7842 FOR SAMPLE 30-11

ELAPSED TIME (SEC)	HEATCOUPLE BOTTOM OUTER (DEG C)	HEATCOUPLE BOTTOM INNER-1 (DEG C)	HEATCOUPLE BOTTOM INNER-2 (DEG C)	HEATCOUPLE SIDE UPPER (DEG C)	HEATCOUPLE SIDE LOWER (DEG C)	HEATCOUPLE DUMMY PLUG OUTER (DEG C)	HEATCOUPLE DUMMY PLUG INNER-1 (DEG C)	HEATCOUPLE DUMMY PLUG INNER-2 (DEG C)
11200E-01	17134E+02	17134E+02	17134E+02	17134E+02	17134E+02	17134E+02	17134E+02	17134E+02
11360E-01	17138E+02	17138E+02	17138E+02	17138E+02	17138E+02	17138E+02	17138E+02	17138E+02
11520E-01	17139E+02	17139E+02	17139E+02	17139E+02	17139E+02	17139E+02	17139E+02	17139E+02
11680E-01	17139E+02	17139E+02	17139E+02	17139E+02	17139E+02	17139E+02	17139E+02	17139E+02
11840E-01	17138E+02	17138E+02	17138E+02	17138E+02	17138E+02	17138E+02	17138E+02	17138E+02
12000E-01	17134E+02	17134E+02	17134E+02	17134E+02	17134E+02	17134E+02	17134E+02	17134E+02
12160E-01	17130E+02	17130E+02	17130E+02	17130E+02	17130E+02	17130E+02	17130E+02	17130E+02
12320E-01	17125E+02	17125E+02	17125E+02	17125E+02	17125E+02	17125E+02	17125E+02	17125E+02
12480E-01	17119E+02	17119E+02	17119E+02	17119E+02	17119E+02	17119E+02	17119E+02	17119E+02
12640E-01	17112E+02	17112E+02	17112E+02	17112E+02	17112E+02	17112E+02	17112E+02	17112E+02
12800E-01	17106E+02	17106E+02	17106E+02	17106E+02	17106E+02	17106E+02	17106E+02	17106E+02
12960E-01	17098E+02	17098E+02	17098E+02	17098E+02	17098E+02	17098E+02	17098E+02	17098E+02
13120E-01	17091E+02	17091E+02	17091E+02	17091E+02	17091E+02	17091E+02	17091E+02	17091E+02
13280E-01	17084E+02	17084E+02	17084E+02	17084E+02	17084E+02	17084E+02	17084E+02	17084E+02
13440E-01	17078E+02	17078E+02	17078E+02	17078E+02	17078E+02	17078E+02	17078E+02	17078E+02
13600E-01	17072E+02	17072E+02	17072E+02	17072E+02	17072E+02	17072E+02	17072E+02	17072E+02
13760E-01	17067E+02	17067E+02	17067E+02	17067E+02	17067E+02	17067E+02	17067E+02	17067E+02
13920E-01	17063E+02	17063E+02	17063E+02	17063E+02	17063E+02	17063E+02	17063E+02	17063E+02
14080E-01	17060E+02	17060E+02	17060E+02	17060E+02	17060E+02	17060E+02	17060E+02	17060E+02
14240E-01	17058E+02	17058E+02	17058E+02	17058E+02	17058E+02	17058E+02	17058E+02	17058E+02
14400E-01	17058E+02	17058E+02	17058E+02	17058E+02	17058E+02	17058E+02	17058E+02	17058E+02
14560E-01	17060E+02	17060E+02	17060E+02	17060E+02	17060E+02	17060E+02	17060E+02	17060E+02
14720E-01	17063E+02	17063E+02	17063E+02	17063E+02	17063E+02	17063E+02	17063E+02	17063E+02
14880E-01	17069E+02	17069E+02	17069E+02	17069E+02	17069E+02	17069E+02	17069E+02	17069E+02
15040E-01	17076E+02	17076E+02	17076E+02	17076E+02	17076E+02	17076E+02	17076E+02	17076E+02
15200E-01	17086E+02	17086E+02	17086E+02	17086E+02	17086E+02	17086E+02	17086E+02	17086E+02
15360E-01	17098E+02	17098E+02	17098E+02	17098E+02	17098E+02	17098E+02	17098E+02	17098E+02
15520E-01	17113E+02	17113E+02	17113E+02	17113E+02	17113E+02	17113E+02	17113E+02	17113E+02
15680E-01	17131E+02	17131E+02	17131E+02	17131E+02	17131E+02	17131E+02	17131E+02	17131E+02
15840E-01	17151E+02	17151E+02	17151E+02	17151E+02	17151E+02	17151E+02	17151E+02	17151E+02
16000E-01	17174E+02	17174E+02	17174E+02	17174E+02	17174E+02	17174E+02	17174E+02	17174E+02
16160E-01	17199E+02	17199E+02	17199E+02	17199E+02	17199E+02	17199E+02	17199E+02	17199E+02
16320E-01	17228E+02	17228E+02	17228E+02	17228E+02	17228E+02	17228E+02	17228E+02	17228E+02
16480E-01	17260E+02	17260E+02	17260E+02	17260E+02	17260E+02	17260E+02	17260E+02	17260E+02
16640E-01	17294E+02	17294E+02	17294E+02	17294E+02	17294E+02	17294E+02	17294E+02	17294E+02

TABLE H-3 (CONTINUED)
FILTERED EXPERIMENT DATA HISTORIES FROM ACPR NO. 7866 CORRECTED FOR RADIATION INDUCED SIGNALS BY
DATA FROM ACPR NO. 7842 FOR SAMPLE 30-11

FLAPSET TIME (SEC)	THERMOCOUPLE		THERMOCOUPLE		THERMOCOUPLE		THERMOCOUPLE		THERMOCOUPLE		THERMOCOUPLE		THERMOCOUPLE	
	BOTTOM OUTER (DEG C)	BOTTOM INNER-1 (DEG C)	BOTTOM INNER-2 (DEG C)	SIDE UPPER (DEG C)	SIDE LOWER (DEG C)	DUMMY PLUG OUTER (DEG C)	DUMMY PLUG INNER-1 (DEG C)	DUMMY PLUG INNER-2 (DEG C)	THERMO COUPLE	DUMMY PLUG	THERMO COUPLE	DUMMY PLUG	THERMO COUPLE	
33599E-01	.23420E+02	.23420E+02	.23420F+02	.23420E+02	.23420E+02	-71253E+02	-71253E+02	-71253E+02	-71253E+02	-71253E+02	-71253E+02	-71253E+02	-71253E+02	
33759E-01	.23594E+02	.23594E+02	.23594F+02	.23594E+02	.23594E+02	-70885E+02	-70885E+02	-70885E+02	-70885E+02	-70885E+02	-70885E+02	-70885E+02	-70885E+02	
33919E-01	.23777E+02	.23777E+02	.23777F+02	.23777E+02	.23777E+02	-70504E+02	-70504E+02	-70504E+02	-70504E+02	-70504E+02	-70504E+02	-70504E+02	-70504E+02	
34079E-01	.23969E+02	.23969E+02	.23969F+02	.23969E+02	.23969E+02	-70110E+02	-70110E+02	-70110E+02	-70110E+02	-70110E+02	-70110E+02	-70110E+02	-70110E+02	
34239E-01	.24171E+02	.24171E+02	.24171F+02	.24171E+02	.24171E+02	-69704E+02	-69704E+02	-69704E+02	-69704E+02	-69704E+02	-69704E+02	-69704E+02	-69704E+02	
34399E-01	.24382E+02	.24382E+02	.24382F+02	.24382E+02	.24382E+02	-69284E+02	-69284E+02	-69284E+02	-69284E+02	-69284E+02	-69284E+02	-69284E+02	-69284E+02	
34559E-01	.24603E+02	.24603E+02	.24603F+02	.24603E+02	.24603E+02	-68852E+02	-68852E+02	-68852E+02	-68852E+02	-68852E+02	-68852E+02	-68852E+02	-68852E+02	
34719E-01	.24835E+02	.24835E+02	.24835F+02	.24835E+02	.24835E+02	-68406E+02	-68406E+02	-68406E+02	-68406E+02	-68406E+02	-68406E+02	-68406E+02	-68406E+02	
34879E-01	.25076E+02	.25076E+02	.25076F+02	.25076E+02	.25076E+02	-67948E+02	-67948E+02	-67948E+02	-67948E+02	-67948E+02	-67948E+02	-67948E+02	-67948E+02	
35039E-01	.25327E+02	.25327E+02	.25327F+02	.25327E+02	.25327E+02	-67476E+02	-67476E+02	-67476E+02	-67476E+02	-67476E+02	-67476E+02	-67476E+02	-67476E+02	
35199E-01	.25589E+02	.25589E+02	.25589F+02	.25589E+02	.25589E+02	-66991E+02	-66991E+02	-66991E+02	-66991E+02	-66991E+02	-66991E+02	-66991E+02	-66991E+02	
35359E-01	.25861E+02	.25861E+02	.25861F+02	.25861E+02	.25861E+02	-66493E+02	-66493E+02	-66493E+02	-66493E+02	-66493E+02	-66493E+02	-66493E+02	-66493E+02	
35519E-01	.26143E+02	.26143E+02	.26143F+02	.26143E+02	.26143E+02	-65941E+02	-65941E+02	-65941E+02	-65941E+02	-65941E+02	-65941E+02	-65941E+02	-65941E+02	
35679E-01	.26436E+02	.26436E+02	.26436F+02	.26436E+02	.26436E+02	-65456E+02	-65456E+02	-65456E+02	-65456E+02	-65456E+02	-65456E+02	-65456E+02	-65456E+02	
35839E-01	.26740E+02	.26740E+02	.26740F+02	.26740E+02	.26740E+02	-64918E+02	-64918E+02	-64918E+02	-64918E+02	-64918E+02	-64918E+02	-64918E+02	-64918E+02	
35999E-01	.27055E+02	.27055E+02	.27055F+02	.27055E+02	.27055E+02	-64367E+02	-64367E+02	-64367E+02	-64367E+02	-64367E+02	-64367E+02	-64367E+02	-64367E+02	
36159E-01	.27380E+02	.27380E+02	.27380F+02	.27380E+02	.27380E+02	-63802E+02	-63802E+02	-63802E+02	-63802E+02	-63802E+02	-63802E+02	-63802E+02	-63802E+02	
36319E-01	.27716E+02	.27716E+02	.27716F+02	.27716E+02	.27716E+02	-63223E+02	-63223E+02	-63223E+02	-63223E+02	-63223E+02	-63223E+02	-63223E+02	-63223E+02	
36479E-01	.28063E+02	.28063E+02	.28063F+02	.28063E+02	.28063E+02	-62632E+02	-62632E+02	-62632E+02	-62632E+02	-62632E+02	-62632E+02	-62632E+02	-62632E+02	
36639E-01	.28421E+02	.28421E+02	.28421F+02	.28421E+02	.28421E+02	-62026E+02	-62026E+02	-62026E+02	-62026E+02	-62026E+02	-62026E+02	-62026E+02	-62026E+02	
36799E-01	.28789E+02	.28789E+02	.28789F+02	.28789E+02	.28789E+02	-61408E+02	-61408E+02	-61408E+02	-61408E+02	-61408E+02	-61408E+02	-61408E+02	-61408E+02	
36959E-01	.29169E+02	.29169E+02	.29169F+02	.29169E+02	.29169E+02	-60776E+02	-60776E+02	-60776E+02	-60776E+02	-60776E+02	-60776E+02	-60776E+02	-60776E+02	
37119E-01	.29560E+02	.29560E+02	.29560F+02	.29560E+02	.29560E+02	-60130E+02	-60130E+02	-60130E+02	-60130E+02	-60130E+02	-60130E+02	-60130E+02	-60130E+02	
37279E-01	.29962E+02	.29962E+02	.29962F+02	.29962E+02	.29962E+02	-59472E+02	-59472E+02	-59472E+02	-59472E+02	-59472E+02	-59472E+02	-59472E+02	-59472E+02	
37439E-01	.30375E+02	.30375E+02	.30375F+02	.30375E+02	.30375E+02	-58799E+02	-58799E+02	-58799E+02	-58799E+02	-58799E+02	-58799E+02	-58799E+02	-58799E+02	
37599E-01	.30799E+02	.30799E+02	.30799F+02	.30799E+02	.30799E+02	-58113E+02	-58113E+02	-58113E+02	-58113E+02	-58113E+02	-58113E+02	-58113E+02	-58113E+02	
37759E-01	.31234E+02	.31234E+02	.31234F+02	.31234E+02	.31234E+02	-57414E+02	-57414E+02	-57414E+02	-57414E+02	-57414E+02	-57414E+02	-57414E+02	-57414E+02	
37919E-01	.31680E+02	.31680E+02	.31680F+02	.31680E+02	.31680E+02	-56702E+02	-56702E+02	-56702E+02	-56702E+02	-56702E+02	-56702E+02	-56702E+02	-56702E+02	
38079E-01	.32137E+02	.32137E+02	.32137F+02	.32137E+02	.32137E+02	-55976E+02	-55976E+02	-55976E+02	-55976E+02	-55976E+02	-55976E+02	-55976E+02	-55976E+02	
38239E-01	.32605E+02	.32605E+02	.32605F+02	.32605E+02	.32605E+02	-55236E+02	-55236E+02	-55236E+02	-55236E+02	-55236E+02	-55236E+02	-55236E+02	-55236E+02	
38399E-01	.33084E+02	.33084E+02	.33084F+02	.33084E+02	.33084E+02	-54483E+02	-54483E+02	-54483E+02	-54483E+02	-54483E+02	-54483E+02	-54483E+02	-54483E+02	
38559E-01	.33574E+02	.33574E+02	.33574F+02	.33574E+02	.33574E+02	-53717E+02	-53717E+02	-53717E+02	-53717E+02	-53717E+02	-53717E+02	-53717E+02	-53717E+02	
38719E-01	.34075E+02	.34075E+02	.34075F+02	.34075E+02	.34075E+02	-52937E+02	-52937E+02	-52937E+02	-52937E+02	-52937E+02	-52937E+02	-52937E+02	-52937E+02	
38879E-01	.34588E+02	.34588E+02	.34588F+02	.34588E+02	.34588E+02	-52144E+02	-52144E+02	-52144E+02	-52144E+02	-52144E+02	-52144E+02	-52144E+02	-52144E+02	
39039E-01	.35111E+02	.35111E+02	.35111F+02	.35111E+02	.35111E+02	-51338E+02	-51338E+02	-51338E+02	-51338E+02	-51338E+02	-51338E+02	-51338E+02	-51338E+02	

TABLE H-3 (CONTINUED)

DATA FROM ACPR NO. 7842 FOR SAMPLE 30-11

[illegible]

TABLE H-3 (CONTINUED)
 FILTERED EXPERIMENT DATA HISTORIES FROM ACPR NO. 7466 CORRECTED FOR RADIATION INDUCED SIGNALS BY
 DATA FROM ACPR NO. 7842 FOR SAMPLE 30-11

ELAPSED TIME (SEC)	THERMOCOUPLE BOTTOM OUTER (DEG C)	THERMOCOUPLE BOTTOM INNER-1 (DEG C)	THERMOCOUPLE BOTTOM INNER-2 (DEG C)	THERMOCOUPLE SIDE UPPER (DEG C)	THERMOCOUPLE SIDE LOWER (DEG C)	THERMOCOUPLE DUMMY PLUG OUTER (DEG C)	THERMOCOUPLE DUMMY PLUG INNER-1 (DEG C)	THERMOCOUPLE DUMMY PLUG INNER-2 (DEG C)
.44794E-01	.61168E+02	.61168E+02	.61168E+02	.61168E+02	.61168E+02	.61168E+02	.61168E+02	.61168E+02
.44959E-01	.62092E+02	.62092E+02	.62092E+02	.62092E+02	.62092E+02	.62092E+02	.62092E+02	.62092E+02
.45119E-01	.63026E+02	.63026E+02	.63026E+02	.63026E+02	.63026E+02	.63026E+02	.63026E+02	.63026E+02
.45279E-01	.63971E+02	.63971E+02	.63971E+02	.63971E+02	.63971E+02	.63971E+02	.63971E+02	.63971E+02
.45439E-01	.64927E+02	.64927E+02	.64927E+02	.64927E+02	.64927E+02	.64927E+02	.64927E+02	.64927E+02
.45599E-01	.65894E+02	.65894E+02	.65894E+02	.65894E+02	.65894E+02	.65894E+02	.65894E+02	.65894E+02
.45759E-01	.66871E+02	.66871E+02	.66871E+02	.66871E+02	.66871E+02	.66871E+02	.66871E+02	.66871E+02
.45919E-01	.67859E+02	.67859E+02	.67859E+02	.67859E+02	.67859E+02	.67859E+02	.67859E+02	.67859E+02
.46079E-01	.68857E+02	.68857E+02	.68857E+02	.68857E+02	.68857E+02	.68857E+02	.68857E+02	.68857E+02
.46239E-01	.69866E+02	.69866E+02	.69866E+02	.69866E+02	.69866E+02	.69866E+02	.69866E+02	.69866E+02
.46399E-01	.70886E+02	.70886E+02	.70886E+02	.70886E+02	.70886E+02	.70886E+02	.70886E+02	.70886E+02
.46559E-01	.71916E+02	.71916E+02	.71916E+02	.71916E+02	.71916E+02	.71916E+02	.71916E+02	.71916E+02
.46719E-01	.72956E+02	.72956E+02	.72956E+02	.72956E+02	.72956E+02	.72956E+02	.72956E+02	.72956E+02
.46879E-01	.74006E+02	.74006E+02	.74006E+02	.74006E+02	.74006E+02	.74006E+02	.74006E+02	.74006E+02
.47039E-01	.75067E+02	.75067E+02	.75067E+02	.75067E+02	.75067E+02	.75067E+02	.75067E+02	.75067E+02
.47199E-01	.76137E+02	.76137E+02	.76137E+02	.76137E+02	.76137E+02	.76137E+02	.76137E+02	.76137E+02
.47359E-01	.77218E+02	.77218E+02	.77218E+02	.77218E+02	.77218E+02	.77218E+02	.77218E+02	.77218E+02
.47519E-01	.78309E+02	.78309E+02	.78309E+02	.78309E+02	.78309E+02	.78309E+02	.78309E+02	.78309E+02
.47679E-01	.79409E+02	.79409E+02	.79409E+02	.79409E+02	.79409E+02	.79409E+02	.79409E+02	.79409E+02
.47839E-01	.80519E+02	.80519E+02	.80519E+02	.80519E+02	.80519E+02	.80519E+02	.80519E+02	.80519E+02
.47999E-01	.81639E+02	.81639E+02	.81639E+02	.81639E+02	.81639E+02	.81639E+02	.81639E+02	.81639E+02
.48159E-01	.82768E+02	.82768E+02	.82768E+02	.82768E+02	.82768E+02	.82768E+02	.82768E+02	.82768E+02
.48319E-01	.83906E+02	.83906E+02	.83906E+02	.83906E+02	.83906E+02	.83906E+02	.83906E+02	.83906E+02
.48479E-01	.85053E+02	.85053E+02	.85053E+02	.85053E+02	.85053E+02	.85053E+02	.85053E+02	.85053E+02
.48639E-01	.86209E+02	.86209E+02	.86209E+02	.86209E+02	.86209E+02	.86209E+02	.86209E+02	.86209E+02
.48799E-01	.87374E+02	.87374E+02	.87374E+02	.87374E+02	.87374E+02	.87374E+02	.87374E+02	.87374E+02
.48959E-01	.88548E+02	.88548E+02	.88548E+02	.88548E+02	.88548E+02	.88548E+02	.88548E+02	.88548E+02
.49119E-01	.89730E+02	.89730E+02	.89730E+02	.89730E+02	.89730E+02	.89730E+02	.89730E+02	.89730E+02
.49279E-01	.90920E+02	.90920E+02	.90920E+02	.90920E+02	.90920E+02	.90920E+02	.90920E+02	.90920E+02
.49439E-01	.92118E+02	.92118E+02	.92118E+02	.92118E+02	.92118E+02	.92118E+02	.92118E+02	.92118E+02
.49599E-01	.93323E+02	.93323E+02	.93323E+02	.93323E+02	.93323E+02	.93323E+02	.93323E+02	.93323E+02
.49759E-01	.94537E+02	.94537E+02	.94537E+02	.94537E+02	.94537E+02	.94537E+02	.94537E+02	.94537E+02
.49918E-01	.95757E+02	.95757E+02	.95757E+02	.95757E+02	.95757E+02	.95757E+02	.95757E+02	.95757E+02
.50078E-01	.96985E+02	.96985E+02	.96985E+02	.96985E+02	.96985E+02	.96985E+02	.96985E+02	.96985E+02
.50239E-01	.98219E+02	.98219E+02	.98219E+02	.98219E+02	.98219E+02	.98219E+02	.98219E+02	.98219E+02

TABLE H-3 (CONTINUED)
 FILTERED EXPERIMENT DATA HISTORIES FROM ACPR NO. 7866 CORRECTED FOR RADIATION INDUCED SIGNALS BY
 DATA FROM ACPR NO. 7842 FOR SAMPLE 30-11

ELAPSED TIME (SEC)	THERMOCOUPLE THERMOCOUPLE		THERMOCOUPLE THERMOCOUPLE		THERMOCOUPLE THERMOCOUPLE		THERMOCOUPLE THERMOCOUPLE		THERMOCOUPLE THERMOCOUPLE	
	BOTTOM OUTER (DEG C)	BOTTOM INNER-1 (DEG C)	BOTTOM INNER-2 (DEG C)	SIDE UPPER (DEG C)	SIDE LOWER (DEG C)	DUMMY PLUG OUTER (DEG C)	DUMMY PLUG INNER-1 (DEG C)	DUMMY PLUG INNER-2 (DEG C)	THERMOCOUPLE THERMOCOUPLE	
50399E-01	.99460E+02	.99460E+02	.99460E+02	.99460E+02	.99460E+02	.35899E+02	.35899E+02	.35899E+02		
50559E-01	.10071E+03	.10071E+03	.10071E+03	.10071E+03	.10071E+03	.37420E+02	.37420E+02	.37420E+02		
50719E-01	.10196E+03	.10196E+03	.10196E+03	.10196E+03	.10196E+03	.38942E+02	.38942E+02	.38942E+02		
50879E-01	.10322E+03	.10322E+03	.10322E+03	.10322E+03	.10322E+03	.40466E+02	.40466E+02	.40466E+02		
51039E-01	.10449E+03	.10449E+03	.10449E+03	.10449E+03	.10449E+03	.41992E+02	.41992E+02	.41992E+02		
51199E-01	.10576E+03	.10576E+03	.10576E+03	.10576E+03	.10576E+03	.43519E+02	.43519E+02	.43519E+02		
51359E-01	.10703E+03	.10703E+03	.10703E+03	.10703E+03	.10703E+03	.45046E+02	.45046E+02	.45046E+02		
51519E-01	.10831E+03	.10831E+03	.10831E+03	.10831E+03	.10831E+03	.46574E+02	.46574E+02	.46574E+02		
51679E-01	.10959E+03	.10959E+03	.10959E+03	.10959E+03	.10959E+03	.48101E+02	.48101E+02	.48101E+02		
51839E-01	.11089E+03	.11089E+03	.11089E+03	.11089E+03	.11089E+03	.49629E+02	.49629E+02	.49629E+02		
51999E-01	.11218E+03	.11218E+03	.11218E+03	.11218E+03	.11218E+03	.51156E+02	.51156E+02	.51156E+02		
52159E-01	.11347E+03	.11347E+03	.11347E+03	.11347E+03	.11347E+03	.52681E+02	.52681E+02	.52681E+02		
52319E-01	.11477E+03	.11477E+03	.11477E+03	.11477E+03	.11477E+03	.54206E+02	.54206E+02	.54206E+02		
52479E-01	.11607E+03	.11607E+03	.11607E+03	.11607E+03	.11607E+03	.55729E+02	.55729E+02	.55729E+02		
52639E-01	.11738E+03	.11738E+03	.11738E+03	.11738E+03	.11738E+03	.57249E+02	.57249E+02	.57249E+02		
52799E-01	.11869E+03	.11869E+03	.11869E+03	.11869E+03	.11869E+03	.58768E+02	.58768E+02	.58768E+02		
52959E-01	.12000E+03	.12000E+03	.12000E+03	.12000E+03	.12000E+03	.60284E+02	.60284E+02	.60284E+02		
53119E-01	.12131E+03	.12131E+03	.12131E+03	.12131E+03	.12131E+03	.61797E+02	.61797E+02	.61797E+02		
53279E-01	.12263E+03	.12263E+03	.12263E+03	.12263E+03	.12263E+03	.63307E+02	.63307E+02	.63307E+02		
53439E-01	.12394E+03	.12394E+03	.12394E+03	.12394E+03	.12394E+03	.64813E+02	.64813E+02	.64813E+02		
53599E-01	.12526E+03	.12526E+03	.12526E+03	.12526E+03	.12526E+03	.66315E+02	.66315E+02	.66315E+02		
53759E-01	.12658E+03	.12658E+03	.12658E+03	.12658E+03	.12658E+03	.67814E+02	.67814E+02	.67814E+02		
53919E-01	.12790E+03	.12790E+03	.12790E+03	.12790E+03	.12790E+03	.69307E+02	.69307E+02	.69307E+02		
54079E-01	.12922E+03	.12922E+03	.12922E+03	.12922E+03	.12922E+03	.70797E+02	.70797E+02	.70797E+02		
54239E-01	.13054E+03	.13054E+03	.13054E+03	.13054E+03	.13054E+03	.72281E+02	.72281E+02	.72281E+02		
54399E-01	.13186E+03	.13186E+03	.13186E+03	.13186E+03	.13186E+03	.73760E+02	.73760E+02	.73760E+02		
54559E-01	.13318E+03	.13318E+03	.13318E+03	.13318E+03	.13318E+03	.75234E+02	.75234E+02	.75234E+02		
54719E-01	.13450E+03	.13450E+03	.13450E+03	.13450E+03	.13450E+03	.76702E+02	.76702E+02	.76702E+02		
54879E-01	.13582E+03	.13582E+03	.13582E+03	.13582E+03	.13582E+03	.78164E+02	.78164E+02	.78164E+02		
55039E-01	.13714E+03	.13714E+03	.13714E+03	.13714E+03	.13714E+03	.79620E+02	.79620E+02	.79620E+02		
55199E-01	.13846E+03	.13846E+03	.13846E+03	.13846E+03	.13846E+03	.81070E+02	.81070E+02	.81070E+02		
55359E-01	.13977E+03	.13977E+03	.13977E+03	.13977E+03	.13977E+03	.82513E+02	.82513E+02	.82513E+02		
55519E-01	.14109E+03	.14109E+03	.14109E+03	.14109E+03	.14109E+03	.83949E+02	.83949E+02	.83949E+02		
55679E-01	.14240E+03	.14240E+03	.14240E+03	.14240E+03	.14240E+03	.85378E+02	.85378E+02	.85378E+02		
55839E-01	.14372E+03	.14372E+03	.14372E+03	.14372E+03	.14372E+03	.86801E+02	.86801E+02	.86801E+02		

TABLE H-3 (CONTINUED)

FILTERED EXPERIMENT DATA HISTORIES FROM ACPR NO. 7866 CORRECTED FOR RADIATION INDUCED SIGNALS BY DATA FROM ACPR NO. 7842 FOR SAMPLE 30-11

ELAPSED TIME (SFC)	<div> THERMOCOUPLE BOTTOM OUTER (DEG C) </div>	<div> THERMOCOUPLE BOTTOM INNER-1 (DEG C) </div>	<div> THERMOCOUPLE BOTTOM INNER-2 (DEG C) </div>	<div> THERMOCOUPLE SIDE UPPER (DEG C) </div>	<div> THERMOCOUPLE SIDE LOWER (DEG C) </div>	<div> THERMOCOUPLE DUMMY PLUG OUTER (DEG C) </div>	<div> THERMOCOUPLE DUMMY PLUG INNER-1 (DEG C) </div>	<div> THERMOCOUPLE DUMMY PLUG INNER-2 (DEG C) </div>
559948-01	.14503E+03	.14503E+03	.14503E+03	.14503E+03	.14503E+03	.88216E+02	.88216E+02	.88216E+02
561548-01	.14634E+03	.14634E+03	.14634E+03	.14634E+03	.14634E+03	.89624E+02	.89624E+02	.89624E+02
563148-01	.14765E+03	.14765E+03	.14765E+03	.14765E+03	.14765E+03	.91024E+02	.91024E+02	.91024E+02
564748-01	.14896E+03	.14896E+03	.14896E+03	.14896E+03	.14896E+03	.92416E+02	.92416E+02	.92416E+02
566348-01	.15026E+03	.15026E+03	.15026E+03	.15026E+03	.15026E+03	.93801E+02	.93801E+02	.93801E+02
567948-01	.15157E+03	.15157E+03	.15157E+03	.15157E+03	.15157E+03	.95178E+02	.95178E+02	.95178E+02
569548-01	.15287E+03	.15287E+03	.15287E+03	.15287E+03	.15287E+03	.96547E+02	.96547E+02	.96547E+02
571148-01	.15417E+03	.15417E+03	.15417E+03	.15417E+03	.15417E+03	.97907E+02	.97907E+02	.97907E+02
572748-01	.15546E+03	.15546E+03	.15546E+03	.15546E+03	.15546E+03	.99260E+02	.99260E+02	.99260E+02
574348-01	.15676E+03	.15676E+03	.15676E+03	.15676E+03	.15676E+03	.10060E+03	.10060E+03	.10060E+03
575948-01	.15805E+03	.15805E+03	.15805E+03	.15805E+03	.15805E+03	.10194E+03	.10194E+03	.10194E+03
577548-01	.15934E+03	.15934E+03	.15934E+03	.15934E+03	.15934E+03	.10327E+03	.10327E+03	.10327E+03
579148-01	.16063E+03	.16063E+03	.16063E+03	.16063E+03	.16063E+03	.10459E+03	.10459E+03	.10459E+03
580748-01	.16192E+03	.16192E+03	.16192E+03	.16192E+03	.16192E+03	.10590E+03	.10590E+03	.10590E+03
582348-01	.16320E+03	.16320E+03	.16320E+03	.16320E+03	.16320E+03	.10720E+03	.10720E+03	.10720E+03
583948-01	.16448E+03	.16448E+03	.16448E+03	.16448E+03	.16448E+03	.10850E+03	.10850E+03	.10850E+03
585548-01	.16576E+03	.16576E+03	.16576E+03	.16576E+03	.16576E+03	.10978E+03	.10978E+03	.10978E+03
587148-01	.16704E+03	.16704E+03	.16704E+03	.16704E+03	.16704E+03	.11107E+03	.11107E+03	.11107E+03
588748-01	.16831E+03	.16831E+03	.16831E+03	.16831E+03	.16831E+03	.11234E+03	.11234E+03	.11234E+03
590348-01	.16959E+03	.16959E+03	.16959E+03	.16959E+03	.16959E+03	.11360E+03	.11360E+03	.11360E+03
591948-01	.17086E+03	.17086E+03	.17086E+03	.17086E+03	.17086E+03	.11486E+03	.11486E+03	.11486E+03
593548-01	.17213E+03	.17213E+03	.17213E+03	.17213E+03	.17213E+03	.11610E+03	.11610E+03	.11610E+03
595148-01	.17340E+03	.17340E+03	.17340E+03	.17340E+03	.17340E+03	.11734E+03	.11734E+03	.11734E+03
596748-01	.17466E+03	.17466E+03	.17466E+03	.17466E+03	.17466E+03	.11858E+03	.11858E+03	.11858E+03
598348-01	.17592E+03	.17592E+03	.17592E+03	.17592E+03	.17592E+03	.11980E+03	.11980E+03	.11980E+03
599948-01	.17719E+03	.17719E+03	.17719E+03	.17719E+03	.17719E+03	.12102E+03	.12102E+03	.12102E+03
601548-01	.17845E+03	.17845E+03	.17845E+03	.17845E+03	.17845E+03	.12223E+03	.12223E+03	.12223E+03
603148-01	.17971E+03	.17971E+03	.17971E+03	.17971E+03	.17971E+03	.12344E+03	.12344E+03	.12344E+03
604748-01	.18097E+03	.18097E+03	.18097E+03	.18097E+03	.18097E+03	.12464E+03	.12464E+03	.12464E+03
606348-01	.18222E+03	.18222E+03	.18222E+03	.18222E+03	.18222E+03	.12583E+03	.12583E+03	.12583E+03
607948-01	.18348E+03	.18348E+03	.18348E+03	.18348E+03	.18348E+03	.12701E+03	.12701E+03	.12701E+03
609548-01	.18473E+03	.18473E+03	.18473E+03	.18473E+03	.18473E+03	.12819E+03	.12819E+03	.12819E+03
611148-01	.18599E+03	.18599E+03	.18599E+03	.18599E+03	.18599E+03	.12937E+03	.12937E+03	.12937E+03
612748-01	.18724E+03	.18724E+03	.18724E+03	.18724E+03	.18724E+03	.13054E+03	.13054E+03	.13054E+03
614348-01	.18849E+03	.18849E+03	.18849E+03	.18849E+03	.18849E+03	.13170E+03	.13170E+03	.13170E+03

TABLE H-3 (CONTINUED)

FILTERED EXPERIMENT DATA HISTORIES FROM ACPR NO. 7842 CORRECTED FOR RADIATION INDUCED SIGNALS BY DATA FROM ACPR NO. 7842 FOR SAMPLE 30-11

ELAPSED TIME (SFC)	THERMOCOUPLE BOTTOM INNER-1 (DEG C)	THERMOCOUPLE BOTTOM INNER-2 (DEG C)	THERMOCOUPLE SIDE UPPER (DEG C)	THERMOCOUPLE SIDE LOWER (DEG C)	THERMOCOUPLE DUMMY PLUG OUTER (DEG C)	THERMOCOUPLE DUMMY PLUG INNER-1 (DEG C)	THERMOCOUPLE DUMMY PLUG INNER-2 (DEG C)
.61598E-01	.18974E+03	.18974E+03	.18974E+03	.18974E+03	.13286E+03	.13286E+03	.13286E+03
.61758E-01	.19100E+03	.19100E+03	.19100E+03	.19100E+03	.13401E+03	.13401E+03	.13401E+03
.61918E-01	.19225E+03	.19225E+03	.19225E+03	.19225E+03	.13516E+03	.13516E+03	.13516E+03
.62078E-01	.19350E+03	.19350E+03	.19350E+03	.19350E+03	.13631E+03	.13631E+03	.13631E+03
.62238E-01	.19475E+03	.19475E+03	.19475E+03	.19475E+03	.13745E+03	.13745E+03	.13745E+03
.62398E-01	.19600E+03	.19600E+03	.19600E+03	.19600E+03	.13859E+03	.13859E+03	.13859E+03
.62558E-01	.19726E+03	.19726E+03	.19726E+03	.19726E+03	.13972E+03	.13972E+03	.13972E+03
.62718E-01	.19851E+03	.19851E+03	.19851E+03	.19851E+03	.14086E+03	.14086E+03	.14086E+03
.62878E-01	.19976E+03	.19976E+03	.19976E+03	.19976E+03	.14198E+03	.14198E+03	.14198E+03
.63038E-01	.20102E+03	.20102E+03	.20102E+03	.20102E+03	.14311E+03	.14311E+03	.14311E+03
.63198E-01	.20227E+03	.20227E+03	.20227E+03	.20227E+03	.14424E+03	.14424E+03	.14424E+03
.63358E-01	.20353E+03	.20353E+03	.20353E+03	.20353E+03	.14536E+03	.14536E+03	.14536E+03
.63518E-01	.20479E+03	.20479E+03	.20479E+03	.20479E+03	.14648E+03	.14648E+03	.14648E+03
.63678E-01	.20605E+03	.20605E+03	.20605E+03	.20605E+03	.14760E+03	.14760E+03	.14760E+03
.63838E-01	.20731E+03	.20731E+03	.20731E+03	.20731E+03	.14872E+03	.14872E+03	.14872E+03
.63998E-01	.20857E+03	.20857E+03	.20857E+03	.20857E+03	.14984E+03	.14984E+03	.14984E+03
.64158E-01	.20984E+03	.20984E+03	.20984E+03	.20984E+03	.15096E+03	.15096E+03	.15096E+03
.64318E-01	.21110E+03	.21110E+03	.21110E+03	.21110E+03	.15208E+03	.15208E+03	.15208E+03
.64478E-01	.21237E+03	.21237E+03	.21237E+03	.21237E+03	.15320E+03	.15320E+03	.15320E+03
.64638E-01	.21364E+03	.21364E+03	.21364E+03	.21364E+03	.15432E+03	.15432E+03	.15432E+03
.64798E-01	.21491E+03	.21491E+03	.21491E+03	.21491E+03	.15544E+03	.15544E+03	.15544E+03
.64958E-01	.21619E+03	.21619E+03	.21619E+03	.21619E+03	.15656E+03	.15656E+03	.15656E+03
.65118E-01	.21747E+03	.21747E+03	.21747E+03	.21747E+03	.15769E+03	.15769E+03	.15769E+03
.65278E-01	.21875E+03	.21875E+03	.21875E+03	.21875E+03	.15881E+03	.15881E+03	.15881E+03
.65438E-01	.22003E+03	.22003E+03	.22003E+03	.22003E+03	.15994E+03	.15994E+03	.15994E+03
.65598E-01	.22132E+03	.22132E+03	.22132E+03	.22132E+03	.16107E+03	.16107E+03	.16107E+03
.65758E-01	.22261E+03	.22261E+03	.22261E+03	.22261E+03	.16220E+03	.16220E+03	.16220E+03
.65918E-01	.22390E+03	.22390E+03	.22390E+03	.22390E+03	.16333E+03	.16333E+03	.16333E+03
.66078E-01	.22520E+03	.22520E+03	.22520E+03	.22520E+03	.16447E+03	.16447E+03	.16447E+03
.66238E-01	.22650E+03	.22650E+03	.22650E+03	.22650E+03	.16560E+03	.16560E+03	.16560E+03
.66398E-01	.22780E+03	.22780E+03	.22780E+03	.22780E+03	.16675E+03	.16675E+03	.16675E+03
.66558E-01	.22910E+03	.22910E+03	.22910E+03	.22910E+03	.16789E+03	.16789E+03	.16789E+03
.66718E-01	.23041E+03	.23041E+03	.23041E+03	.23041E+03	.16904E+03	.16904E+03	.16904E+03
.66878E-01	.23173E+03	.23173E+03	.23173E+03	.23173E+03	.17019E+03	.17019E+03	.17019E+03
.67037E-01	.23304E+03	.23304E+03	.23304E+03	.23304E+03	.17135E+03	.17135E+03	.17135E+03

TABLE 11-3 (CONCLUDED)
 FILTERED EXPERIMENT DATA HISTORIES FROM ACPR NO. 7866 CORRECTED FOR RADIATION INDUCED SIGNALS BY
 DATA FROM ACPR NO. 7842 FOR SAMPLE 30-11

ELAPSED TIME (SEC)	HEATCOUPLE BOTTOM OUTER (DEG C)	HEATCOUPLE BOTTOM INNER-1 (DEG C)	HEATCOUPLE BOTTOM INNER-2 (DEG C)	HEATCOUPLE SIDE UPPER (DEG C)	HEATCOUPLE SIDE LOWER (DEG C)	HEATCOUPLE DUMMY PLUG OUTER (DEG C)	HEATCOUPLE DUMMY PLUG INNER-1 (DEG C)	HEATCOUPLE DUMMY PLUG INNER-2 (DEG C)
671971-01	23436E+03	23436E+03	23436E+03	23436E+03	23436E+03	17251E+03	17251E+03	17251E+03
673571-01	23568E+03	23568E+03	23568E+03	23568E+03	23568E+03	17367E+03	17367E+03	17367E+03
675171-01	23701E+03	23701E+03	23701E+03	23701E+03	23701E+03	17484E+03	17484E+03	17484E+03
676771-01	23834E+03	23834E+03	23834E+03	23834E+03	23834E+03	17601E+03	17601E+03	17601E+03
678371-01	23967E+03	23967E+03	23967E+03	23967E+03	23967E+03	17718E+03	17718E+03	17718E+03
679971-01	24100E+03	24100E+03	24100E+03	24100E+03	24100E+03	17836E+03	17836E+03	17836E+03
681571-01	24234E+03	24234E+03	24234E+03	24234E+03	24234E+03	17954E+03	17954E+03	17954E+03
683171-01	24368E+03	24368E+03	24368E+03	24368E+03	24368E+03	18073E+03	18073E+03	18073E+03
684771-01	24502E+03	24502E+03	24502E+03	24502E+03	24502E+03	18192E+03	18192E+03	18192E+03
686371-01	24637E+03	24637E+03	24637E+03	24637E+03	24637E+03	18312E+03	18312E+03	18312E+03
687971-01	24772E+03	24772E+03	24772E+03	24772E+03	24772E+03	18431E+03	18431E+03	18431E+03
689571-01	24907E+03	24907E+03	24907E+03	24907E+03	24907E+03	18552E+03	18552E+03	18552E+03
691171-01	25042E+03	25042E+03	25042E+03	25042E+03	25042E+03	18672E+03	18672E+03	18672E+03
692771-01	25178E+03	25178E+03	25178E+03	25178E+03	25178E+03	18793E+03	18793E+03	18793E+03
694371-01	25314E+03	25314E+03	25314E+03	25314E+03	25314E+03	18914E+03	18914E+03	18914E+03
695971-01	25449E+03	25449E+03	25449E+03	25449E+03	25449E+03	19035E+03	19035E+03	19035E+03
697571-01	25585E+03	25585E+03	25585E+03	25585E+03	25585E+03	19157E+03	19157E+03	19157E+03
699171-01	25722E+03	25722E+03	25722E+03	25722E+03	25722E+03	19279E+03	19279E+03	19279E+03
700771-01	25858E+03	25858E+03	25858E+03	25858E+03	25858E+03	19401E+03	19401E+03	19401E+03
702371-01	25994E+03	25994E+03	25994E+03	25994E+03	25994E+03	19523E+03	19523E+03	19523E+03
703971-01	26130E+03	26130E+03	26130E+03	26130E+03	26130E+03	19646E+03	19646E+03	19646E+03
705571-01	26266E+03	26266E+03	26266E+03	26266E+03	26266E+03	19769E+03	19769E+03	19769E+03
707171-01	26402E+03	26402E+03	26402E+03	26402E+03	26402E+03	19891E+03	19891E+03	19891E+03
708771-01	26538E+03	26538E+03	26538E+03	26538E+03	26538E+03	20014E+03	20014E+03	20014E+03
710371-01	26674E+03	26674E+03	26674E+03	26674E+03	26674E+03	20137E+03	20137E+03	20137E+03
711971-01	26809E+03	26809E+03	26809E+03	26809E+03	26809E+03	20260E+03	20260E+03	20260E+03
713571-01	26945E+03	26945E+03	26945E+03	26945E+03	26945E+03	20383E+03	20383E+03	20383E+03
715171-01	27080E+03	27080E+03	27080E+03	27080E+03	27080E+03	20505E+03	20505E+03	20505E+03
716771-01	27214E+03	27214E+03	27214E+03	27214E+03	27214E+03	20628E+03	20628E+03	20628E+03
718371-01	27349E+03	27349E+03	27349E+03	27349E+03	27349E+03	20750E+03	20750E+03	20750E+03

TABLE H-4
INTEGRATED REACTOR POWER HISTORIES FROM ACPR NO. 7842 AND ACPR NO. 7866

ELAPSED TIME (SEC)	INTEGRATED REACTOR POWER 7842 (MJ)	INTEGRATED REACTOR POWER 7866 (MJ)	ELAPSED TIME (SEC)	INTEGRATED REACTOR POWER 7842 (MJ)	INTEGRATED REACTOR POWER 7866 (MJ)	ELAPSED TIME (SEC)	INTEGRATED REACTOR POWER 7842 (MJ)	INTEGRATED REACTOR POWER 7866 (MJ)
0.	36668E-06	36668E-06	11200E-01	13844E-02	13844E-02	22400E-01	25832E+01	25832E+01
32000E-03	63528E-06	63528E-06	11520E-01	17217E-02	17217E-02	22720E-01	31668E+01	31668E+01
64000E-03	19257E-05	19257E-05	11840E-01	21323E-02	21323E-02	23040E-01	38735E+01	38735E+01
96000E-03	26723E-05	26723E-05	12160E-01	26339E-02	26339E-02	23360E-01	47278E+01	47278E+01
128000E-03	34807E-05	34807E-05	12480E-01	32467E-02	32467E-02	23680E-01	57507E+01	57507E+01
160000E-03	47294E-05	47294E-05	12800E-01	39927E-02	39927E-02	24000E-01	69639E+01	69639E+01
192000E-03	44857E-05	44857E-05	13120E-01	49099E-02	49099E-02	24320E-01	83943E+01	83943E+01
224000E-03	22784E-05	22784E-05	13440E-01	60434E-02	60434E-02	24640E-01	10064E+02	10064E+02
256000E-03	46621E-06	46621E-06	13760E-01	74370E-02	74370E-02	24960E-01	11983E+02	11983E+02
288000E-03	41531E-05	41531E-05	14080E-01	91605E-02	91605E-02	25280E-01	14151E+02	14151E+02
320000E-03	97600E-05	97600E-05	14400E-01	11314E-01	11314E-01	25600E-01	16562E+02	16562E+02
352000E-03	16312E-04	16312E-04	14720E-01	14004E-01	14004E-01	25920E-01	19189E+02	19189E+02
384000E-03	22712E-04	22712E-04	15040E-01	17370E-01	17370E-01	26240E-01	21989E+02	21989E+02
416000E-03	28364E-04	28364E-04	15360E-01	21604E-01	21604E-01	26560E-01	24905E+02	24905E+02
448000E-03	32228E-04	32228E-04	15680E-01	26936E-01	26936E-01	26880E-01	27881E+02	27881E+02
480000E-03	33919E-04	33919E-04	16000E-01	33637E-01	33637E-01	27200E-01	30858E+02	30858E+02
512000E-03	33195E-04	33195E-04	16320E-01	42052E-01	42052E-01	27520E-01	33774E+02	33774E+02
544000E-03	28640E-04	28640E-04	16640E-01	52610E-01	52610E-01	27840E-01	36578E+02	36578E+02
576000E-03	19800E-04	19800E-04	16960E-01	65849E-01	65849E-01	28160E-01	39234E+02	39234E+02
608000E-03	75668E-05	75668E-05	17280E-01	82391E-01	82391E-01	28480E-01	41705E+02	41705E+02
640000E-03	89504E-05	89504E-05	17600E-01	10297E+00	10297E+00	28800E-01	43968E+02	43968E+02
672000E-03	31179E-04	31179E-04	17920E-01	12859E+00	12859E+00	29120E-01	46017E+02	46017E+02
704000E-03	57452E-04	57452E-04	18240E-01	16051E+00	16051E+00	29440E-01	47855E+02	47855E+02
736000E-03	85446E-04	85446E-04	18560E-01	20000E+00	20000E+00	29760E-01	49484E+02	49484E+02
768000E-03	11626E-03	11626E-03	18880E-01	24883E+00	24883E+00	30080E-01	50915E+02	50915E+02
800000E-03	15238E-03	15238E-03	19200E-01	30942E+00	30942E+00	30400E-01	52164E+02	52164E+02
832000E-03	19441E-03	19441E-03	19520E-01	38439E+00	38439E+00	30720E-01	53241E+02	53241E+02
864000E-03	24304E-03	24304E-03	19840E-01	47698E+00	47698E+00	31040E-01	54159E+02	54159E+02
896000E-03	30161E-03	30161E-03	20160E-01	59156E+00	59156E+00	31360E-01	54941E+02	54941E+02
928000E-03	37385E-03	37385E-03	20480E-01	73294E+00	73294E+00	31680E-01	55605E+02	55605E+02
960000E-03	46302E-03	46302E-03	20800E-01	90686E+00	90686E+00	32000E-01	56166E+02	56166E+02
992000E-03	57518E-03	57518E-03	21120E-01	11212E+01	11212E+01	32320E-01	56637E+02	56637E+02
1024000E-03	71736E-03	71736E-03	21440E-01	13847E+01	13847E+01	32640E-01	57032E+02	57032E+02
1056000E-03	89375E-03	89375E-03	21760E-01	17071E+01	17071E+01	32960E-01	57364E+02	57364E+02
1088000E-03	11117E-02	11117E-02	22080E-01	21017E+01	21017E+01	33280E-01	57644E+02	57644E+02

TABLE h-4 (CONTINUED)
INTEGRATED REACTOR POWER HISTORIES FROM ACPR NO. 7842 AND ACPR NO. 7866

ELAPSED TIME (SEC)	INTEGRATED REACTOR POWER 7842 (MJ)	INTEGRATED REACTOR POWER 7866 (MJ)	ELAPSED TIME (SEC)	INTEGRATED REACTOR POWER 7842 (MJ)	INTEGRATED REACTOR POWER 7866 (MJ)	ELAPSED TIME (SEC)	INTEGRATED REACTOR POWER 7842 (MJ)	INTEGRATED REACTOR POWER 7866 (MJ)
.33600E-01	.57879E+02	.57879E+02	.44799E-01	.59150E+02	.59150E+02	.55999E-01	.59267E+02	.59267E+02
.33920E-01	.58077E+02	.58077E+02	.45119E-01	.59154E+02	.59154E+02	.56319E-01	.59270E+02	.59270E+02
.34240E-01	.58242E+02	.58242E+02	.45439E-01	.59158E+02	.59158E+02	.56639E-01	.59273E+02	.59273E+02
.34560E-01	.58382E+02	.58382E+02	.45759E-01	.59161E+02	.59161E+02	.56959E-01	.59277E+02	.59277E+02
.34880E-01	.58500E+02	.58500E+02	.46079E-01	.59165E+02	.59165E+02	.57279E-01	.59280E+02	.59280E+02
.35200E-01	.58594E+02	.58594E+02	.46399E-01	.59168E+02	.59168E+02	.57599E-01	.59283E+02	.59283E+02
.35519E-01	.58680E+02	.58680E+02	.46719E-01	.59171E+02	.59171E+02	.57919E-01	.59286E+02	.59286E+02
.35840E-01	.58749E+02	.58749E+02	.47039E-01	.59175E+02	.59175E+02	.58239E-01	.59290E+02	.59290E+02
.36159E-01	.58806E+02	.58806E+02	.47359E-01	.59178E+02	.59178E+02	.58559E-01	.59293E+02	.59293E+02
.36479E-01	.58854E+02	.58854E+02	.47679E-01	.59181E+02	.59181E+02	.58879E-01	.59296E+02	.59296E+02
.36800E-01	.58894E+02	.58894E+02	.47999E-01	.59184E+02	.59184E+02	.59199E-01	.59299E+02	.59299E+02
.37119E-01	.58927E+02	.58927E+02	.48319E-01	.59188E+02	.59188E+02	.59519E-01	.59302E+02	.59302E+02
.37440E-01	.58956E+02	.58956E+02	.48639E-01	.59191E+02	.59191E+02	.59839E-01	.59306E+02	.59306E+02
.37759E-01	.58979E+02	.58979E+02	.48959E-01	.59194E+02	.59194E+02	.60159E-01	.59309E+02	.59309E+02
.38079E-01	.59000E+02	.59000E+02	.49279E-01	.59198E+02	.59198E+02	.60479E-01	.59312E+02	.59312E+02
.38399E-01	.59017E+02	.59017E+02	.49599E-01	.59201E+02	.59201E+02	.60799E-01	.59315E+02	.59315E+02
.38719E-01	.59032E+02	.59032E+02	.49919E-01	.59204E+02	.59204E+02	.61119E-01	.59319E+02	.59319E+02
.39039E-01	.59045E+02	.59045E+02	.50239E-01	.59207E+02	.59207E+02	.61439E-01	.59322E+02	.59322E+02
.39359E-01	.59057E+02	.59057E+02	.50559E-01	.59211E+02	.59211E+02	.61759E-01	.59325E+02	.59325E+02
.39679E-01	.59067E+02	.59067E+02	.50879E-01	.59214E+02	.59214E+02	.62079E-01	.59328E+02	.59328E+02
.39999E-01	.59075E+02	.59075E+02	.51199E-01	.59217E+02	.59217E+02	.62399E-01	.59332E+02	.59332E+02
.40319E-01	.59083E+02	.59083E+02	.51519E-01	.59221E+02	.59221E+02	.62719E-01	.59335E+02	.59335E+02
.40639E-01	.59091E+02	.59091E+02	.51839E-01	.59224E+02	.59224E+02	.63039E-01	.59338E+02	.59338E+02
.40959E-01	.59097E+02	.59097E+02	.52159E-01	.59227E+02	.59227E+02	.63359E-01	.59341E+02	.59341E+02
.41279E-01	.59103E+02	.59103E+02	.52479E-01	.59231E+02	.59231E+02	.63679E-01	.59344E+02	.59344E+02
.41599E-01	.59108E+02	.59108E+02	.52799E-01	.59234E+02	.59234E+02	.63999E-01	.59348E+02	.59348E+02
.41919E-01	.59113E+02	.59113E+02	.53119E-01	.59237E+02	.59237E+02	.64319E-01	.59351E+02	.59351E+02
.42239E-01	.59118E+02	.59118E+02	.53439E-01	.59241E+02	.59241E+02	.64639E-01	.59354E+02	.59354E+02
.42559E-01	.59122E+02	.59122E+02	.53759E-01	.59244E+02	.59244E+02	.64959E-01	.59357E+02	.59357E+02
.42879E-01	.59127E+02	.59127E+02	.54079E-01	.59247E+02	.59247E+02	.65279E-01	.59361E+02	.59361E+02
.43199E-01	.59131E+02	.59131E+02	.54399E-01	.59250E+02	.59250E+02	.65599E-01	.59364E+02	.59364E+02
.43519E-01	.59135E+02	.59135E+02	.54719E-01	.59254E+02	.59254E+02	.65919E-01	.59367E+02	.59367E+02
.43839E-01	.59139E+02	.59139E+02	.55039E-01	.59257E+02	.59257E+02	.66239E-01	.59370E+02	.59370E+02
.44159E-01	.59143E+02	.59143E+02	.55359E-01	.59260E+02	.59260E+02	.66559E-01	.59373E+02	.59373E+02
.44479E-01	.59147E+02	.59147E+02	.55679E-01	.59264E+02	.59264E+02	.66879E-01	.59377E+02	.59377E+02

APPENDIX I

DETAILED ASSESSMENT OF EXPERIMENTAL ERRORS

Quantifiable uncertainties are associated with every experimental measurement. In this section, the uncertainties in the EOS measurements are estimated. These estimates are combined to yield estimates of uncertainties in the computed results.

COMBINATION OF ERRORS

To estimate the errors associated with the computed results, it is necessary to recall two relationships. These relationships assume that the errors in the measurements (expressed as standard deviations) which are combined are independent. First, the standard deviation of a sum or difference with individual standard deviations $\sigma_1, \sigma_2, \sigma_3, \dots, \sigma_n$ is given by

$$\sigma_s = \left(\sigma_1^2 + \sigma_2^2 + \sigma_3^2 + \dots + \sigma_n^2 \right)^{\frac{1}{2}} \quad (1)$$

The standard deviation of a product P , where $P = p_1 p_2 \dots p_n$, with individual standard deviations $\sigma_1, \sigma_2, \dots, \sigma_n$ is given by

$$\frac{\sigma_p}{P} = \left[\left(\frac{\sigma_1}{p_1} \right)^2 + \left(\frac{\sigma_2}{p_2} \right)^2 + \dots + \left(\frac{\sigma_n}{p_n} \right)^2 \right]^{\frac{1}{2}} \quad (2)$$

PRESSURE

The uncertainty in pressure is that attributed to the transducer calibration. Two methods were used to calibrate the Kaman pressure transducers after buffer discs were bonded to the sensing

diaphragms. Each transducer was calibrated against a pressure gage from 0 to 1900 psig. This gage could be read to ± 20 psig. The gage was accurate to ± 10 percent over its entire range. Since the percentage errors of the least squares fits to the calibration data were much less than 1 percent, the 10 percent value was assumed as the uncertainty in the pressure measurements.

The transducers used in EEOS-UO2-4 and EEOS-UO2-5 were subsequently calibrated by the Sandia Transducer Laboratory to a precision better than 5 percent from 0 to 5000 psig. However, since the pressure data from all experimental series were used to obtain the final results, the 10 percent uncertainty was applied to the pressure result.

AVERAGE ENERGY INPUT

As shown by equation (11) in Chapter IV, the average energy input history was derived as a product of three measured parameters: the normalized integrated power history, the fraction of the total fission energy that is deposited during the prompt pulse, and the result of the fission product inventories. A comparison of normalized integrated power histories from the four ACPR transients comprising each experimental series showed that they were identical to within ± 1 percent. For the fraction of the total energy release associated with the prompt pulse, a similar comparison of the values of the power integrals at 50 msec and at 3 minutes (relative to the time fiducial) yielded the values shown in Table IV-1 with uncertainties less than ± 1 percent. Finally, as shown in Appendix E, the net uncertainties associated

with the fission product inventory results are approximately ± 4 percent. These errors are combined according to equation (2) to yield

$$\left. \begin{aligned} \frac{\sigma_{\text{avg}}}{E_{\text{avg}}} &= \left[(.01)^2 + (.01)^2 + (.04)^2 \right]^{\frac{1}{2}} \\ &= .043 \end{aligned} \right\} (3)$$

PEAK ENERGY CONTENT

As shown by equation (12) in Chapter IV, the peak energy content history is the product of the average energy input history and the peak-to-average fission density ratio (PTA). The uncertainties in PTA arise from uncertainties in the model and cross-sections used in the neutron transport calculations. While it is difficult to quantify the uncertainties in PTA, they were estimated to be less than ± 5 percent. This estimate can be combined according to equation (2) with the results of equation (3) to yield

$$\left. \begin{aligned} \frac{\sigma_{\text{peak}}}{E_{\text{peak}}} &= \left[(.043)^2 + (.05)^2 \right]^{\frac{1}{2}} \\ &= .066 \end{aligned} \right\} (4)$$

ENERGY LOSSES

There exist two sources of uncertainty in the computation of the energy loss history: the first arises from the computation of the response functions; the second is associated with the experimental temperature measurements. As was shown in

Chapter IV, variations in the thermocouple location and in the material properties used to compute the temperature response functions can yield significant deviations in the computed heat fluxes. From the sensitivity study of the inverse heat conduction technique described in Chapter IV, the resultant uncertainty in the computed heat fluxes during the time interval of interest was estimated to be ± 30 percent.

Since the experiments are axially symmetric, the three bottom inside thermocouples should measure identical temperature histories. However, some differences among the three temperature histories were noted in most of the experiments. A comparison of the temperature histories in each experiment showed variations as large as ± 40 percent. This value was used as the uncertainty in the experimental temperature histories. From Appendix G, it is apparent that uncertainties in the experimental temperatures will yield uncertainties of similar magnitude in the computed heat fluxes.

If it is assumed that the uncertainties in the response functions and in the measured temperatures are independent, then the net uncertainties in the energy loss histories can be estimated as

$$\left. \begin{aligned} \frac{\sigma_{\text{loss}}}{E_{\text{loss}}} &= \left[(.30)^2 + (.40)^2 \right]^{\frac{1}{2}} \\ &= .50 \end{aligned} \right\} (5)$$

In fact, the two sources of error are not independent. The dominant sources of uncertainty in the experimental temperature histories are variations in the installed location of the thermocouples. Hence the ± 50 percent uncertainty value is probably too large.

CORRECTED AVERAGE ENERGY CONTENT

As shown in equation (15) in Chapter IV, the corrected average energy content history was computed as the difference between the average energy input history and the energy loss history. As shown in equation (1), the magnitude of the uncertainties, not the percentages, are needed. From Figures V-4 through V-7, it is noted that the largest uncertainties in E_{avg} and E_{loss} during the leading edge of the pressure pulse occur at the pressure peak. Typical values of E_{avg} and E_{loss} taken at the top of the leading edge of the pressure pulse are 1900 J/g and 200 J/g, respectively. From equations (3) and (5), we find $\sigma_{avg} = 82$ and $\sigma_{loss} = 100$. Thus,

$$\left. \begin{aligned} \sigma_{ac} &= \left[(82)^2 + (100)^2 \right]^{\frac{1}{2}} \\ &= 129 \text{ J/g} \end{aligned} \right\} (6)$$

Therefore

$$\left. \begin{aligned} \frac{\sigma_{ac}}{E_{ac}} &= \frac{129}{1900-200} \\ &= .076 \end{aligned} \right\} (7)$$

Although equation (7) was derived at a single point, its value was assigned to the entire range of corrected average energy content used to generate the lower energy bound to the vapor pressure.

The estimates of errors derived above are summarized in Table V-3.

APPENDIX J

JUSTIFICATION OF THE USE OF SPECIFIC HEAT AT CONSTANT PRESSURE

In order to relate energy content and temperature in these experiments, it was necessary to assume a specific heat model. The question arises as to what model to assume: specific heat at constant pressure (C_p), specific heat at constant volume (C_v), or some other form. This section presents a justification for the use of a specific heat at constant pressure (C_p) model.

The volume of vapor can be assumed to be the initial void volume of the pressure cell ($V_v \approx 200\text{mm}^3$). Now consider a state with a pressure (P) of 10 MPa corresponding to an energy content of 2 K J/g. Assuming the C_p model described in Chapter V, this yields a temperature (T) of approximately 5×10^3 K. If it is assumed that the vapor behaves as an ideal gas, then the mass of vapor can be estimated from the ideal gas law

$$PV = nRT \quad (1)$$

where R is the gas constant ≈ 8.3 J/mole-K, and n is the number of moles of vapor. Thus:

$$n_v = \frac{PV_v}{RT} = \frac{(1 \times 10^7)(.2 \times 10^{-6})}{8.3 (5 \times 10^3)} \approx 5 \times 10^{-5} \text{ moles} \quad (2)$$

For UO_2 the mole weight is 270 g; thus, the mass of vapor is

$$m_v = 270 (n_v) \approx 1.3 \times 10^{-2} \text{ g} \quad (3)$$

Since the sample mass was approximately 1 g, only 1.3 percent of the sample is vapor under the above conditions.

As the sample is heated from room temperature through melt in the pressure cell, it is not constrained, and the specific heat at constant pressure is clearly appropriate. Above melt, however, both the volume and the pressure change as the sample is heated along the saturation curve. Hence, the specific heat along the saturation curve C_{sat} is appropriate. This relationship can be derived as follows:

$$C_{\text{sat}} = \left(\frac{\delta Q}{dT} \right)_{\text{sat}} = T \left(\frac{dS}{dT} \right)_{\text{sat}} \quad (4)$$

where δQ is the incremental heat increase corresponding to the incremental increase in temperature dT in a process along the saturation curve. Entropy, S , can be considered a function of temperature, T , and volume, V . Thus,

$$dS = \left(\frac{\partial S}{\partial T} \right)_V dT + \left(\frac{\partial S}{\partial V} \right)_T dV \quad (5)$$

Division by dT and restriction to changes along the saturation curve yield

$$\left(\frac{dS}{dT} \right)_{\text{sat}} = \left(\frac{\partial S}{\partial T} \right)_V + \left(\frac{\partial S}{\partial V} \right)_T \left(\frac{dV}{dT} \right)_{\text{sat}} \quad (6)$$

Note that:

$$\left(\frac{\partial S}{\partial T} \right)_V = \frac{C_V}{T} \quad (7)$$

and, from the Maxwell relations, that:

$$\left(\frac{\partial S}{\partial V}\right)_T = \left(\frac{\partial P}{\partial T}\right)_V \quad (8)$$

It can be shown that

$$\left(\frac{\partial P}{\partial T}\right)_V = \beta/\kappa \quad (9)$$

where β is the volume expansivity, given by

$$\beta = \frac{1}{V} \left(\frac{\partial V}{\partial T}\right)_P \quad (10)$$

and κ is the isothermal compressibility, given by

$$\kappa = -\frac{1}{V} \left(\frac{\partial V}{\partial P}\right)_T \quad (11)$$

Equations (6), (7), (8), and (9) can be combined to yield

$$C_{\text{sat}} = C_V + \frac{T\beta}{\kappa} \left(\frac{dV}{dT}\right)_{\text{sat}} \quad (12)$$

By considering volume to be a function of T and P , we find an equation similar to equation (6), such that

$$\left(\frac{\partial V}{\partial T}\right)_{\text{sat}} = \left(\frac{\partial V}{\partial T}\right)_P + \left(\frac{\partial V}{\partial P}\right)_T \left(\frac{dP}{dT}\right)_{\text{sat}} \quad (13)$$

It can be shown that

$$C_P - C_V = \frac{T\beta^2 v}{\kappa} \quad (14)$$

Equations (10), (11), (12), (13), and (14) can be combined to yield

$$C_{\text{sat}} = C_P - T\beta v \left(\frac{\partial P}{\partial T} \right)_{\text{sat}} \quad (15)$$

Thus C_{sat} is in general different from C_P or C_V .

To investigate the magnitude of the difference between C_{sat} and C_P , consider the liquid phase at the state defined above. From reference (Le76) for UO_2 above melt, the specific volume v is given by

$$v = \frac{1}{10.97} \left[1 + 9.3 \times 10^{-5} (T-273) \right] \text{ cc/g} \quad (16)$$

From equations (10) and (16), it is found

$$\beta = 8.48 \times 10^{-6} / v \quad (17)$$

At 5000 K

$$\left. \begin{aligned} v &= .131 \text{ cc/g} \\ \beta &= 6.5 \times 10^{-5} \text{ K}^{-1} \end{aligned} \right\} \quad (18)$$

Using the vapor pressure relationship defined by equation (16) in Chapter V, it is found

$$P \text{ (MPa)} = 10^{-7} \exp(69.979 - 76800/T - 4.34 \ln T) \quad (19)$$

$$\left(\frac{\partial P}{\partial T}\right)_{\text{sat}} = \left(\frac{76800}{T^2} - \frac{4.34}{T}\right)_P \quad (20)$$

At 5000 K this results in

$$\left(\frac{\partial P}{\partial T}\right)_{\text{sat}} = .0102 \text{ MPa/K} \quad (21)$$

Combining equations (15), (18), and (21), it is found that at 5000 K

$$\left. \begin{aligned} C_{\text{sat}} &= C_P - 5000 (6.5 \times 10^{-5}) (.131 \times 10^{-6}) (.0102 \times 10^6) \\ &= C_P - 4.34 \times 10^{-4} \text{ J/g} \end{aligned} \right\} \quad (22)$$

Similarly, at 6000 K

$$C_{\text{sat}} = C_P - 1.95 \times 10^{-3} \text{ J/g} \quad (23)$$

For the C_P model defined in Chapter V, it is found that

$$C_P = 0.5 \text{ J/g} \quad (24)$$

at temperatures above melt. Thus, even at 6000 K the difference between C_{sat} and C_P for saturated liquid is less than .4 percent. Thus, the use of C_P introduces negligible error.

This analysis has neglected the latent heat of vaporization which is estimated to be $1700 \pm 200 \text{ J/g}$ (Le76). For the mass of vapor defined above, this yields $22 \pm 3 \text{ J}$ which must be added to the sample to maintain temperature T .

Hence, we conclude that the use of C_p to convert temperatures to energy as

$$\left. \begin{aligned} (E - E_o) &= \int_{T_o}^T C_p dT \\ E_o &= 0 \text{ at } T = T_o \end{aligned} \right\} (25)$$

Neglecting the heat of vaporization should introduce uncertainties in the computed energy of the order of 1 to 2 percent in addition to the uncertainties in the specific heat model. For the purposes of comparing the results of other experiments and vapor pressure formulations with the results of these experiments, that uncertainty is acceptable.

REFERENCES

- Ac56 Ackermann, R. J., P. W. Gilles, R. J. Thorn, "High Temperature Thermodynamic Properties of Uranium Dioxide," *J. Chem. Phys.*, 25, 1089 (1956).
- Ac62-1 Ackermann, R. J., and E. G. Rauh, "Vapor Pressures of Scandium, Yttrium, and Lanthanum," *The Journal of Chemical Physics*, Vol 36, No. 2, pp 448-452 (January 15, 1962).
- Ac62-2 Ackermann, R. J., and R. J. Thorn, "Vaporization Properties of Thorium, Uranium, and Plutonium Metals and Oxides," *Thermodynamics of Nuclear Materials*, International Atomic Energy Agency, Vienna, pp 445-464 (1962).
- Ac65 Ackermann, R. J., M. S. Chandrasekhariah, E. G. Rauh, and R. K. Edwards, ANL-7048 (1965).
- Ac66 Ackermann, R. J., and R. J. Thorn, "The Evaporation Behavior, Thermodynamic Properties, and Systemic Trends of Actinide Metal-Oxygen Systems," *Thermodynamics*, International Atomic Energy Agency, Vienna, Vol 1, pp 243-269 (1966).
- Ac69 Ackermann, R. J., E. G. Rauh, and M. S. Chandrasekhariah, "A Thermodynamic Study of the Urania-Uranium System," *The Journal of Physical Chemistry*, Vol 73, No. 4, pp 762-769 (April 1969).
- As75 Asami, N., M. Nishikawa, M. Taguchi, "Experimental Investigation of the Ultra-High Temperature and Pressure State of Uranium Dioxide," *Thermodynamics of Nuclear Materials*, 1974, International Atomic Energy Agency, Vienna (1975).
- Be56 Bethe, H. A., and J. H. Tait, "An Estimate of the Order of Magnitude of the Explosion When the Core of a Fast Reactor Collapses," IKAEA-RHM (56)/113 (1956).
- Be68 Beck, James V., "Surface Heat Flux Determination Using an Integral Method," *Nuclear Engineering and Design*, 7, pp 170-178 (1968).
- Be75 Benson, D. A., L. D. Posey, K. O. Reil, T. R. Schmidt, A. L. Ouellette, W. H. Buchalew, and R. J. Haushalter, Ch. 4, "Exp. Fast Reactor Safety Research Program," SAND 75 0449, Sandia Laboratories (1977).
- Be76 Benson, D., and W. Buchalew, "The Uranium Dioxide Vapor Equation of State," *ANS Trans.*, 23, 325 (1976).

- Be77 Bergeron, E., Sandia Laboratories, private communication (February 1977).
- Bl73 Blackburn, P. E., "Oxygen Pressures over Fast Breeder Reactor Fuel," *J. Nucl. Mater.*, 46, pp 244-275 (1973).
- BM74 Bonzon, L. L., F. M. Morris, and F. V. Thome, "Annular Core Pulse Reactor (ACPR): Experimenter's Manual," SLA-73-1017 (October 1974).
- Bo75-1 Bober, M., H. U. Karow, K. Schretzmann, "Evaporation Experiments to Determine the Vapor Pressure of UO_2 Fuel (3000-5000 K)," *Thermodynamics of Nuclear Materials*, 1974, International Atomic Energy Agency, Vienna (1975).
- Bo75-2 Bober, M., H. V. Karow, and K. Schretzmann, "Vapor Pressure Measurements of Oxide Fuel Between 3000 and 5000 K Using Laser Heating," *Nuclear Technology*, Vol. 26, pp 237-241 (June 1975).
- Bo74 Bogensberger, H. G., et al., "On the Equation of State of Mixed Oxide Fuel for the Analysis of Fast Reactor Disassembly Accidents," *Proceedings of the Fast Reactor Safety Meeting* (April 1974).
- Br72 Brook, A. J., "Some Preliminary Considerations Relating to an Equation of State for Irradiated Nuclear Fuel," *Nuclear Safety*, Vol 13, No. 6, pp 467-477 (November-December 1972).
- Br75 Breitung, W., "Calculation of Vapor Pressures of Oxide Fuels up to 5000 K in Equilibrium and Non-Equilibrium Evaporation," KFK 2091 (1975).
- Ca59 Carslaw, H. S., and J. C. Jaeger, *Conduction of Heat in Solids*, Oxford: Oxford University Press, pp 30-32 (1959).
- Ch73 Chasanov, M. G., L. Leibowitz, and S. D. Gabelnich, "High Temperature Physical Properties of Fast Reactor Materials," *J. Nucl. Mater.*, 49, pp 129-135 (1973).
- Co65 Cottrell, W. B., and A. W. Savolainen, eds., *U. S. Reactor Containment Technology*, Vol 1, ORNL-NSIC-5 (August 1965).
- Cr72 Croucher, D. W., D. M. Lucoff, T. R. Schmidt, K. O. Reil, and J. R. White, "Measured and Calculated Neutron Spectra in the Experimental Cavity of the ACPR," *Trans. Am. Nucl. Soc.*, 15 (2), pp 905-906 (1972).
- Cr75 Croucher, D. W., "An Examination of Thermal Stress as a Mechanism for Cladding Failure in a Hypothetical LMFBR Transient," A Doctoral Dissertation, University of New Mexico (1975).

- Di61 Dickerman, C. E., E. S. Sowa, D. Okrent, J. Monaweck, and C. B. Mellis, "Studies of Fast Reactor Fuel Element Behavior Under Transient Heating to Failure. I. Initial Experiments on Metallic Samples in the Absence of Coolant," ANL-6334 (August 1961).
- El71 El-Wakil, M. M., *Nuclear Energy Conversion*, Scranton, Pa., International Textbook Co., pp 276-308 (1971).
- Fi76 Fisher, E. A., P. R. Kinsman, and R. W. Ohse, "Critical Assessment of Equation of State Data for UO_2 ," *Journal of Nuclear Materials*, 59, pp 125-136 (1976).
- Ga72 Gabelnich, S. D., and M. G. Chasanov, *A Calculational Approach to the Estimation of Fuel and Fission-Product Vapor Pressures and Oxidation States to 6000 K*, ANL-7867 (October 1972).
- Ga76 Gac, Frank, CMB-6, Los Alamos Scientific Laboratories, letter to Daniel J. Sasmor, Sandia Laboratories (February 9, 1976).
- Gi75 Gillan, M. J., "Derivation of an Equation of State for Liquid UO_2 Using the Theory of Significant Structures," *Thermodynamics of Nuclear Materials*, 1974, International Atomic Energy Agency, Vienna, pp 269-285 (1975).
- He64 Heath, R. L., *Scintillation Spectrometry*, Vol I, Second Edition, Phillips Petroleum (August 1964).
- Hi65 Hicks, E. P., and D. C. Menzies, "Theoretical Studies on the Fast Reactor Maximum Accident in Proceedings of the Conference on Safety, Fuels, and Core Design in Large Fast Power Reactors," USAEC Report ANL-7120, pp 654-670 (October 11-14, 1965).
- Hi67 Hirakawa, N., "MARS - A Two Dimensional Excursion Code," Report APDA-198, Edison Electric Institute (June 1967).
- Ho59 Hougan, Olaf A., Et al., *Chemical Process Principles, Part II*, John Wiley and Sons, Inc., New York, pp 556-638 (1959).
- Ho72 Ho, C. Y., R. W. Powell, K. E. Lilay, "Thermoconductivity of the Elements," *Journal of Physical and Chemical Reference Data*, Vol I, II (1972).
- Iv62 Ivanov, V. E., et al., "Determination of the Vapor Pressures of Uranium-Containing Compounds," *Thermodynamics of Nuclear Materials*, International Atomic Energy Agency, Vienna, 735 (1962).

- Ja72 Jackson, J. F., and R. B. Nickolson, "VENUS-II: An LMFBR Disassembly Program," ANL-7951 (September 1972).
- Ka74 Katz, Morris Schwarzblat, *An Equation of State for Mixed-Oxide Fast Reactor Fuels*, Dissertation, University of Arizona (1974).
- Ke70 Kelber, C. N., et al., *Safety Problems of Liquid Metal Cooled Fast Breeder Reactors*, ANL-7659 (Reactor Technology) (February 1970).
- Ke73 Kelber, Charles N., "Phenomenological Research in LMFBR Accident Analysis," *Nuclear Safety*, Vol 14, No. 4, pp 304-314 (July-August 1973).
- La70 Lathrop, K. D., and F. W. Brinkley, "Theory and Use of the General Geometry TWOTRAN Program," LA-4432 (1970).
- Le67 Lewis, D. R., J. D. Gaski, and L. R. Thompson, "CINDA-3G, Chrysler Improved Numerical Differencing Analysis for Third Generation Computers," Chrysler Corporation Space Division, TN-AP-67-287 (1967).
- Le68 Lederer, C. M., J. M. Hollander, and I. Perlman, *Table of Isotopes*, Sixth Edition, John Wiley and Sons, Inc., New York (1968).
- Le76 Leibowitz, L., et al., *Properties for LMFBR Safety Analysis*, ANL-CEN-RSD-76-1 (1976).
- Ma74 Manson, S. S., "Non-Ferrous Alloys - Inconel Alloy 718," *Aerospace Structural Metals Handbook*, (March 1974).
- Me65 Meyer, R. A., B. Wolfe, and N. F. Friedman, "A Parameter Study of Large Fast Reactor Meltdown Accidents in Proceedings of the Conference on Safety, Fuels, and Core Design in Large Fast Power Reactors," USAEC Report ANL-7120, pp 671-685 (October 11-14, 1965).
- Me66 Menzies, D. C., *The Equations of State of Uranium Dioxide at High Temperatures and Pressures*, TRG Report 1119 (February 1966).
- Mi65 Miller, David, "A Critical Review of the Properties of Materials at High Temperatures and Pressures Significant for Fast Reactor Safety," ANL-7120, pp 641-653 (1965).
- Mi70 Miller, D., "The Effect of Melting on UO_2 Thermodynamic Properties," ANL-7610, pp 335-337 (1970).

- MW64 Meyer, R. A., and B. E. Wolfe, "High-Temperature Equations of State of Uranium Dioxide, *Transactions of the ANS*, Vol 7, No. 1, pp 111-112 (June 1964).
- Ni64 Nicholson, Richard B., "Methods for Determining the Energy Release in Hypothetical Fast Reactor Meltdown Accidents," *Nuclear Sciences and Engineering*, 18, pp 207-219 (1964).
- Oh66 Ohse, Roland, W., "High-Temperature Vapor Pressure Studies of UO_2 by the Effusion Method and Its Thermodynamics Interpretation," *The Journal of Chemical Physics*, Vol 44, No. 4, pp 1375-1378 (February 15, 1966).
- Oh75 Ohse, R. W., P. G. Berrie, H. G. Bogensberger, E. A. Fischer, "Measurement of Vapor Pressure of $(\text{U}, \text{Pu})\text{O}_2$ and UO_2 to 5000 K for Fast Reactor Safety Analysis and the Contribution of the Radial C Distribution to Fuel Pin Failure," *Thermodynamics of Nuclear Materials*, 1974, International Atomic Energy Agency (1975).
- Oh76 Ohse, R. W., P. G. Berrie, H. G. Bogensberger, E. A. Fischer, "Extension of Vapor Pressure Measurements of Nuclear Fuels $(\text{U}, \text{Pu})\text{O}_2$ and UO_2 to 7000 K for Fast Reactor Safety Analysis," *Journal of Nuclear Materials*, 59, pp 112-124 (1976).
- Ok59 Okrent, D., et al., "Ax-1, A Computing Program for Coupled Neutronics-Hydrodynamic Calculations on the IBM-704," USAEC Report ANL-5977 (May 1959).
- Ok69 Okrent, D., "Design and Safety in Large Fast Power Reactors," *Atomic Energy Review*, Vol 7, No. 2, pp 135-223 (1969).
- Po71 Powell, J. E., A. R. Phillips, H. L. Kefauver, "The Use of a Time-Shared, On-Line Computer to Support Basic and Applied Radiation Research," *IEEE Trans. on Nuclear Science*, Vol NS-18 (1), pp 307-311 (February 1971).
- Ra67 Rand, M. H., and T. L. Markin, "Some Thermodynamic Aspects of $(\text{U}, \text{Pu})\text{O}_2$ Solid Solutions and Their Use as Nuclear Fuels," *Thermodynamics of Nuclear Materials*, International Atomic Energy Agency, Vienna (1967).
- Re72 Reedy, G. T., and M. G. Chasanov, "Total Pressure of Uranium-Bearing Species over Molten Urania," *Journal of Nuclear Materials*, Vol 42, pp 341-344 (1972).
- Ro65 Roark, R. J., *Formulas for Stress and Strain*, New York: McGraw-Hill Book Company (1965).

- Ro66 Robbins, E. J., *Limits for the Equation of State of Uranium Dioxide*, TRG Report 1344 (October 1966).
- Sc74 Schmidt, T. R., D. M. Lucoff, K. O. Reil, and D. W. Croucher, "Pulsed Irradiation of Enriched UO_2 in the Annular Core Pulse Reactor (ACPR)," TRIGA's Owners Conference, Albuquerque, CONF-740206 (February 1974).
- Sh69 Sha, William T., and Alan E. Walter, "Fast Reactor Disassembly Calculation Utilizing a Temperature-Density Dependent Equation of State," *Transactions of the ANS*, Vol 12, No. 2, pp 825-826 (1969).
- Sh70 Sha, William T., and T. H. Hughes, "VENUS: A Two-Dimensional Coupled Neutronics-Hydrodynamics Computer Program for Fast Reactor Power Excursions," ANS-7701 (1970).
- Sh71 Sha, William T., and Alan E. Walter, "An Integrated Model for Analyzing Disruptive Accidents in Fast Reactors," *Nuclear Science and Engineering*, No. 44, pp 135-156 (1971).
- St75 Stearns, Samuel D., *Digital Signal Analysis*, Hayden Book Company, Inc., Rochelle, New Jersey (1975).
- Sz68 Szwarc, R., and R. E. Latta, "Vapor Pressure of Hypo-stoichiometric Urania as a Function of Composition," *Journal of the American Ceramic Society*, Vol 51, No. 5, pp 264-268 (May 1968).
- Te70 Tetenbaum, M., and P. D. Hunt, "Total Pressure of Uranium-Bearing Species over Oxygen-Deficient Urania," *Journal of Nuclear Materials*, Vol 34, pp 86-91 (1970).
- Ti77 Tills, Jack L., August W. Cronenberg, and Theodore R. Schmidt, "A Prediction of the Thermal Conductivity of UO_2 Vapor," *Journal of Nuclear Materials*, 67 (1977) - To be published.
- To67 Touloukian, Y. S., ed., *Thermophysical Properties of High Temperature Solid Materials*, Vol 1: Elements, MacMillan Company, New York, pp 83-191 (1967).

CURRICULUM VITAE

Kenneth O. Reil was born in 1947 in Reno, Nevada. He graduated from Carson City High School, Carson City, Nevada, as valedictorian of his class. In 1970, he graduated with High Distinction from the University of Nevada, Reno, with a Bachelor of Science degree in Engineering Science. He was elected to Phi Kappa Phi and Sigma Tau as a junior and received the 1970 Hamilton Watch Award at the University of Nevada. During his undergraduate studies, he was employed by the Laboratory of Atmospheric Physics, Desert Research Institute, University of Nevada. He pursued his graduate studies at the University of New Mexico with the support of an AEC/ERDA Special Fellowship. He received a Master of Science degree in Nuclear Engineering in 1972. Assisted by an Associated Western Universities Fellowship, Sandia Laboratories in Albuquerque, New Mexico, and the U. S. Nuclear Regulatory Commission, he continued his studies performing research involving pulsed irradiation of fast reactor fuel materials. He is married and has two children. He is currently working in the Reactor Studies Division of Sandia Laboratories performing inpile experimental fast reactor safety research.